

# EDITORIAL BOARD

Professor Dr. Roland Benz (*Wuerzburg, Germany*)  
Professor Dr. Hans G.L. Coster (*Sydney, Australia*)  
Dr. Wojciech Gozdz (*Warsaw, Poland*)  
Professor Dr. Yury A. Ermakov (*Moscow, Russia*)  
Professor Dr. Sylvio May (*Fargo, USA*)  
Professor Dr. Bruce L. Kagan (*Los Angeles, USA*)  
Professor Dr. Wolfgang Knoll (*Mainz, Germany*)  
Professor Dr. A. Leitmannova Liu (*USA*)  
Professor Dr. Reinhard Lipowsky (*Potsdam, Germany*)  
Professor Dr. Yoshinori Muto (*Gifu, Japan*)  
Professor Dr. Ian R. Peterson (*Coventry, UK*)  
Professor Dr. Tibor Hianik (*Bratislava, Slovakia*)  
Dr. Michael Rappolt (*Basovizza, Italy*)  
Professor Dr. Bernhard Schuster (*Vienna, Austria*)  
Professor Dr. Masao Sugawara (*Tokyo, Japan*)  
Professor Dr. Yoshio Umezawa (*Tokyo, Japan*)  
Professor Dr. Nir Gov (*Rehovot, Israel*)  
Professor Dr. Philip J. White (*Wellesbourne, UK*)  
Professor Dr. Mathias Winterhalter (*Bremen, Germany*)  
Professor Dr. Dixon J. Woodbury (*Provo, USA*)  
Professor Dr. P.B. Sunil Kumar (*Chennai, India*)  
Dr. Rumiana Dimova (*Germany*)

Academic Press is an imprint of Elsevier  
Linacre House, Jordan Hill, Oxford OX2 8DP, UK  
32 Jamestown Road, London NW1 7BY, UK  
30 Corporate Drive, Suite 400, Burlington, MA 01803, USA  
525 B Street, Suite 1900, San Diego, California 92101-4495, USA

First edition 2010

Copyright © 2010 Elsevier Inc. All rights reserved

No part of this publication may be reproduced or transmitted in any form or by any means, electronic or mechanical, including photocopy, recording, or any information storage and retrieval system, without permission in writing from the publisher

Permissions may be sought directly from Elsevier's Science & Technology Rights Department in Oxford, UK: phone (+44) 1865 843830, fax: (+44) 1865 853333; E-mail: [permissions@elsevier.com](mailto:permissions@elsevier.com). You may also complete your request online via the Elsevier homepage (<http://elsevier.com>), by selecting "Support & Contact" then "Copyright and Permission" and then "Obtaining Permissions"

#### Notice

No responsibility is assumed by the publisher for any injury and/or damage to persons or property as a matter of products liability, negligence or otherwise, or from any use or operation of any methods, products, instructions or ideas contained in the material herein. Because of rapid advances in the medical sciences, in particular, independent verification of diagnoses and drug dosages should be made

#### Library of Congress Cataloging-in-Publication Data

A catalog record for this book is available from the Library of Congress

#### British Library Cataloguing-in-Publication Data

A catalogue record for this book is available from the British Library

ISBN: 978-0-12-381013-7

ISSN: 1554-4516

For information on all Academic Press publications  
visit our website at [www.elsevierdirect.com](http://www.elsevierdirect.com)

Printed and bound in USA

10 11 12 10 9 8 7 6 5 4 3 2 1

Working together to grow  
libraries in developing countries

[www.elsevier.com](http://www.elsevier.com) | [www.bookaid.org](http://www.bookaid.org) | [www.sabre.org](http://www.sabre.org)

ELSEVIER

BOOK AID  
International

Sabre Foundation

## PREFACE

Volume 11 is a continuation of the previous concept where the subjects of the chapters cover a broad range of topics, from theoretical to experimental studies devoted to different lipid micro and nanostructures, including liposomes. Due to the extremely fast development of physics and chemistry of lipid structures, the contents of the *Advances in Planar Lipid Bilayers and Liposomes* are no longer limited to planar lipid bilayers and liposomes. Accordingly, this volume also includes chapters that describe interesting but diverse subjects such as molecular interpretation of lipid droplet biogenesis, electroporation of planar lipid bilayers, formation of stable and reproducible bilayer lipid membranes based on silicon microfabrication techniques, electrostatics of charged planar lipid bilayers, X-ray and neutron scattering studies of lipid-sterol lipid membranes, and molecular modeling of lipid bilayers.

I would like to express my gratitude to all authors who have contributed their chapters—Drs. J. Zanghellini, P. Kramar, A. Hirano-Iwata, S. Takeuchi, E. Gongadze, V.A. Raghunathan, Roland Faller, and their co-authors. I also very much appreciate the continuous support of Clare Caruana from Elsevier Office in London together with her coworkers from Elsevier's Chennai Office in India, Paul Prasad Chandramohan and Ezhilvijayan Balakrishnan. I would like to use this occasion to express my gratitude to the new members of the Editorial Board of APLBL, Dr. Rumiana Dimova, Prof. Sylvio May, Prof. P.B. Sunil Kumar, Prof. Nir Gov, Prof. Tibor Hianik, Dr. Michael Rappolt, and Dr. Wojciech Gozdz, who did most of the work in preparing this volume of APLBL. Special thanks to the previous editor Prof. Angelica Leitmannova Liu.

Aleš Iglič  
Editor

# CONTRIBUTORS

## **Klemen Bohinc**

Faculty of Health Sciences, University of Ljubljana, Zdravstvena pot 5, SI-1000 Ljubljana, Slovenia and Laboratory of Biophysics, Faculty of Electrical Engineering, University of Ljubljana, Tržaška 25, SI-1000 Ljubljana, Slovenia

## **Roland Faller**

Department of Chemical Engineering & Materials Science, University of California-Davis, One Shields Avenue, Davis, California, USA

## **Ekaterina Gongadze**

Institute of General Electrical Engineering, University of Rostock, Justus-von-Liebig-Weg 2, 18059 Rostock, Germany

## **Ayumi Hirano-Iwata**

Graduate School of Biomedical Engineering, Tohoku University, 6-6-04 Aoba, Aramaki, Aoba-ku, Sendai, Japan and PRESTO, Japan Science and Technology Agency (JST), 4-1-8 Honcho Kawaguchi, Saitama, Japan

## **Aleš Igljč**

Laboratory of Biophysics, Faculty of Electrical Engineering, University of Ljubljana, Tržaška 25, SI-1000 Ljubljana, Slovenia

## **Christian Jungreuthmayer**

Austrian Institute of Technology, Wien, Austria

## **Sanat Karmakar**

Department of Physics, Jadavpur University, Kolkata 700 032, India

## **Yasuo Kimura**

Laboratory for Nanoelectronics and Spintronics, Research Institute of Electrical Communication, Tohoku University, 2-1-1 Katahira, Aoba-ku, Sendai, Miyagi, Japan

## **Malgorzata Kotulska**

Institute of Biomedical Engineering and Instrumentation, Wroclaw University of Technology, Wroclaw, Poland

**Veronika Kralj-Iglič**

Laboratory of Clinical Biophysics, Faculty of Medicine, University of Ljubljana, Lipičeva 2, SI-1000 Ljubljana, Slovenia

**Peter Kramar**

Faculty of Electrical Engineering, University of Ljubljana, Ljubljana, Slovenia

**Alenka Maček Lebar**

Faculty of Electrical Engineering, University of Ljubljana, Ljubljana, Slovenia

**Damijan Miklavčič**

Faculty of Electrical Engineering, University of Ljubljana, Ljubljana, Slovenia

**Michio Niwano**

Graduate School of Biomedical Engineering, Tohoku University, 6-6-04 Aoba, Aramaki, Aoba-ku, Sendai, Japan and Laboratory for Nanoelectronics and Spintronics, Research Institute of Electrical Communication, Tohoku University, 2-1-1 Katahira, Aoba-ku, Sendai, Miyagi, Japan

**Azusa Oshima**

Graduate School of Biomedical Engineering, Tohoku University, 6-6-04 Aoba, Aramaki, Aoba-ku, Sendai, Japan

**V.A. Raghunathan**

Raman Research Institute, Bangalore 560 080, India

**David Ruckerbauer**

Institute of Molecular Biosciences, University of Graz, Graz, Austria

**Bibhu Ranjan Sarangi**

Raman Research Institute, Bangalore 560 080, India

**Shoji Takeuchi**

Center for International Research on Micro/Nano Mechatronics (CIRMM), Institute of Industrial Science (IIS), The University of Tokyo, Japan and Kanagawa Academy of Science and Technology (KAST), Japan

**Ursula van Rienen**

Institute of General Electrical Engineering, University of Rostock, Justus-von-Liebig-Weg 2, 18059 Rostock, Germany

**Hans-Hennig von Grünberg**

Institute of Chemistry, University of Graz, Graz, Austria

**Florian Wodlei**

Institute of Chemistry, University of Graz, Graz, Austria

**Chenyue Xing**

MAP Pharmaceuticals Inc., Mountain View, California, USA

**Jürgen Zanghellini**

Phenomics and Bioinformatics Research Centre, School of Mathematics and Statistics, University of South Australia, Mawson Lakes 5095 SA, and Australian Centre for Plant Functional Genomics, Hartley Grove, Urrbrae PMB 1 Glen Osmond SA 5064, Australia

# PHOSPHOLIPID DEMIXING: MOLECULAR INTERPRETATION OF LIPID DROPLET BIOGENESIS

Jürgen Zanghellini,<sup>1,\*</sup> David Ruckerbauer,<sup>2</sup> Florian Wodlei,<sup>3</sup> Hans-Hennig von Grünberg,<sup>3</sup> and Christian Jungreuthmayer<sup>4</sup>

## Contents

1. Introduction	2
2. Theoretical Model	4
2.1. Shape Approximation	5
2.2. Free Gibbs Energy of an LD	6
2.3. Parameter Estimation	7
3. Molecular Interpretation	11
4. Results	12
5. Discussion	19
5.1. Lipid Demixing in Curved Membrane Regions	19
5.2. Demixing Forces Induce Membrane Curvature	20
5.3. Demixing—A Potential Method to Recruit Proteins from the ER Membrane	21
5.4. The Birth of a Lipid Droplet	21
5.5. Model Limitations	23
6. Summary	24
Acknowledgments	25
References	25

## Abstract

The biogenesis of lipid droplets (LDs) in the yeast *Saccharomyces cerevisiae* was theoretically investigated on the basis of a biophysical model. In accordance with the prevailing model of LD formation, we assumed that neutral lipids

\* Corresponding author. E-mail address: [juergen.zanghellini@unisa.edu.au](mailto:juergen.zanghellini@unisa.edu.au)

<sup>1</sup> Phenomics and Bioinformatics Research Centre, School of Mathematics and Statistics, University of South Australia, Mawson Lakes 5095 SA, and Australian Centre for Plant Functional Genomics, Hartley Grove, Urrbrae PMB 1 Glen Osmond SA 5064

<sup>2</sup> Institute of Molecular Biosciences, University of Graz, Graz, Austria

<sup>3</sup> Institute of Chemistry, University of Graz, Graz, Austria

<sup>4</sup> Austrian Institute of Technology, Wien, Austria

oil-out between the membrane leaflets of the endoplasmic reticulum (ER), resulting in LDs that bud off when a critical size is reached.

Mathematically, LDs were modeled as spherical protuberances in an otherwise planar ER membrane. We estimated the local phospholipid (PL) composition, and calculated the change in elastic free energy of the membrane caused by nascent LD. Our simulations are based on the phenomenological Helfrich Hamiltonian. However, by describing lipids as compressible cones, we demonstrate that the Hamiltonian can easily be reformulated to support a molecular interpretation. Based on this model calculation, we found a gradual demixing of lipids in the membrane leaflet that goes along with an increase in surface curvature at the site of LD formation. While demixing, the PL monolayer was able to gain energy during LD growth, which suggested that the formation of curved interfaces was supported by or even driven by lipid demixing. In addition, we show that demixing is thermodynamically necessary as LDs cannot bud off otherwise.

In the case of *S. cerevisiae*, our model predicts an LD bud-off diameter of about 12 nm. This diameter is far below the experimentally determined size of typical yeast LD. Thus, we concluded that if the standard model of LD formation is valid, LD biogenesis is a two-step process. Small LDs are produced from the ER, which subsequently ripe within the cytosol through a series of fusions.

## 1. INTRODUCTION

Lipid droplets (LDs) are depots for neutral lipids (NL). They exist virtually in all kinds of living cells, from bacteria, to yeasts, to plants and mammals. A LD consists of a hydrophobic, NL-containing core surrounded by a phospholipid (PL) monolayer containing a small amount of proteins [1]. In *Saccharomyces cerevisiae*, LDs are mainly formed by triacylglycerols (TAG) and steryl esters (SE) in roughly equal amounts [2–4]. Conversion of free fatty acids (FAs) and sterols to NL and their subsequent storage in LDs is an organism's strategy to risklessly save intrinsically toxic FA and sterols for later use. If required, FAs and sterols may be rapidly released from LDs and used as prefabricated building blocks for membrane lipid synthesis as well as other complex lipids, and/or as a source of chemical energy [5–7]. Also, LDs are assumed to have a function in transporting sterols to the plasma membrane [3]. Indeed, it is now recognized that rather than being inert storage pools, LDs are remarkably flexible, dynamic organelles [6,8,9]. LD biogenesis is everything but clear. According to a widely accepted model, NL accumulate within distinct regions of the endoplasmic reticulum (ER) membrane, initially forming a lens-shaped and then a spherical bulge in the membrane (Fig. 1). After reaching a critical size, mature LDs will bud off, being encapsulated in a PL monolayer that is directly derived from the cytoplasmic ER leaflet [1,3,5,6,10]. This budding model is in line with several experimental findings. (i) In yeast, the same ER proteins, except for



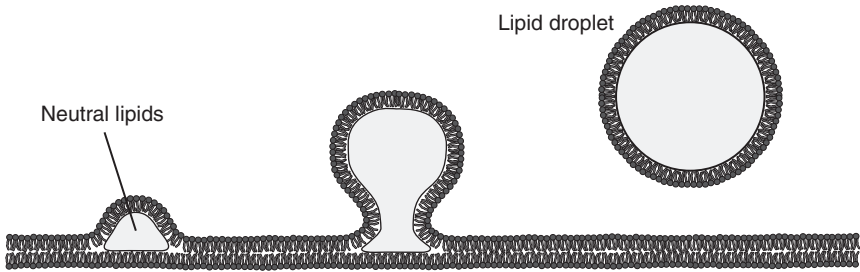


**Figure 1** LD formation according to the standard model. During their biosynthesis, NL “oil-out” in between the leaflets of the ER bilayer, forming spherical structures. Mature LDs then bud off and form independent organelles.

very few, are also detected on the LD membrane [11,12]. (ii) Most LD proteins lack transmembrane spanning domains [13]. (iii) In yeast mutants which are unable to synthesize TAG and SE, LDs do not form. Nonetheless all typical LD proteins are found in these strains, but now solely localized to the ER [14] and the cytosol. It has also been hypothesized that developing LDs might not bud off, but are cut out from the ER in form of bicelles, leaving a transient hole in the ER membrane [15].

A nascent LD trapped within the leaflets of the ER has never been observed experimentally, thus other mechanisms for its formation have been suggested (see Refs. [16,17] for reviews). The most prominent alternative is based on vesicular budding [18–20]. In such a process small bilayer vesicles are formed, which are subsequently filled with NL [21,22]. As yet, neither model has been conclusively verified experimentally. Whether this has to be attributed to low resolution of microscopic approaches or indicates that the proposed scenarios are wrong is still a matter of debate. In this chapter, we take up the former position. Moreover, we here assume that LD formation takes place according to Fig. 1. That is to say, NL-filled bulges are formed in the cytosolic monolayer of the ER membrane, from where they subsequently bud off. Taking this scenario seriously, we calculate biophysical consequences for the process of LD biogenesis.

Our analysis has been motivated by experimental findings in yeast that the PL monolayer composition of LD differs from the ER membrane [2,23,24]. This suggests that the PL composition is related to the local curvature of the monolayer in agreement with similar observations from theory and experiment [25,26]. Lipids with a cone-like molecular shape (inducing a positive or convex curvature) are expected to be more adapted to the spherical surface of LD than wedge-like shaped ones, which induce a negative or concave curvature. Thus, the former should be enriched on LD surfaces (relative to their value in the ER membrane) while the latter ought to be depleted. For instance, due to their geometrical shape, we expect to find more lysophosphatidylcholine (LPC) and less phosphatidylethanolamine (PE) in the membrane of LD compared to the ER.

In contrast to the well-established view that PL demixing is curvature-dependent, we here argue the converse, that is, that the demixing of a lipid membrane supports the generation of membrane curvature. We use yeast LDs as an example and present calculations based on the standard model of LD formation. They reveal that due to lipid demixing, the PL monolayer is able to gain energy during its shape transition, thus supporting LD formation. Additionally, we show that depending on its volume and the curvature of its surface, a nascent LD is prevented from budding-off through a demixing-controlled energy barrier, the height of which decreases with increasing LD volume. We predict that at an LD diameter of about 12 nm, this barrier completely vanishes and the LD is released from the ER. We thus address two essential questions [5]: How do nascent LDs bud off from membranes? How is the mature size of LDs determined?

## 2. THEORETICAL MODEL

To study local deformations in an extended lipid monolayer, we use the Helfrich Hamiltonian [27],

$$U = \int_{\mathcal{A}} dA \left\{ \frac{k_c}{2} [H(\mathbf{r}) - 2c_0]^2 + \bar{k}_c K(\mathbf{r}) \right\}, \quad (1)$$

which relates the local total and Gaussian curvature,  $H = c_1 + c_2$  and  $K = c_1 c_2$ , respectively, of a two-dimensional surface,  $\mathcal{A}$ , to its elastic energy,  $U$ . Here,  $c_1$  and  $c_2$  denote the two principal curvatures at any given point  $\mathbf{r}$  on the surface. The thin lipid membrane is characterized by its spontaneous curvature,  $c_0$ , and its mean and Gaussian bending moduli,  $k_c$ , and  $\bar{k}_c$ , respectively.

Equation (1) describes a continuous membrane, without any reference to its internal structure. However, to be able to model a mixed membrane (i.e., a membrane consisting of various different types of PLs), we assume that Eq. (1) is valid not only for a monolayer as a whole but also for every single PL molecule. Thus,

$$U_i(\mathbf{r}) = A_{p,i} \left\{ \frac{k_{c,i}}{2} [H(\mathbf{r}) - 2c_{0,i}]^2 + \bar{k}_{c,i} K(\mathbf{r}) \right\}, \quad (2)$$

denotes the potential energy of a single lipid where the index  $i$  distinguishes between the different types of PLs (PE, LPC, ..., see below). In this equation, we assume that across each molecule's head-group area the change in the local membrane curvature is so small, that the integration in Eq. (1) simplifies to a multiplication with the pivotal area,  $A_{p,i}$ , occupied by a lipid of type  $i$ . The pivotal area of lipid,  $A_{p,i}$ , is defined as the area that remains

unchanged in its size upon spherical bending [28] (see Fig. 3 for an illustration). Note that in writing Eq. (2), we disregard contributions due to orientational ordering [29], and implicitly assume properly aligned lipids.

We may construct the PL monolayer's average free Gibbs energy,  $G$ , per lipid, as the sum of independent, single molecule energies,  $U_i$ , plus their corresponding configuration entropies, that is,

$$g := \frac{G}{N} = \frac{1}{\mathcal{A}} \int_{\mathcal{A}} dA \sum_{i=1}^n [x_i U_i(\mathbf{r}) + x_i k_B T \ln x_i], \quad (3)$$

with,  $x_i$ , the local lipid mole fraction in the membrane;  $n$ , the number of lipid species in the monolayer; and,  $N$ , the total number of lipids. In the special case of a planar membrane ( $H \rightarrow 0, K \rightarrow 0$ )  $g$  approaches

$$g_p = \sum_{i=1}^n x_{p,i} \mu_{p,i}, \quad \mu_{p,i} = 2k_{c,i} c_{0,i}^2 + k_B T \ln x_{p,i}, \quad (4)$$

where we have used  $x_{p,i}$  and  $\mu_{p,i}$  to denote the mole fraction and chemical potential of a flat membrane, respectively.

According to Eq. (3), the elastic energy of a mixed membrane depends on both its composition and the local curvature of the surface. We are interested in whether or not the total, interfacial energy of curved membrane surfaces can be reduced by changing the lipid composition relative to the composition of the flat membrane.

In equilibrium, the local lipid composition,  $x_i$ , in Eq. (3) is given by the Boltzmann factor,

$$x_i = \frac{\exp[-(U_i(\mathbf{r}) - \mu_{p,i})/k_B T]}{\sum_{j=1}^n \exp[-(U_j(\mathbf{r}) - \mu_{p,j})/k_B T]}, \quad (5)$$

and can be interpreted as the probability for a lipid of type  $i$  to populate regions of energy  $U_i(\mathbf{r})$ , while the planar part of the membrane acts as a reservoir, which either provides or absorbs lipids depending on the difference between  $x_j$  and  $x_{p,j}$ . Note that for a flat membrane, Eq. (5) recovers the limiting planar lipid composition, that is, ( $H \rightarrow 0, K \rightarrow 0$ )  $\Rightarrow x_i \rightarrow x_{p,i}$ .

## 2.1. Shape Approximation

Equations (3) and (5) allow to estimate the energy change caused by local adaptations of both the lipid composition and the surface curvature. Next, we make further assumptions regarding the shape evolution of emerging LD that form from initially flat ER membranes.

In every stage of their biogenesis, nascent LDs are assumed to form perfectly spherical protuberances of cap radius,  $R_c$ . The spherical cap approximation assumes a sudden transition from the planar to the spherical region of the membrane.

Figure 2 illustrates two possible geometrical configurations. In both cases, the total volume of the LD,  $V_{\text{cap}}$ , is identical. In the following, it is convenient to discuss the effect of the LD volume in terms of the radius,  $R_{\text{LD}}$ , of an associated, full sphere of equal volume.

If we let  $R_c$  denote the radius of a spherical cap, the cap surface  $A_c(R_c, R_{\text{LD}})$  enclosing a cap volume  $V_{\text{cap}} = 4\pi R_{\text{LD}}^3/3$ , as well as its corresponding pinch-off area  $A_1(R_c, R_{\text{LD}})$ , can be written as

$$A_c(R_c, R_{\text{LD}}) = 2\pi R_c^2 H(R_{\text{LD}}/R_c), \quad (6)$$

$$A_1(R_c, R_{\text{LD}}) = \pi R_c^2 [2H(R_{\text{LD}}/R_c) - H^2(R_{\text{LD}}/R_c)], \quad (7)$$

$$H(x) = 1 - 2 \cos \left[ \frac{1}{3} \arccos(1 - 2x^3) + \frac{\pi}{3} \right], \quad (8)$$

where  $H_c = R_c H(R_{\text{LD}}/R_c)$  gives the total height of the spherical calotte (see Fig. 2). While  $R_{\text{LD}}$  is a measure of the LD volume, the radius  $R_c$  is the representative of the shape of the nascent LD. A LD detaches if its pinch-off area,  $A_1$ , vanishes. Thus, for matured LDs,  $R_{\text{LD}} = R_c$  and  $H(1) = 2$ , such that  $A_1 = 0$  and  $A_c = 4\pi R^2$ .

## 2.2. Free Gibbs Energy of an LD

In the spherical cap approximation, the local and Gaussian curvatures are independent of the position on the cap surface and simply given by  $H = 2/R_c$  and  $K = 1/R_c^2$ , respectively. Thus, the free Gibbs energy per lipid,

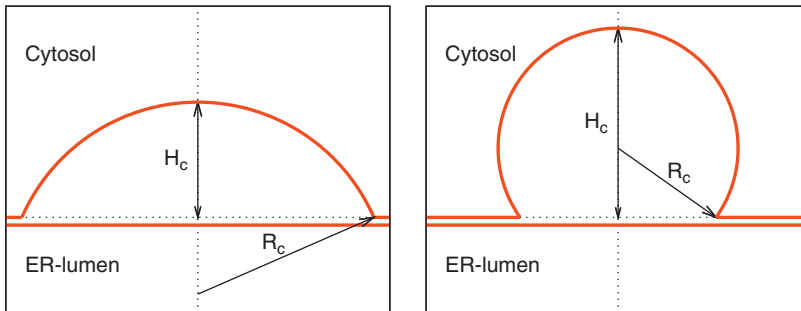


**Figure 2** A LD is modeled as a spherical cap of radius,  $R_c$ , and height  $H_c$ , in an otherwise planar membrane (sectional view). Thick lines represent the cytosolic and luminal leaflets of the ER membrane. The two panels illustrate situations for different values of  $R_c$ , but constant cap volume,  $V_{\text{cap}}$ .

$$g_{\text{cap}}(R_c) = \sum_{i=1}^n [x_i U_i(R_c) + x_i k_B T \ln x_i], \quad (9)$$

depends parametrically on the cap radius.

With an expression for the surface at hand it is possible to estimate the average number of lipids on nascent LDs as  $N_{\text{cap}} = \sum_{i=1}^n x_i A_c / A_{p,i}$ , as well as the number of lipids which originally were found in the pinch-off area but migrated as  $N_p = \sum_{i=1}^n x_{p,i} A_1 / A_{p,i}$ . Then, the change in Gibbs energy due to demixing becomes

$$\Delta G_{\text{mix}} = N_{\text{cap}} g_{\text{cap}} - N_p g_p. \quad (10)$$

The difference in the lipid composition of the LD and ER monolayer causes tension at the contact line between the domains, which adds to the total energy. The corresponding energy density is called line tension,  $\tau$ . It measures the excess free energy along the domain boundary, that is, the circumference of the LD neck. Thus, the edge energy is given by

$$\Delta G_{\text{edge}} = 2\pi R_1 = 2\sqrt{\pi A_1 (R_c, R_{\text{LD}})}. \quad (11)$$

$R_1 = \sqrt{A_1/\pi}$  denotes the neck radius of the LD according to Eq. (7).

Finally, the total change in Gibbs energy is given by the sum of these contributions, that is,

$$\Delta G = \Delta G_{\text{mix}} + \Delta G_{\text{edge}} \quad (12)$$

$$\Delta G = N_{\text{cap}} g_{\text{cap}} - N_p g_p + 2\sqrt{\pi A_1}. \quad (13)$$

In the following, we will keep the total LD volume,  $V_{\text{cap}}$ , constant and ask which configuration, of all possible values of  $R_c$ , is energetically favored.

### 2.3. Parameter Estimation

Glycero-PLs, in particular phosphatidic acid (PA), phosphatidyl choline (PC), PE, phosphatidyl inositol (PI), LPC, and phosphatidyl serine (PS), are major constituents of ER membranes [23]. According to Eq. (2), our modeling approach requires four characteristic numbers per lipid species  $i$ , two of which provide structural information ( $A_{p,i}$  and  $c_{0,i}$ ), while the remaining two describe elastic properties ( $k_{c,i}$  and  $\bar{k}_{c,i}$ ). The latter were found to vary little for different lipid species [30], and experimental results suggest that

$$\bar{k}_{c,i} \approx 0.8k_{c,i}, \quad (14)$$

irrespective of specific lipids [30].

However, literature values on geometrical data for lipids scatter substantially. Partly because data, such as the head-group area or chain length, depend on temperature, salt content, the phase of the membrane, etc., but also because of variations in experimental methods. For instance, Ref. [31] presents 10 published head-group areas for fluid phase dipalmitoyl-PC, ranging from 57 to 73 Å<sup>2</sup>. We have compiled representative values of structural data of lipids (Table 1), being fully aware that these values may only be considered as rough estimates.

PE is the only lipid for which both,  $a_{0,i} = 54$  Å<sup>2</sup> and  $b_{0,i} = 105$  Å<sup>2</sup> have been determined experimentally [33]. Together with  $c_{0,i} = -0.043$  Å<sup>-1</sup> [28] and Eq. (15), one obtains  $l_i = 22$  Å, which is roughly half the thickness of a

**Table 1** Structural data of various PLs

	PE	PA	PC	PS	PI	O-LPC
$a_{0,i}$ (Å <sup>2</sup> )	54 <sup>a</sup>	45 <sup>*</sup>	72 <sup>b,c</sup>	54 <sup>d</sup>	84 <sup>*</sup>	60 <sup>a</sup>
$A_{p,i}$ (Å <sup>2</sup> )	73 <sup>a</sup>	59 <sup>*</sup>	82 <sup>e</sup>	50 <sup>*</sup>	75 <sup>*</sup>	45 <sup>a</sup>
$b_{0,i}$ (Å <sup>2</sup> )	105 <sup>a</sup>	73	87.8	45	65 <sup>*</sup>	33
$S_i$	1.47	1.31	1.11	0.92	0.89	0.78
$c_{0,i}$ (Å <sup>-1</sup> )	-0.043	-0.029	-0.010	0.0075	0.01	0.020
$R_{w,i}$ (Å)	-23 <sup>f</sup>	-35	-100	133	100	49
$R_{p,i}$ (Å)	-28.5 <sup>g</sup> -30 <sup>j</sup>	-46 <sup>h</sup>	-87.3 <sup>i</sup> -95 <sup>b</sup> -143 <sup>e</sup>	144 <sup>j</sup>	89	38 <sup>a</sup>
$k_{c,i}$ (k <sub>B</sub> T)	11.34 <sup>k</sup>	10 <sup>*</sup>	9 <sup>i</sup>	10 <sup>j</sup>	10 <sup>*</sup>	10 <sup>*</sup>
$\bar{k}_{c,i}$ (k <sub>B</sub> T)	8.8	8	7.2	8	8	8

Literature values are marked by alphabetical footnotes, estimated values are indicated with <sup>\*</sup>, calculated values [using Eqs. (14)–(16)] are printed without any tag, and framed lines contain data which enter the calculation. (Additionally, we use the line tension,  $\tau = 0.024k_B T/\text{Å}$  [32].) Abbreviations:  $a_0$ , lipid head-group area;  $A_p$ , molecular area of the pivotal plane;  $b_0$ , base area;  $S$ , shape factor;  $c_0$ , spontaneous curvature of the membrane monolayer;  $R_w$ , cylinder radius to the lipid–solvent interface;  $R_p$ , cylinder radius to the pivotal plane;  $k_c$  and  $\bar{k}_c$ , mean and Gaussian curvature elastic moduli, respectively.

<sup>a</sup> Ref. [33].

<sup>b</sup> Ref. [28].

<sup>c</sup> Ref. [36].

<sup>d</sup> Ref. [37].

<sup>e</sup> Ref. [30].

<sup>f</sup> Ref. [34].

<sup>g</sup> Ref. [35].

<sup>h</sup> Ref. [31].

<sup>i</sup> Ref. [38].

<sup>j</sup> Ref. [39].

<sup>k</sup> G. Pabst, Unpublished data.

typical PE bilayer ranging between 40 and 50 Å [40]. It also compares well with the value  $l = 18 \text{ Å}$  obtained by Marsh [35].

To estimate data for PC, we followed an idea of Marsh [30], who estimated  $c_0$  values for lipid dioleoylphosphatidyl-PE/DOPC mixtures by fitting experimental data [28]. We assumed  $a_{0,i}$  of PC to be  $72 \text{ Å}^2$  [31,35] and used Eq. (15) as fitting function for the data in Ref. [28]. An excellent fit is obtained, giving a value of  $b_{0,i} = 87.8 \text{ Å}^2$  and subsequently  $c_{0,i} = -0.01 \text{ Å}^{-1}$ , which agrees with the values given in Refs. [35,38,39].

For PA, PI, and PS, the situation is less clear. As we have been unable to find experimentally measured head-group areas of PA and PI, we have estimated these values by extrapolating the linear relationship between molecular volume and head-group area obtained for PC, PE, and O-LPC. Also, the molecular area at the pivotal plane  $A_{p,i}$  is unknown for PS, PI, and PA; again, values have been guessed by comparison with corresponding values of other lipids.

Here, we describe lipids based on a geometrical packing parameter,  $S_i$ , which roughly characterizes the shapes of lipids by relating their entire volume  $V_i$ , to the volume given by their head-group areas  $a_{0,i}$ , times the lipid length  $l_i$ , that is,  $S_i = V_i/(a_{0,i}l_i)$ . Then the spontaneous curvature,  $c_{0,i}$ , of a monolayer of identical lipids for a cylindrical system can be expressed as [35,41]

$$c_{0,i} = \frac{1}{R_{w,i}} = \frac{2}{l_i}(1 - S_i) = \frac{1}{l_i} \left( 1 - \frac{b_{0,i}}{a_{0,i}} \right). \quad (15)$$

In the last part of the equation, we have approximated the volume of a PL by the volume of a truncated cone,  $V_i = (a_{0,i} + b_{0,i})l_i/2$ , where  $a_{0,i}$  and  $b_{0,i}$  are the lipid's head- and base area, respectively (Fig. 3).  $R_{w,i}$  is typically measured in fully hydrated lipid phases and refers to the radius of curvature of the lipid-water interface. For simplicity and despite substantial variations in the lipid's length, we assume that all lipid-types are basically as long as PE, that is,  $l = l_i = 22 \text{ Å}$  [28]. To further ease analysis, we define the pivotal plane to sit midway between the base and head area of a lipid, thus

$$R_{w,i} = R_{p,i} + l/2. \quad (16)$$

However, according to experiments the neutral plane sits closer to the boundary between the hydrocarbons and polar group. For PE, a representative value is  $0.37l$  [33].

A classification according to the packing parameter,  $S$ , reveals three major groups; PE and PA have  $S_i \gg 1$ , forming wedge-shaped, inverted truncated cones, while PC as well as PS, with  $S \approx 1$ , are quite cylindrical in shape.

Finally, PI and LPC have  $S$  values between 0.7 and 0.9, corresponding to truncated cones with lipid foot areas much smaller than their head-group areas.

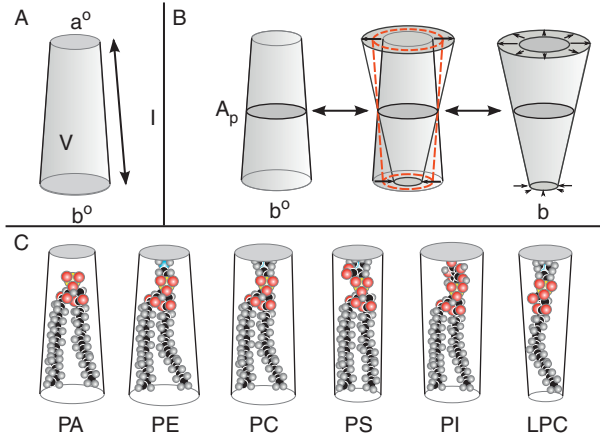


**Figure 3** Characterization of different PL according to their structure factor,  $S_i = (1 + b_0/a_{0,i})/2$ , panel A and C.  $S > 1$  indicates a cone-like shape, which favors concave membranes.  $S < 1$  describes lipids as inverted cones, which produce convex curvatures. Panel B illustrates the pivotal plane, which by definition does not change in size upon spherical bending.

**Table 2** Literature values for experimentally measured PL composition of ER ( $x_{pi}$ ) and LD ( $x_i$ ) membranes

	PE	PC	PS	PI	O-LPC	PA
$x_{p,i}^a$	0.336	0.515	0.068	0.077	0.002	0.002
$x_i^a$	0.243	0.382	0.141	0.208	0.013	0.013
$x_i^b$	0.203	0.368	0.055	0.320	0.027	0.027

Data listed in Refs. [2,23] for “other lipids” have been redistributed such that each column sums up to one. An illustration of these data sets may be found in Fig. 10.

<sup>a</sup> Ref. [23].

<sup>b</sup> Ref. [2].

Finally, Table 2 lists PL compositions of membranes for both the LD [2,23] and the ER [23]. The two data sets agree well for PC and PE, showing a considerable reduction of both lipids in the LD membrane relative to the ER. Also, both data sets reflect a substantial increase in PA and PI. Conflicting results are obtained for PS; while the fraction of PS is doubled in Ref. [23], it is found to be slightly reduced in Ref. [2]. Precise values for LPC are not known, but it has been reported that LPC is enriched in the LD membrane [42]. To study the packing effects even on LPC, we assume its  $x_{p,i}$  equal to that of PA.

The line tension,  $\tau$ , between the LD and ER domain will, in general, be influenced by the compositional differences between them [43,44].



However, to simplify analysis, we assume  $\tau$  to be constant. Theoretical studies suggest values for the line tension in the order of 10 pN [45,46]. On the other hand, recent measurements show that these values are over-estimated by an order of magnitude [32,43,47]. Hence, we set  $\tau = 1$  pN [32].

### 3. MOLECULAR INTERPRETATION

In this work, we have characterized lipids as small, truncated cones. These cones are compressible and tightly packed in order to form a continuous membrane (Fig. 4). This means that depending on its initial shape, the lipid's head and foot area are either stretched or compressed. However, since we only assume spherical bending, the pivotal plane,  $A_{p,i}$ , remains unchanged. Thus, if the foot is stretched, the head is compressed, and vice versa. If such a lipid cone sits on a spherical region, then the ratios of various cone areas are given by the radius of curvature of the sphere (see Figs. 3 and 4),

$$b_i/A_{p,i} = [1 - l/(2R_c)]^2 \approx 1 - l/R_c, \quad (17)$$

$$\frac{b_i}{a_i} = \left(\frac{R_c - l/2}{R_c + l/2}\right)^2 \approx \left(1 - \frac{l}{R_c}\right)^2 \approx \frac{b_i^2}{A_{p,i}^2}, \quad (18)$$

if  $l/2 \ll R_c$ . Here,  $b_i$  and  $a_i$  denote the deformed foot and head areas of the lipid cones.

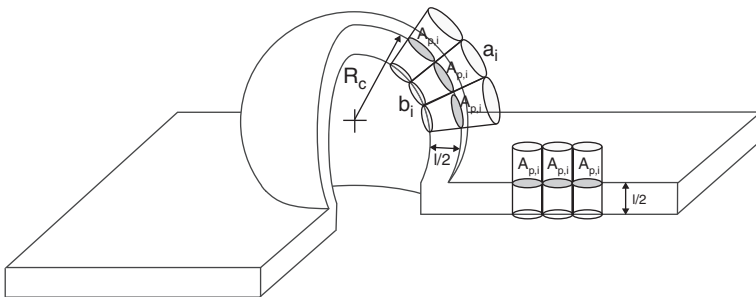


**Figure 4** Spherical protuberance of radius,  $R_c$ , representing a nascent LD, in an otherwise planar leaflet of the ER membrane.  $l/2$  is the distance between the lipid's base area,  $b_i$ , and its pivotal area,  $A_{p,i}$ . While  $A_{p,i}$  is independent of the local curvature, the foot area  $b_i$ , decreases with increasing curvature. Thus, compression is strongest for lipids with  $S > 1$  and weaker for lipids with  $S < 1$ , making it energetically favorable to change the lipid composition on the protuberance relative to its value in the plane.

These relations allow to express the mean and Gaussian curvature,  $H = 2/R_c$  and  $K = 1/R_c^2$  of a sphere in terms of the dimension of the lipid cones on that surface, that is,

$$H = 2(1 - b_i/A_{p,i})/l, \quad K = (1 - b_i/A_{p,i})^2/l^2. \quad (19)$$

Finally, on combining these expressions with Ref. (15), we can restate the Helfrich energy of a single lipid cone, Eq. (2), in terms of its molecular properties,

$$U_i = \frac{1}{A_{p,i}l^2} [2k_{c,i}(b_i - \alpha b_{0,i})^2 + \bar{k}_{c,i}(b_i - A_{p,i})^2], \quad (20)$$

with  $\alpha = b_{0,i}/A_{p,i}$ . Rewritten in this way, the Helfrich energy can be easily understood in terms of harmonic potentials, that is, lipids act as linear elastic materials (springs) according to Hooke's law. We may use the aforementioned expression together with Eq. (2) and solve for

$$b_i = A_{p,i} \left[ \frac{2\alpha^2 k_{c,i} + \bar{k}_{c,i}}{2k_{c,i} + \bar{k}_{c,i}} + \sqrt{\frac{U_i l^2}{A_{p,i}(2k_{c,i} + \bar{k}_{c,i})} - \frac{2(1 - \alpha^2)^2 k_{c,i} \bar{k}_{c,i}}{(2k_{c,i} + \bar{k}_{c,i})^2}} \right] \quad (21)$$

to get insight into internal stress conditions. For  $R_c \rightarrow \infty \Rightarrow U_i \rightarrow 2A_{p,i} k_{c,i} c_{0,i}^2$  and using Eq. (18) to approximate  $c_{0,i} l \approx 1 - \alpha^2$ , we retrieve  $b_i \rightarrow A_{p,i}$  consistent with Eq. (17).

## 4. RESULTS

The optimal PL composition,  $x_i$ , of an LD membrane was evaluated as a function of cap radius,  $R_c$ , using Eq. (5). Figure 5 illustrates the predicted lipid distribution in the LD monolayer (upper panel) originating from a planar ER with PL composition according to Ref. [23].  $R_c$  represents the radius of a spherical protuberance in an otherwise planar lipid layer (Fig. 2). Its inverse,  $c = 1/R_c$ , may be interpreted as the mean curvature of the associated sphere and Fig. 5 can be understood in terms of the curvature dependence of the lipid composition.

Figure 5 describes the demixing process that occurs for curved membranes. For small curvatures ( $c < 0.005 \text{ nm}^{-1} \Leftrightarrow R_c > 200 \text{ nm}$ ), the local PL composition in the ER membrane is only weakly affected and close to the lipid distribution of the unperturbed planar ER. On the other hand, for small capradii ( $R_c < 100 \text{ nm} \Leftrightarrow c > 0.01 \text{ nm}^{-1}$ ), a significant demixing is observable; while generally lipids with  $S_i > 1$  (PE, PA, and PC; thin lines

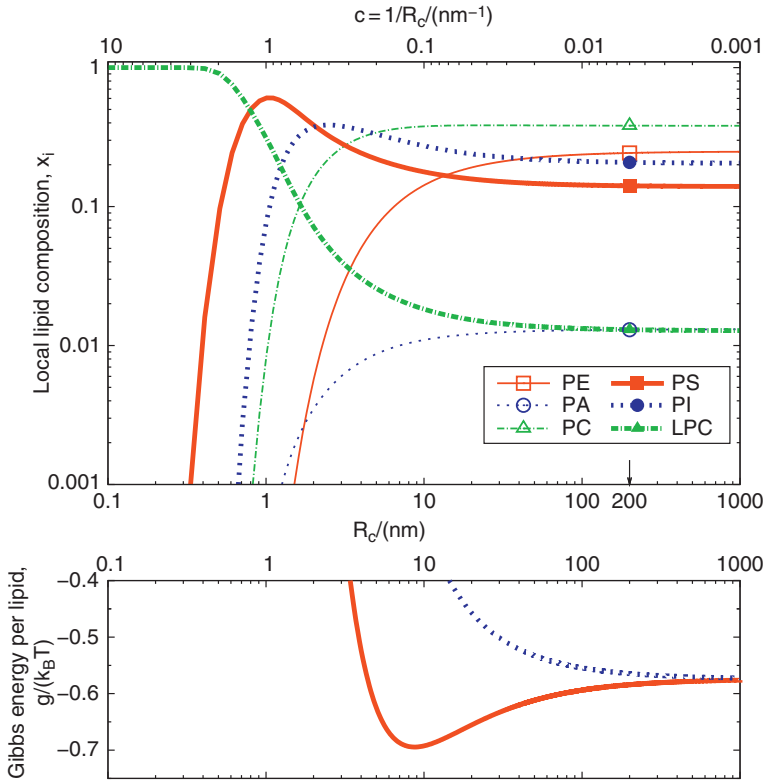


**Figure 5** Predicted lipid composition,  $x_i(R_c)$ , of a PL monolayer covering a spherical surface of radius  $R_c$  (lines in upper panel). For  $R_c \rightarrow \infty$ , the curves slowly converge to the measured composition  $x_{p,i}$  of the planar ER membrane [23]. The lipid composition of ripe, detached LD, as determined by Ref. [23], is indicated by symbols at the position of best fit (arrow). Lower panel, average free Gibbs energy per lipid,  $g$  as function of cap radius,  $R_c$ . It shows the impact of spherical bending on  $g$  for a compositionally optimized lipid membrane (full line) and a compositionally rigid membrane with frozen-in ER composition (dashed line).

in Fig. 5) decrease with decreasing  $R_c$ , the fractions of PS, PI, and LPC ( $S_i < 1$ ; thick lines) considerably increase. The observation is consistent with expectation, as lipids with  $S > 1$  tend to form convex surfaces, while  $S < 1$  favors concave topologies. However, this trend changes at high curvatures, where PI and PS content peaks. Thus, for even higher curvatures, that is,  $R_c < 1$  nm, the monolayer enriches only on LPC at the expense of all other PLs.

PC is an exception to the rule stated earlier. Despite its  $S$  value being larger than 1 ( $S_i = 1.11$ ), it does not migrate but slightly increases for intermediate values of  $R_c$ . Eventually, however, even PC drifts off for

$R_c < 5$  nm. Only a small fraction of this discrepancy can be attributed to the differences in elastic moduli. For instance, if  $k_{c,i}$  is changed from  $9k_B T$  to  $10k_B T$  (plus the corresponding changes in  $\bar{k}_{c,i}$ ), then the maximum PC content in the membrane decreases by only 2% (data not shown).

In the lower panel of Fig. 5, we show the change of Gibbs energy per lipid accompanied by the demixing process (full line) according to Eq. (9). For comparison, we have also plotted the  $R_c$  dependence for a membrane with frozen-in ER composition [dotted line; Eq. (9) together with the setting  $x_i = x_{p,i}, \forall R_c$ ]. Both lines converge for  $R_c \rightarrow \infty$ . However, while for a membrane with fixed composition the energy increases with decreasing  $R_c$ , the behavior is more subtle for a membrane which optimizes its lipid composition. In this case, the Gibbs energy initially decreases with decreasing  $R_c$ , reaching a pronounced minimum at  $R_c \approx 9$  nm. Thus, an optimized packing is able to overcompensate the increase in elastic energy caused by spherical distortion of an originally planar surface. Only at very high curvatures is regrouping of lipids unable to balance the rise in bending energy and the Gibbs energy sharply increases.

The drop in the Gibbs energy results from an optimized packing. This is better understood within the framework of our molecular interpretation. Figure 6 illustrates the effective, available base area for a particular lipid  $i$  sitting in the spherical cap according to Eq. (21). The data are normalized to

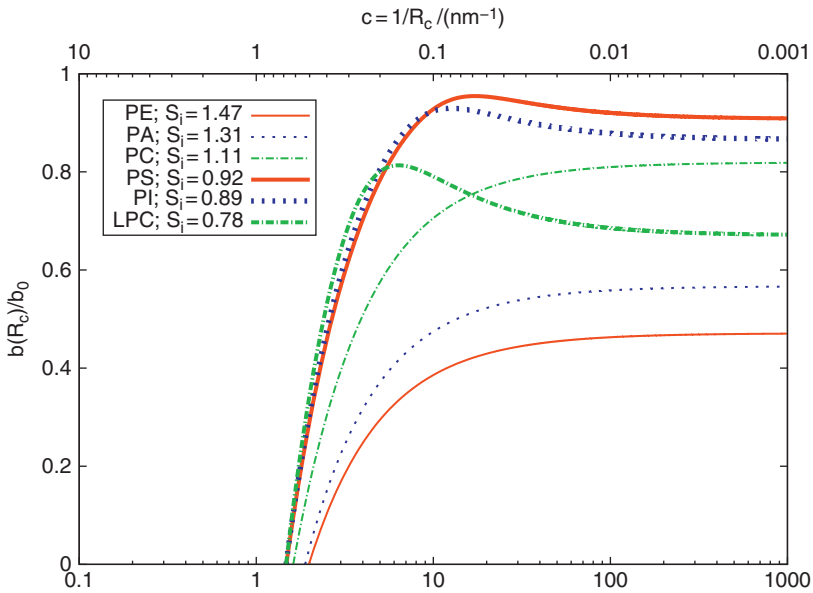


**Figure 6** Molecular area ratio,  $b_i/b_{0,i}$ , as a function of  $R_c$  according to Eq. (21) for various lipid components.

the unstrained foot area,  $b_{0,i}$ . Thus, a value of “1” indicates the special case where the lipid’s molecular volume is neither compressed nor expanded. [Figure 6](#) reveals that PE, PA, and PC are highly compressed. If the membrane starts to bend, these lipids are squeezed even more. Thus, they should migrate in order to reduce the overall energy of the membrane cap. On the other hand, PS, PI, and LPC, having  $S < 1$ , accommodate a convex curvature much better. Upon bending, these lipids are able to relieve tension as their spontaneous curvature is better adapted to the increasing curvature, thus reducing the overall energy. However, if the curvature increases even further ( $R_c < 3\text{--}10$  nm), these lipids, too, are compressed, causing the steep increase in the Gibbs energy. As LPC has the smallest  $S$  value, it is best adapted to high curvatures. Consistently, LPC is still able to reduce its internal stress, while PI and PS already experience augmenting pressure. Finally, for very low  $R_c$ , even LPC cannot adapt to the high curvature without increasing its stress state. However, compared to all other lipid types, LPC shows the lowest size deformation in the high-curvature region. Thus, the LD cap will eventually be made up of LPC only, consistent with the behavior shown in [Fig. 5](#). In [Fig. 6](#),  $b_i$  reaches zero for  $R_c \approx 2$  nm. This is an artifact of our analysis, as the requirement  $R_c \gg l/2 = 1.1$  nm [see [Eq. \(17\)](#)] is no longer fulfilled. Also note that we here base our argument solely on a comparison of the lipid’s foot area. This is possible since all lipids have similar elastic properties ( $k_{c,i} \approx 10 k_B T$  and  $\bar{k}_{c,i} \approx 8 k_B T$ , see [Table 1](#)).

To predict the change in energy due to demixing for a nascent LD of volume  $4\pi R_{LD}^3/3$  and cap radius  $R_c$ , we evaluate [Eq. \(12\)](#). [Figure 7](#) shows  $\Delta G_{\text{mix}}(R_c; R_{LD})$  as function of  $R_c$ . Note that  $\Delta G_{\text{mix}}$  depends parametrically on the LD volume, represented by  $R_{LD}$ . That is, each line in [Fig. 7](#) shows the dependency of the energy on  $R_c$  for a fixed LD volume. Depending on the size of the LD, that is on the value of  $R_{LD}$ , the free Gibbs energy shows a single minimum at values  $R_c/R_{LD} > 1$  (for  $R_{LD} < 4.2$  nm), or two minima—one at  $R_c/R_{LD} = 1$  and the other at  $R_c/R_{LD} > 1$  (for  $4.2$  nm  $< R_{LD} < 6.5$  nm)—or exactly one minimum at  $R_c/R_{LD} = 1$  (for  $R_{LD} > 6.5$  nm).

[Figure 7](#) may be interpreted in such a way that for constant LD volume, minima in the Gibbs energy single out preferred configurations, that is, identify likely values of  $R_c$  for a given LD volume (thick full and dashed line).  $R_c/R_{LD} = 1$  indicates that an LD does no longer form a spherical cap, but a full sphere. Thus, if the minimum in energy shows up at such a point, the LD has been fully fabricated and detaches from the ER. If, however, a minimum appears at values  $R_c/R_{LD} > 1$ , then the nascent LD forms a stable spherical protuberance of volume  $4\pi R_{LD}^3/3$  and cap radius  $R_c$ , but remains an integral part of the ER membrane. The position of the minima,  $R_{c,\text{opt}}$ , as function of LD size,  $R_{LD}$ , is illustrated in the inset of [Fig. 7](#). In this plot, points along the dotted line ( $R_c/R_{LD} = 1$ ) indicate fully detached LD.

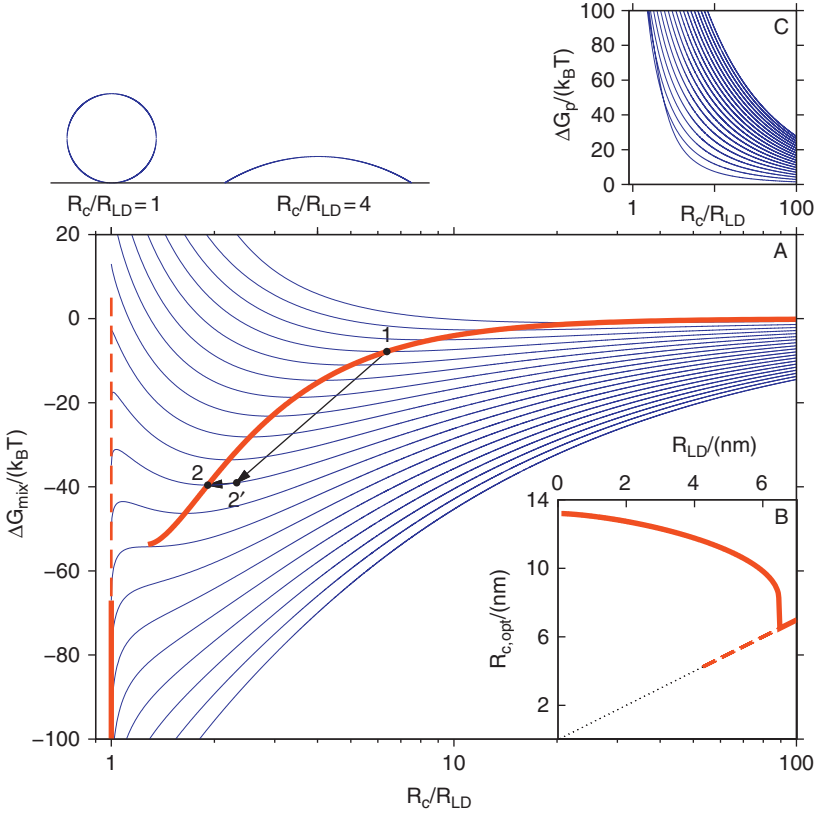


**Figure 7** (A) Energy change due to demixing,  $\Delta G_{\text{mix}}(R_c; R_{LD})$ , as function of the normalized cap radius,  $R_c/R_{LD}$ . Each full, thin line represents the energy dependence for a fixed but constant LD volume ( $R_{LD} = [0.5, 10]$  nm, increment 0.5 nm). The observed (local) minima are marked by thick lines. For a better understanding of the meaning of the normalized  $x$ -axis, the effective geometrical conformation is illustrated for two exemplary values on top.  $R_c$  denotes the cap radius, while  $R_{LD}$  represents the equivalent spherical radius of the cap. (B) Position of the local energy minima,  $R_{c,\text{opt}}$ , as function of LD size,  $R_{LD}$ . The thick lines correspond to the thick lines in the main figure. The dotted line indicates points where  $R_{c,\text{opt}} = R_{LD}$ . (C) As (A), but for an ER membrane with frozen-in composition,  $x_p$ . The change in energy was calculated in analogy to Eq. (10), that is,  $\Delta G_p = N_{\text{cap}} \sum_{i=1}^n [x_{p,i} U_i(R_c) + x_{p,i} k_B T \ln x_{p,i}] - N_{p,g}$ .

The stability of a nascent LD retained in the ER may be best estimated by the height of the energy barrier between the position of the minimum,  $R_{c,\text{opt}}$ , and the point where the cap becomes a full sphere, that is, at  $R_c = R_{LD}$ . This barrier shrinks with increasing LD volume. In our calculation, we find that for LD diameters larger than  $2R_{LD} = 13$  nm this barrier vanishes completely and does not reappear again. Thus, such LDs are fully matured and detach from

the ER. It is important to note that if we keep the lipid composition of the ER membrane fixed, then no decreasing energy barrier is observable (Fig. 7C), and LDs remain as integral part of the ER—in contrast to experimental findings. Thus, lipid demixing is an essential part in the budding process. Moreover, we conclude that our lipid demixing model can explain the budding process based on biophysical reasons only.

To understand the reason for the disappearance of the energy barrier, consider the change in energy associated with LD formation (12). In essence,  $\Delta G_{\text{mix}}(R_c; R_{\text{LD}})$  depends on the product between  $g_{\text{cap}}(R_c)$  and  $A_c(R_c; R_{\text{LD}})$ . Since  $A_c(R_c; R_{\text{LD}})$  has values just for  $R_c > R_{\text{LD}}$ , only these distances contribute to the product. On the other hand,  $g_{\text{cap}}(R_c)$  does not depend on  $R_{\text{LD}}$ , and neither does its minimum at  $R_c \approx 9$  nm. Therefore, if  $R_{\text{LD}}$  is small enough so that  $R_{\text{LD}}$  lies to the left of the minimum in Fig. 5, then also the total energy exhibits a pronounced minimum and  $\Delta G_{\text{mix}}$  rises sharply in between. An energy barrier is formed. On the other hand, if  $R_{\text{LD}}$  lies to the right of the minimum, then  $g_{\text{cap}}(R_c)$  is cut off before it reaches its minimum, a stabilizing energy barrier cannot form and LDs detach from the ER. Thus, the position of the minimum in  $g_{\text{cap}}(R_c)$  in relation to the LD size, that is,  $R_{\text{LD}}$ , is decisive for the appearance of an energy barrier due to  $g_{\text{cap}}(R_c)$ .

The predicted bud-off diameter depends on the initial ER membrane composition. To what extent the bud-off radius can be controlled by the ER membrane composition has not been investigated. However, we successfully checked whether we get similar results if the PL composition of LD rather than the one of the ER is used as an input for the simulation. Therefore, we solved Eq. (5) such that at a typical LD size of  $R_c = 200$  nm [4] the measured PL composition [23] is retrieved. In that case, we predicted a bud-off diameter of 6.7 nm (see Fig. 8).

So far, we have focused on lipid demixing, disregarding the tension arising along the edge between the developing LD and the ER membrane. However, our analysis stays essentially valid even in the presence of a line tension,  $\tau$ . Figure 9 illustrates the dependence of the total free Gibbs energy for a finite value of  $\tau$ . The line tension acts as an additional force supporting the budding process [45,46]. Thereby, it reduces the final bud-off diameter from 13 to 12 nm (Fig. 9, inset). Only for  $R_{\text{LD}} \leq 2$  nm, the line tension is the dominating contribution to the driving force, significantly altering the position of the energy minimum. This can be seen in the inset of Fig. 9, which compares  $R_{c,\text{opt}}$  with and without line tension (dashed-dotted and full line, respectively).

Using the parameter settings in Table 1, our model is able to describe budding. At the bud-off diameter,  $2R_{\text{LD}} = 12$  nm, we observed a significantly altered membrane composition in comparison with the ER. Consistently, we got a similar scale for the budding size, if we fit  $R_c$  such that the computed composition (taken from Fig. 5) best approximates the

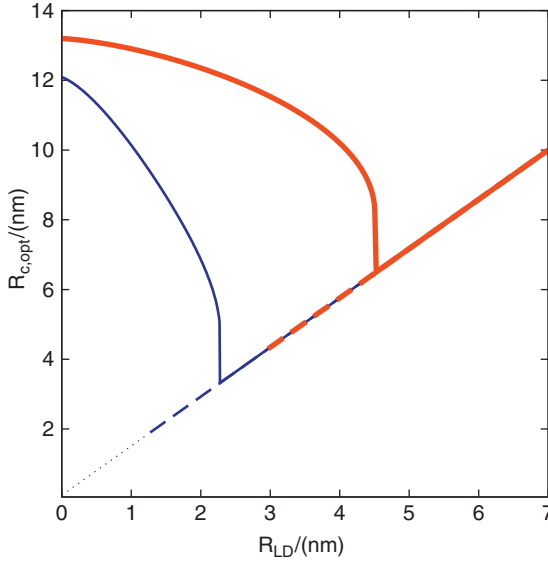


**Figure 8** Dependence of the predicted LD bud-off radius on the experimental data [23]. Position of the local energy minima in Gibbs energy,  $R_{c,opt}$ , as function of LD size,  $R_{LD}$ . Thick lines are calculated using the measured ER composition [23] and correspond to the ones in Fig. 7B. Thin lines are based on the measured values for the LD composition [23]. The dotted line indicates points where  $R_{c,opt} = R_{LD}$ .

measured data. By doing so, we obtained  $R_{LD} = 18.5$  nm and  $R_{LD} = 3.2$  nm for the data in Refs. [23] and [2], respectively (see Fig. 10). However, in any case our predicted bud-off radius is an order of magnitude lower than the typical LD radius of 200 nm [4]. This suggested that if the standard model of LD biogenesis is correct, then it is a two-step process: Step one, growth of a nanosized LD nucleus within the ER membrane and Step two, cytosolic ripening of nano-LDs after they have budded off from the ER.

With these bud-off radii we are able to justify our assumption that the ER membrane acts as a PL reservoir. Yeast contains approximately 15 mg PL per gram dry weight biomass [48], that is 0.23 pg PL per cell (assuming a typical dry weight of  $1.5 \times 10^{-11}$  g [49]). We estimate that roughly 50% of these PL are used for the ER membrane. Further, if we assume an average molecular weight of 800 g/mol, then the ER membrane contains  $8 \times 10^7$  PL. On the other hand, according to the estimated bud-off radii only  $N_{cap} = 6000$  PL tops are needed to form the LD membrane. Thus, even if the cell massively produces LDs, the ER's PL composition remains virtually unaltered. Additionally, LDs are produced in logarithmically growing cells [50]. Thus, with each cell cycle the ER's PL reservoir is refilled.



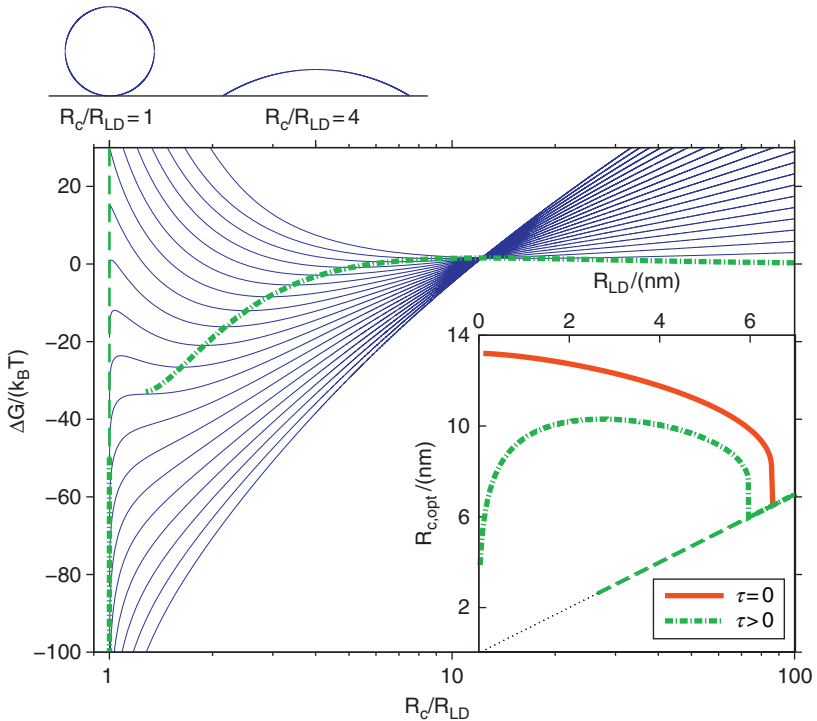


**Figure 9** Total free Gibbs energy,  $\Delta G(R_c; R_{LD})$ , as function of the normalized cap radius,  $R_c/R_{LD}$ . Parameters are as in Fig. 7. Each full, thin line represents the energy dependence for a fixed but constant LD volume ( $R_{LD} = [0.5, 10]$  nm, increment 0.5 nm). The observed (local) minima are marked by thick lines. For a better understanding of the meaning of the normalized  $x$ -axis, the effective geometrical conformation is illustrated for two exemplary values on top.  $R_c$  denotes the cap radius, while  $R_{LD}$  represents the equivalent spherical radius of the cap. Inset: Position of the local energy minima,  $R_{c,opt}$ , as function of LD size,  $R_{LD}$ . The thick lines correspond to the thick lines in the main figure and Fig. 7, respectively. The dotted line indicates points where  $R_{c,opt} = R_{LD}$ .

## 5. DISCUSSION

### 5.1. Lipid Demixing in Curved Membrane Regions

We have presented a thermodynamic model to describe LD formation and investigated the interplay between membrane curvature and demixing in the PL composition. In fact, lipids favoring a convex surface ( $S < 1$ , i.e., PS, PI, LPC) are enriched while PE, PA, and PC are depleted. Curvature-induced demixing is hardly surprising and already well documented [25]. All the more important, however, is the observation that the free energy per

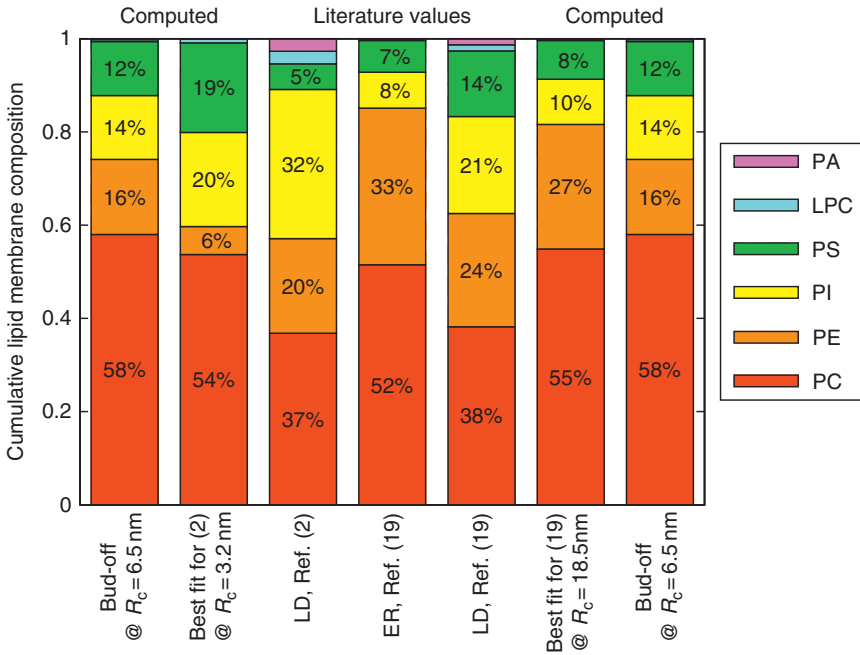


**Figure 10** Literature values for experimentally measured PL compositions of ER and LD membranes compared to our thermodynamic model at various radii  $R_c$ . Data listed in Refs. [2,23] for “other lipids” have been redistributed such that each column sums up to one. (For actual numerical values, see Table 2.) Note that both outermost columns are identical. They have been duplicated to facilitate easier comparison.

lipid for a curvature-optimized packing can drop below that of a planar monolayer. In other words, moderately deforming an originally planar mixed PL monolayer does not necessarily cost energy, but can result in an energy gain—provided that the lipid system can optimize its composition.

## 5.2. Demixing Forces Induce Membrane Curvature

Our analysis showed that during lipid demixing of membranes, energy is gained rather than consumed. Thus, we argue that demixing at least supports if not drives membrane deformation. Such a view is evoked by Fig. 7. By increasing the NL content in the ER, one moves between two isolines (transition from 1 to 2'; note that due to normalization the transition appears as a tilted line even though  $R_c$  remained constant). At 2' the membrane perceives a “demixing force” which further distorts the monolayer and pushes the system toward a new minimum at point 2, thereby sucking NL in the nascent LD. Note that in Fig. 7 demixing forces occur to the right of

the thick line, while to its left forces are fueled by elastic energy. Thus, demixing is a general feature of our model. It does not require LD biogenesis proceeding along the energy minima in Fig. 7.

At this point it has become clear that only the existence of a spherical surface—as a topological alternative to the plane—renders the molecular shape an energetically relevant quantity. This makes it energetically worthwhile for the membrane to separate the different lipids according to their molecular shapes. In that sense, the spherical topology is the real agent of the predicted demixing process.

### 5.3. Demixing—A Potential Method to Recruit Proteins from the ER Membrane

We speculate that not only lipids but also tracer components of the ER membrane are enriched or depleted on nascent LD as dictated by their specific molecular shape factor. In principle, such a mechanism would be able to explain the clustering of specific proteins on raised membrane domains. For example, cone-shaped membrane proteins (as long as they are not transmembrane proteins) should react to the positive curvature of developing LDs. This mechanism is potentially able to explain the so-far-unaccounted-for accumulation of overexpressed caveolin-1 on LD [51,52]. Caveolin-1 has a hairpin-like structure, with both terminals facing the cytosol. Thus, its structure factor is smaller than 1 and therefore, like PS, enriches on the LD surface. Likewise, proteins with molecular shapes akin to PE should be depleted. This offers the interesting perspective of an efficient, self-organized, biophysical “protein sorting” mechanism that performs the recruiting of proteins from the pool of ER proteins according to their molecular shape.

### 5.4. The Birth of a Lipid Droplet

We argued that PL demixing in developing LDs is not a consequence of the membrane curvature, but rather its driving force. The existence of pronounced minima in the Gibbs energy (Fig. 7) leads to demixing forces during LD growth. Thus, the following thermodynamic, budding mechanism is suggested: An LD forms by accumulating NL within the ER membrane, thereby producing a membrane protuberance. Its curvature is adjusted by a demixing force in such a way that it minimizes the interfacial energy of the cytoplasmic monolayer (see Fig. 7, transition from 2' to 2). As long as the NL volume, that is the size of the protuberance measured by  $R_{LD}$ , is small enough, the LD is prevented from detaching by an insurmountable energy barrier. This barrier is traced back to the sharp rise in the elastic energy at very high curvatures. However, for NL volumes,  $V$ , for which  $R_{LD} = \sqrt[3]{3V/(4\pi)} > 6.5$  nm, the developing LD does not buckle enough. The increase in bending energy is too small and a stabilizing energy

barrier cannot mold. Thus, such large LDs do not exist within the ER membrane, as they have budded off already at an earlier stage of their development.

At first it might appear counterintuitive that the elastic properties of a thin skin such as a PL monolayer should ultimately be responsible for the formation of LD. However, considering an LD suspension as some sort of macroemulsion, these ideas are far from new: in fact, it has been shown that type and stability of oil-in-water emulsions are determined by sign and value of the monolayer's spontaneous curvature [53].

LD size distributions based on electron microscopic pictures for various yeast mutant strains are well reproducible and rather narrow, showing values between 250 and 550 nm in diameter, with a maximum at about 400 nm [4]. Nevertheless, these radii are an order of magnitude larger than those predicted by our model. What could be the reason for this discrepancy? Obviously, the experimentally observed distribution reflects the size of the LD suspension in the cytosol. This distribution does not necessarily have to be identical to the size of freshly released LD, implying that there exists a second, subsequent phase of LD ripening within the cytosol. Thus, small LDs produced from the ER would undergo a series of fusions through conglomeration and coalescence until they reach their full-grown size [5]. A number of observations support this view.

Although current experimental methods allow for the detection of 400-nm structures, a fully matured LD, which is still part of the ER, has never been observed in any cell. Neither have smaller ones. This is probably because such LDs are too small to be resolved with conventional experimental techniques [6,54]. Even with the usage of electron microscopy, which provides the ultimate resolution, nascent LD would be difficult to observe. By cutting a section of 80–90 nm through a fixed cell, it is unlikely to section also an attached LD. Nevertheless, very recently, large NL globules were detected by electron microscopy within special subcompartments of the ER membrane in human hepatoma cells [55]. The authors hypothesized that tight binding of anomaly lipidated apolipoproteins suppressed detaching and allowed detecting giant NL structures within the ER membrane. Whether this observation presents the missing link in validating the standard model of LD formations remains to be seen.

TAG accumulates either in LDs dispersed in the cytosol or in membrane microdomains [56]. These microdomains are tiny TAG depots residing between two membrane leaflets [57]. Such depots were estimated to have a size between 22 and 28 nm which is roughly consistent with our diameters. This would suggest that these small inclusions are simply nascent LD. However, based on their data [56], an ultimate conclusion is not possible.

Artificially prepared PL membranes on a solid surface showed time-dependent changes in the membrane topography after externally initiating NL production [58]. Droplet-like structures were formed at the surface

with an average diameter of about 50 nm. Again, this is comparable to the size regime suggested by our model. Then, in a second process stage, smaller LD coalesced into larger structures. Additionally, LD fusion has also been shown *in vivo* [59].

If LD biogenesis proceeds in a two-step process, that is budding of nano-LDs, which later merge, then fusion will dramatically change the surface to volume ratio and we also expect alterations in the PL composition of the LD [60]. In fact, if, for simplicity, we assume that LD bud off at a diameter of 40 nm, then 1000 nano-LDs are needed to produce a typically sized LD. The total surface of these nano-LDs will be 10 times larger than the surface of the full-blown LD. This excess of PL may be used as a reservoir, which would allow the growing LD to remix its PL composition in order to accommodate the decreasing curvature. However, this reservoir will not be accessible as a whole, as it is unlikely that all 1000 nano-LDs merge simultaneously in a single big fusion. Thus, lipid remixing due to fusing of LD ultimately depends on the process of coalescence. Nevertheless we expect it to be less efficient than the original lipid demixing in the ER membrane. In fact, in our model, we obtained PL compositions for stable nano-LDs that are similar to those of fully matured ones (see Fig. 10). Thus, the lack of accessible PL-depots during the ripening process could explain why nano-LDs and matured LDs have similar compositions, despite their different sizes.

However, any remixing would change the composition but leaves the total number of excess PL unaltered. On the other hand, many LDs are found to be surrounded by or adherent to double-layered structures [60; H. Wolinski, unpublished data]. These membranes are neither part of the ER nor do they form continuous structures with LDs. Their origin and function is unclear. Here, we speculate that these membranes are a waste dump sprouting from excess PL during LD fusion.

It is also interesting to link our results to mammalian very low-density lipoproteins (VLDL), which are another kind of lipid particles. Their NL cores are of the same order of magnitude (30–90 nm) as our predicted nano-LD [61]. This observation would support the so-far-untested hypothesis of Alexander *et al.* [62], who suggested that ready-made nano-LDs fuse with apoproteins to form VLDL.

## 5.5. Model Limitations

Our model assumes that LDs, though forming between the leaflets of the ER membrane, lead to a protuberance only of the cytoplasmic leaflet, while the endoplasmic leaflet remains unaffected. Such an asymmetry may be real and caused by certain membrane proteins, differences in the PL composition of the leaflets, or different properties of the solvents adjacent to the

leaflets. However, a rigid endoplasmic leaflet is not an essential assumption. Our model could be adopted to account for LD growth in both leaflets.

To describe the stress along the boundary between the LD and the ER membrane, we have used a finite, but constant value for the line tension independent of the domain composition. However, this is unrealistic, as the line tension highly depends on the compositional differences in the membrane domains [43]. In particular for small  $R_{LD}$ , that is little demixing, we expect our model to overestimate the impact of the edge tension.

An essential part of our approach is the spherical cap approximation, which has been proved helpful in the context of the Young equation, which relates the contact angle of a liquid droplet on a solid surface to the interfacial energies of all three phases involved [63]. However, this approximation neglects contributions from the neck region. The neck connects the planar ER membrane with the LD monolayer and has the geometrical shape of a torus. In contrast to the cap, the neck region consists of both positive and negative curvatures.

Our current model is not able to address neck formation. However, it was demonstrated theoretically that the neck shape is generated by an interplay between the local curvature and the membrane composition [64,65]. Similar to the observation reported here (accumulation of  $S < 1$ -lipids at high curvatures), it was shown that the neck region predominately consists of lipids with anisotropic, saddle-like intrinsic curvature. This is consistent with our results as these lipids are best adapted to the torus-shaped neck. We are currently working on including the neck in our description. However, we do not expect any significant impact on our conclusions, because firstly the neck region is small in comparison with the spherical cap and secondly contributions to the total energy will be attenuated by lipid demixing.

## 6. SUMMARY

A biophysical model to describe LD biogenesis has been presented. We have estimated the local composition of a PL monolayer, which is part of a spherical protuberance in an otherwise planar membrane. Four major results are obtained: (i) In order to use the available surface area economically, PL with shape factors,  $S < 1$  (PI, PS, LPC), tend to accumulate on spherical surfaces. Conversely, lipids with  $S > 1$  (PE, PC, PA) migrate. Therefore, a spherical protuberance of radius,  $R_c$ , in an otherwise planar membrane causes a local lipid demixing on the curved membrane monolayer. (ii) As a consequence of the optimized packing of lipids, the energy per lipid  $g_{cap}(R_c)$  drops with decreasing  $R_c$ , that is, with increasing curvature. Thus, induced by lipid demixing, a monolayer gains energy by

forming a spherical protuberance of weak to intermediate curvature. Only at very high curvatures,  $g_{\text{cap}}(R_c)$  increases again, leading to a clear minimum in  $g_{\text{cap}}(R_c)$  at 9 nm. (iii) This energy minimum is key in understanding the formation of an energy barrier, which controls the budding of LD. (iv) The height of the energy barrier depends on the volume of the protuberance; it stabilizes protuberances of smaller volumes, but completely vanishes at higher volumes. Our model predicts that LDs detach from the ER at a diameter in the order of 12 nm.

In this chapter, we have suggested that LD formation is driven by lipid demixing. This finding is based on a model calculation. The main ingredient entering this model is the geometrical structure of various lipids, described by the shape factor. Thus, by changing the shape factor, we expect different demixing effects and ultimately different bud-off sizes, which could be verified by *in vitro* measurements, similar to those performed in Ref. [58]. The shape factor may be influenced by varying the chain length of FA in lipids, or by manipulating the pH of the solvent which influences the head-group areas.

## ACKNOWLEDGMENTS

Intensive discussions with Sepp D. Kohlwein, Günther Daum, Martin Peifer, Georg Pabst, Mihnea Hristea, and Klaus Natter are gratefully acknowledged.

This work was supported by a grant from the Austrian Federal Ministry for Science and Research (Project GOLD within the framework of the Austrian GEN-AU program).

## REFERENCES

- [1] S. Martin, R.G. Parton, Lipid droplets: a unified view of a dynamic organelle, *Nat. Rev. Mol. Cell. Biol.* 7(5) (2006) 373–378.
- [2] R. Leber, E. Zinser, G. Zellnig, F. Paltauf, G. Daum, Characterization of lipid particles of the yeast, *Saccharomyces cerevisiae*, *Yeast* 10(11) (1994) 1421–1428.
- [3] T. Czabany, K. Athenstaedt, G. Daum, Synthesis, storage and degradation of neutral lipids in yeast, *Biochim. Biophys. Acta* 1771(3) (2007) 299–309.
- [4] T. Czabany, A. Wagner, D. Zweytick, K. Lohner, E. Leitner, E. Ingolic, G. Daum, Structural and biochemical properties of lipid particles from the yeast *Saccharomyces cerevisiae*, *J. Biol. Chem.* 283(25) (2008) 17065–17074.
- [5] D.J. Murphy, J. Vance, Mechanisms of lipid-body formation, *Trends Biochem. Sci.* 24(3) (1999) 109–115.
- [6] T. Fujimoto, Y. Ohsaki, J. Cheng, M. Suzuki, Y. Shinohara, Lipid droplets: a classic organelle with new outfits, *Histochem. Cell Biol.* 130(2) (2008) 263–279.
- [7] J. Zanghellini, K. Natter, C. Jungreuthmayer, A. Thalhammer, C.F. Kurat, G. Gogg-Fassolter, S.D. Kohlwein, H. von Grünberg, Quantitative modeling of triacylglycerol homeostasis in yeast—metabolic requirement for lipolysis to promote membrane lipid synthesis and cellular growth, *FEBS J.* 275(22) (2008) 5552–5563.
- [8] S. Murphy, S. Martin, R. Parton, Lipid droplet–organelle interactions; sharing the fats, *Biochim. Biophys. Acta* 1791(6) (2009) 441–447.

- [9] S. Olofsson, P. Boström, L. Andersson, M. Rutberg, J. Perman, J. Boren, Lipid droplets as dynamic organelles connecting storage and efflux of lipids, *Biochim. Biophys. Acta* 1791(6) (2009) 448–458.
- [10] D.J. Murphy, The biogenesis and functions of lipid bodies in animals, plants and microorganisms, *Prog. Lipid Res.* 40(5) (2001) 325–438.
- [11] W. Huh, J.V. Falvo, L.C. Gerke, A.S. Carroll, R.W. Howson, J.S. Weissman, E.K. O’Shea, Global analysis of protein localization in budding yeast, *Nature* 425 (6959) (2003) 686–691.
- [12] K. Natter, P. Leitner, A. Faschinger, H. Wolinski, S. McCraith, S. Fields, S.D. Kohlwein, The spatial organization of lipid synthesis in the yeast *Saccharomyces cerevisiae* derived from large scale green fluorescent protein tagging and high resolution microscopy, *Mol. Cell. Proteomics* 4(5) (2005) 662–672.
- [13] K. Athenstaedt, D. Zweytick, A. Jandrositz, S.D. Kohlwein, G. Daum, Identification and characterization of major lipid particle proteins of the yeast *Saccharomyces cerevisiae*, *J. Bacteriol.* 181(20) (1999) 6441–6448.
- [14] D. Sorger, K. Athenstaedt, C. Hrastnik, G. Daum, A yeast strain lacking lipid particles bears a defect in ergosterol formation, *J. Biol. Chem.* 279(30) (2004) 31190–31196.
- [15] H.L. Ploegh, A lipid-based model for the creation of an escape hatch from the endoplasmic reticulum, *Nature* 448(7152) (2007) 435–438.
- [16] T.C. Walther, R.V. Farese Jr., The life of lipid droplets, *Biochim. Biophys. Acta* 1791(6) (2009) 459–466.
- [17] C. Thiele, J. Spandl, Cell biology of lipid droplets, *Curr. Opin. Cell Biol.* 20(4) (2008) 378–385.
- [18] H.T. McMahon, I.G. Mills, Cop and clathrin-coated vesicle budding: different pathways, common approaches, *Curr. Opin. Cell Biol.* 16(4) (2004) 379–391.
- [19] G.J. Praefcke, H.T. McMahon, The dynamin superfamily: universal membrane tubulation and fission molecules? *Nat. Rev. Mol. Cell Biol.* 5(2) (2004) 133–147.
- [20] D. Corda, A. Colanzi, A. Luini, The multiple activities of ctbp/bars proteins: the golgi view, *Trends Cell Biol.* 16(3) (2006) 167–173.
- [21] H. Robenek, M.J. Robenek, I. Buers, S. Lorkowski, O. Hofnagel, D. Troyer, N.J. Severs, Lipid droplets gain pat family proteins by interaction with specialized plasma membrane domains, *J. Biol. Chem.* 280(28) (2005) 26330–26338.
- [22] H. Robenek, O. Hofnagel, I. Buers, M.J. Robenek, D. Troyer, N.J. Severs, Adipophilin-enriched domains in the ER membrane are sites of lipid droplet biogenesis, *J. Cell Sci.* 119(Pt. 20) (2006) 4215–4224.
- [23] E. Zinser, C.D. Sperka-Gottlieb, E.V. Fasch, S.D. Kohlwein, F. Paltauf, G. Daum, Phospholipid synthesis and lipid composition of subcellular membranes in the unicellular eukaryote *Saccharomyces cerevisiae*, *J. Bacteriol.* 173(6) (1991) 2026–2034.
- [24] K. Tauchi-Sato, S. Ozeki, T. Houjou, R. Taguchi, T. Fujimoto, The surface of lipid droplets is a phospholipid monolayer with a unique fatty acid composition, *J. Biol. Chem.* 277(46) (2002) 44507–44512.
- [25] A. Roux, D. Cuvelier, P. Nassoy, J. Prost, P. Bassereau, B. Goud, Role of curvature and phase transition in lipid sorting and fission of membrane tubules, *EMBO J.* 24(8) (2005) 1537–1545.
- [26] H. Jiang, T.R. Powers, Curvature-driven lipid sorting in a membrane tubule, *Phys. Rev. Lett.* 101(1) (2008) 018103.
- [27] W. Helfrich, Elastic properties of lipid bilayers: theory and possible experiments, *Z. Naturforsch.* 28C(11) (1973) 693–703.
- [28] R.P. Rand, N.L. Fuller, S.M. Gruner, V.A. Parsegian, Membrane curvature, lipid segregation, and structural transitions for phospholipids under dual-solvent stress, *Biochemistry* 29(1) (1990) 76–87.



- [29] V. Kralj-Iglic, A. Iglic, G. Gomisecek, F. Sevsek, V. Arrigler, H. Hagerstrand, Microtubes and nanotubes of a phospholipid bilayer membrane, *J. Phys. A: Math. Theor.* 35(7) (2002) 1533–1549.
- [30] D. Marsh, Lateral pressure profile, spontaneous curvature frustration, and the incorporation and conformation of proteins in membranes, *Biophys. J.* 93(11) (2007) 3884–3899.
- [31] J.F. Nagle, S. Tristram-Nagle, Structure of lipid bilayers, *Biochim. Biophys. Acta* 1469(3) (2000) 159–195.
- [32] T. Baumgart, S.T. Hess, W.W. Webb, Imaging coexisting fluid domains in biomembrane models coupling curvature and line tension, *J. Phys. France II* 425 (2003) 821–824.
- [33] N. Fuller, R.P. Rand, The influence of lysolipids on the spontaneous curvature and bending elasticity of phospholipid membranes, *Biophys. J.* 81(1) (2001) 243–254.
- [34] E.E. Kooijman, V. Chupin, N.L. Fuller, M.M. Kozlov, B. de Kruijff, K.N. Burger, P.R. Rand, Spontaneous curvature of phosphatidic acid and lysophosphatidic acid, *Biochemistry* 44(6) (2005) 2097–2102.
- [35] D. Marsh, Intrinsic curvature in normal and inverted lipid structures and in membranes, *Biophys. J.* 70(5) (1996) 2248–2255.
- [36] S. Leikin, M.M. Kozlov, N.L. Fuller, R.P. Rand, Measured effects of diacylglycerol on structural and elastic properties of phospholipid membranes, *Biophys. J.* 71(5) (1996) 2623–2632.
- [37] N. Fuller, C.R. Benatti, R.P. Rand, Curvature and bending constants for phosphatidylserine-containing membranes, *Biophys. J.* 85(3) (2003) 1667–1674.
- [38] J.A. Szule, N.L. Fuller, R.P. Rand, The effects of acyl chain length and saturation of diacylglycerols and phosphatidylcholines on membrane monolayer curvature, *Biophys. J.* 83(2) (2002) 977–984.
- [39] Z. Chen, R.P. Rand, The influence of cholesterol on phospholipid membrane curvature and bending elasticity, *Biophys. J.* 73(1) (1997) 267–276.
- [40] M. Rappolt, P. Laggner, G. Pabst, Structure and elasticity of phospholipid bilayers in the  $L_x$  phase: a comparison of phosphatidylcholine and phosphatidylethanolamine membranes, *Recent Res. Dev. Biophys.* 3 (2004) 363–392.
- [41] J.N. Israelachvili, *Intermolecular and Surface Forces, Second Edition: With Applications to Colloidal and Biological Systems (Colloid Science)*. Academic Press, San Diego, CA, 1992.
- [42] K. Tauchi-Sato, S. Ozeki, T. Houjou, R. Taguchi, T. Fujimoto, The surface of lipid droplets is a phospholipid monolayer with a unique fatty acid composition, *J. Biol. Chem.* 277(46) (2002) 44507–44512.
- [43] A. Tian, C. Johnson, W. Wang, T. Baumgart, Line tension at fluid membrane domain boundaries measured by micropipette aspiration, *Phys. Rev. Lett.* 98 (2007) 208102.
- [44] P.I. Kunzmin, S.A. Akimov, Y.A. Chizmadzhev, J. Zimmerberg, F.S. Cohen, Line tension and interaction energies of membrane rafts calculated from lipid splay and tilt, *Biophys. J.* 88 (2005) 1120–1133.
- [45] R. Lipowsky, Domain-induced budding of fluid membranes, *Biophys. J.* 64 (1993) 1133–1138.
- [46] R. Lipowsky, Budding of membranes induced by intramembrane domains, *J. Phys. France II* 2 (1992) 1825–1840.
- [47] C.D. Blanchette, W.-C. Lin, C.A. Orme, T.V. Ratto, M.L. Longo, Using nucleation rates to determine the interfacial line tension of symmetric and asymmetric lipid bilayer domains, *Langmuir* 23(11) (2007) 5875–5877.
- [48] J. Förster, I. Famili, P. Fu, B.O. Palsson, J. Nielsen, Genome-Scale reconstruction of the *Saccharomyces cerevisiae* metabolic network, *Genome Res.* 13(2) (2003) 244–253.
- [49] F. Sherman, Getting started with yeast, *Methods Enzymol.* 350 (2002) 3–41.

- [50] C.F. Kurat, K. Natter, J. Petschnigg, H. Wolinski, K. Scheuringer, H. Scholz, R. Zimmermann, R. Leber, R. Zechner, S.D. Kohlwein, Obese yeast: triglyceride lipolysis is functionally conserved from mammals to yeast, *J. Biol. Chem.* 281(1) (2006) 491–500.
- [51] A.G. Ostermeyer, J.M. Paci, Y. Zeng, D.M. Lublin, S. Munro, D.A. Brown, Accumulation of caveolin in the endoplasmic reticulum redirects the protein to lipid storage droplets, *J. Cell Biol.* 152(5) (2001) 1071–1078.
- [52] S. Cermelli, Y. Guo, S.P. Gross, M.A. Welte, The lipid-droplet proteome reveals that droplets are a protein-storage depot, *Curr. Biol.* 16(18) (2006) 1783–1795.
- [53] A. Kabalnov, H. Wennerström, Macroemulsion stability: the oriented wedge theory revisited, *Langmuir* 12(2) (1996) 276–292.
- [54] D.J. Lacey, F. Beaudoin, C.E. Dempsey, P.R. Shewry, J.A. Napier, The accumulation of triacylglycerols within the endoplasmic reticulum of developing seeds of *Helianthus annuus*, *Plant J.* 17(4) (1999) 397–405.
- [55] Y. Ohsaki, J. Cheng, M. Suzuki, A. Fujita, T. Fujimoto, Lipid droplets are arrested in the ER membrane by tight binding of lipidated apolipoprotein B-100, *J. Cell Sci.* 121(14) (2008) 2415–2422.
- [56] J.M. Hakumaki, R.A. Kauppinen, <sup>1</sup>H NMR visible lipids in the life and death of cells, *Trends Biochem. Sci.* 25(8) (2000) 357–362.
- [57] C.E. Mountford, L.C. Wright, Organization of lipids in the plasma membranes of malignant and stimulated cells: a new model, *Trends Biochem. Sci.* 13(5) (1988) 172–177.
- [58] M. Waltermann, A. Hinz, H. Robenek, D. Troyer, R. Reichelt, U. Malkus, H.J. Galla, R. Kalscheuer, T. Stoveken, P. von Landenberg, A. Steinbüchel, Mechanism of lipid-body formation in prokaryotes: how bacteria fatten up, *Mol. Microbiol.* 55(3) (2005) 750–763.
- [59] P. Bostrom, M. Rutberg, J. Ericsson, P. Holmdahl, L. Andersson, M.A. Frohman, J. Boren, S. Olofsson, Cytosolic lipid droplets increase in size by microtubule-dependent complex formation, *Arterioscler. Thromb. Vasc. Biol.* 25(9) (2005) 1945–1951.
- [60] L. Kuerschner, C. Moessinger, C. Thiele, Imaging of lipid biosynthesis: how a neutral lipid enters lipid droplets, *Traffic* 9(3) (2008) 338–352.
- [61] Y. Ohsaki, J. Cheng, M. Suzuki, Y. Shinohara, A. Fujita, T. Fujimoto, Biogenesis of cytoplasmic lipid droplets: from the lipid ester globule in the membrane to the visible structure, *Biochim. Biophys. Acta* 1791(6) (2009) 399–407.
- [62] C.A. Alexander, R.L. Hamilton, R.J. Havel, Subcellular localization of B apoprotein of plasma lipoproteins in rat liver, *J. Cell Biol.* 69(2) (1976) 241–263.
- [63] H.-J. Butt, K. Graf, M. Kappl, *Physics and Chemistry of Interfaces*, Wiley-VCH, New York, 2003.
- [64] A. Iglic, B. Babnik, K. Bohinc, M. Fosnaric, H. Hagerstrand, V. Kralj-Iglic, On the role of anisotropy of membrane constituents in formation of a membrane neck during budding of a multicomponent membrane, *J. Biomech.* 40(3) (2007) 579–585.
- [65] H. Hagerstrand, L. Mrwczyska, U. Salzer, R. Prohaska, K.A. Michelsen, V. Kralj-Iglic, A. Iglic, Curvature-dependent lateral distribution of raft markers in the human erythrocyte membrane, *Mol. Membr. Biol.* 23(3) (2006) 277–288.

# VOLTAGE- AND CURRENT-CLAMP METHODS FOR DETERMINATION OF PLANAR LIPID BILAYER PROPERTIES

Peter Kramar,<sup>1</sup> Damijan Miklavčič,<sup>1</sup> Malgorzata Kotulska,<sup>2</sup>  
and Alenka Maček Lebar<sup>1,\*</sup>

## Contents

1. Introduction	30
2. Measurement Systems	32
2.1. Voltage Clamp	33
2.2. Current Clamp	46
3. Methods for Determination of Planar Lipid Bilayer Properties	49
3.1. Capacitance ( $C$ )	49
3.2. Resistance ( $R$ )	53
3.3. Breakdown Voltage ( $U_{br}$ )	54
3.4. Fluctuations ( $\psi$ )	57
3.5. Other Physical Properties	58
4. Conclusions	60
References	66

## Abstract

Biological membranes, the barriers that envelope the cell and its inner organelles, play a crucial role in the normal functioning of cells. The simplest model of these biological membranes is the planar lipid bilayer. Because its geometry allows chemical and electrical access to both sides of the bilayer, the physical properties of this model membrane can be easily measured. Usually, a thin bimolecular film composed of specified phospholipids and organic solvent is formed on a small aperture in a hydrophobic partition separating two compartments containing aqueous solutions. From the electrical point of view, a planar lipid bilayer can be considered as an imperfect capacitor; therefore, two electrical properties,

\* Corresponding author: Tel.: +386 1 4768 770; Fax: +386 1 4264 658

E-mail address: [alenka.macek.lebar@fe.uni-lj.si](mailto:alenka.macek.lebar@fe.uni-lj.si)

<sup>1</sup> Faculty of Electrical Engineering, University of Ljubljana, Ljubljana, Slovenia

<sup>2</sup> Institute of Biomedical Engineering and Instrumentation, Wrocław University of Technology, Wrocław, Poland

capacitance ( $C$ ) and resistance ( $R$ ), determine most of its behavior. Electrodes placed in the aqueous compartments on each side of the planar lipid bilayer permit the measurement of current and voltage across the model membrane. The two measuring techniques most commonly used to measure the properties of planar lipid bilayers are voltage-clamp methods and current-clamp methods.

The focus of this chapter is to review measurement systems and methods for the determination of the physical properties of planar lipid bilayers.

## 1. INTRODUCTION

Biological membranes, the barriers that envelope the cell and its inner organelles, play an important role in normal functioning of the cells. The membranes maintain crucial concentration gradients by acting as a selective filter for water-soluble ions and molecules [1]. Although biological membranes are composed of lipids, proteins, and small amounts of carbohydrates, the barrier function is assured by the thin layer of amphipathic phospholipids, which in polar liquid environments spontaneously arranges in various forms of lipid bilayers. A basic understanding of the properties and functioning of biological membranes can be obtained by investigating model systems, such as artificial liposomes or vesicles, which mimic the geometry and size of cell membranes, but are void of ion channels and the multitude of other embedded components commonly present in cells. The artificial planar bilayer lipid membrane (BLM) is the simplest model of a lipid system. It is usually formed across a small hole in a hydrophobic partition that separates two compartments filled with aqueous solutions. The advantage of the BLM is that both sides of the membrane can be easily altered and probed by electrodes.

Two methods of BLM formation are in common use. In one technique, the BLM is created by spreading a solution of lipids dissolved in an organic solvent. This method was introduced by Mueller and colleagues [2] and is named the painting technique. Both compartments of the chamber are filled with salt solutions and a dispersion of lipids is drawn across the hole in the partition separating them using a small paintbrush or a plastic rod. The cluster of lipids thins out in the center of the hole spontaneously forming a bilayer (Fig. 1). In the other procedure, the bilayer is formed from the apposition of two lipid monolayers [3]. A lipid solution in a volatile solvent is spread on the water-air interface of each compartment. Evaporation of the solvent creates a monolayer on the surface of the aqueous solution. When the monolayer formation is completed the water level in both compartments is raised above the hole and the bilayer is formed (Fig. 2).

A number of techniques have been developed to allow investigations of the functions and physical properties of these thin and fragile structures. Electrical measurements are a straightforward way to characterize the barrier

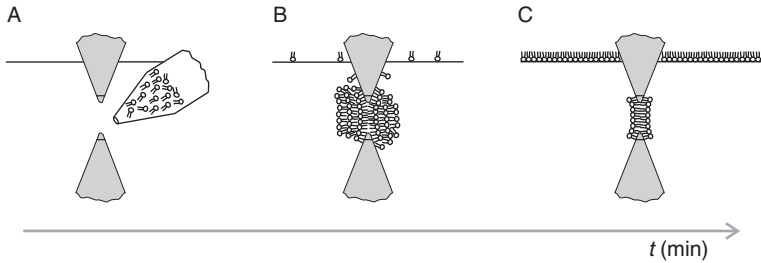


**Figure 1** Planar lipid bilayer formation by the painted technique [2]. (A) Lipid molecules are painted on the aperture by pipette or brush. (B) The cluster of lipid molecules on the aperture. Lipid molecules are slowly spreading across the aperture. Nonused lipid molecules flow to the water solution surface. (C) Planar lipid bilayer is formed on the hole by thinning process.

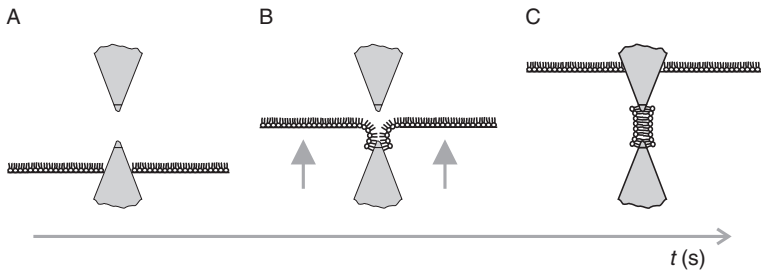


**Figure 2** The folding method [3]. (A) Layer of lipid molecules on the salt solution. (B) The levels of the salt solution are slowly raised above the hole. (C) Planar lipid bilayer is formed on the hole.

function of a bilayer—its ability to prevent the flow of ions. From an electrical point of view, a planar lipid bilayer can be easily imagined as an imperfect capacitor, which means that the capacitance ( $C$ ) has a finite parallel resistance ( $R$ ). The typical resistance is very high since the hydrophobic core is impermeable to any charged species, and it is called a gigaseal. But the resistance drops dramatically even if a few nanometer-sized holes are present in a lipid bilayer. Formation of pores can be induced by a strong electric field externally applied to the BLM, and electrical measurements permit determination of BLM breakdown voltage ( $U_{br}$ ). The electrical properties of the BLM are dependent on the physical properties of the lipids that compose the bilayer. Elasticity modulus and surface tension, for example, can be calculated from the electrical characteristics of the BLM.

Two electrical measurement methods are common (Fig. 3): the voltage-clamp method and the current-clamp method. When the voltage-clamp method is used, a voltage signal is applied to the planar lipid bilayer: a step change [4], pulse [5–7], linear rising [8], or some other shape of the

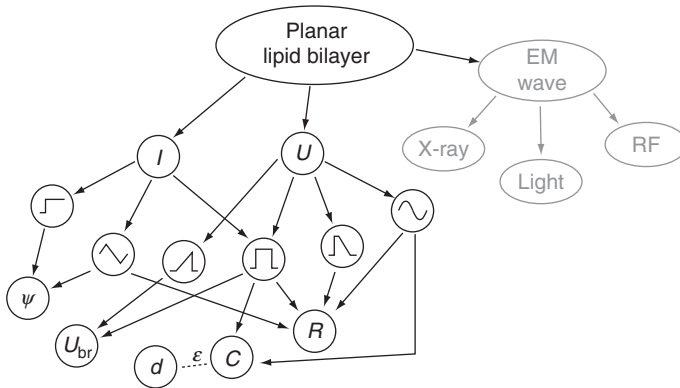


**Figure 3** Measuring concepts and electrical properties of planar lipid bilayers. Resistance ( $R$ ), capacitance ( $C$ ), thickness ( $d$ ), voltage breakdown ( $U_{br}$ ), and mass fluctuation ( $\psi$ ) are measured with application of current ( $I$ ) or voltage ( $U$ ) signals of various shapes.

voltage signal. When the current-clamp method is used, a current is applied to the lipid bilayer [9]. Although these two methods are interchangeable when applied to objects of constant impedance, the situation changes when the electrical properties of a measurement subject are transient and related to the electrical signal. Separation of these two methods is useful, for example, in BLMs when electrically induced pores are studied. The shape of these pores is very unstable and their conductance is constantly changing throughout experiments.

A combination of electrical recording techniques with different kinds of high-frequency electromagnetic fields offers additional possibilities of investigating the structure–function relationships of planar lipid bilayer and of membrane interacting peptides [10–13].

In the following, we review electrical measuring principles and methods that have been applied for determination of planar lipid bilayer properties. According to the fact that each planar lipid bilayer property can be measured in many ways (Fig. 3) and therefore by different measuring systems, the main goal of the chapter is only to describe the existing measuring principles and to point out their experimental abilities. The choice of the most appropriate measuring system should be determined by combination of planar lipid bilayer properties that has to be followed.

## 2. MEASUREMENT SYSTEMS

The first stable planar lipid bilayer membranes were reported by Mueller and coworkers in 1962 [14]. Since then, a variety of measuring systems have been designed for studying planar lipid bilayer properties.

Measuring principles have been improved during the years, as well as the lipid chambers and measurement instrument accuracies. This review of measuring systems is divided into two parts according to the nature of the stimulus—voltage or current. Some basic characteristics of the systems, such as type of stimulating signal, number and material of electrodes volume of the chamber, etc., are given in [Appendix A](#).

## 2.1. Voltage Clamp

### 2.1.1. System Hanai–Haydon–Taylor

The system was published in 1964 [15]. Within this system, DC and AC signals were applied to a planar lipid bilayer ([Fig. 4](#)). The DC signal was supplied by an accumulator. The voltage was controlled by a potentiometer. The current and resistance measurements were taken by electrometer. In the AC measurements, the capacitance and conductance were measured by two bridges, the Universal Bridge and Radio Frequency Bridge, which were designed on the basis of the transformer ratio-arm principle. The accuracy of the measurements was generally better than 1%. Two signal generators covering the ranges 50 Hz–100 kHz and 100 kHz–5 MHz were used, calibrated against standard frequencies. The bridge balance was detected with an oscilloscope with a preamplifier and a communications receiver. Two Ag–AgCl electrodes for DC measurements and two black platinum electrodes for AC measurements were immersed in salt solution.

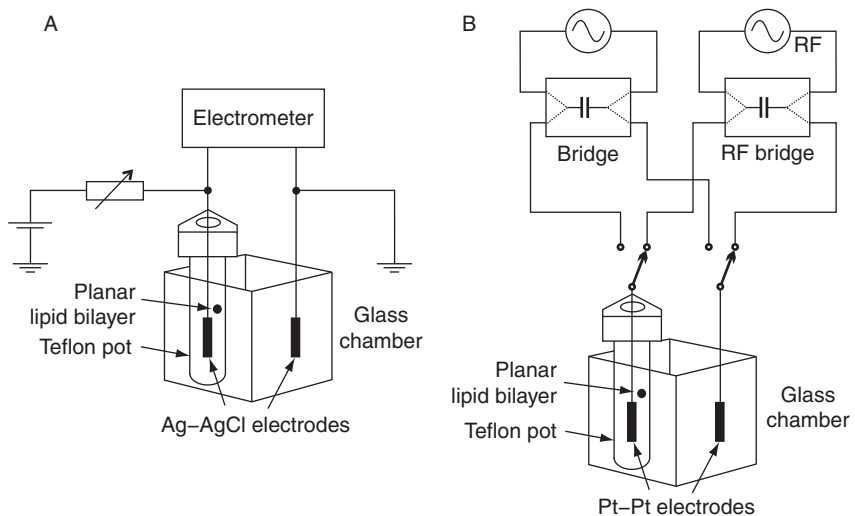


**Figure 4** System Hanai–Haydon–Taylor. The figure was drawn according to description in [Ref. \[15\]](#).

The chamber had outer and inner parts. The outer part was made of glass cell from tubing of 4 cm × 4 cm bore. The inner part was made out of Teflon rod. The aperture for planar lipid bilayer was about 0.141 cm in diameter made by punching. The thickness of Teflon around the aperture was about 0.05 cm. The whole chamber was enclosed in a double-walled box for temperature stabilization by a water shell. The temperature during experiments was controlled with an accuracy of  $\pm 0.5$  °C. Planar lipid bilayer was formed by the painted technique with a small brush.

The system was applied to quantitative assessment of the BLM molecular composition. Membrane thickness was obtained from the capacitance measurements that were obtained by a capacitance to voltage conversion method.

### 2.1.2. System Rosen–Sutton

The system was first published in 1968 [16]. Its main part was an AC signal generator with amplitude of 5 mV and frequency range from 100 Hz to 2 MHz (Fig. 5). Electrodes were connected to the transformer ratio-arm bridge. The bridge was initially balanced at a given planar lipid bilayer capacitance, which allowed DC potential to be applied between the electrodes during the AC measurements. The amplitudes of the DC potentials were up to 200 mV. An oscilloscope monitored Lassajous figures to permit observation of the conductance and capacitance contribution. The AC signal was applied through the bridge to planar lipid bilayer and to X channel of the oscilloscope. The planar lipid bilayer response was traced on Y channel. Four electrodes were immersed in salt solution. Two Calomel electrodes were used for measurement of transmembrane voltage by electrometer while voltage signal was delivered by two platinum electrodes. The planar lipid bilayer was painted across a round hole of about 1 mm in diameter.

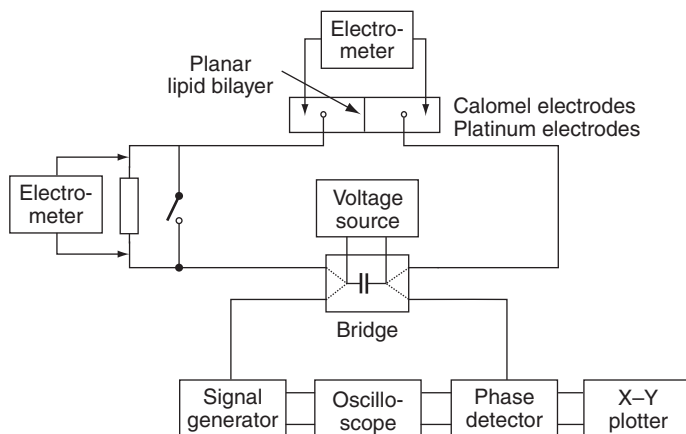


**Figure 5** System Rosen–Sutton [16].



The system was applied to study an influence of the temperature and concentration of the salt solution on the electrical parameters of planar lipid bilayer [16].

### 2.1.3. System White

The system was first published in 1970 [17]. The basic idea follows the construction of the Rosen–Sutton system. The planar lipid bilayer capacitance was obtained from impedance measurements with an AC Winston bridge (Fig. 6). The chamber was made of Plexiglas with Teflon partition. Four platinized Ag–AgCl electrodes were used. A planar lipid bilayer was painted across round aperture of about 1 mm in diameter [17,18].

The authors studied the influence of the BLM thickness changes on BLM capacitance. They also investigated the planar lipid bilayer capacitance in dependence of the transmembrane voltage. The capacitance measurements were done by a capacitance to voltage conversion method.

### 2.1.4. System Wobschall

The system was published in 1971 [19,20]. The basic idea follows the construction of the Rosen–Sutton system but it was upgraded for planar lipid bilayer elasticity measurements (Fig. 7). The volume of one compartment of the chamber could be regulated by a flexible diaphragm with an acoustic oscillator. Pressure changes were measured with a pressure-sensitive transistor. The AC voltage signal was supplied by a function generator and a DC source. Both were regulated by a feedback circuit. The bridge excitation voltage with a frequency of 4 kHz varied from 5 to 15 mV. Four Ag–AgCl electrodes were immersed in a salt solution. The planar lipid bilayer was formed by the painted technique.

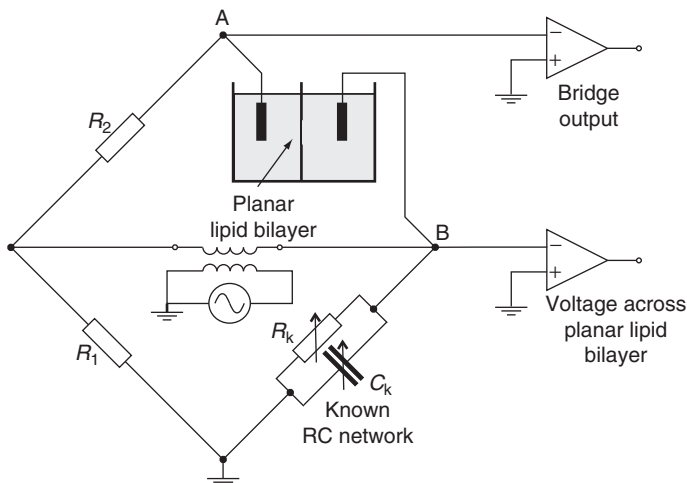


**Figure 6** System White [17].

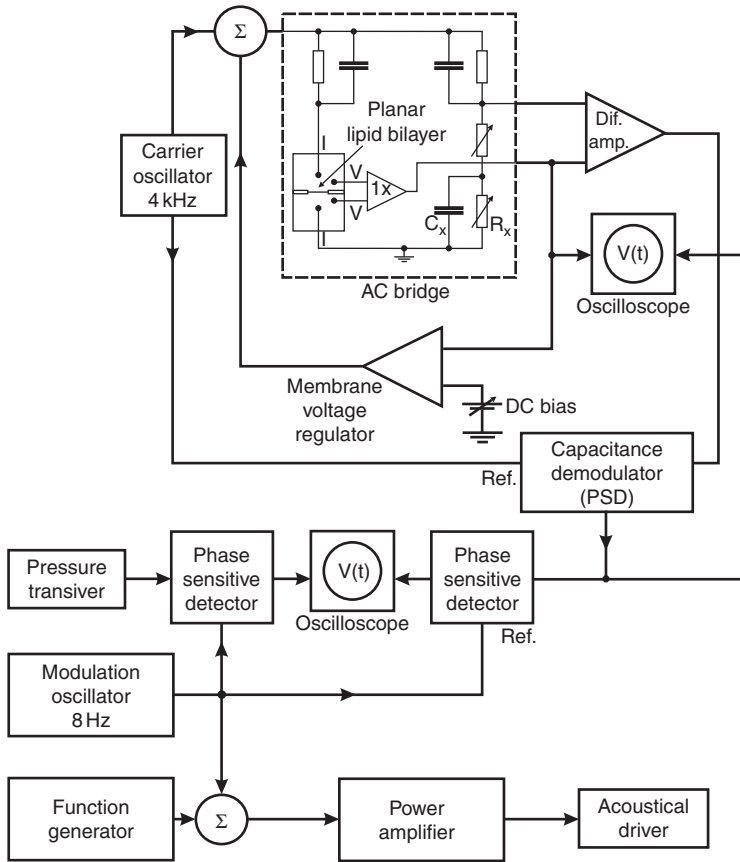


**Figure 7** System Wobshall [19,20].

The capacitance of planar lipid bilayer in dependence of voltage and frequency was measured by a capacitance to voltage conversion method.

The construction of the chamber had a possibility of concaving the planar lipid bilayer in the shape of lens, which extended the area of BLM. This idea was employed to study the BLM capacitance in relation to its surface [20]. The elasticity of planar lipid bilayer at its breakdown was determined [19].

In the latter versions of this experimental system, the bridge was replaced by an impedance meter [21].

### 2.1.5. System Montal–Mueller

Montal and Mueller published the design of their measuring system in 1972 [3]. It was one of the first measuring systems that combined concepts of both measuring principles: voltage clamp and current clamp. The measuring

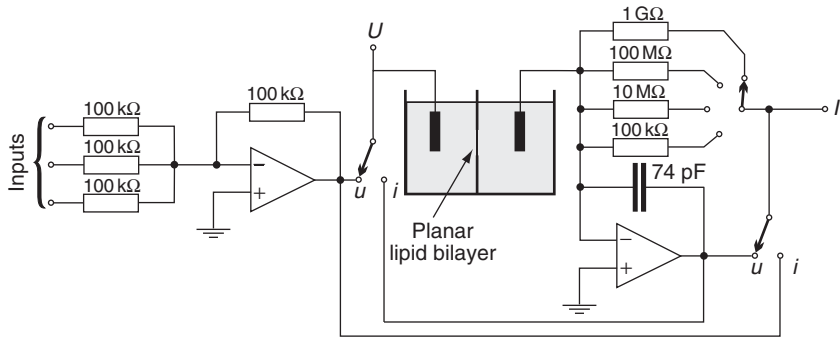


**Figure 8** System Montal–Mueller [3].

principle was selected by two switches (Fig. 8). In the scheme, two amplifier circuits are present; the circuit on the left is voltage amplifier while the circuit on the right is current to voltage converter in the voltage-clamp mode (the switches are in position *u*) and voltage to current converter in the current-clamp mode (the switches are in position *i*). In voltage-clamp mode, the applied voltage is measured at connecting point *U* and the voltage that corresponds to current flowing through the planar lipid bilayer is measured at connecting point *I*. In the current-clamp mode, the applied current is recorded at connecting point *I* and the transmembrane voltage is measured at connecting point *U*. For planar lipid bilayer stimulation and corresponding measurements, two Calomel electrodes immersed in salt solution were used. The salt solution filled the Teflon chamber, which was divided into two compartments by 25  $\mu\text{m}$  thick Teflon foil with an aperture of about 0.25 mm in diameter. The dimension of each compartment was  $(18 \times 12) \text{ mm}^2$ . The planar lipid bilayer was formed by the folding method [3].

The system was used for measurement of BLM capacitance and resistance. The capacitance was measured by charging method.

### 2.1.6. System Benz

The system was published in 1976 [6,7]. It is one of the simplest systems for observing planar lipid bilayers (Fig. 9). It consists of DC signal generator with the amplitude range from 10 mV to 5.4 V, switch, and battery supplied charge generator. The function of the switch was accomplished with FET transistor 2N5653. The output signal was a square pulse with duration from 500  $\mu\text{s}$  to 500 ms. Oscilloscope Tektronix 7633 was used to measure the voltage response on planar lipid bilayer. The signal was filtered to the band of 80 Hz to 40 MHz. Two Ag–AgCl electrodes were immersed in a salt solution. The volume of each compartment of the Teflon chamber was of about 3  $\text{cm}^3$ . In most cases, the area of the aperture was of about 2  $\text{mm}^2$ . The planar lipid bilayer was formed by painted technique.

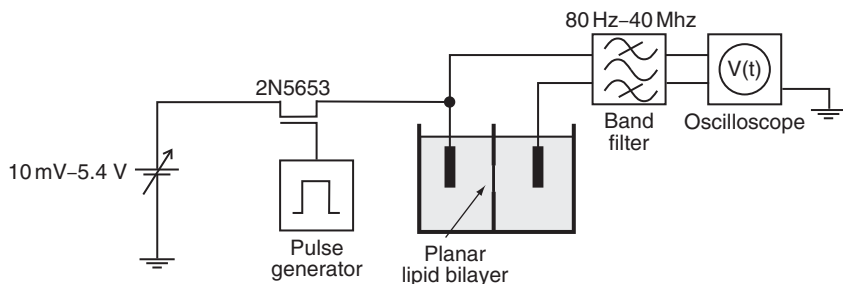


**Figure 9** System Benz. The figure was drawn according to description in Ref. [6].

Benz *et al.* studied the capacitance of planar lipid bilayers using a discharge method. Most of the phospholipids used in their studies were synthesized in their own laboratory. In most cases, they used 0.1 M NaCl as the salt solution. They estimated thickness of the planar lipid bilayers and observed the thinning process of the planar lipid bilayers by capacitance measurement. The same system was used to investigate voltage breakdown as a function of salt concentration and pH [7].

The system was applied by the group of Chernomordik, whose experimental and theoretical studies made a great impact on understanding of the planar lipid bilayer breakdown process and related phenomena [4,22,23]. They observed fluctuations of the current with amplitude of about  $10^{-11}$  A as a consequence of applying the voltage (100 mV–1 V) to the BLM. The membrane lifetime at a given voltage was also tested, defined as the time corresponding to the onset of an irreversible growth of current.

### 2.1.7. System Alvarez-Latorre

The system was published in 1978 [24]. The construction of the system was similar to the measuring systems based on the Winston Bridge [16,17,19]. Since the authors were interested in measuring changes in membrane capacitance rather than the absolute capacitance, they used differential amplifier to subtract the charging current of the membrane from the charging current of the equivalent  $RC$  network (Fig. 10). The resistance and capacitance of the equivalent  $RC$  network was set by the planar lipid bilayer capacitance measurement. The method based on 5 kHz, 10 mV peak-to-peak voltage waveform, which was only applied on a planar lipid bilayer. Two Ag–AgCl electrodes, one on each side of planar lipid bilayer, were immersed in the salt solution. The Teflon chamber consisted of two parts; each part had an area of  $4 \text{ cm}^2$ . A thin Teflon sheet of  $19 \mu\text{m}$  was inserted between the reservoirs. The planar lipid bilayer was formed by the folding method. The output of the differential amplifier was further amplified and recorded with a sampling frequency of 2 MHz.

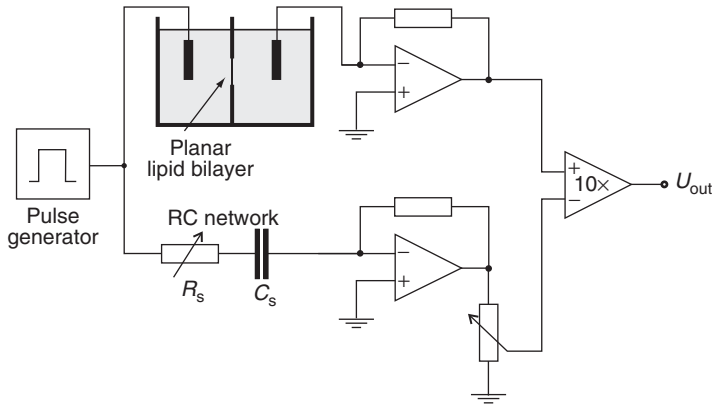


**Figure 10** System Alvarez–Latorre [24].

They observed the capacitance of a planar lipid bilayer as a function of transmembrane potential and derived the thickness of planar lipid bilayers.

### 2.1.8. System Chanturya

The system proposed by Chanturya [25] was based on the system Benz [6]. The only difference in their designs is in a compensating capacitor, placed between the input of the operational amplifier and the inverter of the transmembrane potential (Fig. 11). The capacitor compensated almost all the reactive component of the current. Therefore, the author was able to use high-speed potential changes and obtain high resolution of measurements.

The system was applied for a study on the capacitance and resistance changes due to insertion of channel-forming proteins into the planar lipid bilayer [25].

### 2.1.9. System Wilhelm–Winterhalter–Zimmermann–Benz

The system was published in 1993 [26]. It was used in many other subsequent studies because it was simple and well defined [26–30]. The planar lipid bilayer was charged by a short voltage pulse with a commercial pulse generator. Instead of the switch, a diode with a reverse resistance  $\gg 10^{12} \Omega$  was used to discharge the planar lipid bilayer only through the oscilloscope (Fig. 12). The pulse generator produced square pulses with durations from 0.2 to 10.0  $\mu\text{s}$ . Two Ag–AgCl electrodes were immersed in salt solution that filled the Teflon chamber. Authors used different sizes of the apertures in the wall between two compartments—their areas were between 0.3 and 3  $\text{mm}^2$ . The planar lipid bilayers were formed by the painted technique. The actual voltage on planar lipid bilayer was amplified with an operational amplifier and recorded with an oscilloscope. The data was processed by a connected computer.

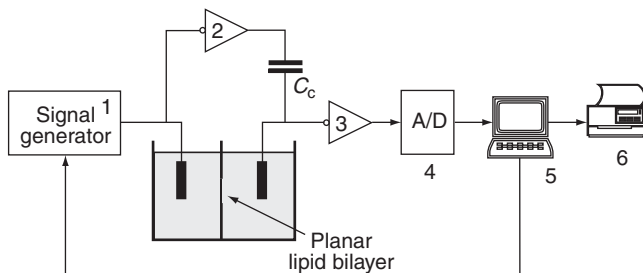


**Figure 11** Sistem Chanturya [25]. 1. Signal Generator, 2. and 3. invertors, 4. analog to digital converter, 5. Personal Computer, 6. Printer.

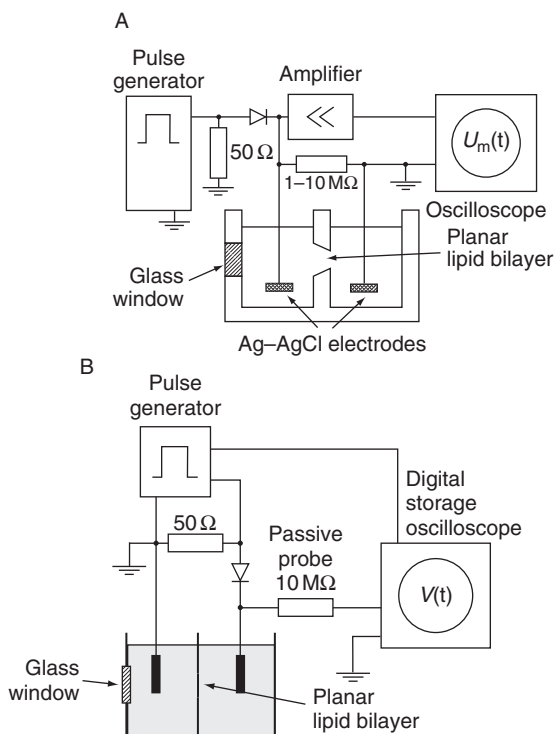


**Figure 12** (A) System Wilhelm–Winterhalter–Zimmermann–Benz [26]. (B) Updated version of the system with an Digital Storage Oscilloscope described in Refs. [27–30].

Because many studies were based on this measuring system, a palette of lipids was tested [27–30]. Salt solutions differed from study to study as well as the volume of the lipids. The influence of the planar lipid bilayer composition on the breakdown voltage, capacitance, and rupture kinetics [27–29] was investigated [26,30].

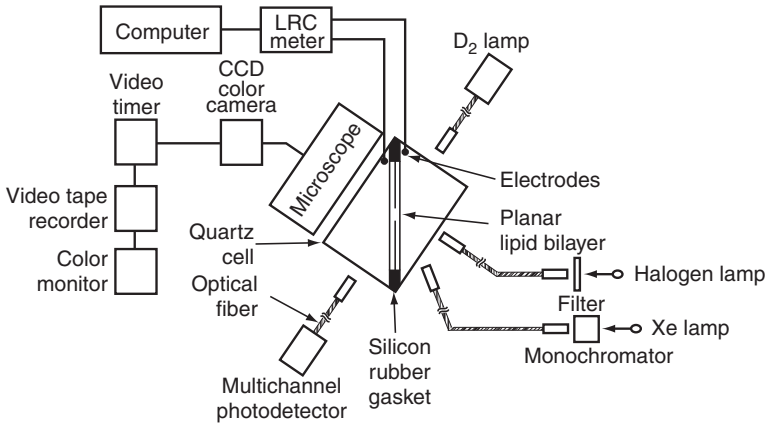


**Figure 13** Sistem Yamaguchi–Nakanishi [12].

### 2.1.10. System Yamaguchi–Nakanishi

The system was published in 1993 [12]. It used combination of electric and optic measurements of planar lipid bilayer properties (Fig. 13). The authors simultaneously measured electrical characteristics and molecular structures of planar lipid bilayer as well as morphological changes. Planar lipid bilayer was exposed to sinus signal  $7 \text{ mV}_{\text{RMS}}/1 \text{ KHz}$ . The response was measured with LCR meter. The measured data was acquired to the computer. During the electric measurement, the halogen or xenon light was used. Light reflection of planar lipid bilayer was observed and recorded by a color video camera. Two platinum/platinum electrodes were immersed in a salt solution. Chamber consisted of two quartz cells separated by Teflon 0.05 mm thick film, where an aperture of 0.7 mm in diameter was formed. The planar lipid bilayer was formed by the painted technique [12].

The authors measured changes in capacitance and resistance of planar lipid bilayer upon the irradiation by light.

### 2.1.11. System Sharma–Stebe–Tung

The system was an upgrade of the Benz system and it was described in 1996 [5,31]. FET switch was replaced by fast two pole analog switch. One of the switch poles was connected to the signal generator output and the other pole was connected on resistor of  $1 \text{ M}\Omega$ . Voltage source consisted of an arbitrary waveform synthesizer board interfaced to a computer (Fig. 14). A square voltage pulse, which decayed linearly to zero to constitute a negative sloped ramp, and square voltage pulses from  $10 \mu\text{s}$  to  $10 \text{ s}$  were generated. Four Ag–AgCl electrodes were inserted in the Teflon chamber via agar bridges. Two electrodes served to measure voltage across the bilayer by differential amplifier and the other two to apply voltage across the planar

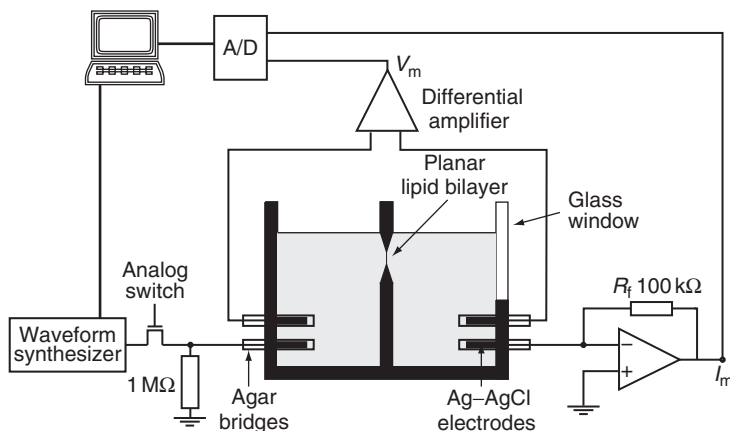


**Figure 14** Sistem Sharma–Stebe–Tung [5,31].

lipid bilayer and measure the transmembrane current. The volume of each compartment of the Teflon chamber was about  $3 \text{ cm}^3$ . The diameter of the aperture in the Teflon foil was  $105 \mu\text{m}$ . The planar lipid bilayers were formed by the folding technique. Current and voltage signals were recorded by a digital oscilloscope.

The system was used for studying the effects of nonionic surfactants (poloxamer 188,  $\text{C}_{12}\text{E}_8$ ) on capacitance, conductance, and voltage breakdown of planar lipid bilayers [5,31]. Breakdown voltages of planar lipid bilayers were determined by applying a rectangular voltage pulse.

### 2.1.12. System Gallucci–Micelli

The system was published in 1996 [32]. The dynamic capacitance and resistance of a planar lipid bilayer could be measured simultaneously as is described in Section 3.2. Voltage signal of 1 kHz and adjustable amplitude, which was applied on planar lipid bilayer, was modulated by the signal of amplitude 2 mV and frequency of 1 kHz (Fig. 15). The electrodes were made of platinum. Experiments were performed in a Teflon chamber. The volume of each compartment was 4 ml. The aperture between the two compartments had a diameter of 1.3 mm. Current through the planar lipid bilayer was measured and amplified. The output signal from the amplifier was divided into two parts. In the first part, active two-stage 1 kHz band filter was used. The signal was then amplified, level adjusted, and rectified. Rectified voltage corresponds to the capacitance of planar lipid bilayer. In the second part, two-stage 1 kHz low pass filter was used. The signal was then amplified, level adjusted, and filtered to measure the resistance of the planar lipid bilayer [32–34].



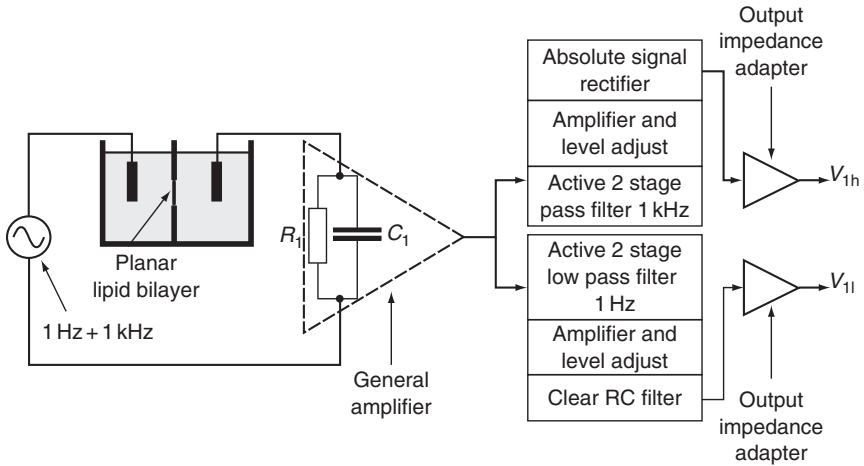


**Figure 15** Sistem Gallucci–Micelli [32–34].

The general aim of the authors was investigation of channel insertion into planar lipid bilayer and corresponding electrical properties. The dynamic capacitance and resistance of planar lipid bilayers were measured simultaneously.

### 2.1.13. System Hanyu–Yamada–Matsumoto

Hanyu and coworkers [11] developed an experimental system that could measure ionic current and fluorescence emission of an artificial planar lipid bilayer, while controlling the membrane potential. Their experimental work was mostly dedicated to structural changes and functioning of ion channels.

The main part of the measuring system was an Axopatch200A (Axon Instruments, Inc. Foster City, USA). The program pClamp was used for voltage generation as well as for measuring the current through the planar lipid bilayer and analyses. Four Ag–AgCl electrodes were inserted in the specially designed chamber via agar bridges. Two electrodes served to measure current across the bilayer while the other two applied the voltage across the planar lipid bilayer. As in the previous system designed by Sharma *et al.* [31], the thin Teflon foil (25  $\mu\text{m}$  thick) was inserted between two symmetrical parts of Teflon chamber. The diameter of the hole in the foil was 120  $\mu\text{m}$ . The planar lipid bilayer was formed by the folding technique.

Schematic diagram of the experimental system developed for measuring the fluorescent emissions from the planar lipid bilayer is shown in Fig. 16. The excitation light was focused on the planar lipid bilayer (80  $\mu\text{m}$  in diameter) with an objective lens so that only an area of the planar lipid bilayer was irradiated. The fluorescent emissions were collected through the

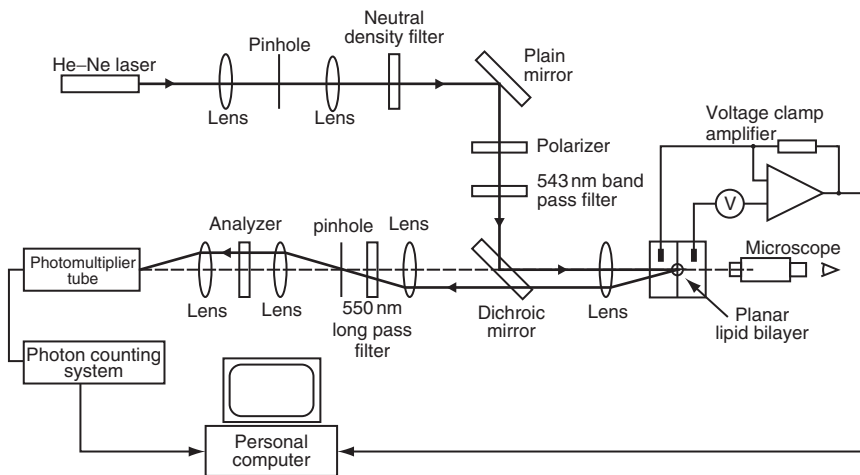


**Figure 16** Hanyu–Yamada–Matsumoto [11].

objective lens and sent to the photomultiplier. Any fluorescence from other areas was blocked and scattered light was eliminated. The intensity of fluorescence was measured by photon-counting methods, while a multi-channel analyzer was used for the emission spectrum measurements.

#### 2.1.14. System Naumowicz–Petelska–Figaszewski

The system was published in 2003 [35]. It was similar to the system of Wobschall and the Rosen–Sutton system. It allowed applying pressure to planar lipid bilayer. Electrical properties of BLM were examined by impedance spectroscopy (Fig. 17). Four electrodes were immersed in a salt solution: two platinum current electrodes (CE) and two Ag–AgCl measuring electrodes (RE). The volume of one side of the organic glass chamber was modulated by external thread screw. The planar lipid bilayer was formed by the painted technique. Impedance measurement was carried out using an AC impedance system with a personal computer, two-phase lock-in amplifier, and potentiostat/galvanostat. Measuring electrodes were connected with a potentiostat via a high impedance input differential amplifier.

Impedance spectroscopy was used to measure planar lipid bilayer capacitance and resistance [35–37]. The interfacial tension of planar lipid bilayer was measured [38].

#### 2.1.15. System Kramar–Miklavcic–Macek Lebar

The system was published in 2007 [8,39]. It was based on the Sharma–Stebertung system. It included a signal generator, Teflon chamber, voltage and current measurement circuit, and digital storage oscilloscope (Fig. 18). Signal generator was a generator of an arbitrary type. It provided voltage amplitudes

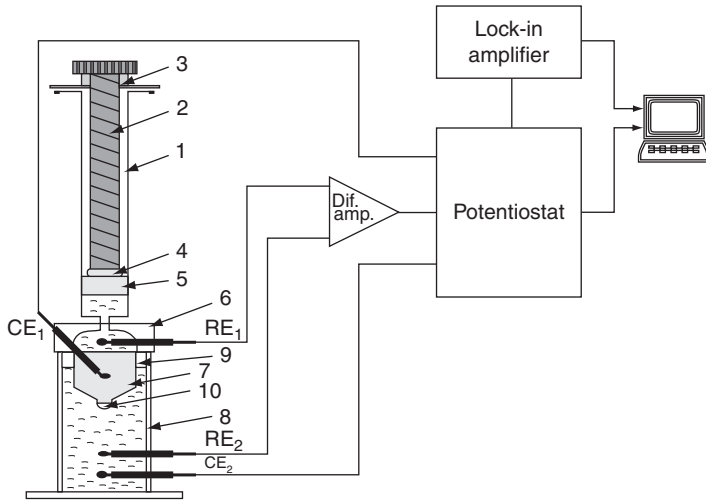


**Figure 17** System Naumowicz–Petelska–Figaszewski [37]. 1. Syringe, 2. External thread screw, 3. Handwheel, 4. Steel tube, 5. Tight Teflon Piston, 6. Connector made of organic glass, 7. Platinum current electrode, 8. The chamber made of organic glass, 9. A tight Teflon attachment, 10. A forming sphere for planar lipid bilayer.

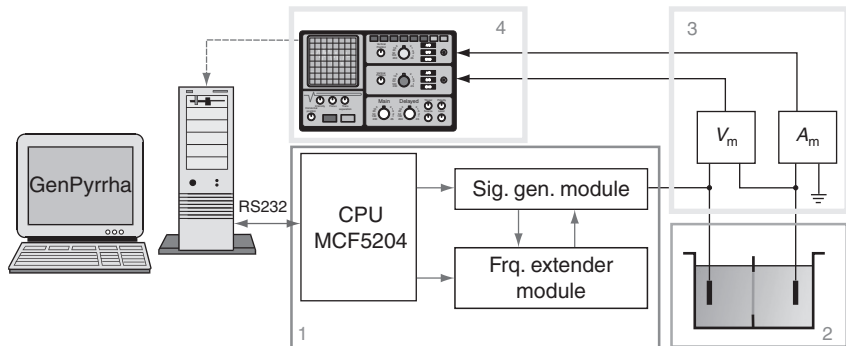


**Figure 18** Experimental system. 1. The microprocessor board with MCF5204 processor and two modules. Signal generator module generates arbitrary signals. Frequency extender module is realized in programmable integrated circuit (FPGA) and is used for frequency extension. 2. Chamber for forming planar lipid bilayer and two Ag–AgCl electrodes. 3. Modules for current and voltage amplification. 4. Oscilloscope for data collection and storage.

from  $-5$  to  $+5$  V. It was controlled by custom designed software (Genpyrrha), which allowed drawing of arbitrary voltage signals. On the output of the signal generator was a switch that disconnected the output of the signal generator and connected the electrodes to the  $1\text{ M}\Omega$  resistor. The switch was able to turn off

the signal generator in 2 ns. This way planar lipid bilayer capacitance was measured. Two Ag–AgCl electrodes, one on each side of the planar lipid bilayer, were inserted into the salt solution. The Teflon chamber consisted of two parts—each part was a cubed reservoir of  $5.3 \text{ cm}^3$  in volume. Between the reservoirs a  $25 \text{ }\mu\text{m}$  thin Teflon sheet was inserted. A diameter of the aperture was  $105 \text{ }\mu\text{m}$ . The planar lipid bilayer was formed by the folding method. Transmembrane voltage was measured by LeCroy differential amplifier 1822. The same electrodes were also used to measure the transmembrane current. Both signals were stored by the oscilloscope LeCroy Waverunner-2 354M in Matlab format. All sampled signals could be analyzed in Matlab<sup>TM</sup> software after the experiments.

The authors measured  $U_{\text{br}}$  by means of a linearly rising signal and the capacitance of the planar lipid bilayers of various compositions [8].

## 2.2. Current Clamp

### 2.2.1. System Carius

The system was published in 1976 [40]. Symmetric AC Bridge was the main part of the measuring system (Fig. 19). The variable resistor  $R_K$  and the capacitor decade  $C_K$ , used for compensation, were in series. Without a planar lipid bilayer in the chamber, the electrode and electrolyte resistance were compensated with  $R_K=R_0$  and  $C_K=C_0$ , when the capacitor  $C_0$  was in series with the cell by means of switch S. With the planar lipid bilayer in the chamber, the increase in the compensation resistance needed ( $R_K-R_0$ ) corresponded to the loss of the planar lipid bilayer capacitor, represented by the equivalent series planar lipid bilayer resistance. A DC bias voltage up to  $\pm 200 \text{ mV}$  was provided at the planar lipid bilayer by a voltage controlled current source. The bridge balance was controlled by a phase-sensitive detector (lock-in amplifier) tuned to the frequency of the oscillator. When the out-of-phase signal vanished at proper settings  $R_K$ , the in-phase signal output of the lock-in amplifier was proportional to  $(C_{\text{BLM}} - C_K)$ , provided that the difference was small compared to  $C_K$ . The AC voltage on the planar lipid bilayer was 3 or 6  $\text{mV}_{\text{RMS}}$ , when only the capacitance was recorded. Another lock-in amplifier was used for the detection of the second harmonic. For these measurements, the AC voltage on the planar lipid bilayer was 20–60  $\text{mV}_{\text{RMS}}$  and the DC voltage varied between 0 and  $\pm 160 \text{ mV}$ . When the second and third harmonics were measured simultaneously by the two lock-in amplifiers, bridge balance was controlled by an AC voltmeter with a band pass filter at the input. The electrodes were Ag–AgCl–platinum black electrodes. The chamber was made of Teflon. In most cases, the diameter of the aperture was about 0.9 mm. The planar lipid bilayer was formed by the painted technique. The output signals were recorded.

The system was applied to measurements of the transmembrane voltage dependence on the BLM capacitance.

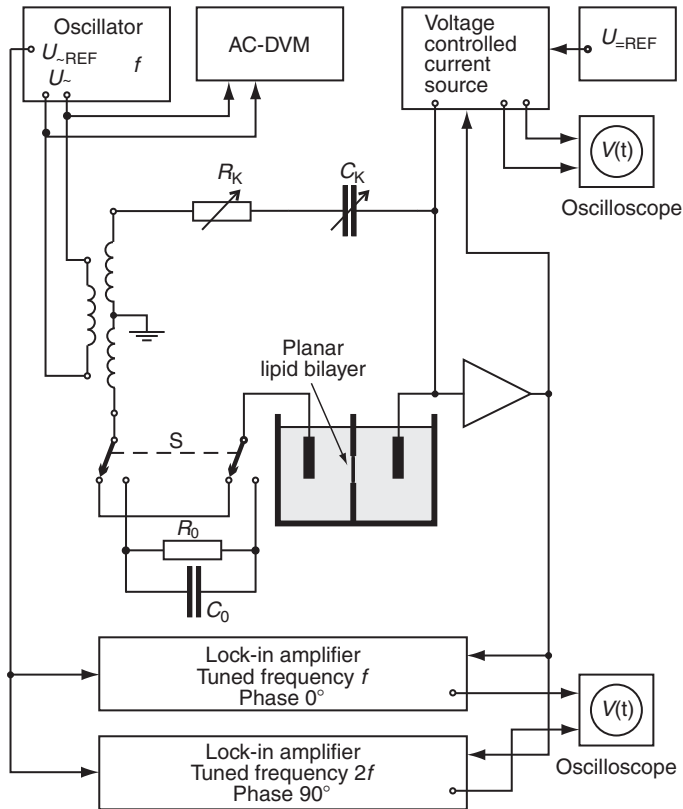


**Figure 19** System Carius [40].

### 2.2.2. System Robello–Gliozzi

The system was published in 1989 [41]. The group performed experiments on current–voltage relationship of planar lipid bilayer under voltage-clamp condition in previous years [42]. Later on, they changed their measuring system to a current-clamp mode. The planar lipid bilayer was in a feedback network of the operational amplifier which acted as a current–voltage converter (Fig. 20). The current value was selected with resistor on the amplifier input. The current–voltage characteristics were obtained by exposing the planar lipid bilayer to a triangular signal with 8–10 min period [41]. By constant current of 10–20 pA, the fluctuations in planar lipid bilayers were studied [43–45]. Two Ag–AgCl electrodes were immersed in salt solution. The volume of each compartment of the Teflon chamber was about 2 ml. The Teflon foil between two compartments was 12  $\mu\text{m}$  thick. The diameter of the apertures was from 100 to 200  $\mu\text{m}$ . The planar lipid bilayer was formed by the folding method. The output signal was low-pass filtered at 250 Hz (24 db/octave) and recorded to the computer with a sampling frequency of 1 kHz.

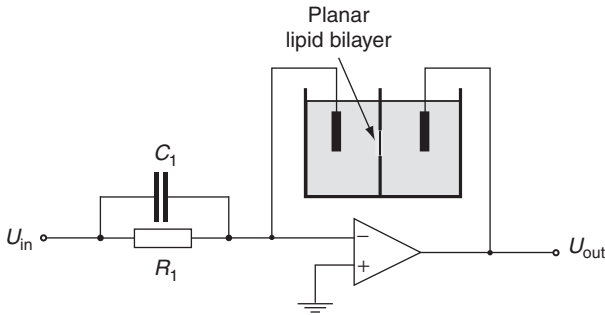


**Figure 20** System Robello–Gliozzi [41–47].

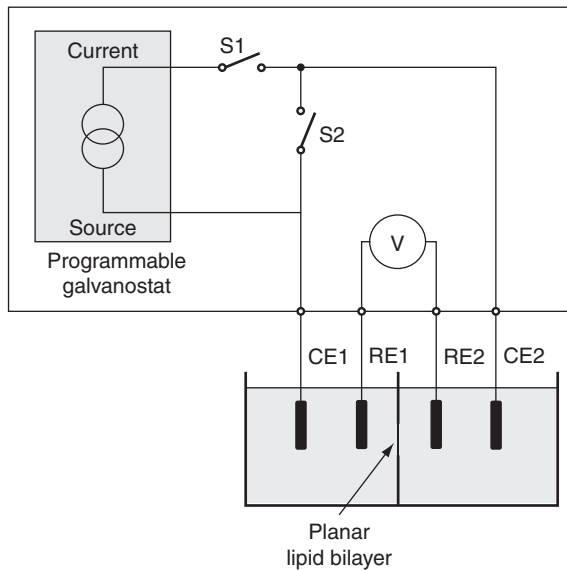


**Figure 21** System Kalinowski–Figaszewski [48–51].

The authors observed voltage breakdown, current–voltage characteristic, and fluctuations of planar lipid bilayer. The system was later on upgraded to extremely low current value source (10 pA) [47].

### 2.2.3. System Kalinowski–Figaszewski

The system was published in 1992 [48]. The system included two modules (Fig. 21). The first module was capacity to period converter, used for measuring the BLM capacitance [48,49] (see Section 3.1). The second module was a potentiostat–galvanostat for planar lipid bilayer studies under current clamp [50]. Both modules were controlled with a personal computer.

The output signal was programmable [51]. The potentiostat had a negative feedback for equalization of operational amplifier input voltage. The chamber was made of one piece Teflon with two compartments, each 10 cm<sup>3</sup> of volume. Between the compartments was the aperture of 1 mm in diameter. Four Ag–AgCl electrodes were immersed in a salt solution; two of them were CE and two other reference electrodes (RE). The switch S1 disconnected the current flowing through the electrodes. The switch S2 caused short circuit of the CE and forced planar lipid bilayer potential to zero.

The system was applied for recording the transmembrane voltage, especially for the electroporation studies the trace of building voltage on planar lipid bilayer was observed due to constant current clamp [9,52].

### 3. METHODS FOR DETERMINATION OF PLANAR LIPID BILAYER PROPERTIES

#### 3.1. Capacitance (*C*)

The capacitance (*C*) is the parameter considered the best tool for probing the stability and integrity of planar lipid bilayers and for this reason it is measured for every bilayer, even when other properties are the main focus of the measurements. There are three main methods for determination of planar lipid bilayer capacitance: a discharge method, a capacitance to period conversion method, and a capacitance to voltage conversion method. For comparison between different studies, the measured value of the capacitance must be normalized to the size of the planar lipid bilayer surface and the specific capacitance of the planar lipid bilayer, that is, the capacitance per unit area, is usually given.

##### 3.1.1. Discharge method

The most common and simplest method for measuring planar lipid bilayer capacitance is measurement of the voltage discharge time constant [5,6,8,26,27,30,31,39,53]. Only a voltage generator, a fast switch, and an oscilloscope are needed for its implementation. To make the measurement, a planar lipid bilayer is first charged by a voltage pulse. At the end of the pulse, the charged lipid bilayer is discharged through a resistor of known resistance and the discharging process monitored with an oscilloscope (Fig. 22).

The voltage  $u(t)$  on the planar lipid bilayer decreases exponentially:

$$u(t) = U_0 e^{-t/\tau}. \quad (1)$$

Here,  $U_0$  is the amplitude of the voltage pulse and  $\tau$  is a time constant. The time constant depends on the capacitance (*C*) and resistance (*R*) which come from the planar lipid bilayer and the electronic system,

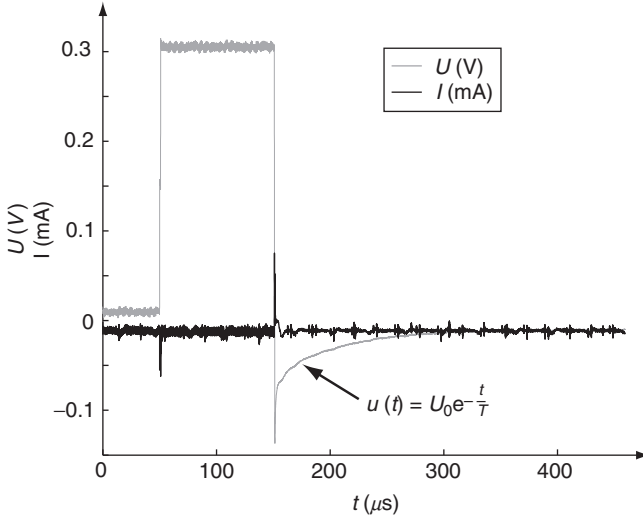


**Figure 22** Planar lipid bilayer capacitance measurement by discharge method.

$$\tau = RC. \quad (2)$$

The resistance of the electronic system is usually known and is much lower than the resistance of planar lipid bilayer ( $\sim 10^8 \Omega$ ); therefore, the capacitance of planar lipid bilayer can be determined in two steps. First, the capacitance of the electronic system is measured without the planar lipid bilayer,  $C_{\text{SYS}}$ . Then, the capacitance of the electronic system with the planar lipid bilayer and salt solution  $C_{\text{SBLM}}$  is determined. The capacitance of planar lipid bilayer  $C_{\text{BLM}}$  is then obtained as a difference between  $C_{\text{SYS}}$  and  $C_{\text{SBLM}}$ :

$$C_{\text{BLM}} = C_{\text{SYS}} - C_{\text{SBLM}}. \quad (3)$$

In early experiments, the planar lipid bilayer charging process was also used for planar lipid bilayer capacitance determination. Montal and Mueller [3] calculated the capacitance of planar lipid bilayers from the current records in response to a voltage step signal:

$$C = \frac{I}{\Delta U} \int_0^{\infty} I dt, \quad (4)$$

where  $I$  is the current and  $\Delta U$  the amplitude of the voltage. In the constant voltage mode, the time constant and gain of the current record depends on the value of the feedback resistor in the current measuring amplifier. Because the capacity currents are small, the feedback resistance was kept about 100 k $\Omega$ .



### 3.1.2. A capacitance to period conversion method

The electrical parameters of the planar lipid bilayer can also be measured by means of an alternating voltage signal, which offers the advantage of eliminating the effect of possible electrode polarization.

Kalinowski and Figaszewski [48] constructed an instrument (Fig. 23), which converts planar lipid bilayer capacitance to a train of rectangular pulses. During the measurement, the planar lipid bilayer is charged and discharged with a constant current. The charge–discharge cycle duration is proportional to the membrane capacitance.

In the circuit in Fig. 23, the capacitance of planar lipid bilayer is represented by the capacitor  $C_{\text{BLM}}$ . The voltage at the point D is amplified by a noninverting amplifier with the gain  $k$ :

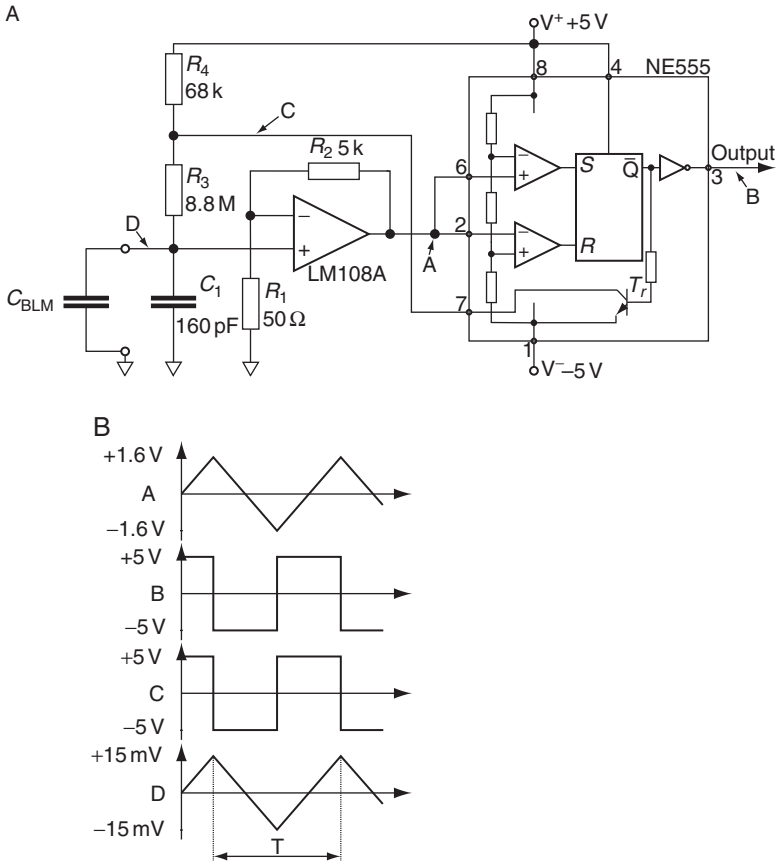


**Figure 23** Measurement of planar lipid bilayer capacitance by capacitance to period conversion method. (A) Schematic diagram of the capacity-to-period converter [48]. (B) Voltage wave of the capacity-to-period converter [48].

$$k = \frac{R_1 + R_2}{R_2}. \quad (5)$$

The amplified signal is an input of the integrated circuit NE555. Two voltage comparators are contained in the integrated circuit, both with one of their inputs connected to the voltage from the amplifier output (A) while the other input is one of the voltages from the voltage divider, which is realized by three resistors. Depending on the voltage levels at the inputs  $R$  and  $S$ , the output of the cell (B) is switched to a low or high state. The result is a square wave signal, which has a well-defined period. The voltage across the planar lipid bilayer can be calculated as

$$U_{\text{BLM}} = \frac{2}{3} V \frac{1}{k} = \frac{2VR_1}{3(R_1 + R_2)}. \quad (6)$$

The measurement is divided into two steps. First, the capacitor is charged with the current passing across resistors  $R_4$  in  $R_3$  and transistor  $T_r$  is off. Then, the capacitor is discharged due to the current across the transistor, which is a consequence of a changed state of the cell. The current flows across resistor  $R_3$  and transistor  $T_r$ . The product of the voltage and time in one period is:

$$TV = U_{\text{BLM}}(R_3 + R_4)C_{\text{BLM}} + U_{\text{BLM}}R_3C_{\text{BLM}}. \quad (7)$$

If  $R_4 \ll R_3$  and  $V = V^+ = |V^-|$ , then the period is:

$$T = \frac{2U_{\text{BLM}}R_3C_{\text{BLM}}}{V}. \quad (8)$$

### 3.1.3. A capacitance to voltage conversion method

When a sinusoidally varying signal is applied to the planar lipid bilayer, its impedance is important. Since capacitors “conduct” current in proportion to the rate of voltage change, they pass more current for faster changing voltages, and less current for slower changing voltages. Therefore, the capacitive part of the impedance—capacitive reactance in ohms for any capacitor is inversely proportional to the frequency of the alternating current. According to this theory, the capacitances of planar lipid bilayers were often measured using AC Wheatstone bridge [15–17], which contain a variable resistor in parallel with a variable capacitor in the known arm. When the bridge is balanced at a given frequency, the settings of the known arm give the parallel equivalent capacitance and resistance of the circuit connected to its unknown terminals. Since the planar lipid bilayer is immersed in electrolyte, the bridge measures the parallel equivalent impedance of the membrane–electrolyte system.

The parallel equivalent capacitance can be represented by the membrane capacitance and the stray capacitance associated with electrodes in series with electrolyte resistance; therefore, appropriate equivalent circuit and transform equations should be used to relate membrane capacitance to the elements of the bridge. A convenient technique for displaying AC impedance data is the Cole–Cole diagram.

Micelli *et al.* [33] measured the capacitance of planar lipid bilayers by applying sinusoidally varying voltage with amplitude of 2 mV and the frequency of 1 kHz. At this high frequency, almost all of the current crosses the reactive part of the planar lipid bilayer and its resistance is negligible. The rectified voltage is proportional to the planar lipid bilayer capacitance. By using a set of test values for the capacitance, which were one by one included in measuring system, they parameterized the relation between measured voltage and capacitance. The hyperbolic relation with two known parameters  $a$  and  $b$  was obtained:

$$C_{\text{BLM}} = a \frac{V_{1h}}{b - V_{1h}}. \quad (9)$$

### 3.2. Resistance ( $R$ )

Planar lipid bilayer membranes exhibit resistance in the range of few gigaohms. The resistance is usually calculated in accordance with Ohm's law as a ratio of voltage applied to (or measured on) the planar lipid bilayer and current which flows through it. As mentioned earlier, the electrical parameters of planar lipid bilayer can also be measured by means of an alternating current. The continuous monitoring of capacitance is useful in tracking membrane thickness, while the continuous monitoring of the resistance allows studies of protein–lipid interactions and planar lipid bilayer fluctuations.

Gallucci and coworkers [32] presented an electrical circuit appropriate for continuous monitoring of planar lipid bilayer capacitance and resistance simultaneously. An input voltage was composed of two sinusoidally varying signals: one with variable amplitude (0.1–1.5 V) and frequency of 1 Hz and another with amplitude of 2 mV and frequency of 1 kHz. The planar lipid bilayer and the measuring device are shown with equivalent circuits on the left side in Fig. 24. According to the associated vector graph on the right side in Fig. 24, the following relations can be written:

$$V_1 \cos(\varphi - \varphi_1) + V_{\text{BLM}} \cos(\varphi_{\text{BLM}} - \varphi) = V_s \quad (10)$$

$$V_1 \sin(\varphi - \varphi_1) = V_{\text{BLM}} \sin(\varphi_{\text{BLM}} - \varphi) \quad (11)$$

$$\omega C_{\text{BLM}} V_{\text{BLM}} = I \sin \varphi_{\text{BLM}}. \quad (12)$$

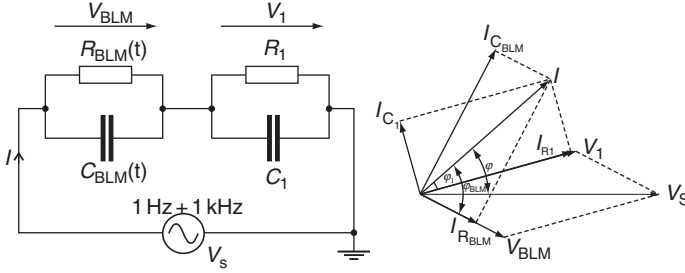


**Figure 24** Left: Equivalent circuit of the planar lipid bilayer (BLM) and of the measurement device.  $V_s$  is an input voltage.  $V_{\text{BLM}}$  and  $V_1$  are the planar lipid bilayer and output voltages, respectively.  $R_1$  is electrical resistance and  $C_1$  the capacitance of the measuring circuit;  $R_{\text{BLM}}$  and  $C_{\text{BLM}}$  are the resistance of planar lipid bilayer and capacitance, respectively. Right: Vector scheme of the voltages and currents in the circuit no the left [32–34].

The current  $I$  is the vector sum of the currents crossing the resistance  $R_1$  and capacitance  $C_1$  of the measuring device:

$$I = V_1 \sqrt{(\omega C_1)^2 + \left(\frac{1}{R_1}\right)^2}. \quad (13)$$

If the capacitance of the planar lipid bilayer has already been measured (see Section 3.1), the phase angles  $\varphi_{\text{BLM}}$  and  $\varphi$  as well as the voltage  $V_{\text{BLM}}$  can be determined. The resistance of the planar lipid bilayer is then obtained from the relation:

$$R_{\text{BLM}} = \frac{V_{\text{BLM}}}{I \cos \varphi}. \quad (14)$$

### 3.3. Breakdown Voltage ( $U_{\text{br}}$ )

The electrical modulation of biological membrane physical properties caused by electrical oscillations and excitations are natural processes in living organisms. Applications of external electric fields, especially those based on the phenomenon of electroporation, have gained increasing importance for manipulations in biological cells and tissues [54]. The structural changes in biological membranes induced by an external electric field involve rearrangement of the phospholipid bilayer and lead to the formation of aqueous pores. If the electric field does not exceed some critical adequate strength and duration, the membrane returns to its normal state after the end of the exposure to the electric field; the electroporation is reversible. However, if the exposure to the electric field is too long or the strength of the electric field is too high, the membrane does not reseal after the end of the exposure,

and the electroporation is irreversible. The underlying mechanisms for these properties are dependent on the lipid component of biological membrane, and can be studied on planar lipid bilayers.

Application of a steady voltage in the order of few hundred millivolts across a planar lipid bilayer causes the membrane to break. Most often the breakdown voltage ( $U_{br}$ ) of the planar lipid bilayer is determined by applying a rectangular voltage pulse ( $10 \mu\text{s}$ – $10 \text{s}$ ) (Fig. 25). The amplitude of the voltage pulse is increased in small steps until the breakdown of the bilayer is obtained [5]. First, the voltage pulse charges up the planar lipid bilayer. Above a critical voltage ( $U_{br}$ ) defects are created in the planar lipid bilayer allowing an increase of the current through the bilayer [4]. Usually, planar lipid bilayer collapses when the breakdown voltage is exceeded.

Using the rectangular voltage pulse measuring protocol, the number of applied voltage pulses is not known in advance and each planar lipid bilayer is exposed to a voltage stress many times. Such a pretreatment of the planar lipid bilayer affects its stability and consequently the determined breakdown voltage of the planar lipid bilayer [4]. Another approach for the breakdown voltage determination was suggested by Kramar *et al.* [8]. Using a linear rising signal, the breakdown voltage of a planar lipid bilayer is determined by only a single voltage exposure (Fig. 26).

The slope of the linear rising signal and the peak voltage of the signal must be selected in advance. The breakdown voltage ( $U_{br}$ ) is defined as the voltage at the moment  $t_{br}$  when a sudden increase of the current through the planar lipid bilayer is observed. Time ( $t_{br}$ ) is defined as the lifetime of the planar lipid bilayer at a chosen slope of the linear rising signal (Fig. 26). Because the planar lipid bilayer lifetime depends on the applied voltage [5,55] and the planar lipid bilayer pretreatment [4],  $U_{br}$  and  $t_{br}$  are measured at a variety of slopes. Using nonlinear regression (Fig. 27), a two parameter curve can be fitted to the data

$$U = \frac{a}{1 - e^{-t/b}}, \quad (15)$$

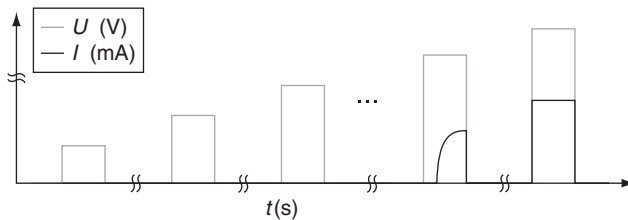


**Figure 25** Measurement of planar lipid bilayer breakdown voltage ( $U_{br}$ ) by successional rectangular pulses. The amplitude of the voltage pulse (gray) is incremented in small steps until the breakdown of the bilayer is observed as sudden increase of current (black) [5].

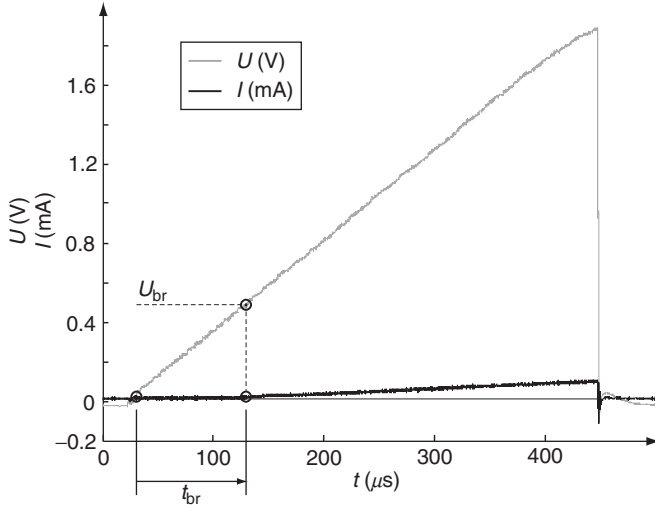


**Figure 26** Measurement of planar lipid bilayer breakdown voltage ( $U_{br}$ ) by linear rising signal. Breakdown voltage is defined as the voltage (gray) at the moment  $t_{br}$  when sudden increase of the current (black) through the planar lipid bilayer is observed [8].

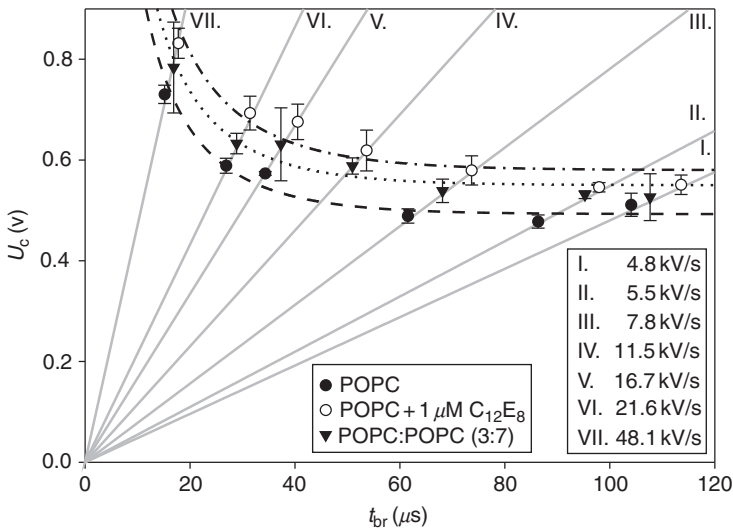


**Figure 27** The breakdown voltage ( $U_{br}$ ) (dots and triangles) of planar lipid bilayers with different chemical composition as a function of lifetime  $t_{br}$ . The gray lines show seven different slopes of applied linear rising voltage signal. Dash, dotted, and dash-dotted curves represent two parameters curve [15] fitted to data.

where  $U$  is  $U_{br}$  measured at different slopes;  $t$  is corresponding  $t_{br}$ ; and  $a$  and  $b$  are parameters. Parameter  $a$  is an asymptote of the curve which corresponds to minimal breakdown voltage  $U_{brMIN}$  for a specific planar lipid bilayer chemical composition. Parameter  $b$  governs the inclination of the curve.

### 3.4. Fluctuations ( $\psi$ )

Fluidity of the lipid membrane must produce local fluctuations of the membrane microscopic parameters. Appearance of transient defects and pores in the membrane structure affects its conductance, producing fluctuations. Transient changes of the membrane electrical properties also accompany protein insertion into the membrane. Voltage-clamp studies with low-value fields are typically applied for recording capacitance and conductance changes, following insertion of channel-forming proteins into the planar lipid bilayer (e.g., Ref. [25]).

The fluctuations are even more pronounced under a strong electric field that is sufficient to electroporate the membrane. The pore appearance is preceded by lipid reorganization resulting in the events of transient membrane permeability to ions. Related to these phenomena, fluctuations of the current were observed prior to an irreversible breakdown of a planar lipid bilayer [4]; the fluctuation amplitude was about  $10^{-11}$  A. After electroporation, it is very unlikely for an electropore to maintain its rim fixed, hence pore fluctuations are theoretically expected. Since the electroporation under voltage-clamp conditions results in very fast pore expansion leading to rapid membrane breakdown, an experimental study on the pore dynamics, in the voltage-clamp mode, required application of very short pulses that could protect the membrane from destruction [56,57]. The experiment reported in Ref. [57] approximated a typical lifetime of an electropore created under voltage-clamp conditions (250 mV) as 3 ms. Conductance fluctuations recorded in these experiments were attributed to a pore dynamics. In such a study, however, the voltage was clamped above the breaking potential and, because of the high value of the potential, the appearance of multiple pores is almost certain. The combined dynamics of several pores may have accounted for the observed fluctuations and single pore dynamics was blurred. At higher voltages, an irreversible membrane breakdown was studied by voltage-clamp techniques [27,31].

Exposure of the planar lipid bilayer to a constant current (0.1–2.0 nA) does not rupture the bilayer rapidly. The membrane slowly accumulates the charge and when the first pore appears, the transmembrane potential decreases, preventing subsequent electropore appearance, which permits the hypothesis of a single pore formation. Fluctuations observed in these current-clamp experiments are caused by opening and closing of a single pore [9,49–52,58]. The natural electropore fluctuations are enhanced by a negative feedback inherent to the current-clamp electroporation method.

The feedback results from interplay between the pore surface and the transmembrane voltage. As a consequence of the electropore expansion, the membrane resistance decreases and the voltage across planar lipid bilayer is reduced. This prevents further increase of the electropore, which usually starts shrinking instead—increasing the transmembrane voltage. This chain of events accounts for the pore stabilization and its fluctuations. The pore can live for several hours. The fluctuations show regular stochastic properties, which are partly due to the feedback and partly due to the pore dynamics and membrane elastic properties [58,59]. Elimination of the feedback in the voltage-clamp experiment, before which the pore that is formed and stabilized under current-clamp conditions, shows very interesting non-Gaussian properties of the electropore dynamics. The parameters of the long-tailed Levy-stable probability density function, which characterizes electropore dynamics, are related to the lipid composition of the membrane, salt properties, and the pore diameter (Fig. 28) [52].

### 3.5. Other Physical Properties

#### 3.5.1. Thickness (*d*)

The thickness of planar lipid bilayer is usually determined from its capacitance according to the relation valid for parallel plate capacitor:

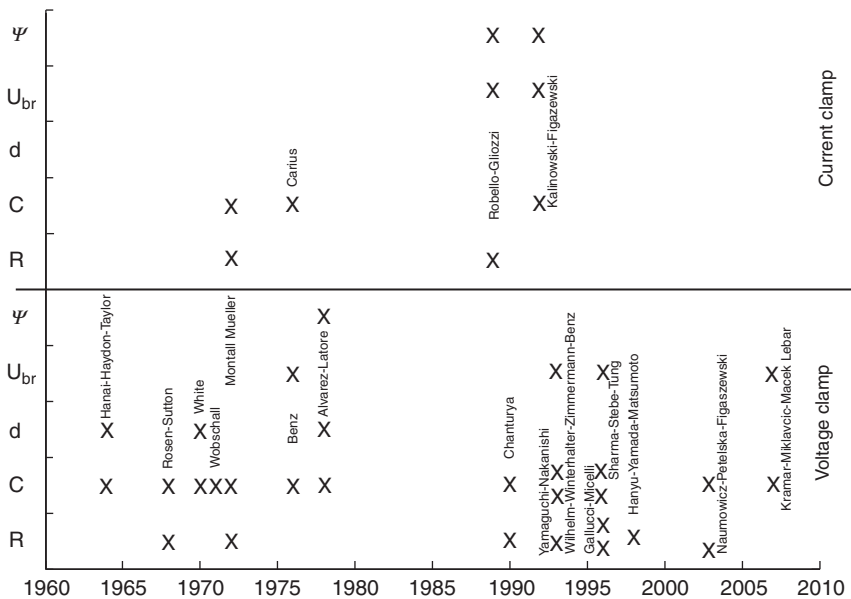


**Figure 28** Time perspective of systems for planar lipid bilayer properties determination.



$$d = \varepsilon\varepsilon_0 \frac{A}{C_{\text{BLM}}}. \quad (16)$$

In this equation,  $A$  stands for the area of planar lipid bilayer and  $C_{\text{BLM}}$ ,  $\varepsilon_0$ , and  $\varepsilon$  for its capacitance, the permittivity of the free space, and the relative static permittivity, respectively. It is usually assumed that the relative static permittivity inside lipid bilayer equals to 2.1 [24].

### 3.5.2. Elasticity ( $E$ ) and surface tension ( $\sigma$ )

A macroscopic approach using the theory of elasticity of solid bodies and liquid crystals can be applied to describe mechanical properties of lipid bilayers. In 1973, Helfrich proposed a theory and possible experiments of elastic properties measurements on planar lipid bilayers [60]. As the anisotropy of lipid bilayers is clearly expressed, several elasticity modules are required to describe its viscoelastic properties. Depending on the directions of the membrane deformation, we distinguish volume compressibility, area compressibility, unilateral extension along membrane plane, and transversal compression.

Experimentally, lipid bilayer mechanical properties were commonly measured on giant unilamellar vesicles [61–64]. Pressure was applied on a membrane with micropipette aspiration method; the properties were measured by means of video microscopy [65]. From experiments on planar lipid bilayer, Winterhalter and coworkers [66] reported that dynamics light scattering allowed quantifying viscoelastic properties in nonperturbative way, while Wobschall calculated membrane elasticity and breaking strength from measurement of capacitance of the planar lipid bilayer as it was bowed under a known pressure. Transversal elasticity modulus cannot be measured directly due to small thickness of the membrane and extremely small changes of the thickness upon deformation. It can be estimated through capacitance measurement with a special electrostriction method which is based on measurements of the amplitude of higher current harmonics [67].

Sabotin with coworkers [68] presented an estimation of the planar lipid bilayer transversal elasticity ( $E$ ) and surface tension ( $\sigma$ ) by means of viscoelastic predictive model of Dimitrov [69] and measured planar lipid bilayer capacitance and break down voltage. The model considers the lipid bilayer as a viscoelastic, isotropic material that can be represented as a standard solid model, composed of a Kelvin body in series with a linear spring. Originally, this model predicts the critical voltage and critical time needed to collapse a membrane at applied voltage. Critical voltage corresponds to breakdown voltage ( $U_{\text{brMIN}}$ ) and critical time to life time ( $t_{\text{br}}$ ) of planar lipid bilayer. The parameters of model are Young's transversal elasticity modulus ( $E$ ), surface tension ( $\sigma$ ), viscosity ( $\mu$ ), thickness of the membrane ( $h$ ), and

permittivity of membrane ( $\epsilon_m$ ). If  $U_{br}$  is measured by linear rising signal (Fig. 26), the corresponding planar lipid bilayer lifetime ( $t_{br}$ ) is always finite [8]. Generic model equation that still contains  $t_{br}$  [69] gives the relation:

$$U_{br} = \sqrt[4]{n + \frac{k}{t_{br}}}. \quad (17)$$

The relation can be fitted to the data obtained experimentally by the breakdown voltage determination using linear rising signal [8]. Parameters  $n$  and  $k$ , which are obtained through fitting, served to calculate Young's elasticity modulus ( $E$ ) and surface tension ( $\sigma$ ) of planar lipid bilayer. Specific capacitance ( $c_{BLM}$ ) has to be measured, while other parameters such as thickness ( $h = 3.5$  nm) and viscosity ( $\mu = 6$  Ns/m<sup>2</sup>) can be taken from Ref. [69].

## 4. CONCLUSIONS

In this chapter, we have reviewed setups and experimental methods applied to study of the properties of planar lipid bilayers. The planar lipid bilayer presents a good model of the plasma membrane where the behavior of the lipid part is not obscured by other components of the real cell membrane. In particular, the influence of the conductive protein ion channels could be eliminated. The development of measuring systems was enabled by discovery of the first technique for forming stable planar lipid bilayers in 1962. This discovery permitted design of a range of instruments useful for measuring planar lipid bilayer characteristics by different methods, allowing a more complete picture of planar lipid bilayer physical properties and membrane-related phenomena like electroporation. The measurement methods vary from simple electrical setups, which allowed for the first experiments and demonstrated basic lipid bilayer characteristics, to more recent advanced systems, frequently combining electrical and nonelectrical methods, such as optical or mechanical.

In the field of electrical measurements on biological objects with non-constant resistance, there are two major approaches to the topic. One method is based on the voltage-controlled measurements, in which different shapes of an alternating voltage are applied on the planar lipid bilayer. In the other method, the current shape and value are controlled. The planar lipid bilayer characteristics that are observed during the experiment dictate the choice of the measuring principle. The experiments carried out by the presented systems showed viscoelastic properties of planar lipid bilayers, temporal changes in the electroporated membrane, and fluctuation characteristics of an electropore.


## APPENDIX A. REVIEW OF MEASURING SYSTEMS

**Table 1** Description of measuring systems

System	Stimulating signal	Lipid	Salt solution	Lipid preparation	Volume of the chamber	Electrodes	Aperture diameter	Temperature (°C)
Rosen–Sutton [16]	AC: 5 mV/500 Hz, DC: $\pm 200$ mV	Lecitin	1 mM, 10 mM, 100 mM, 1 M KCl or NaCl	1% (w/v)	–	2 Calomel + 2 Pt	1 mm	22
White [17,18]	AC: 20 mV/100 Hz	Oxidized cholesterol, lecithin	KCl, pH 7.1	35 mg/ml	–	4 platinized Ag–AgCl	1.6 mm	20
Wobshall [19,20]	AC: 5–15 mV <sub>RMS</sub> / 4kHz	Cholesterol, HDTAC	40 mM KCl, pH 6.7	12 mg/ml	–	4 Ag–AgCl	1.68 mm	30
Montal–Mueller [3]	Voltage pulse 10 ms, 37.5 mV; Constant current 20 pA	Egg lecithin, cholesterol, glyceroldioleate, bovin cardiolipin, gramicidin	0.01 M NaCl, pH 5.5	–	(18 × 12) mm <sup>2</sup> / compartment	2 Calomel	0.25 mm	Room temperature
Benz [6,7]	10 mV–2 V/500 $\mu$ s– 500 ms	PC, DPhPC, DOPC, POPC, PE, Ox Ch	1 M KCl, 0.1 M NaCl, pH 6	2% (w/v)	3 cm <sup>3</sup> / compartment	2 Ag–AgCl	2 mm <sup>2</sup> (area); 0.2–0.3 mm	25
Abidor– Chernomordik– Chizmadzhev– Pastushenko [4]	100 mV/1 $\mu$ s, 400 mV/1 $\mu$ s	Egg lecithin; Ch: lecitin 2:1	0.1 M NaCl + 10 M Tris– HCl, pH 7.4	40 mg/cm <sup>3</sup>	–	–	1 mm	27

(continued)

**Table 1** (continued)


















System	Stimulating signal	Lipid	Salt solution	Lipid preparation	Volume of the chamber	Electrodes	Aperture diameter	Temperature (°C)
Alvares-Latore [24]	10 mV/5 kHz	–	–	–	4 cm <sup>2</sup> / compartment	2 Ag–AgCl	–	–
Robello–Gliozzi [41,43–45]	Square waves 40 mV, current ramp (0.17 pA/s), triangular signal $2.5 \times 10^{-3}$ Hz	Egg lecithin:Ch 1:1, PC:Ch (4:1), PC, Ch, DPhPC, PS	10 mM Tris–Cl, pH=7.5, 0.1 M, 1 M KCl	10 mg/ml	2 ml / compartment	2 Ag–AgCl	100–150, 160, 200 $\mu$ m	25
Chanturya [25,70]	10 mV–1 V/10–100 $\mu$ s	PC:Ch 2:1	10 mM Tris, pH=7.4	20 mg/ml	9 ml	Ag–AgCl	0.6 mm	26–29
Kalinovski-Figazewski [48–50]	Constant current: 0.005, 0.2, 0.3, 2 nA; step 0.2 nA/10 s; rectangular signal: $8 \times 0.2$ nA/10 s	PC:Ch, lecithin, PS	0.1 M KCl, pH 7.0	20 mg/ml	10 cm <sup>3</sup> / compartment	4 Ag–AgCl (0.5 $\times$ 80) mm	1 mm	23–25
Wilhelm–Winterhalter–Zimmermann–Benz [26–30]	10 mV–2 V/500 $\mu$ s–500 ms	Ox Ch (+ DOPC or + PE), azolectin, DPHPC, PS, DOPC, DOPE	10 mM, 100 mM, 1 M, 2 M, 3 M KCl, pH=6,7	1 $\mu$ l, 5 mg/ml, 10 mg/ml, 40 mg/ml	5 ml/ compartment, 15 ml/ compartment	2 Ag–AgCl	100–200 $\mu$ m, 0.3–3 mm, 1 mm, 2 mm <sup>2</sup> (area)	20, 22, 25, 30
Yamaguchi–Nakanishi [12]	7 mV <sub>RMS</sub> /1 kHz	GMO	0.1 M KCl	62 mg/ml	–	2 Pt	0.7 mm	25
Sharma–Stebe–Tung [5,31]	100 mV/10 $\mu$ s, 510 $\mu$ s 	POPC, azolectin	100 mM KCl, pH=7.4	10 mg/ml 20 mg/ml	3 ml/compartment	4 Ag–AgCl	75–100 $\mu$ m, 105 $\mu$ m	22–24











Gallucci–Micelli [32–34]	Variable amplitude $V_{pp}/1 \text{ Hz} +$ $2 \text{ mV}/1 \text{ kHz}$	PI, Ox Ch	0.1 M, 0.5 M, 1 M KCl, pH 7.0	1% (w/v)	4 ml/compartment	2 Pt	1.3 mm	22–24
Hanyu–Yamada– Matsumoto [11]	0.1–1 V	Azolectin	–	5 mg/ml	–	4 Ag–AgCl	120 $\mu\text{m}$	–
Naumowicz– Petelska– Figaszewski [35–37]	4 mV/0.01–10 kHz	Lecithin, Ch, lecithin:Ch 1:1	0.1 M KCl, pH 7.4	20 mg/cm <sup>3</sup>	–	2 Ag–AgCl, 1 Pt	–	–
Kramar [8,68]	Linear rising voltage (4.8–48.1 kV/s)	POPC, POPS	0.1 M KCl	10 mg/ml	5.3 cm <sup>3</sup> / compartment	2 Ag–AgCl	105 $\mu\text{m}$	Room temperature

For each system the stimulating signal, number and material of electrodes, volume of the chamber, and a diameter of the aperture are given. Lipids, which were used in described experiments, corresponding salt solutions and the temperature, at which the experiments were conducted, are also listed. Ch, cholesterol.

## APPENDIX B. REVIEW OF MEASURED PROPERTIES ON PLANAR LIPID BILAYER

**Table 2** Properties of planar lipid bilayers of various lipid compositions and parameters at which they were measured

Lipid	Salt solution	$T$ ( $\mu$ s)	Shape of the signal	$U_{br}$ (mV)	$C$ ( $\mu$ F/cm <sup>2</sup> )	$R$ (M $\Omega$ cm <sup>2</sup> )	$d$ (nm)	References
Azolecitin	0.1 M KCl	10		423.4 $\pm$ 29.4	0.59 $\pm$ 0.21	–	–	[31]
		510		441.6 $\pm$ 23.2				
DOPC	0.1 M NaCl	–		–	0.37 $\pm$ 0.01	0.40	4.97 $\pm$ 0.17	[6]
DOPE	0.1 M NaCl	–		–	0.37 $\pm$ 0.01	0.40	5.00 $\pm$ 0.16	[6]
DPhPC	0.1 M KCl	–		390 $\pm$ 20	0.6–0.75	7.85–17.76	–	[41,43,45,46]
	1 M KCl	–		–	0.74–1.13	24.3–54.9	–	[43,44]
	0.1 M KCl	10		546 $\pm$ 15	–	–	–	[27,30,44]
	0.1 M NaCl	–		–	0.36 $\pm$ 0.02	0.40	5.08 $\pm$ 0.21	[6]
	0.1 M KCl	–		–	0.9–1	–	–	[57]
DPhPS	0.1 M KCl	10		530 $\pm$ 15	–	–	–	[27,30]
Lecithin	1e–3–1 M NaCl or KCl	–		–	0.32–0.64	1–10	–	[16]
Ox Ch	1 M KCl	–		–	0.40	0.25	–	[34]
	0.1 M KCl	–		–	0.45 $\pm$ 0.01	0.21 $\pm$ 0.01	–	[32]
	0.5 M KCl				0.47 $\pm$ 0.04	0.23 $\pm$ 0.01		
	1 M KCl				0.40 $\pm$ 0.01	0.20 $\pm$ 0.03		
PC	1 M KCl	10		–	0.56	–	3.3	[7]
	0.1 M KCl	–		280 $\pm$ 30	0.75	–	–	[41,46]
	0.1 M NaCl	–		–	0.34 $\pm$ 0.01	0.40	5.48 $\pm$ 0.17	[6]
PE	0.1 M NaCl	–		–	0.33 $\pm$ 0.01	0.40	5.67 $\pm$ 0.22	[6]

PI	1 M KCl	–		–	0.25	0.4	–	[34]
	0.1 M KCl	–		–	0.30±0.01	0.37±0.01	–	[32]
	0.5 M KCl	–			0.27±0.01	0.34±0.01		
	1 M KCl	–			0.25±0.01	0.38±0.06		
POPC	0.1 M KCl	10		400±6	–	–	–	[27,30]
	0.1 M KCl	10		450±24	0.59±0.15	–	–	[5]
		100		398±19				
		10 <sup>3</sup>		331±20				
		10 <sup>4</sup>		282±26				
		10 <sup>5</sup>		258±9				
		10 <sup>6</sup>		213±18				
	10 <sup>7</sup>		167±6					
POPS	0.1 M KCl	10		410±20	–	–	–	[27,30]
PS	0.1 M KCl	–		500 ± 50	–	–	–	[46]
PC + Ch	0.1 M KCl	–		270 ± 20	–	–	–	[46]
PC + PE	0.1 NaCl	–		–	0.1	–	–	[25]
Lecithin	0.1 M KCl	–		–	0.38–0.61	0.014–2.12	–	[20]
+ Ch 1:1	10 mM Tris–Cl	–		–	–	–	–	[21]

For each lipid composition break down voltage ( $U_{br}$ ), capacitance ( $C$ ), resistance ( $R$ ), and thickens ( $d$ ) are given. Salt solution that was used in experiments, as well as shape and duration of the stimulating signal are also presented.

## REFERENCES

- [1] R.B. Gennis, *Biomembranes, Molecular Structure and Function*, Springer, New York, 1989.
- [2] P. Mueller, D.O. Rudin, H.T. Tien, W.C. Wescott, Methods for the formation of single bimolecular lipid membranes in aqueous solution, *J. Phys. Chem.* 67 (1963) 534–535.
- [3] M. Montal, P. Mueller, Formation of bimolecular membranes from lipid monolayers and a study of their electrical properties, *PNAS* 69 (1972) 3561–3566.
- [4] I.G. Abidor, V.B. Arakelyan, L.V. Chernomordik, Y.A. Chizmadzhev, V.F. Pastushenko, M.R. Tarasevich, Electric breakdown of bilayer lipid membranes I. The main experimental facts and their qualitative discussion, *Bioelectrochem. Bioenerg.* 6 (1979) 37–52.
- [5] G.C. Troiano, L. Tung, V. Sharma, K.J. Stebe, The reduction in electroporation voltages by the addition of surfactant to planar lipid bilayer, *Biophys. J.* 75 (1998) 880–888.
- [6] R. Benz, K. Janko, Voltage-induced capacitance relaxation of lipid bilayer membranes; effects on membrane composition, *Biochim. Biophys. Acta* 455 (1976) 721–738.
- [7] R. Benz, F. Beckers, U. Zimmermann, Reversible electrical breakdown of lipid bilayer membranes: A charge-pulse relaxation study, *J. Membr. Biol.* 48 (1979) 181–204.
- [8] P. Kramar, D. Miklavčič, A. Maček Lebar, Determination of the lipid bilayer breakdown voltage by means of a linear rising signal, *Bioelectrochemistry* 70 (2007) 23–27.
- [9] S. Kalinowski, G. Ibrón, K. Bryl, Z. Figaszewski, Chronopotentiometric studies of electroporation of bilayer lipid membranes, *Biochim. Biophys. Acta* 1396 (1998) 204–212.
- [10] A. Blume, *Lipids*, in: D. Waltz, J. Teissie, G. Milazzo (Eds.), *Bioelectrochemistry of Membranes* Birkhauser, Basel-Boston-Berlin, 2004, pp. 24–61.
- [11] Y. Hanyu, T. Yamada, G. Matsumoto, Simultaneous measurement of spectroscopic and physiological signals from a planar bilayer system: Detecting voltage-dependent movement of a membrane-incorporated peptide, *Biochemistry* 1998 (1998) 15376–15382.
- [12] H. Yamaguchi, H. Nakanishi, Characterization of the preparation process and the photochemical control of electrical properties of bilayer lipid membranes containing azobenzene chromophores, *Biochim. Biophys. Acta* 1148 (1993) 179–184.
- [13] T.F. Eibert, M. Alaydrus, F. Wilczewski, V.W. Hansen, Electromagnetic and thermal analysis for lipid bilayer membranes exposed to RF fields, *IEEE Trans. Biomed. Eng.* 46 (1999) 1013–1021.
- [14] P. Mueller, D.O. Rudin, H.T. Tien, W.C. Wescott, Reconstitution of a cell membrane structure in vitro and its transformation into an excitable system, *Nature* 194 (1962) 979–980.
- [15] T. Hanai, D.A. Haydon, J. Taylor, An investigation by electrical methods of lecitin-in-hydrocarbon films in aqueous solutions, *Proc. R. Soc. Lond. Ser. A Math. Phys. Sci.* 281 (1964) 377–391.
- [16] D. Rosen, A.M. Sutton, The effects of a direct current potential bias on the electrical properties of bimolecular lipid membranes, *Biochim. Biophys. Acta* 163 (1968) 226–233.
- [17] S.H. White, A study of lipid bilayer membrane stability using precise measurements of specific capacitance, *Biophys. J.* 10 (1970) 1127–1147.
- [18] S.H. White, T.E. Thompson, Capacitance, area, and thickness variations in thin lipid films, *Biochim. Biophys. Acta* 323 (1973) 7–22.
- [19] D. Wobschall, Bilayer membrane elasticity and dynamic response, *J. Colloid Interface Sci.* 36 (1971) 385–423.



- [20] D. Wobschall, Voltage dependence of bilayer membrane capacitance, *J. Colloid Interface Sci.* 40 (1972) 417–423.
- [21] K.U. Maheswari, T. Ramachandran, D. Rajaji, Interaction of cisplatin with planar model membranes—dose dependent change in electrical characteristics, *Biochim. Biophys. Acta* 1463 (2000) 230–240.
- [22] L.V. Chernomordik, S.I. Sukharev, I.G. Abidor, Y.A. Chizmadzhev, Breakdown of lipid bilayer membranes in an electric field, *Biochim. Biophys. Acta* 736 (1983) 203–213.
- [23] L.V. Chernomordik, S.I. Sukharev, S.V. Popov, V.F. Pastushenko, A.V. Sokirko, I.G. Abidor, et al. The electrical breakdown of cell and lipid membranes: the similarity of phenomenologies, *Biochim. Biophys. Acta* 902 (1987) 360–373.
- [24] O. Alvarez, R. Latorre, Voltage-dependent capacitance in lipid bilayers made from monolayers, *Biophys. J.* 21 (1978) 1–17.
- [25] A.N. Chanturiya, Detection of transient capacitance increase associated with channel formation in lipid bilayers, *Biochim. Biophys. Acta* 1026 (1990) 248–250.
- [26] C. Wilhelm, M. Winterhalter, U. Zimmermann, R. Benz, Kinetics of pore size during irreversible electrical breakdown of lipid bilayer membranes, *Biophys. J.* 64 (1993) 121–128.
- [27] A. Diederich, G. Bahr, M. Winterhalter, Influence of surface charges on the rupture of black lipid membranes, *Phys. Rev. E* 58 (1998) 4883–4889.
- [28] A. Diederich, G. Bahr, M. Winterhalter, Influence of polylysine on the rupture of negatively charged membranes, *Langmuir* 14 (1998) 4597–4605.
- [29] A. Diederich, M. Strobel, W. Meier, M. Winterhalter, Viscosity- and inertia-limited rupture of dextran-supported black lipid membranes, *J. Phys. Chem. B* 103 (1999) 1402–1407.
- [30] W. Meier, A. Graff, A. Diederich, M. Winterhalter, Stabilization of planar lipid membranes: a stratified layer approach, *Biochim. Biophys. Acta* 2000 (2000) 4559–4562.
- [31] V. Sharma, K. Uma Maheswari, J.C. Murphy, L. Tung, Poloxamer 188 decreases susceptibility of artificial lipid membranes to electroporation, *Biophys. J.* 71 (1996) 3229–3241.
- [32] E. Gallucci, S. Micelli, G. Monticelli, Pore formation in lipid bilayer membranes made of phosphatidylinositol and oxidized cholesterol followed by means of alternating current, *Biophys. J.* 71 (1996) 824–831.
- [33] S. Micelli, E. Gallucci, V. Picciarelli, Studies of mitochondrial porin incorporation parameters and voltage-gated mechanism with different black lipid membranes, *Bioelectrochemistry* 52 (2000) 63–75.
- [34] S. Micelli, E. Gallucci, D. Meleleo, V. Stipani, V. Picciarelli, Mitochondrial porin incorporation into black lipid membranes: ionic and gating contribution to the total current, *Bioelectrochemistry* 75 (2002) 97–106.
- [35] M. Naumowicz, A.D. Petelska, Z.A. Figaszewski, Capacitance and resistance of the bilayer lipid membrane formed of phosphatidylcholine and cholesterol, *Cell. Mol. Biol. Lett.* 8 (2003) 5–18.
- [36] M. Naumowicz, Z.A. Figaszewski, Impedance spectroscopic investigation of the bilayer lipid membranes formed from the phosphatidylserine–ceramide mixture, *J. Membr. Biol.* 227 (2009) 67–75.
- [37] M. Naumowicz, A.D. Petelska, Z.A. Figaszewski, Impedance analysis of phosphatidylcholine–cholesterol system in bilayer lipid membranes, *Electrochim. Acta* 50 (2005) 2155–2161.
- [38] A.D. Petelska, M. Naumowicz, Z.A. Figaszewski, Complex formation equilibria in two-component bilayer lipid membrane: interfacial tension method, *J. Membr. Biol.* 228 (2009) 71–77.

- [39] P. Kramar, D. Miklavčič, A. Maček-Lebar, A system for the determination of planar lipid membrane voltage and its applications, *IEEE Trans. Nanobiosci.* 8 (2009) 132–138.
- [40] W. Carius, Voltage dependence of bilayer membrane capacitance. Harmonic response to ac excitation with dc bias, *J. Colloid Interface Sci.* 57 (1976) 301–307.
- [41] M. Robello, A. Gliozzi, Conductance transition induced by an electric field in lipid bilayers, *Biochim. Biophys. Acta* 982 (1989) 173–176.
- [42] M. Robello, M. Fresia, L. Maga, A. Grasso, S. Ciani, Permeation of divalent cations through  $\alpha$ -latrotoxin channels in lipid bilayers: steady-state current-voltage relationships, *J. Membr. Biol.* 95 (1987) 55–62.
- [43] A. Ridi, E. Scalas, M. Robello, A. Gliozzi, Linear response of a fluctuating lipid bilayer, *Thin Solid Films* 327–329 (1998) 796–799.
- [44] E. Scalas, A. Ridi, M. Robello, A. Gliozzi, Flicker noise in bilayer lipid membranes, *Europhys. Lett.* 43 (1998) 101–105.
- [45] A. Ridi, E. Scalas, A. Gliozzi, Noise measurements in bilayer lipid membranes during electroporation, *The Eur. Phys. J. E* 2 (2000) 161–168.
- [46] I. Genco, A. Gliozzi, A. Relini, M. Robello, E. Scalas, Electroporation in symmetric and asymmetric membranes, *Biochim. Biophys. Acta* 1149 (1993) 10–18.
- [47] E. Pescio, A. Ridi, A. Gliozzi, A picoampere current generator for membrane electroporation, *Rev. Sci. Instrum.* 71 (2000) 1740–1744.
- [48] S. Kalinowski, Z. Figaszewski, A new system for bilayer lipid membrane capacitance measurements: method, apparatus and applications, *Biochim. Biophys. Acta* 1112 (1992) 57–66.
- [49] S. Kalinowski, Z. Figaszewski, A four-electrode system for measurement of bilayer lipid membrane capacitance, *Meas. Sci. Technol.* 6 (1995) 1034–1049.
- [50] S. Kalinowski, Z. Figaszewski, A four-electrode potentiostat–galvanostat for studies of bilayer lipid membranes, *Meas. Sci. Technol.* 6 (1995) 1050–1055.
- [51] S. Koronkiewicz, S. Kalinowski, K. Bryl, Programmable chronopotentiometry as a tool for the study of electroporation and resealing of pores in bilayer lipid membranes, *Biochim. Biophys. Acta* 1561 (2002) 222–229.
- [52] M. Kotulska, Natural fluctuations of an electropore show fractional Levy stable motion, *Biophys. J.* 92 (2007) 2412–2421.
- [53] J. Vargas, J.M. Alarcon, E. Rojas, Displacement currents associated with the insertion of Alzheimer Disease amyloid (beta)-peptide into planar bilayer membranes, *Biophys. J.* 79 (2000) 934–944.
- [54] D. Miklavčič, M. Puc, *Electroporation*, Wiley Encyclopedia of Biomedical Engineering, Wiley, New York, 2006.
- [55] A. Maček-Lebar, G.C. Troiano, L. Tung, D. Miklavčič, Inter-pulse interval between rectangular voltage pulses affects electroporation threshold of artificial lipid bilayers, *IEEE Trans. Nanobiosci.* 1 (2002) 116–120.
- [56] V.F. Antonov, V.V. Petrov, A.A. Molnar, D.A. Predvoditelev, A.S. Ivanov, The appearance of single ion channels in unmodified lipid bilayer membrane at the phase transition temperature, *Nature* 283 (1980) 585–588.
- [57] K.C. Melikov, V.A. Frolov, A. Shcherbakov, A.V. Samsonov, Y.A. Chizmadzhev, L.V. Chernomordik, Voltage-induced nonconductive pre-pores and metastable single pores in unmodified planar lipid bilayer, *Biophys. J.* 80 (2001) 1829–1836.
- [58] M. Kotulska, S. Koronkiewicz, S. Kalinowski, Self-similar processes and flicker noise from a fluctuating nanopore in a lipid membrane, *Phys. Rev. E* 69 (2004) 031920–031930.
- [59] S. Koronkiewicz, K. Bryl, Cholesterol-induced variations in fluctuations of the pores in bilayer lipid membrane, *Cell. Mol. Biol. Lett.* 4 (1999) 567–582.

- [60] W. Helfrich, Elastic properties of lipid bilayers—theory and possible experiments, *Z. Naturforsch. C J. Biosci. C* 28 (1973) 693–703.
- [61] R. Kwok, E.A. Evans, Thermoelasticity of large lecithin bilayer vesicles, *Biophys. J.* 35 (1981) 637–652.
- [62] E. Evans, D. Needham, Physical properties of surfactant bilayer membranes: thermal transitions, elasticity, rigidity, cohesion, and colloidal interactions, *J. Phys. Chem.* 91 (1987) 4219–4228.
- [63] B.L.-S. Mui, P.R. Cullis, E.A. Evans, T.D. Madden, Osmotic properties of large unilamellar vesicles prepared by extrusion, *Biophys. J.* 64 (1993) 443–453.
- [64] E. Evans, W. Rawicz, Elasticity of “fuzzy” biomembranes, *Phys. Rev. Lett.* 79 (1997) 2379–2382.
- [65] J. Genova, A. Zheliaskova, M.D. Mitov, The influence of sucrose on the elasticity of SOPC lipid membrane studied by the analysis of thermally induced shape fluctuations, *Colloids Surf. A—Physicochem. Eng. Asp.* 282 (2006) 420–422.
- [66] M. Winterhalter, Black lipid membranes, *Curr. Opin. Colloid Interface Sci.* 5 (2000) 250–255.
- [67] T. Hianik, Structure and physical properties of biomembranes and model membranes, *Acta Phys. Slovaca* 56 (2006) 687–806.
- [68] I. Sabotin, A. Maček Lebar, D. Miklavčič, P. Kramar, Measurement protocol for planar lipid bilayer viscoelastic properties, *IEEE Trans. Dielectr. Electr. Insul.* 16 (2009) 1236–1242.
- [69] D.S. Dimitrov, Electric field-induced breakdown of lipid bilayers and cell-membranes—a thin viscoelastic film model, *J. Membr. Biol.* 78 (1984) 53–60.
- [70] A.N. Chanturiya, G. Basanez, U. Schubert, P. Henklein, J.W. Yewdell, J. Zimmerberg, PB1-F2, an influenza A virus-encoded proapoptotic mitochondrial protein, creates variably sized pores in planar lipid membranes, *J. Virol.* 78 (2004) 6304–6312.

# STABLE AND REPRODUCIBLE BILAYER LIPID MEMBRANES BASED ON SILICON MICROFABRICATION TECHNIQUES

Ayumi Hirano-Iwata,<sup>1,2,\*</sup> Azusa Oshima,<sup>1</sup> Yasuo Kimura,<sup>3</sup>  
and Michio Niwano<sup>1,3</sup>

## Contents

1. Introduction	72
2. Reproducible BLM Formation Studied by Infrared Absorption Spectroscopy (IRAS)	73
2.1. Microfabricated Silicon Chips for IRAS Study	73
2.2. MIR-IRAS Monitoring of BLM Formation in Microfabricated Apertures	75
2.3. Self-Formation of BLMs by the Painting Method Studied by MIR-IRAS	75
3. Formation of Stable Free-Standing BLMs	78
3.1. Microfabricated Silicon Chips for Stable BLMs	78
3.2. Preparation of BLMs in Microfabricated Apertures	79
3.3. Stability of BLMs in Microfabricated Silicon Chips	81
4. Conclusion	84
References	84

## Abstract

In this chapter, we will discuss our recent approaches for improving the reproducibility and stability of free-standing bilayer lipid membranes (BLMs) by combining with BLM formation and silicon microfabrication techniques. Membrane formation by the painting method on agarose-gel-coated silicon substrate was monitored with infrared absorption spectroscopy in a multiple-internal

\* Corresponding author. Tel.: +81 22 795 4865; Fax: +81 22 217 5503  
E-mail address: [ahirano@bme.tohoku.ac.jp](mailto:ahirano@bme.tohoku.ac.jp)

<sup>1</sup> Graduate School of Biomedical Engineering, Tohoku University, 6-6-04 Aoba, Aramaki, Aoba-ku, Sendai, Japan

<sup>2</sup> PRESTO, Japan Science and Technology Agency (JST), 4-1-8 Honcho Kawaguchi, Saitama, Japan

<sup>3</sup> Laboratory for Nanoelectronics and Spintronics, Research Institute of Electrical Communication, Tohoku University, 2-1-1 Katahira, Aoba-ku, Sendai, Miyagi, Japan

reflection geometry. It was demonstrated that the appearance of the C=O stretching modes of phospholipid just after the lipid application can be a measure for the successful and reproducible formation of BLMs with gigaohm seal. For preparation of stable BLMs, we have fabricated a tapered aperture with nanometer-scale smoothness. Owing to this structure, the stress on lipid bilayers at the contact with the septum was minimized, leading to improved membrane stability. Tolerance of the present BLMs to repetitive solution exchanges demonstrates high mechanical stability of the membranes. Such reproducible and stable BLMs will open up variety of applications, including a high-throughput drug screening for ion channels.

## 1. INTRODUCTION

Ion channel proteins play key roles in physiology and pathology and are the majority of drug targets. Reconstitution of ion channel proteins in artificial planar bilayer lipid membranes (BLMs) provides an excellent system for drug screening under chemically controlled conditions [1]. In addition, ion channel proteins embedded in planar BLMs are useful for designing highly sensitive biosensors, because channel proteins have signal amplification ability as well as specific recognition ability to their ligands [2,3]. Conventional BLMs have been prepared by classical methods, for example, painting (black membrane) [4], monolayer folding [5,6], and tip-dip methods [7] (Fig. 1A). These membranes have been used for functional analysis of channel proteins and various biosensor applications [3]. However, two drawbacks of BLMs hinder the widespread applications of the BLM systems: low success probability of membrane formation and mechanical instability of BLMs.

Recent advances in the field of micro total analysis systems and lab-on-a-chip have enabled the coupling of microfabricated devices with BLM formation [8–12] (Fig. 1B(4,5)). Fabrication of apertures (from sub-micrometer to  $\sim 100 \mu\text{m}$ ) in substrates, such as silicon and various polymer materials, is currently well established. The sizes of the fabricated apertures are comparable to those used for the conventional painting and monolayer folding methods. In this chapter, we will discuss our recent approaches for the preparation of reproducible and stable BLMs through the combination of silicon microfabrication techniques and BLM formation. The point of our design to improve the membrane stability is also discussed. Successful coupling of BLMs and silicon microfabrication will realize widespread applications of artificial lipid bilayers, including high-throughput drug screening and sophisticated biosensors.

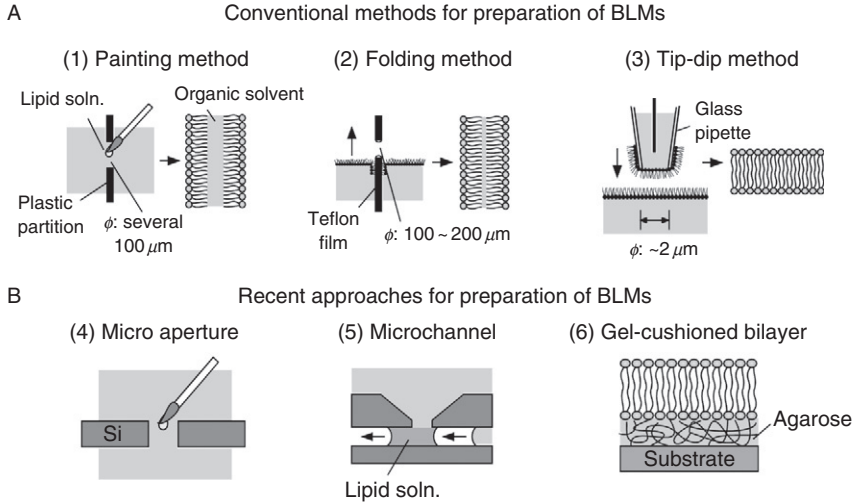


**Figure 1** Schematic illustration of the conventional and microfabricated methods for the preparation of planar BLMs. (1) Painting method (black membrane); (2) folding method (reduced-solvent BLM); (3) tip-dip method (solvent-free BLM); BLM formation in (4) microfabricated aperture and (5) microchannel; (6) BLM cushioned on agarose gel.

## 2. REPRODUCIBLE BLM FORMATION STUDIED BY INFRARED ABSORPTION SPECTROSCOPY (IRAS)

### 2.1. Microfabricated Silicon Chips for IRAS Study

Planar BLMs cushioned on agarose gels introduced in 1998–1999 (Fig. 1B(6)) showed improved membrane stability while allowing channel current recordings [13,14]. Gels can work as a hydrophilic spacer between BLMs and solid supports, and consequently, functional activities of channel proteins are preserved in these BLMs. Although the BLMs still suffered from insufficient membrane stability, the geometry of the BLMs allows one to investigate the structure and function of the membranes by using surface-sensitive techniques, such as surface plasmon resonance [15], atomic force microscopy [16], and infrared absorption spectroscopy (IRAS) in a multiple-internal reflection (MIR) geometry [17] or attenuated total reflection (ATR) mode [18]. Among them, MIR-IRAS has the advantage to provide information on multiple structural sites of BLMs, including polar head groups [19,20] and water molecules surrounding BLMs [21,22]. We have investigated formation process of BLMs cushioned on agarose-coated Si

using MIR-IRAS together with electrophysiological measurements to explore empirical rules for reproducible formation of BLMs [23].

As a platform for BLM formation and MIR-IRAS measurements, we have fabricated arrays of apertures with a diameter of  $100\ \mu\text{m}$  in SU-8 resist spun on a Si substrate (Fig. 2A). The arrayed design was used because large surface area is necessary to obtain detectable IRAS signals, while increase in the BLM size leads to decrease in mechanical stability of the membranes. A large total area of BLMs was split into many arrayed membranes. Figure 2B shows the procedure for the fabrication of Si prisms. A rectangular Si chip ( $12 \times 30 \times 0.45\ \text{mm}^3$ ) was prepared from a double-side-polished, Si(100) wafer with a resistivity of  $5250\text{--}7050\ \Omega\ \text{cm}$ . The prism had  $45^\circ$  bevels on each of the short edges. Thin gold films were first evaporated onto one side of the prism in order to apply a potential. Then a layer of SU-8-3010 resist was spun onto the other side of the prism and patterned by the standard photolithography to form apertures. A 0.2% (w/v) agarose solution was spun on the SU-8 layer and then dried.

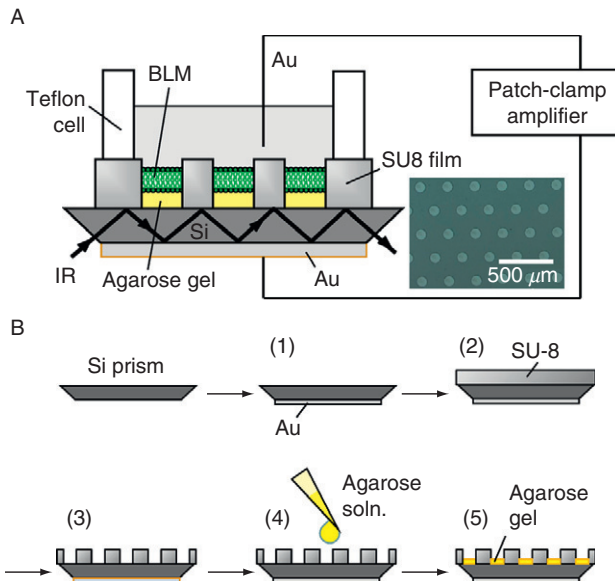


**Figure 2** (A) Schematic of the cells used for MIR-IRAS and electrophysiological measurements. Inset shows a microscopic image of a SU-8 film prepared on a Si prism. Scale bar:  $500\ \mu\text{m}$ . (B) Procedure for aperture fabrication: (1) Au evaporation, (2) spin coating of SU-8 resist, (3) patterning, (4) casting of agarose solution, and (5) spin coating of agarose solution.

## 2.2. MIR-IRAS Monitoring of BLM Formation in Microfabricated Apertures

The agarose-coated Si prism fabricated as above was set on the bottom of a Teflon cell for IRAS study (Fig. 2A). Infrared light beam from an interferometer (MB-100, BOMEM) was focused at normal incidence onto one of the two bevels of the Si prism, and penetrated through the prism. The light that exited the prism through the other bevel was focused onto a liquid-nitrogen-cooled mercury-cadmium-telluride detector. The resolution of the interferometer was set at  $4\text{ cm}^{-1}$ .

A  $200\ \mu\text{l}$  portion of  $\text{D}_2\text{O}$  containing  $0.15\text{ M NaCl}$  and  $10\text{ mM HEPES/NaOD}$  ( $\text{pD} = 7.4$ , denoted as  $\text{Na}^+-\text{D}_2\text{O}$  buffer) was filtered through a cellulose acetate filter (pore size:  $0.2\ \mu\text{m}$ ) and then added to the cell in which the fabricated silicon chip was placed. A  $\text{D}_2\text{O}$  solution containing  $0.15\text{ M KCl}$  and  $10\text{ mM HEPES/NaOD}$  ( $\text{pD} = 7.4$ , denoted as  $\text{K}^+-\text{D}_2\text{O}$  buffer) was also used. The apertures in the SU-8 layer were painted with an *n*-decane solution containing  $16\text{ mg/ml L-}\alpha\text{-phosphatidylcholine (PC)}$  and  $4\text{ mg/ml cholesterol (Chol)}$  using a paintbrush. BLM formation process was monitored with MIR-IRAS spectra and membrane resistance, which was measured using a patch-clamp amplifier (Axopatch 1D, Axon Instruments).

## 2.3. Self-Formation of BLMs by the Painting Method Studied by MIR-IRAS

Figure 3 shows two examples of IR absorption spectra after painting the apertures with a lipid solution composed of PC, Chol, and *n*-decane (solvent). When the final membrane resistance reached a  $1\text{ G}\Omega$  level (left panel), a broad band due to the C=O stretching mode of PC was observed around  $1740\text{ cm}^{-1}$  just after the lipid application. The intensity of this band increased with time, accompanied with a peak broadening with a shoulder around  $1720\text{ cm}^{-1}$ . After 60 min, the spectrum appeared to be a summation of component bands centered around  $1720$  and  $1740\text{ cm}^{-1}$ . The band at  $\sim 1720\text{ cm}^{-1}$  was assigned to the C=O stretching mode of PC, which participated in hydrogen bonding with water, while the band at  $1740\text{ cm}^{-1}$  was assigned to the non-hydrogen-bonded C=O mode [19,20]. Since the C=O stretching bands are sensitive to changes in the polarity of local environments surrounding phospholipids [20], such spectral changes were induced during BLM formation. These peaks due to C=O stretching modes were observed only when the final membrane resistance reached a  $\text{G}\Omega$  level (“gigaseal”), which is a requisite for recording channel currents [3]. Out of 18 membranes that attained gigaseal, 11 membranes showed absorption bands due to the C=O stretching modes within 10 min. On the other hand, no noticeable bands were observed in the C=O mode region even after waiting for 60 min when the membrane resistance did not attain



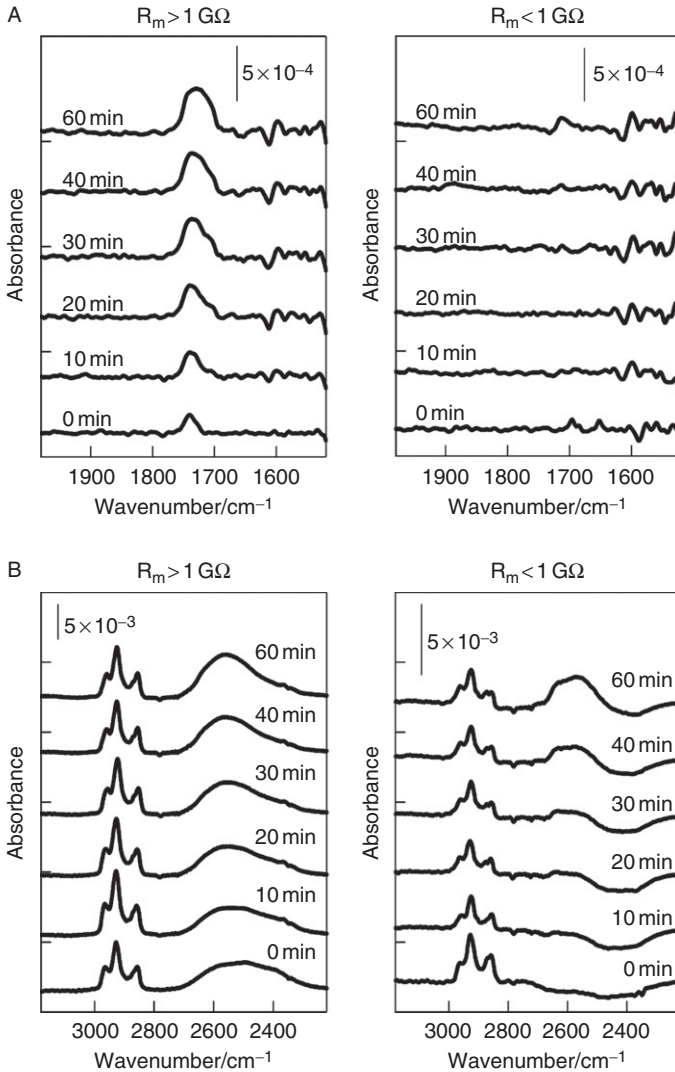


**Figure 3** IR absorption spectra after painting *n*-decane solution containing PC and Chol on agarose-coated Si prisms. Reference was the spectrum before painting the lipid solution. (A) IR spectra in the lower wave number region. (B) IR spectra in the higher wave number region. Left: (A, B) BLM with final resistance of 1.2 G $\Omega$ . Right: (A, B) BLM with final resistance of 0.54 G $\Omega$ .

gigaseal ( $n = 5$ , Fig. 3A, right panel). These results suggest that the appearance of the C=O stretching modes immediately after the lipid application can be a measure for successful formation of BLMs having G $\Omega$  resistance.

In the higher wave number region, a broad band around  $2560\text{ cm}^{-1}$  and three bands around  $2860\text{--}2970\text{ cm}^{-1}$  were observed for BLMs which attained gigaseal (Fig. 3B, left panel). The broad peak at  $\sim 2560\text{ cm}^{-1}$ , which was assigned to OD stretching mode of  $\text{D}_2\text{O}$  [22], appeared just after the lipid application. The band intensity increased with time, accompanied with a decrease in bandwidth. Such narrowing may reflect the gradual changes in the ordering of water molecules surrounding the lipid phase. The three bands around  $2860\text{--}2970\text{ cm}^{-1}$  were assigned to  $\text{CH}_x$  stretching modes of acyl chains [24]. Since the band intensity was about 10 times higher than that of the  $\text{C}=\text{O}$  modes of PC, these  $\text{CH}_x$  bands mainly arose from *n*-decane acyl chains rather than phospholipid ones. The band intensity decreased with time, suggesting that *n*-decane was slowly expelled from the surface. Similar time-dependent changes in absorption around  $2560$  and  $2860\text{--}2970\text{ cm}^{-1}$  were also observed with BLMs which failed to attain gigaseal (Fig. 3B, right panel). However, these changes were less prominent with a smaller OD stretching band which appeared only after 30 min. These results demonstrate that the observed time-dependent changes in the IRAS peaks reflect the self-thinning of the lipid solution to form BLMs: the solvent *n*-decane was expelled to the edge of the apertures, at the same time, phospholipid molecules self-assembled to form bilayer structures, and consequently,  $\text{D}_2\text{O}$  phase came to closer vicinity of the Si surface. Similar but less clear IRAS changes for the low-resistance BLM indicates an incomplete thinning process.

The functionality of the present BLMs was also confirmed by incorporating gramicidin channels into the membranes. Gramicidin is a natural ion channel-forming peptide. When their monomeric peptides form a membrane-spanning dimer by hydrogen bonding at their N-terminal, gramicidin forms a channel that is permeable to monovalent cations. Since incorporation of gramicidin into BLMs can be achieved just by adding the gramicidin solution to aqueous compartments surrounding BLMs, gramicidin is one of the most commonly used ion channels to investigate the functionality of the artificial BLMs. Figure 4 shows an example of gramicidin multichannel currents recorded in  $\text{Na}^+\text{-D}_2\text{O}$  buffer. The number of open gramicidin channels was calculated to be  $\sim 10^2$  based on the reported single-channel conductance ( $5\text{--}6\text{ pS}$ ) in similar conditions [25,26]. Solution exchange from  $\text{Na}^+\text{-D}_2\text{O}$  buffer to  $\text{K}^+\text{-D}_2\text{O}$  buffer caused further decrease in membrane resistance, suggesting that the BLM containing gramicidin shows higher conductance in  $\text{K}^+$  than in  $\text{Na}^+$  media. This observation is in agreement with the ionic selectivity of gramicidin [25,26], confirming that the present BLMs allow recording functional activities of gramicidin channels.

In summary, we have investigated *in situ* the formation process of functional planar BLMs on agarose-coated Si surfaces by simultaneous monitoring of IRAS spectra and membrane resistance. It was demonstrated

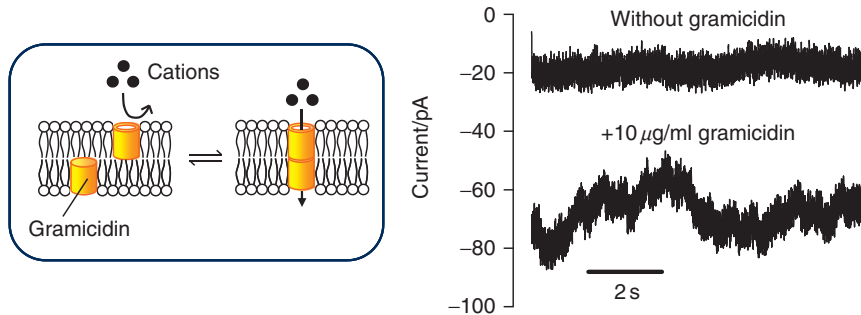


**Figure 4** An example of gramicidin channel current recorded at  $-70$  mV from a BLM containing PC and Chol. Cartoon of the reversible dimerization of gramicidin in BLMs is also shown.

that the appearance of the C=O stretching modes of phospholipid just after the lipid application can be a measure for the successful formation of BLMs with gigaohm seal. This peak is a useful empirical measure for the reproducible formation of BLMs. However, the mechanical stability of the agarose-cushioned BLMs in the SU-8 resist was insufficient for exchanging aqueous solutions surrounding BLMs. When we consider general applications of artificial BLM systems, tolerance to solution exchanges is one of the most desirable parameters for BLMs. In the next section, we will discuss our recent approach for preparation of BLMs which are stable enough for repetitive solution exchanges.

### 3. FORMATION OF STABLE FREE-STANDING BLMs

#### 3.1. Microfabricated Silicon Chips for Stable BLMs

Recent advances in lithography techniques have enabled the coupling of microfabricated devices with BLM formation. Extensive studies have been made to improve the stability of free-standing BLMs [8–12,27,28]. These efforts led to prolonged membrane lifetimes of several tens of hours [29,30]. However, patch-clamped membranes with the lifetime of several hours are still more widely used in physiology fields than the BLM reconstitution systems. This is partly because drugs acting on channels in the membranes can be easily applied and removed by solution exchanges, which is a requisite for screening drug effects. One of the most desirable goals of membrane stability for the free-standing BLMs is tolerance to solution exchanges while allowing channel current recordings rather than just the improvement of membrane durability. We have proposed a

microfabrication-based method for preparing free-standing BLMs which are stable enough for repetitive solution exchanges and allow single-channel recordings [31].

Figure 5A shows our design of silicon chips for suspending BLMs. The chip has an aperture ( $\phi$ : 20–30  $\mu\text{m}$ ) with a smoothly tapered edge in a nanometer-thick  $\text{Si}_3\text{N}_4$  septum deposited on a Si substrate. BLMs are prepared by folding up two lipid monolayers in the apertures (Fig. 5B). Owing to the tapered shape of the aperture edge, the stress on lipid bilayers at the contact with the  $\text{Si}_3\text{N}_4$  septum is expected to be minimized, leading to improvement of membrane stability. Procedures for the aperture fabrication are schematically illustrated in Fig. 5C. Apertures were fabricated in a 200- $\mu\text{m}$ -thick FZ Si(100) wafer ( $>9000 \Omega \text{ cm}$ ), one side of which was coated with a 240-nm-thick  $\text{Si}_3\text{N}_4$  layer. The wafer was first thermally oxidized and then the  $\text{Si}_3\text{N}_4$  side was coated with a  $\text{SiO}_2$  layer using the sputtering method. The former oxide layer was photolithographically patterned, followed by anisotropic etching in 25% tetramethylammonium hydroxide at 90 °C. Then a  $\text{SiO}_2$  layer was deposited on the bare  $\text{Si}_3\text{N}_4$  surfaces formed by the anisotropic etching. After photolithographic patterning, circular holes were fabricated in the  $\text{Si}_3\text{N}_4$  layer by isotropic etching in 85% phosphoric acid at 150 °C. Finally, the  $\text{SiO}_2$  layer beneath the holes was removed by 5% hydrofluoric acid to form apertures.

### 3.2. Preparation of BLMs in Microfabricated Apertures

The Si chip fabricated as above was silanized by treating with 2% (v/v) 3-cyanopropyltrimethylchlorosilane (CPDS) in acetonitrile for 24 h, and then set in the middle of a Teflon chamber. The chip separated two 1.5 ml compartments in the chamber. The  $\text{Si}_3\text{N}_4$  layer was precoated with a thin layer of *n*-hexadecane by dropping a 10- $\mu\text{l}$  aliquot of 0.1% *n*-hexadecane in chloroform. A 1400  $\mu\text{l}$  portion of 2.0 M KCl solution containing 10 mM HEPES/KOH (pH 7.4, abbreviated as KCl buffer), filtered just before use through a cellulose acetate filter (pore size: 0.20  $\mu\text{m}$ ), was added to each side of the chamber. The water level in both compartments was set below the aperture. Then a small amount (10  $\mu\text{l}$ ) of a lipid solution was spread on the aqueous solutions. The composition of the lipid solution was 2 mg/ml PC: L- $\alpha$ -phosphatidylethanolamine (PE): Chol = 7:1:2 (w/w) in chloroform/*n*-hexane (1:1, v/v). After solvent evaporation, BLMs were formed by gradually raising the water level until it surpassed the aperture. The successful preparation of a BLM was known by observing an increase in the membrane resistance from  $\sim 10 \text{ k}\Omega$  to over 1  $\text{G}\Omega$  at an applied potential of  $\pm 100 \text{ mV}$ . The incorporation of gramicidin into the BLMs was performed by adding 10–30  $\mu\text{l}$  aliquot of 1  $\mu\text{g}/\text{ml}$  gramicidin solution to the KCl buffer in the both compartments, under constant stirring.

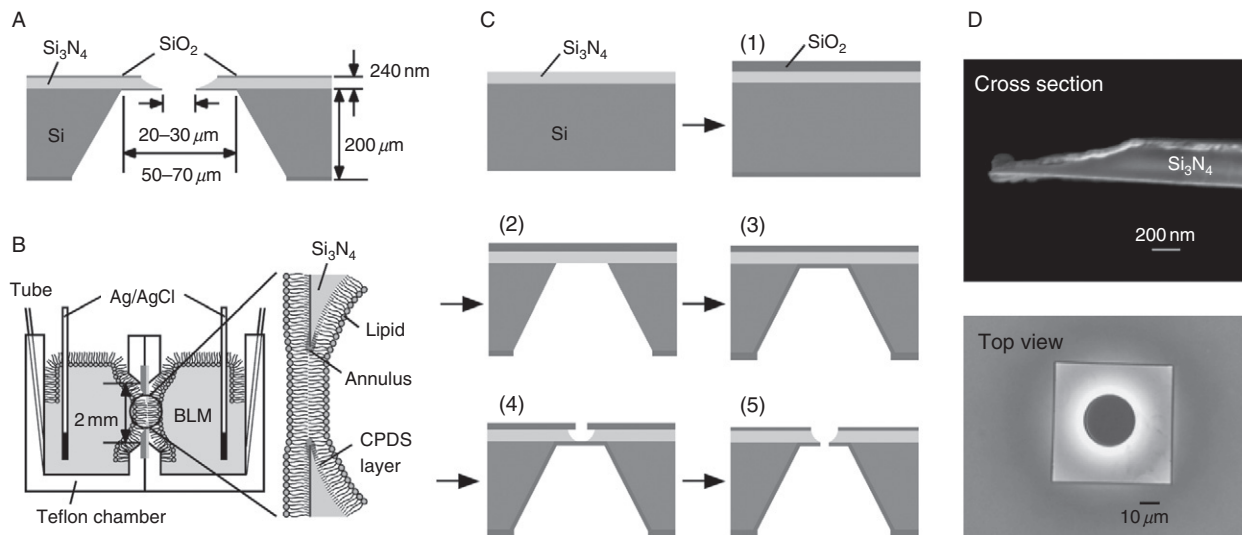


**Figure 5** (A) Schematic of a microfabricated silicon chip suspending BLMs. (B) Schematic of a BLM formed across an aperture in the silicon chip. (C) Procedure for aperture fabrication: (1) thermal oxidation and sputtering of  $\text{SiO}_2$ , (2) patterning and anisotropic etching of Si, (3) sputtering of  $\text{SiO}_2$ , (4) isotropic etching of  $\text{Si}_3\text{N}_4$ , and (5)  $\text{SiO}_2$  removal. (D) Top: Cross-sectional SEM image of an aperture edge. The aperture was fabricated in a  $\text{Si}_3\text{N}_4$  septum by the isotropic etching. Bottom: Microscopic image of an aperture from the  $\text{Si}_3\text{N}_4$  side.

Current recordings were performed with an Axopatch 200B patch-clamp amplifier (Molecular Devices). The signal was filtered at 1.0 kHz low-pass filter, digitized at 10 kHz, and stored online using a digital data acquisition system (Digidata 1440 and pCLAMP software version 10.2, Molecular Devices). The data were analyzed with a pCLAMP version 10.2 using a 500 Hz low-pass filter.

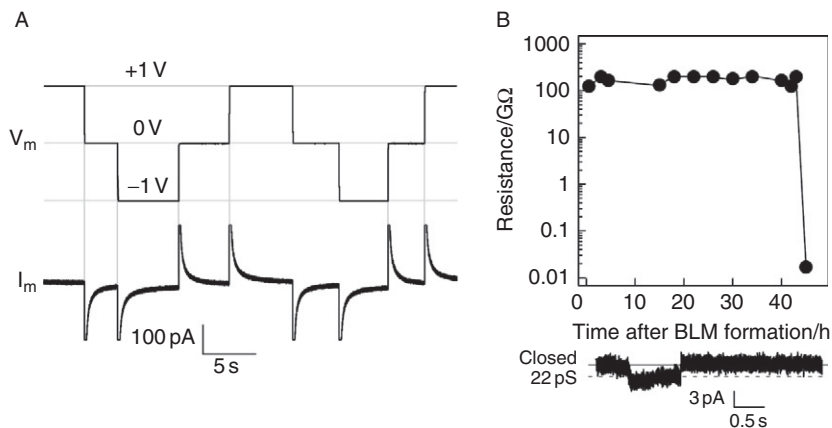
### 3.3. Stability of BLMs in Microfabricated Silicon Chips

Figure 5D shows a scanning electron microscopy (SEM) image of the edge of an aperture fabricated in a  $\text{Si}_3\text{N}_4$  septum. The aperture edge was smoothly thinned with the edge angle of about  $9\text{--}22^\circ$  by the use of the isotropic etching. Since the shape of the annulus that connects BLMs and the edge of the  $\text{Si}_3\text{N}_4$  septum is important for the membrane stability and the annulus–septum contact angle should be small for a stable arrangement of BLMs [30,32,33], the tapered shape of the aperture in a 240-nm-thick  $\text{Si}_3\text{N}_4$  septum appears suitable for the formation of stable BLMs.

BLM formation in the microfabricated apertures was examined after silanization of the chip surface with CPDS. This treatment made the chip surface hydrophobic, which was expected to accelerate deposition of a lipid monolayer with the hydrophobic tails oriented to the chip surface [28]. Free-standing BLMs were prepared by folding up two lipid monolayers across the aperture. BLMs having the resistance of  $3\text{--}>100\text{ G}\Omega$  were formed in the apertures with high probability ( $>90\%$ ) when the  $\text{Si}_3\text{N}_4$  septum around the aperture was precoated with a thin layer (10 nL) of *n*-hexadecane. Solvent-free BLMs were also formed without the precoating; however, the success probability decreased to  $\sim 30\%$ . Therefore, BLMs formed after the precoating were investigated for the following study.

The present BLMs exhibited high stability as well as high-sealing property. The membranes were not broken by electrical shocks, such as plugging off and reconnecting the Ag/AgCl electrodes inserted in the aqueous solutions surrounding the BLMs. Membranes survived when a constant voltage of  $\pm 1\text{ V}$  was applied (100%,  $n = 10$ ). Even when the applied potential was switched stepwise  $+1\text{ V} \rightarrow 0\text{ V} \rightarrow -1\text{ V}$  and *vice versa*, still 90% of the membranes (9 out of 10) survived these treatments ( Fig. 6A). Considering that the breakdown voltage for conventional BLMs has been reported  $\sim 300\text{--}500\text{ mV}$  [34,35], the present membrane showed much higher stability to electrical stimulation.

Membrane lifetime, defined as the duration for which BLMs retained membrane resistance higher than  $1\text{ G}\Omega$ , was 15–48 h ( $n = 2$ ) without incorporated channels. When gramicidin ion channels were incorporated into BLMs, these membranes also showed a similar lifetime of 15–43 h ( $n = 3$ ). The longest lifetime was obtained from a BLM containing gramicidin channel. As shown in Fig. 6B, the BLM exhibited resistance higher



**Figure 6** (A) An example of membrane current ( $I_m$ ) when the applied potential ( $V_m$ ) was switched stepwise  $+1\text{ V} \rightarrow 0\text{ V} \rightarrow -1\text{ V}$  and *vice versa*. (B) Top: A time-course of the resistance obtained from a BLM which exhibited the longest lifetime of 43 h. Membrane resistance higher than  $200\text{ G}\Omega$  was counted as  $200\text{ G}\Omega$ . Bottom: An example of gramicidin single-channel current recorded 43 h after the BLM formation. Applied potential was  $-100\text{ mV}$ .

than  $100\text{ G}\Omega$  up to 43 h and then the resistance decreased below  $1\text{ G}\Omega$  after 45 h. The current trace at the bottom of Fig. 6B shows an example of gramicidin single-channel current recorded 43 h after the BLM formation. Stepwise current with the single-channel conductance of  $22\text{ pS}$  was observed in KCl ( $2.0\text{ M}$ ) buffer. This single-channel conductance is in the range ( $20\text{--}25\text{ pS}$  in  $2.0\text{ M}$  KCl) of conductance reported by others [25,36], suggesting the functionality of the present BLM even over 40 h after the membrane formation.

Next, the tolerance of BLMs to solution exchanges was investigated. Figure 7 shows examples of single-channel currents from a BLM containing gramicidin when aqueous solutions were exchanged in series  $\text{KCl} \rightarrow \text{CsCl} \rightarrow \text{KCl}$ . In KCl ( $2.0\text{ M}$ ) buffer, single-channel current with the conductance level of  $20\text{ pS}$  was observed. Then the aqueous solutions surrounding the BLM were exchanged by sucking up KCl buffer with tubes and subsequently adding CsCl buffer with a micropipette. To rule out the possibility of membrane refolding, the water level was kept higher than the aperture in which the BLM was formed. After repeating this process 5–15 times for a thorough solution exchange, single-channel currents were still observed with a higher conductance level of  $53\text{ pS}$ . The observed conductance levels ( $20\text{ pS}$  in  $2.0\text{ M}$  KCl and  $53\text{ pS}$  in  $2.0\text{ M}$  CsCl) were very close to those reported for gramicidin channel in  $2\text{ M K}^+$  ( $25\text{ pS}$ ) and  $2\text{ M Cs}^+$  ( $55\text{ pS}$ ) at  $100\text{ mV}$  [25]. Changing the aqueous solutions back to

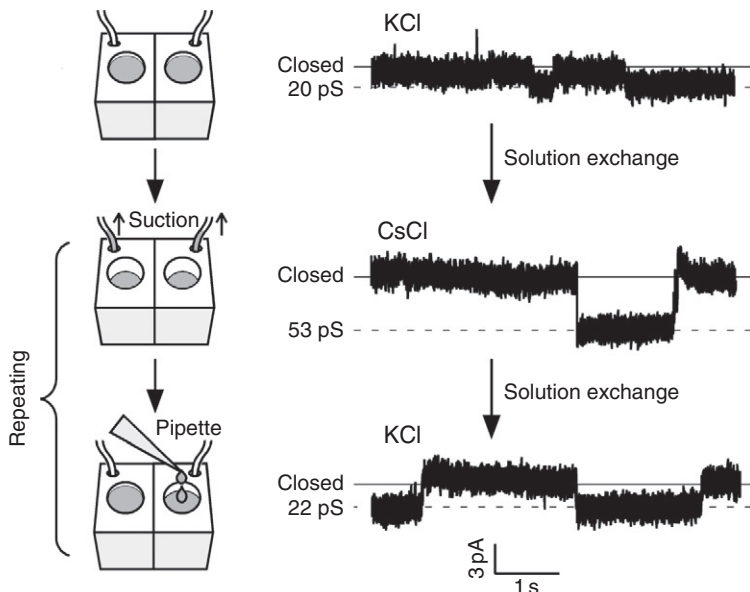


**Figure 7** Single-channel currents recorded from a BLM containing gramicidin channel at an applied potential of  $-100$  mV. The aqueous solutions surrounding the BLM were exchanged from KCl to CsCl and then back to KCl by the repetition of sucking up the solutions and subsequently adding new solutions. The water level was kept higher than the aperture in which the BLM was formed. A schematic of this procedure is also shown in the left.

KCl buffer led to the observation of channel currents with the single-channel conductance of  $22$  pS. These results demonstrate that the present BLM containing a single gramicidin channel survived repetitive solution exchanges without any perturbation of single-channel conductance. When the solution exchange experiments were examined with different BLMs, including a solvent-free membrane, all the BLMs containing gramicidin showed tolerance to solution exchanges ( $n = 7$ ), confirming the high stability of the present BLM system.

The background current noise was  $2\text{--}3$  pA after filtered at  $500$  Hz, which was relatively large for BLMs prepared in apertures of  $\phi 20\text{--}30$   $\mu\text{m}$ . This is probably due to large capacitance (mean  $\pm$  SEM was  $252 \pm 19$  pF) of the present system. Similar large capacitance of several hundred picofarad has also been reported for BLMs prepared on apertures in a Si chip [29]. Since silicon has high dielectric constant of  $11\text{--}12$ , the use of silicon resulted in the large capacitance of the total chip containing the BLMs.

The open time of the gramicidin channel in the present BLMs was distributed in the range from  $59$  ms to  $6.0$  s with the mean open time of  $0.35 \pm 0.04$  s ( $n = 191$ ). The range of open time and mean open time was



similar to those reported for gramicidin incorporated into BLMs prepared by the conventional method [26,37,38]. Transient current changes were observed for the transitions between the closed and opened states:  $12 \pm 2$  ms for openings and  $13 \pm 2$  ms for closings ( $n = 191$ ). The transients were slower than that ( $\sim 4$  ms) obtained with conventional black films [25]. The slower transient currents are again probably due to the large capacitance from silicon. Further improvement is necessary for recording channel currents with fast open  $\leftrightarrow$  close kinetics, for example, the application of capacitance-reducing layer to the silicon chips, which can also work for reducing background current noise.

## 4. CONCLUSION

Low formation reproducibility and mechanical instability has been an obstacle for the widespread application of BLM systems. While a large number of fabrication techniques have been proposed, most of these studies are based on large amount of unvolatile organic solvents to form BLMs. Since large amount of solvents may denature vulnerable channels, we showed a different approach to form stable BLMs, where amount of solvents required to form BLMs was minimized. The key feature that stabilized BLMs is the nanometer-scale design of the microfabricated septum: an aperture with a smoothly tapered edge allows reduction of the stress on the bilayer structure at the contact with the septum. The stable BLMs tolerable to solution exchanges enable analysis of channel functions under various solution conditions from the same BLM preparations. Since our fabrication process is compatible with integrated circuit technology, the present approach will lead to realization of various applications of BLMs, including a smart miniature biosensor and a high-throughput analysis of ion-channel proteins on Si chips.

## REFERENCES

- [1] C. Miller, *Ion Channel Reconstitution*, Plenum Press, New York, 1986.
- [2] M. Sugawara, A. Hirano, P. Bühlmann, Y. Umezawa, Design and application of ion-channel sensors based on biological and artificial receptors, *Bull. Chem. Soc. Jpn (Accounts)* 75 (2002) 187–201.
- [3] A. Hirano-Iwata, M. Niwano, M. Sugawara, The design of molecular sensing interfaces with lipid-bilayer assemblies, *Trends Anal. Chem.* 27 (2008) 512–520.
- [4] P. Mueller, D.O. Rudin, T. Tien, W.C. Wescott, Reconstitution of cell membrane structure in vitro and its transformation into an excitable system, *Nature (London)* 194 (1962) 979–980.

- [5] M. Takagi, K. Azuma, U. Kishimoto, A new method for the formation of bilayer membranes in aqueous solution, *Annul. Rep. Biol. Works Fac. Sci. Osaka Univ.* 13 (1965) 107–110.
- [6] M. Montal, P. Mueller, Formation of bimolecular membranes from lipid monolayers and a study of their electrical properties, *Proc. Natl Acad. Sci. USA* 69 (1972) 3561–3566.
- [7] R. Coronado, R. Lattore, Phospholipid bilayers made from monolayers on patch-clamp pipettes, *Biophys. J.* 43 (1983) 231–236.
- [8] C. Schmidt, M. Mayer, H. Vogel, A chip-based biosensor for the functional analysis of single ion channels, *Angew. Chem. Int. Ed.* 39 (2000) 3137–3140.
- [9] R. Pantoja, D. Sigg, R. Blunck, F. Bezanilla, J.R. Heath, Bilayer reconstitution of voltage-dependent ion channels using a microfabricated silicon chip, *Biophys. J.* 81 (2001) 2389–2394.
- [10] S.J. Wilk, L. Petrossian, M. Goryll, T.J. Thornton, S.M. Goodnick, J.M. Tang, et al. Integrated electrodes on a silicon based ion channel measurement platform, *Biosens. Bioelectron.* 23 (2007) 183–190.
- [11] K. Funakoshi, H. Suzuki, S. Takeuchi, Lipid bilayer formation by contacting monolayers in a microfluidic device for membrane protein analysis, *Anal. Chem.* 78 (2006) 8169–8174.
- [12] B.L. Pioufle, H. Suzuki, K.V. Tabata, H. Noji, S. Takeuchi, Lipid bilayer microarray for parallel recording of transmembrane ion currents, *Anal. Chem.* 80 (2008) 328–332.
- [13] R.F. Costello, I.R. Peterson, J. Heptinstall, N.G. Byrne, L.S. Miller, A robust gel-bilayer channel biosensor, *Adv. Mater. Opt. Electron.* 8 (1998) 47–52.
- [14] T. Ide, T. Yanagida, An artificial lipid bilayer formed on an agarose-coated glass for simultaneous electrical and optical measurement of single ion channels, *Biochem. Biophys. Res. Commun.* 265 (1999) 595–599.
- [15] C.A. Keller, K. Glasmästar, V.P. Zhdanov, B. Kasemo, Formation of supported membranes from vesicles, *Phys. Rev. Lett.* 84 (2000) 5443–5446.
- [16] S.D. Connell, D.A. Smith, The atomic force microscope as a tool for studying phase separation in lipid membranes, *Mol. Membr. Biol.* 23 (2006) 17–28.
- [17] A. Hirano-Iwata, R. Yamaguchi, K. Miyamoto, Y. Kimura, M. Niwano, *In situ* real-time monitoring of biomolecular interactions by using surface infrared spectroscopy, *J. Appl. Phys.* 105 (2009) 102039.
- [18] M.C. Hull, L.R. Cambrea, J.S. Hovis, Infrared spectroscopy of fluid lipid bilayers, *Anal. Chem.* 77 (2005) 6096–6099.
- [19] A. Blume, W. Hübner, G. Messner, Fourier transform infrared spectroscopy of  $^{13}\text{C}=\text{O}$ -labeled phospholipids hydrogen bonding to carbonyl groups, *Biochemistry* 27 (1988) 8239–8249.
- [20] R.N.A.H. Lewis, R.N. McElhaney, W. Pohle, H.H. Mantsch, Components of the carbonyl stretching band in the infrared spectra of hydrated 1,2-diacylglycerolipid bilayers: a reevaluation, *Biophys. J.* 67 (1994) 2367–2375.
- [21] H. Binder, Water near lipid membranes as seen by infrared spectroscopy, *Eur. Biophys. J.* 36 (2007) 265–279.
- [22] V.V. Volkov, D.J. Palmer, R. Righini, Heterogeneity of water at the phospholipid membrane interface, *J. Phys. Chem. B* 111 (2007) 1377–1383.
- [23] A. Hirano-Iwata, A. Oshima, K. Onodera, K. Aoto, T. Taira, R. Yamaguchi, et al. Self-formation of bilayer lipid membranes on agarose-coated silicon surfaces studied by simultaneous electrophysiological and surface infrared spectroscopic measurements, *Appl. Phys. Lett.* 94 (2009) 243906.
- [24] G. Socrates, *Infrared and Raman Characteristic Group Frequencies*, third ed., Wiley, Chichester, 2001.

- [25] O.S. Andersen, Ion movement through gramicidin A channels, Single-channel measurements at very high potentials, *Biophys. J.* 41 (1983) 119–133.
- [26] A. Hirano, M. Wakabayashi, Y. Matsuno, M. Sugawara, A single-channel sensor based on gramicidin controlled by molecular recognition at bilayer lipid membranes containing receptor, *Biosens. Bioelectron.* 18 (2003) 973–983.
- [27] J.A. Maurer, V.E. White, D.A. Dougherty, J.L. Nadeau, Reconstitution of ion channels in agarose-supported silicon orifices, *Biosens. Bioelectron.* 22 (2007) 2577–2584.
- [28] R.J. White, E.N. Ervin, T. Yang, X. Chen, S. Daniel, P.S. Cremer, et al. Single ion-channel recordings using glass nanopore membranes, *J. Am. Chem. Soc.* 129 (2007) 11766–11775.
- [29] X. Han, A. Studer, H. Sehr, I. Geissbühler, M.D. Berardino, F.K. Winkler, et al. Nanopore arrays for stable and functional free-standing lipid bilayers, *Adv. Mater.* 19 (2007) 4466–4470.
- [30] B. Liu, D. Rieck, B.J.V. Wie, G.J. Cheng, D.F. Moffett, D.A. Kidwell, Bilayer lipid membrane (BLM) based ion selective electrodes at the meso-, micro-, and nano-scales, *Biosens. Bioelectron.* 24 (2009) 1843–1849.
- [31] A. Hirano-Iwata, K. Aoto, A. Oshima, T. Taira, R. Yamaguchi, Y. Kimura, et al., Free-standing lipid bilayers in silicon chips-membrane stabilization based on micro-fabricated apertures with a nanometer-scale smoothness, *Langmuir* 26 (2010) 1949–1952.
- [32] S.H. White, Analysis of the torus surrounding planar lipid bilayer membranes, *Biophys. J.* 12 (1972) 432–445.
- [33] M. Eray, N.S. Dogan, L. Liu, A.R. Koch, D.F. Moffett, M. Silber, et al. Highly stable bilayer lipid membranes (BLMs) formed on microfabricated polyimide apertures, *Biosens. Bioelectron.* 9 (1994) 343–351.
- [34] P. Kramar, D. Miklavcic, A.M. Lebar, Determination of the lipid bilayer breakdown voltage by means of linear rising signal, *Bioelectrochemistry* 70 (2007) 23–27.
- [35] M. Mayer, J.K. Kriebel, M.T. Tosteson, G.M. Whitesides, Microfabricated Teflon membranes for low-noise recordings of ion channels in planar lipid bilayers, *Biophys. J.* 85 (2003) 2684–2695.
- [36] D.D. Busath, C.D. Thulin, R.W. Hendershot, L.R. Phillips, P. Maughan, C.D. Cole, et al. Noncontact dipole effects on channel permeation. I. Experiments with (5F-Indole)Trp<sup>13</sup> gramicidin A channels, *Biophys. J.* 75 (1998) 2830–2844.
- [37] Y. Matsuno, C. Osono, A. Hirano, M. Sugawara, Single-channel recordings of gramicidin at agarose-supported bilayer lipid membranes formed by the tip-dip and painting methods, *Anal. Sci.* 20 (2004) 1217–1221.
- [38] J.R. Elliott, D. Needham, J.P. Dilger, D.A. Haydon, The effects of bilayer thickness and tension on gramicidin single-channel lifetime, *Biochim. Biophys. Acta* 735 (1983) 95–103.

# FORMATION OF PLANAR LIPID BILAYER MEMBRANES AND VESICLES USING MICROFLUIDIC TECHNOLOGY

Shoji Takeuchi<sup>1,2</sup>

---

## Contents

1. Introduction	88
2. Planar Lipid Bilayer Membranes	88
2.1. A Contact Method to Form Planar Lipid Bilayers	88
2.2. A Planar Lipid Bilayer Array	91
3. Monodisperse Lipid Vesicles	93
3.1. The “Blowing Vesicle” Method	93
3.2. Using the “Blowing Vesicle” Method in a Microfluidic Device	94
4. Arraying Technology	97
5. Conclusions	99
Acknowledgments	99
References	99

## Abstract

This chapter describes how microfluidic technology can be used to form two types of artificially reconstituted lipid bilayers: (i) planar lipid bilayers and (ii) lipid vesicles. These membranes are powerful tools for the functional analysis of membrane proteins, but have typically been prohibitively difficult to create. Here, several types of microfluidic techniques are introduced, including (i) a contact method by which a planar lipid bilayer membrane can be formed by contacting two lipid monolayers in an organic solvent, (ii) a blowing-vesicle method by which a planar lipid bilayer can be deformed into a vesicle via application of a pulse-jet flow, and (iii) a dynamic microarray technology by which monodisperse particles such as vesicles or beads can be trapped sequentially into trapping spots in an array and can be selectively released by applying an optical laser under a microscope. These devices may offer excellent abilities in the

<sup>1</sup> Center for International Research on Micro/Nano Mechatronics (CIRMM), Institute of Industrial Science (IIS), The University of Tokyo, Japan

<sup>2</sup> Kanagawa Academy of Science and Technology (KAST), Japan

control of fluid flow, and thus are useful for the formation and manipulation of lipid bilayer membranes that can be applied in various research fields such as membrane protein analysis, artificial cell studies, and highly sensitive biosensors.

## 1. INTRODUCTION

Artificially reconstituted lipid bilayers are important in a variety of research fields, since they facilitate membrane protein analysis and artificial cell studies and can be used to develop highly sensitive biosensors. They can be categorized into two main groups: (i) planar lipid bilayers and (ii) lipid vesicles. This chapter describes several methods for forming lipid bilayers using microfluidic technology. This technology has recently received much attention as it permits the handling of very small quantities of samples and reagents [1,2]; moreover, fluids behaving at low Reynolds number are easily controlled with laminar flow.

This chapter focuses on (i) a contact method by which a planar lipid bilayer membrane can be formed by contacting monolayer lipids in an organic solvent, (ii) a blowing-vesicle method by which a planar lipid bilayer can be deformed into a vesicle via application of a pulse-jet flow, and (iii) a dynamic microarray technology by which monodisperse particles such as vesicles or beads can be trapped sequentially in an array and then selectively released by application of an optical laser under a microscope. Although the conventional methods generally have low reproducibility in the bilayer formation, the microfluidic techniques described here minimize this difficulty and are powerful tools that enable the functional analysis of membrane proteins.

## 2. PLANAR LIPID BILAYER MEMBRANES

### 2.1. A Contact Method to Form Planar Lipid Bilayers

Planar lipid bilayers, also known as black lipid membrane (BLM), are usually formed across tiny apertures opened in a solid support [3,4]. BLMs are often formed with either the painting method or the Langmuir–Blodgett (LB) method. In the painting method, a lipid solution (an organic solvent containing phospholipid) is applied across a tiny aperture that separates two aqueous compartments. In the LB method, lipid monolayers at the water–air interface are brought together when they are raised above the aperture. Planar bilayers facilitate the study of membranes in precisely defined environments—for instance, investigations of buffer composition at both the *cis* and *trans* sides and membrane potentials. The electrical seal of the BLM system is superior to that of the cell patch-clamping system, allowing highly

sensitive detection, ideally down to single molecular level [5–7]. However, bilayers produced using the conventional methods are often fragile, unsteady, and difficult to reproduce; this reduces their usefulness in high-throughput systems for pharmaceutical screenings.

Our group has recently developed a reproducible method, the “contact method,” for forming planar bilayers without apertures, using a simple fluidic control [8]. The principle of this approach is shown in Fig. 1A and B. The monolayer assembles spontaneously at the interface between water and the organic solvent containing amphiphilic molecules (phospholipids; Fig. 1A). Once the two interfaces come into contact with each other, they form a lipid bilayer (Fig. 1B). This method can easily be performed by injecting two water droplets into a well that is already filled with lipid

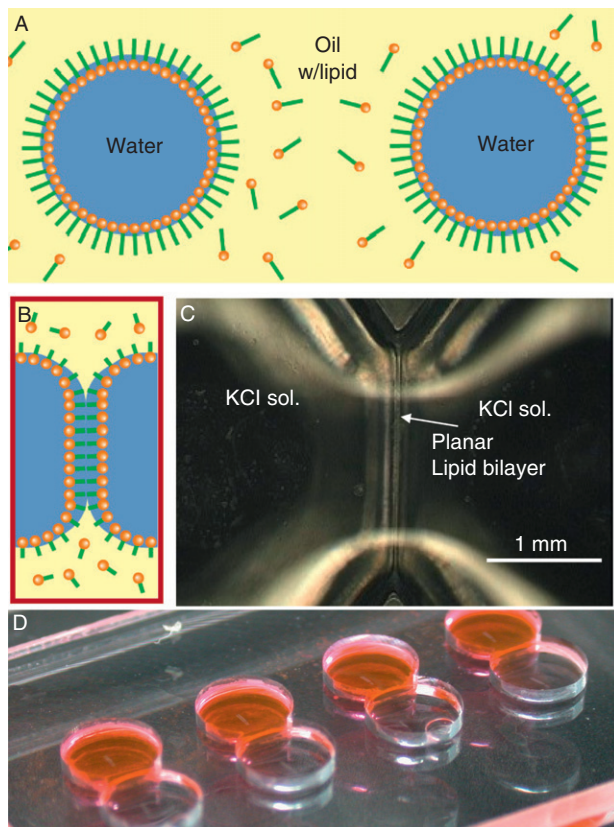


**Figure 1** (A, B) Schematic views of the contact method. Two water droplets come into contact and form a lipid bilayer at the interface between the droplets. (C) Top view of the contacted membrane. (D) Multiple membrane can be easily formed with this method.

solution. The success of the technique can be verified by capacitance measurements made between the membrane and ion channel signals, through peptide channels reconstituted into the membrane. Figure 1C shows the top view of the contacted membranes. The interface does not rupture when an organic solution containing lipid molecules is used; the two droplets stay unmixed for over an hour (Fig. 1D). Thus, this system is both straightforward and stable.

When performed in microchannels allowing precise control of fluids (e.g., the contact procedure), this technique makes the bilayer formation process particularly reliable. Figure 2 shows the interface, formed in the cross-shaped fluidic channel, of two electrolytes separated by the organic solvent containing phospholipids. In this configuration, the formation and disassembly of the lipid bilayer can be controlled by pushing and withdrawing the aqueous phase; thus, for the quantitative analysis, it is possible to determine the beginning and end of the membrane transport phenomenon. This technique also allows the cross-sectional observation of both compartments separated by the lipid bilayer.

Membrane ion channel recordings were performed with an  $\alpha$ -hemolysin ( $\alpha$ HL) reconstituted into the contacted membrane; the  $\alpha$ HL forms a nanopore allowing passage of ions through the membrane (Fig. 3). A few minutes after the two droplets are contacted, 80–100 pS conductance was measured,

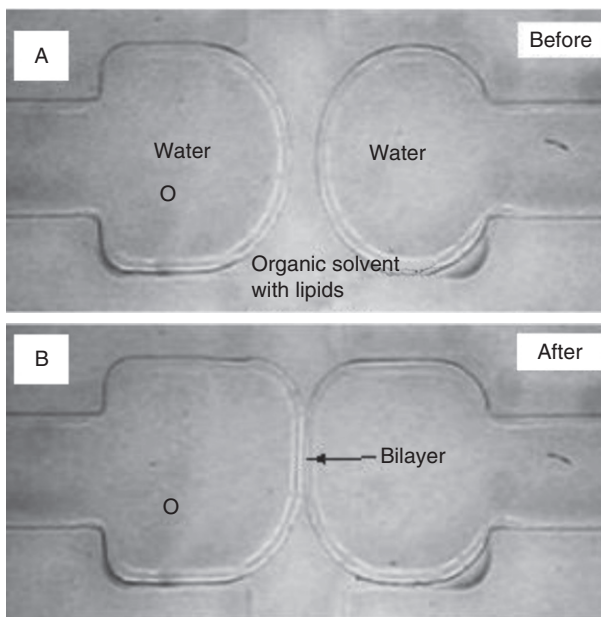


**Figure 2** The contact method performed in a microfluidic channel. The membrane forms just after contacting the two water phase.

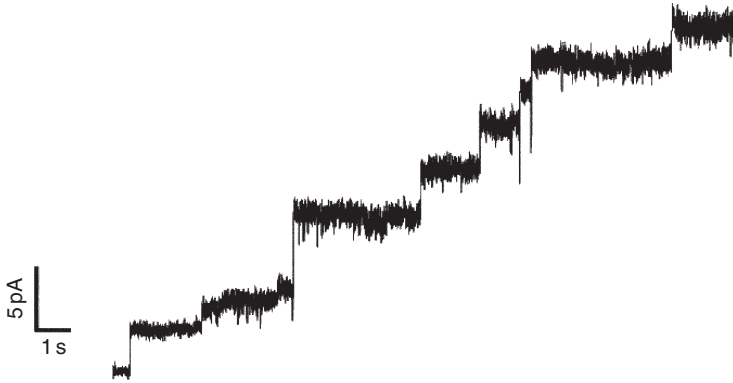


**Figure 3** A measurement result of the single channel current recording through  $\alpha$ HL nanopores incorporated into the contacted membrane.

indicating that the single  $\alpha$ HL pores have been incorporated; the single  $\alpha$ HL channel conductance in 0.1 M KCl solution is around 100 pS [9]. Thus, a functional lipid bilayer can be formed at the interface of two droplets, facilitating the functional study of reconstituted membrane proteins.

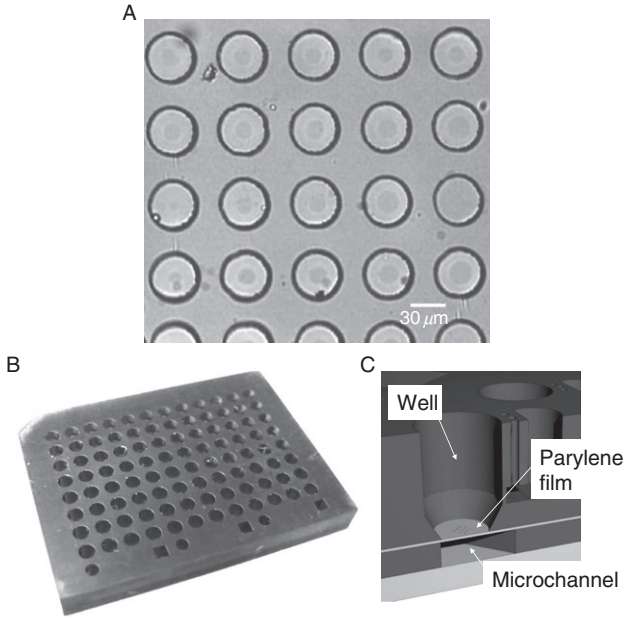
## 2.2. A Planar Lipid Bilayer Array

Since the contact method is easy and reproducible, it is useful for producing an array of lipid bilayer membranes; such array is very important for the high-throughput analysis of membrane proteins (e.g., ion channel proteins, transporters). In fact, this method has been used to develop many micro-devices with microapertures and microfluidic channels for the formation of multiple lipid membranes [10–13].

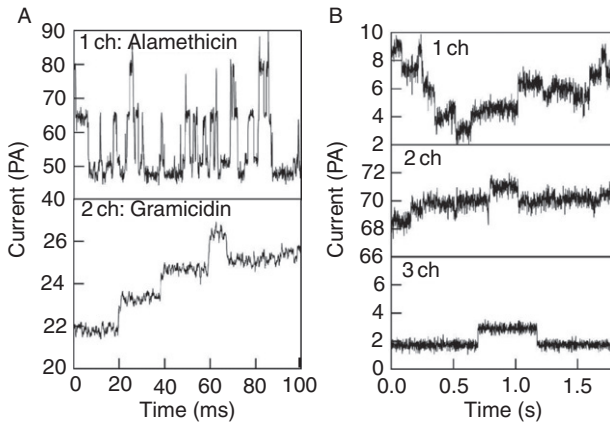
One example of the formation process of multiple lipid membranes is explained as follows. A 20- $\mu$ m-thick parylene film is vapor-deposited on a single-crystalline silicon substrate. Then, aluminum is deposited on parylene and patterned by the standard photolithographic process. By using aluminum as a mask, parylene is selectively etched by oxygen plasma. The aluminum is removed, and the parylene sheet with microapertures (30–50  $\mu$ m in diameter) is peeled off from the silicon substrate with tweezers; the lipid membranes are formed over the microapertures (Fig. 4A). To create an array for multiple ion channel recordings with the preformed microapertures, the parylene film is integrated in a microfluidic device fabricated by rapid stereolithography; the stereolithography enables easy fabrication of three-dimensional structures such as wells and microfluidic channels on a submillimeter scale (Fig. 4B and C).

Figure 5 shows the measurement results of simultaneous recording of antibiotic ion channels using these devices [13]. Multiple recording on a





**Figure 4** (A) Multiple lipid membranes formed in the microapertures on a Parylene film. (B) A microfluidic device having the microapertures between the wells and microfluidic channels. (C) A cross-sectional view of the device.



**Figure 5** (A) Simultaneous recording of alamethicin and gramicidin transmembrane pores in two adjacent wells. Clamping voltage in each well was 80 mV. (B) Simultaneous recording of gramicidin current in three adjacent wells at 100 mV clamping voltage.

large scale is also possible with devices that have 96 ( $12 \times 8$ ) addressable recording wells [14]. In this case, channel recordings are performed by sequentially moving the recording electrode between wells; this technique has been used to successfully detect channel currents of the membrane protein gramicidin A in 44 of 96 wells. These results suggest that it is possible to conduct parallel ion channel recordings in order to perform high-throughput screening of ion channel proteins in artificial lipid bilayer systems [15].

### 3. MONODISPERSE LIPID VESICLES

#### 3.1. The “Blowing Vesicle” Method

Liposomes are synthetic lipidic containers with membrane structures similar to those of cell membranes. Liposomes come in a variety of sizes; those with a diameter  $> 10 \mu\text{m}$  are known as giant liposomes or giant vesicles [16]. These have been widely used in medical and biological applications, as encapsulating containers for biological materials, chemicals, and drugs. Since they provide small reaction volumes similar to those of living cells, they are also primary models for the study of cell systems [17]; artificial cell studies require vesicles of uniform size with biologically functionalized membranes.

Conventional vesicle formation methods based on the self-assembly of lipid molecules (e.g., the gentle hydration method) produce polydisperse vesicles with low encapsulation efficiency [18–25]. Although the reverse emulsion method (or the “spin-down” method) overcame such problems and allows to generate unilamellar vesicles, the vesicle size is not directly controllable and throughput is limited [17,26]. Another strategy is to use monodisperse water-in-oil-in-water emulsions with phospholipids dissolved in oil as templates of the vesicles [27]. Although this technique makes most of the benefits from the drop-based microfluidics [28,29], it is still difficult to create the unilamellar vesicles by simply thinning down the oil phase.

A straightforward method for the preparation of lipid vesicles was inspired from the formation of soap bubbles from a soap film [30]. In this “blowing vesicle” method, lipid vesicles are blown out of a preformed biofunctional planar lipid membrane, directly encapsulating ejected materials (Fig. 6A). This method allows rapid preparation of uniformly sized vesicles, without postprocessing. A vertical planar lipid bilayer membrane ( $1 \times 1 \text{ mm}^2$ ), where membrane proteins can be reconstituted, has been formed using the contact method described above. A fine capillary jet nozzle ( $\phi = 60 \mu\text{m}$ ) was positioned  $200 \mu\text{m}$  away from the membrane, and a short pulse jet flow was created by briefly opening the microdispenser’s electromagnetic valve (Fig. 6B).

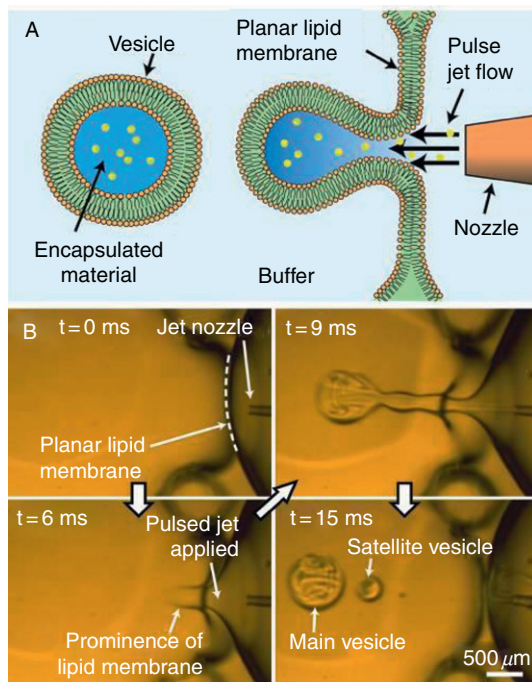


**Figure 6** (A) A schematic view of the “blowing vesicle” method. (B) Sequential images of vesicle formation captured by a high-speed CCD camera. A planar membrane was deformed into spherical vesicles within 10 ms.

When the valve was opened for 1.5 ms at 400 kPa, vesicles were generated with coefficient of variation smaller than 10%. When the jet was applied, the membrane deformed and stretched significantly, and the neck of the stretched column was pinched off. Occasionally, satellite vesicles were also generated. This process can be repeated to form a number of vesicles. The most important advantage of this method is that any ejected materials are directly encapsulated, regardless of their size, concentration, and chemical properties.

### 3.2. Using the “Blowing Vesicle” Method in a Microfluidic Device

This method can also be used to generate monodisperse, cell-sized, uni-lamellar vesicles with a microfluidic device [31]. A poly(dimethylsiloxane) (PDMS) microfluidic T-junction device with a number of small chambers in its wall is fabricated using standard soft-lithographic techniques. Each small chamber is further connected to a much larger chamber through a

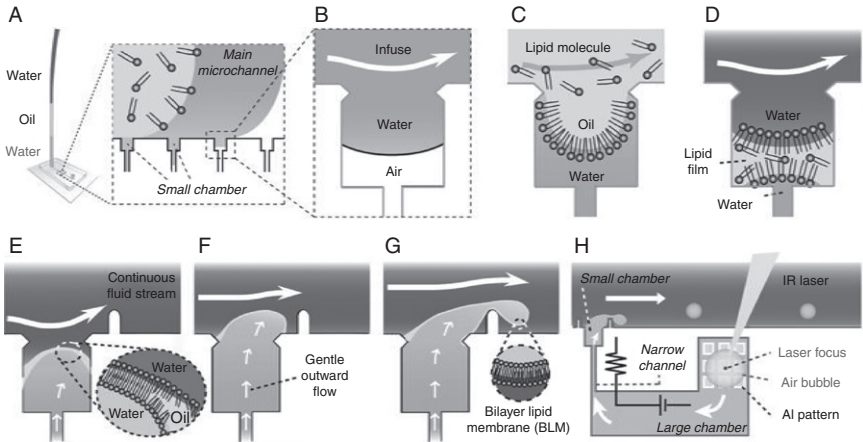


**Figure 7** (A) A microfluidic device having a main channel with many chambers in its walls was used. Water, oil with dissolved lipids, and water are sequentially infused into the device. (B) Water fills the device while pushing out air through the PDMS. (C) Oil flushes away the water in the channel, but confines the rest to the chambers. (D) Water again flushes away the oil and the residue forms an oil film, in which amphiphilic lipid molecules form two monolayers at the interface of water and oil. (E) A cross flow at the microfluidic T-junction thins the lipid film and drives the contact of monolayers to form a bilayer. (F) The gentle outward flow further bends out the bilayer. (G) Shear forces from the continuous fluid stream leads to the fission of the leading edge of the bilayer, that is, the generation of a unilamellar vesicle. (H) The system for continuous vesicle formation integrated with an optically generated microbubble.

narrow channel (Fig. 7). At first, the device is filled with an aqueous solution, while pushing air out through the PDMS (Fig. 7A and B). This first solution will become the contents of the vesicles, once the vesicles are created. Next, a sequentially infused immiscible oil containing dissolved phospholipids is used to flush the first solution from the channel, while it is also retained in the other chambers (Fig. 7C). Finally, another aqueous solution is used to remove oil in the channel, while leaving a very thin layer of oil in each small chamber; this layer becomes an oil-containing lipid film (Fig. 7D). In this film, the amphiphilic lipid molecules self-assemble into two monolayers at both water–oil interfaces. By causing the fluid in the chamber to flow outward, the film bends and thins, and a bilayer is created when the two monolayers come into contact (Fig. 7E); this formation process is the same as that occurring in the contact method.

To supply the outward flow, aluminum is patterned in the large chamber and heated with an infrared (IR) laser to generate a microbubble. The narrow channel in the chamber is designed to have high fluidic resistance; this resistance prevents the bubble from swelling rapidly and subsequently slows the outward flow. Eventually, sufficiently gentle deformation of the

lipid bilayer is accomplished without breaking it up. Finally, high shear forces from the continuous fluid stream pinch off the leading edge of the deformed bilayer to form the monodisperse unilamellar vesicles (Figs. 7F–H and 8A). Since the original bilayer remains intact throughout the experiment, multiple vesicles can be produced. Maintenance of a constant flow allows generation of vesicles with a narrow size distribution; the coefficient of variation of the vesicles formed in this method is less than 5% (Fig. 8B).

To demonstrate the effectiveness of the phospholipid vesicles, a cell-free gene expression system from *Escherichia coli* was encapsulated. A feeding solution containing a buffer and nutrients (mainly ribonucleotides and amino acids) was used as the continuous aqueous phase. After expression of the GFP gene, fluorescence intensity was measured inside the vesicle; this experiment was performed in the device at room temperature (25 °C). The expression of fluorescent GFP molecules continued over 5 h (Fig. 9). This demonstration indicates that the vesicle is able to encapsulate a solution as complex as a cell-free extract.

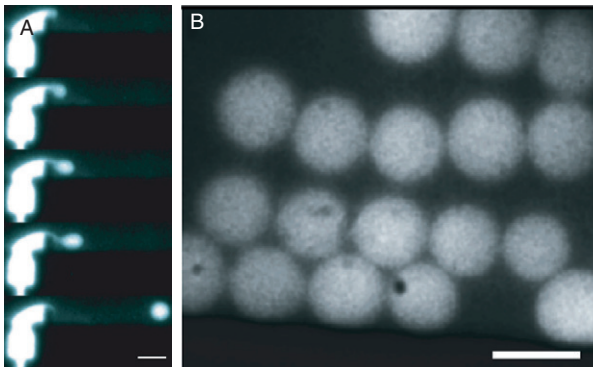


**Figure 8** (A) Individual fluorescence images of vesicle formation were sequentially taken by a high-speed camera (250 fps). (Scale bar: 20  $\mu\text{m}$ ) (B) Fluorescence image of vesicles generated from a single chamber and collected in a microfluidic channel. Scale bar: 20  $\mu\text{m}$ .

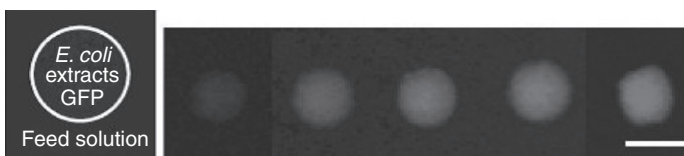


**Figure 9** Time-sequential images of the vesicle fluorescence of GFP, corresponding to 0, 1, 2, 5, and 15 h after starting observation by optical microscopy. Scale bar: 20  $\mu\text{m}$ .

## 4. ARRAYING TECHNOLOGY

Microarray technology has been popular for basic scientific studies [32,33], drug-discovery [34,35], and diagnostic purposes [36], as the technology allows rapid and high-throughput assays involving small sample sizes. Microarrays of cell-sized liposomes expressing membrane proteins are useful in studies of both pathological and physiological phenomena; this technique has enormous potential for diagnostic applications, including drug testing and toxicology studies. However, this potential has yet to be fully realized due to the lack of reliable multifunctional platforms to transport and immobilize particles, infuse reagents, observe the reaction, and retrieve selected cells.

Our group has used a dynamic microarray technology to overcome this problem [37]. This technology allows us to achieve all aforementioned functions in a single integrated device, by combining hydrodynamic and optical approaches, including (i)  $\mu$ -Fluidic traps (hydrodynamic confinement and arraying of particles), wherein hydrodynamic forces allow simultaneous transportation and immobilization of large numbers of particles without the need for complicated controls; and (ii) optical-based microbubbles for retrieval of particles, which provides dexterity in handling individual particles without the need for complicated circuitry.

The  $\mu$ -Fluidic trap is made up of a meander-shaped channel (loop channel) superimposed onto a straight channel (Fig. 10A) [37]. The traps are narrowed regions along the straight channel. When they are empty, flow resistance is lower along the straight channel than in the loop channel; as a result, the main stream flows along the straight channel. A bead in the flow will be reproducibly carried by the main stream into the trap (trapping mode); Fig. 10D and E shows 10,000 microbeads (15  $\mu\text{m}$  in a diameter) trapped in a  $\mu$ -Fluidic trap array. Once the trap is filled, flow resistance is increased drastically along the straight channel, and the main flow is redirected along the loop channel. Subsequent beads will be carried along the loop channel, by-passing the filled trap (by-passing mode). Because of the unique design of this  $\mu$ -Fluidic trap, beads will not be able to enter traps that are already occupied. Since the efficiency of this trap is near 100%, it is suitable for use with small sample volumes. The device is highly amenable to automatic processing and can be easily scaled up for use in fast, high-throughput, highly parallel screening. Theoretically, scaled-down versions of this trap would also work, enabling single cells to be directly trapped and arrayed for cell assays.

Aluminum patterns function as heaters where bubbles form when illuminated with lasers; trapped beads are released when these bubbles displace them into the main flow, where they are carried toward the

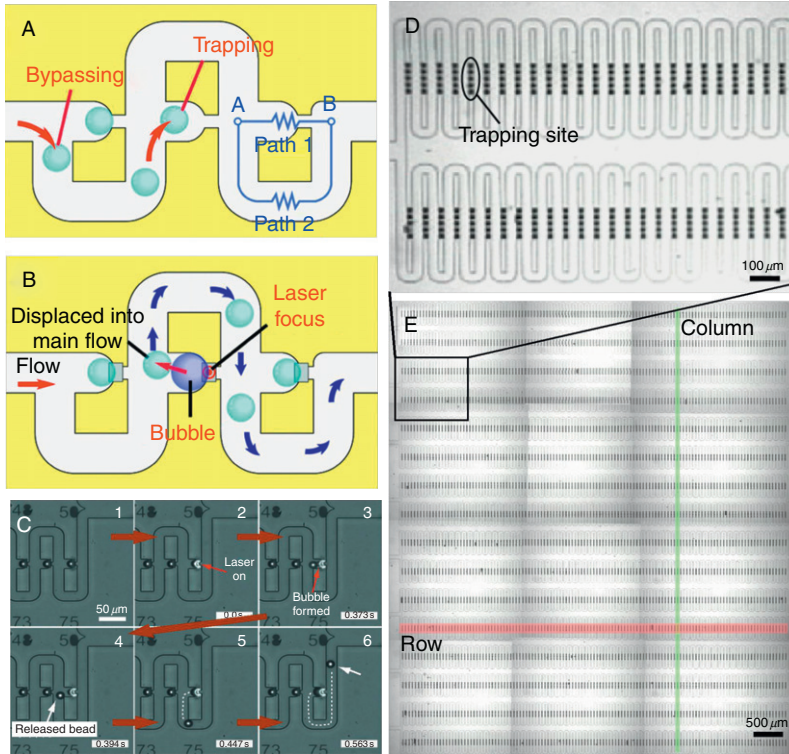


**Figure 10** A schematic diagram of (A) the trapping and (B) the releasing mechanism. (C) Sequential images of releasing a single microbead. (D) A close-up image of device capable of immobilization of  $15\ \mu\text{m}$  microbeads. (E) An overall image of the microarray having approximately 10,000 microbeads. Ninety-nine percent of the traps contain only one bead.

outlet (Fig. 10B). Figure 10C shows a trapped bead being released by a “laser-activated” bubble, as photographed by a high-speed camera. Although the device requires only short bursts of laser to form microbubbles, the temperature near the heaters may still compromise activities of biological materials such as DNA, proteins, and cells. This problem can be solved by the following modifications [38]: (i) the incorporation of cavities as nucleation sites, (ii) indirect retrieval using bubble powered jet, and (iii) the use of low boiling point fluid to realize a gentle optical-based retrieval method. These modifications dramatically reduced both the intensity and duration of applied laser for bubble formation. The method was also found to be gentle enough to maintain the viability of cells, indicating that the modified device is useful for the handling of biomaterials.

## 5. CONCLUSIONS

Microfluidic technology has progressed remarkably over the past 20 years. Devices for analytical chemistry, cell biology, and diagnosis have been particularly well developed. This technology allows the handling of very small amounts of liquids containing biological samples (e.g., proteins, lipids, etc.); it also facilitates delivery of these biomaterials into specific areas at specific times. The examples in this chapter illustrate how this technology can be used to construct lipid membranes, such as planar lipid bilayers and liposomes. Planar lipid bilayer arrays incorporating different membrane proteins can be used for a variety of purposes, including next-generation diagnosis, drug discovery, and highly sensitive ion-channel-based biosensors. Monodisperse vesicles are useful not only for studying membrane proteins, but also for acting as vehicles for drug delivery and as artificial cells. Dynamic microarray is an attractive technique for efficiently handling multiple vesicles simultaneously. These approaches may provide a new route to the high-throughput production of lipid bilayer membranes.

## ACKNOWLEDGMENTS

Much of the work described in this chapter was performed by members of my research group. In particular, I thank Hiroaki Suzuki, Bruno Lepioufle, Toshihisa Osaki, Wei-Heong Tan, Kei Funakoshi, and Sadao Ota.

## REFERENCES

- [1] G.M. Whitesides, *Nature* 442 (2006) 368–373.
- [2] P.S. Dittrich, K. Tachikawa, A. Manz, *Anal. Chem.* 78 (2006) 3887–3908.
- [3] C. Miller, *Ion Channels Reconstitution* Plenum Press, New York, 1986.
- [4] H.T. Tien, A. Ottova, *Planar Lipid Bilayers (BLMs) and Their Applications*, Elsevier, Amsterdam, 2003.
- [5] N. Fertig, R.H. Blick, J.C. Behrends, *Biophys. J.* 82 (2002) 3056–3062.
- [6] M. Mayer, J.K. Kriebel, M.T. Tosteson, G.M. Whitesides, *Biophys. J.* 85 (2003) 2684–2695.
- [7] R. Pantoja, D. Sigg, R. Blunck, F. Bezanilla, J.R. Heath, *Biophys. J.* 81 (2001) 2389–2394.
- [8] K. Funakoshi, H. Suzuki, S. Takeuchi, *Anal. Chem.* 78 (2006) 8169–8174.
- [9] D. Deamer, D. Branton, *Acc. Chem. Res.* 35 (2002) 817–825.
- [10] H. Suzuki, K. Tabata, Y. Kato-Yamada, H. Noji, S. Takeuchi, *Lab Chip* 4 (2004) 502–505.
- [11] H. Suzuki, K.V. Tabata, H. Noji, S. Takeuchi, *Langmuir* 22 (2006) 1937–1942.
- [12] H. Suzuki, K.V. Tabata, H. Noji, S. Takeuchi, *Biosens. Bioelectron.* 22 (2007) 1111–1115.



- [13] B. Le Pioufle, H. Suzuki, K. Tabata, H. Noji, S. Takeuchi, *Anal. Chem.* 80 (2008) 328–332.
- [14] H. Suzuki, B. Lepioufle, S. Takeuchi, *Biomed. Microdevices* 11 (2009) 17–22.
- [15] T. Osaki, H. Suzuki, B. Lepioufle, S. Takeuchi, *Anal. Chem.* 81 (2009) 9866–9870.
- [16] P.L. Luisi, P. Walde, *Giant Vesicles*, Wiley, New York, 2000.
- [17] V. Noireaux, A. Libchaber, *Proc. Natl. Acad. Sci. USA* 101 (2004) 17669–17674.
- [18] J.P. Reeves, R.M. Dowben, *J. Cell. Physiol.* 73 (1969) 49–60.
- [19] F. Olson, C.A. Hunt, F.C. Szoka, W.J. Vail, D. Papahadjopoulos, *Biochim. Biophys. Acta* 557 (1979) 9–23.
- [20] G. Tresset, S. Takeuchi, *Biomed. Microdevices* 6 (2004) 213–218.
- [21] G. Tresset, S. Takeuchi, *Anal. Chem.* 77 (2005) 2795–2801.
- [22] K. Kuribayashi, G. Tresset, Ph. Coquet, H. Fujita, S. Takeuchi, *Meas. Sci. Technol.* 17 (2006) 3121–3126.
- [23] M.I. Angelova, D.S. Dimitrov, *Liposome electroformation*, *Faraday Discuss.* 81 (1986) 303–311.
- [24] M. Karlsson, et al. *Anal. Chem.* 72 (2000) 5857–5862.
- [25] F. Szoka, D. Papahadjopoulos, *Proc. Natl. Acad. Sci. USA* 75 (1978) 4194–4198.
- [26] S. Pautot, B.J. Frisken, D.A. Weitz, *Proc. Natl. Acad. Sci. USA* 100 (2003) 10718–10721.
- [27] H.C. Shum, D. Lee, I. Yoon, T. Kodger, D.A. Weitz, *Langmuir* 24 (2008) 7651–7653.
- [28] T. Thorsen, R. Roberts, F. Arnold, S. Quake, *Phys. Rev. Lett.* 86 (2001) 4163–4166.
- [29] A.S. Utada, E. Lonrenceau, D.R. Link, P.D. Kaplan, H.A. Stone, D.A. Weitz, *Science* 308 (2005) 537–541.
- [30] K. Funakoshi, H. Suzuki, S. Takeuchi, *J. Am. Chem. Soc.* 129 (2007) 12608–12609.
- [31] S. Ota, S. Yoshizawa, S. Takeuchi, *Angew. Chem. Int. Ed.* 48 (2009) 6533–6537.
- [32] N. Winsinger, S. Ficarro, P.G. Schultz, J.L. Harris, *Proc. Natl. Acad. Sci. USA* 99 (2002) 11139–11144.
- [33] K.S. Lam, R. Liu, S. Miyamoto, A.L. Lehman, J.M. Tuscano, *Acc. Chem. Res.* 36 (2003) 370–377.
- [34] J. Schlessinger, *Nat. Biotechnol.* 20 (2002) 232–233.
- [35] S.E. Salmon, R.H. Liu-Stevens, Y. Zhao, M. Lebl, V. Krchnak, K. Wertman, N. Sepetov, K.S. Lam, *Mol. Divers.* 2 (1996) 57–63.
- [36] W.H. Robinson, C. DiGennaro, W. Hueber, B.B. Haab, M. Kamachi, E.J. Dean, S. Fournel, D. Fong, M.C. Genovese, H.E. Neuman de Vegvar, et al. *Nat. Med.* 8 (2002) 295–301.
- [37] W.H. Tan, S. Takeuchi, *Proc. Natl. Acad. Sci. USA* 104 (2007) 1146–1151.
- [38] S. Takeuchi, W.H. Tan, *Lab Chip* 7 (2008) 259–266.

# SPATIAL VARIATION OF PERMITTIVITY NEAR A CHARGED MEMBRANE IN CONTACT WITH ELECTROLYTE SOLUTION

Ekaterina Gongadze,<sup>1,\*</sup> Klemen Bohinc,<sup>2,3</sup> Ursula van Rienen,<sup>1</sup>  
Veronika Kralj-Iglič,<sup>4</sup> and Aleš Iglič<sup>3</sup>

## Contents

1. Introduction	102
2. Orientation of Water Molecules near a Charged Membrane Surface	102
3. Excluded Volume Effect	108
4. Excluded Volume Effect and Orientation of Water Molecules	111
4.1. Modified Poisson–Boltzmann Equation	111
4.2. Linearized Modified Poisson–Boltzmann Equation	115
5. Phenomenological Model of Spatial Variation of Permittivity and the Membrane Surface Potential	118
6. Conclusions	123
References	125

## Abstract

The interaction between a charged membrane bilayer surface and an electrolyte solution causes the formation of an electrical double layer, which has been a subject of extensive study for more than a century. This chapter provides a statistical mechanical description of orientational ordering of water molecules and of excluded volume effect of ions near the charged membrane surface. The space variation of the permittivity of the electrolyte solution near the charged membrane surface obtained by statistical mechanical model is then included in a phenomenological model for the membrane surface potential for highly charged membranes.

\* Corresponding author. *E-mail address:* [ekaterina.gongadze@uni-rostock.de](mailto:ekaterina.gongadze@uni-rostock.de)

<sup>1</sup> Institute of General Electrical Engineering, University of Rostock, Justus-von-Liebig-Weg 2, 18059 Rostock, Germany

<sup>2</sup> Faculty of Health Sciences, University of Ljubljana, Zdravstvena pot 5, SI-1000 Ljubljana, Slovenia

<sup>3</sup> Laboratory of Biophysics, Faculty of Electrical Engineering, University of Ljubljana, Tržaška 25, SI-1000 Ljubljana, Slovenia

<sup>4</sup> Laboratory of Clinical Biophysics, Faculty of Medicine, University of Ljubljana, Lipičeva 2, SI-1000 Ljubljana, Slovenia

## 1. INTRODUCTION

The contact between a negatively charged bilayer membrane surface and an electrolyte solution implies a particular ion distribution and water orientation near the charged surface. In other words, an electrical double layer (EDL) [1–4] is formed.

Within the so-called Poisson–Boltzmann (PB) theory [2,3,5,6], the ions in electrolyte solution are treated as dimensionless, while uniform permittivity of the electrolyte solution is assumed. The Stern model [4] was the first attempt to incorporate finite size of ions in EDL theory by combining the Helmholtz [1] and Gouy–Chapman [2,3] model. Helmholtz treated the double layer mathematically as a simple capacitor, based on a physical model in which a layer of ions with a single layer of solvent around each ion is adsorbed to the surface. Gouy [2] and Chapman [3] considered the thermal motion of ions and pictured a diffuse double layer composed of ions of opposite charge (counterions) attracted to the surface and ions of the same charge (coions) repelled from it. Ions are embedded in a dielectric continuum while the electric potential is subject to the PB differential equation [6–9]. Generally, Stern model [4] consists of an inner Helmholtz plane (coions bound near the surface due to specific adsorption), the so-called outer Helmholtz plane (hydrated counterions at the distance of closest approach), and a diffuse double layer.

Most of the theoretical models describing EDL assume that the permittivity in the whole system is constant. But actually, close to the charged surface, due to accumulation of counterions near the charged surface, the water molecules are partially depleted from this region [8]. The water dipoles show a distinct preferential orientation in the direction perpendicular to the charged surface [10–14]. All these result in a spatial variation of the permittivity near the charged surface [12,13,15]. In this work, we present different models of EDL, which take into account the spatial variation of permittivity. The orientational ordering of water molecules and excluded volume effect near the planar bilayer membrane surface are described within the modified PB theory. The results of this theory are then included in a generalized phenomenological PB model via the space dependency of the permittivity near the charged planar surface.

## 2. ORIENTATION OF WATER MOLECULES NEAR A CHARGED MEMBRANE SURFACE

The distribution of ions in the electrolyte solution close to the charged membrane surface is described within the PB theory [6,16] by the competition between the electrostatic interactions and the entropy of

the ions in the solution. Due to the electrostatic forces between the charged surface and the ions in the solution, the counterions (the ions with the charge of the opposite sign than the charged surface) are accumulated close to the surface and the coions (the ions with the charge of the same sign than the surface) are depleted from the surface [6]. Near the charged surface, water molecules show a distinct preferential orientation and a strongly reduced permittivity [11]. In this section, the PB theory modified by orientational ordering of water is briefly described. In the model, the finite volumes of ions in the electrolyte solution (i.e., the excluded volume) are not taken into account. Therefore, the predictions of the model are restricted to the cases of low surface charge densities and low bulk ionic strengths when accumulation of the counterions near charged membrane surface is not very pronounced.

We consider a planar charged membrane bilayer surface in contact with solution of ions and water (Langevin) dipoles. The Langevin dipoles describe a water molecule with a nonzero dipole moment ( $\mathbf{p}$ ). The membrane bilayer surface bears charge with surface charge density  $\sigma$ . We assume that counterions and coions are distributed according to the Boltzmann distribution functions [6,11,16]

$$n_+(x) = n_0 e^{-\Psi}, \quad n_-(x) = n_0 e^{\Psi}, \quad (1)$$

while the number density of water molecules ( $n_w(x)$ ) is assumed to be constant everywhere in the electrolyte solution and equal to its bulk value ( $n_{0w}$ ):

$$n_w(x) = n_{0w}. \quad (2)$$

Here  $n_+(x)$  and  $n_-(x)$  are the number densities of counterions and coions, respectively and

$$\Psi(x) = e_0 \phi(x) / kT \quad (3)$$

is the reduced electrostatic potential,  $\phi(x)$  is the electrostatic potential,  $e_0$  is the elementary charge,  $kT$  is the thermal energy, and  $n_0$  is the bulk number density of positively and negatively charged ions in electrolyte solution. The axis  $x$  is perpendicular to the membrane surface and points in the direction of bulk solution.

The charges of counterions, coions, and water molecules (Langevin dipoles) contribute to the average microscopic volume charge density:

$$\varrho(x) = e_0(n_+(x) - n_-(x)) - \frac{dP}{dx}. \quad (4)$$

The polarization  $P$  is given by

$$P(x) = n_{0w} \langle \mathbf{p}(x, \omega) \rangle_B, \quad (5)$$

where  $\mathbf{p}$  is the water (Langevin) dipole moment and  $\langle \mathbf{p}(x, \omega) \rangle_B$  is its average over the angle distribution in thermal equilibrium.  $P(x)$  is positive if the polarization vector  $\mathbf{P}$  points in the direction of  $x$ -axis and negative if  $\mathbf{P}$  points in the direction pointing from bulk to the charged membrane surface. According to the Boltzmann function law [5], the relative probability of finding the water dipole in an element of the angle  $d\Omega = 2\pi \sin \omega d\omega$  is proportional to the Boltzmann factor  $\exp(-W_d/kT)$ , where

$$W_d = -\mathbf{p} \cdot \mathbf{E} = \mathbf{p} \cdot \nabla \phi = (kT/e_0)p_0 |\Psi'| \cos(\omega) \quad (6)$$

is the energy of the water (Langevin) dipole  $\mathbf{p}$  in the electric field  $\mathbf{E} = -\nabla \phi$  and  $\omega$  is the angle between the dipole moment vector  $\mathbf{p}$  and the vector  $\nabla \phi$ . Hence

$$\begin{aligned} \langle \mathbf{p}(x, \omega) \rangle_B &= \frac{\int_0^\pi p_0 \cos \omega \exp\left(-p_0 |\Psi'| \cos \omega / e_0\right) 2\pi \sin \omega d\omega}{\int_0^\pi \exp\left(-p_0 |\Psi'| \cos \omega / e_0\right) 2\pi \sin \omega d\omega} \\ &= \frac{p_0 \int_0^\pi \cos \omega \exp\left(-p_0 |\Psi'| \cos \omega / e_0\right) d(\cos \omega)}{\int_0^\pi \exp\left(-p_0 |\Psi'| \cos \omega / e_0\right) d(\cos \omega)} \\ &= -p_0 \left( \coth\left(\frac{p_0 |\Psi'|}{e_0}\right) - \frac{e_0}{p_0 |\Psi'|} \right) = -p_0 \mathcal{L}\left(\frac{p_0 |\Psi'|}{e_0}\right), \end{aligned} \quad (7)$$

where  $p_0$  is the magnitude of the water dipole moment. The function  $\mathcal{L}(u) = (\coth(u) - 1/u)$  is the Langevin function. The Langevin function  $\mathcal{L}(p_0 |\Psi'| / e_0)$  describes the average magnitude of the Langevin dipole moments at given  $x$ . In our derivation we assumed the azimuthal symmetry. Inserting the ion Boltzmann distribution functions Eq. (1) and expression for polarization (Eq. (5)) into Eq. (4), we get the expression for the volume charge density in electrolyte solution:

$$\varrho(x) = -2e_0 n_0 \sinh \Psi + n_{0w} p_0 \frac{d}{dx} \left[ \mathcal{L}\left(p_0 |\Psi'| / e_0\right) \right]. \quad (8)$$

Inserting the above expression for volume charge density  $\rho(x)$  (Eq. (8)) into Poisson equation

$$\Psi'' = -4\pi l_B \rho / \epsilon_0, \quad (9)$$

we get:

$$\Psi'' = 4\pi l_B \left( 2n_0 \sinh \Psi - n_{0w} \frac{p_0}{\epsilon_0} \frac{d}{dx} \left[ \mathcal{L} \left( p_0 |\Psi'| / \epsilon_0 \right) \right] \right), \quad (10)$$

where  $l_B$  is the Bjerrum length:

$$l_B = e_0^2 / 4\pi \epsilon_0 kT \quad (11)$$

and  $\epsilon_0$  the permittivity of the free space. Dipolar PB differential equation (10) is subject to two boundary conditions. The first boundary condition is obtained by integrating the differential equation (10):

$$\Psi'(x=0) = -\frac{4\pi l_B}{\epsilon_0} \left[ \sigma + n_{0w} p_0 \mathcal{L} \left( p_0 |\Psi'| / \epsilon_0 \right) \Big|_{x=0} \right]. \quad (12)$$

The condition requiring electroneutrality of the whole system was taken into account in the derivation of Eq. (12). The second boundary condition is

$$\Psi'(x \rightarrow \infty) = 0. \quad (13)$$

Based on Eqs. (5)–(7), we can express the relative permittivity of the electrolyte solution ( $\epsilon = \epsilon_r$ ) in contact with the planar charged membrane bilayer surface as [17]

$$\epsilon = 1 + \frac{1}{\epsilon_0} \frac{d|P|}{dE} = 1 + n_{0w} \frac{p_0}{\epsilon_0} \frac{d(\mathcal{L}(p_0 E / kT))}{dE}. \quad (14)$$

while the corresponding effective permittivity ( $\epsilon_{\text{eff}}$ ) can be defined as

$$\epsilon_{\text{eff}} = 1 + \frac{|P|}{\epsilon_0 E} = 1 + n_{0w} \frac{p_0}{\epsilon_0} \frac{\mathcal{L}(p_0 E / kT)}{E}, \quad (15)$$

where  $E = |\phi'|$  is the magnitude of electric field strength.

Figure 1 shows the dependence of the effective permittivity  $\epsilon_{\text{eff}}$  on the magnitude of the electric field strength  $E$  calculated within the PB theory (Eq. (15)) which takes into account the orientational ordering of water molecules by considering them as Langevin dipoles. The excluded volume

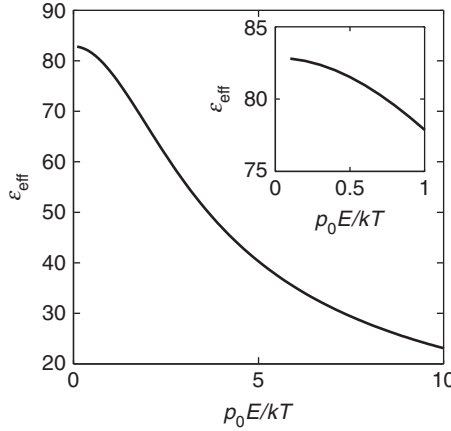


**Figure 1** Calculated effective permittivity (see Eq. (15)) as a function of the magnitude of electric field strength  $E = |\phi'|$ . The dipole moment of the water Langevin dipoles  $p_0 = 5D$ , bulk concentration of water dipoles is  $n_{0w}/N_A = 55$  mol/l, the Bjerrum length  $l_B = 54.6$  nm.

principle is not taken into account. It can be seen in Fig. 1 that  $\epsilon_{\text{eff}}$  decreases with increasing magnitude of electric field strength  $E$ . Since the value of  $E$  decreases with increasing distance from the membrane charge surface (see, e.g., [6]),  $\epsilon_{\text{eff}}$  increases with the increasing distance from the charged surface. In accordance with the results of other authors, it can be concluded that due to the distinct preferential orientation of water dipoles in the close vicinity of the charged membrane surface, the effective permittivity  $\epsilon_{\text{eff}}$  near the membrane surface is reduced relative to its bulk value (see, e.g., [11]).

If the Boltzmann distribution function is assumed also for water (Langevin) dipoles:

$$n_+(x) = n_0 e^{-\Psi}, \quad (16)$$

$$n_-(x) = n_0 e^{\Psi}, \quad (17)$$

$$n_w(x) = n_{0w} \left\langle e^{-p_0 |\Psi'| \cos \omega / \epsilon_0} \right\rangle_{\omega}, \quad (18)$$

where

$$\left\langle e^{-p_0 |\Psi'| \cos \omega / \epsilon_0} \right\rangle_{\omega} = \frac{2\pi \int_0^{\pi} d(\cos \omega) e^{-p_0 |\Psi'| \cos \omega / \epsilon_0}}{4\pi} = \frac{e_0}{p_0 |\Psi'|} \sinh \frac{p_0 |\Psi'|}{e_0}, \quad (19)$$

a similar procedure as described above leads to the extension of the PB equation in the form [18]

$$\Psi'' = 4\pi l_B \left( 2n_0 \sinh \Psi - n_{0w} \frac{p_0}{\epsilon_0} \frac{d}{dx} \left[ \mathcal{F} \left( p_0 |\Psi'| / \epsilon_0 \right) \right] \right), \quad (20)$$

where the function  $\mathcal{F}$  is defined as

$$\mathcal{F}(u) = \mathcal{L}(u) \frac{\sinh u}{u}. \quad (21)$$

The corresponding effective permittivity ( $\epsilon_{\text{eff}}$ ) can be defined as [18]

$$\epsilon_{\text{eff}} = 1 + n_{0w} \frac{p_0 \mathcal{F}(p_0 E / kT)}{\epsilon_0 E}. \quad (22)$$

Figure 2 shows the dependence of the effective permittivity  $\epsilon_{\text{eff}}$  on the magnitude of electric field strength  $E = |\phi'|$  calculated within the dipolar PB theory which takes into account the Boltzmann distribution for water molecules (Eqs. (18) and (19)) as well as the orientational ordering of water molecules by considering them as Langevin dipoles (Eq. (22)). It can be seen in Fig. 2 that according to Eq. (22), the effective permittivity  $\epsilon_{\text{eff}}$  increases as a function of increasing  $E$ . Since the magnitude of electric field strength

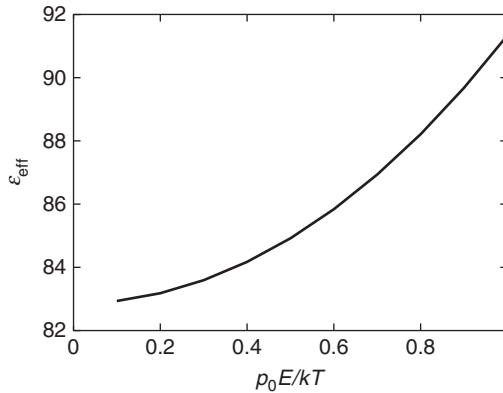


**Figure 2** Calculated effective permittivity Eq. (22) as a function of the magnitude of electric field strength  $E = |\phi'|$  assuming the Boltzmann space distribution of water dipoles (Eqs. (18) and (19)). Dipole moment of water (Langevin) dipoles is  $p_0 = 5D$ , bulk concentration of water is dipoles  $n_{0w}/N_A = 55$  mol/l, Bjerrum length is  $l_B = 54.6$  nm.



in electrolyte solution increases towards the charged membrane surface, Eq. (22) predicts the increase of  $\epsilon_{\text{eff}}$  in the vicinity of the charged membrane surface [18]. This is a consequence of the accumulation of water dipoles near the charged surface (due to Boltzmann distribution for water molecules) which prevails over the decrease of  $\epsilon_{\text{eff}}$  due to an increased orientational ordering of water molecules in a strong electric field as shown in Fig. 1. Neglecting the finite volumes of ions and water molecules is thus reflected in the predicted unrealistic increase of  $\epsilon_{\text{eff}}$  near the charged membrane surface [12,18,22].

In Section 3 we first describe the PB theory modified by the excluded volume principle, that is, the finite volumes of ions are taken into account within a simple lattice statistics [8]. In the model, each site of the lattice (of the width  $a_s$ ) is occupied by one and only one of the three kinds of molecules. The ordering of water molecules in electric field is not taken into account.

Finally, in Section 4 the excluded volume and orientation of water dipoles are considered within same modified PB theory. The predicted decrease of effective permittivity  $\epsilon_{\text{eff}}$  near the charged membrane surface relative to its bulk value is the consequence of two effects, that is, the depletion of water molecules near the charged membrane surface on the account of accumulation of counterions, and a pronounced orientational ordering of water dipoles in the strong electric field in the vicinity of the charged membrane surface [12].

### 3. EXCLUDED VOLUME EFFECT

A number of different attempts have been made to incorporate excluded volume effect (i.e., the finite volumes of ions) into the PB equation. Freise [19] introduced the excluded volume effect by a pressure-dependent potential, while Wicke and Eigen [20] used a thermodynamic approach, multiplying the numerical density of ions by a factor containing the number of the vacant sites. The fluctuation potential [16] due to the self-atmosphere of ion and the ion-ion exclusion volume term were taken into account in the modified PB equation [21–23]. More recently, the finite size of ions has been incorporated into the EDL theory in a different way [24,25], among others by using lattice statistics model [8,26], leading to the PB equation modified by the excluded volume effect in the form [8,27] (for monovalent cations and counterions)

$$\frac{d^2\Psi(x)}{dx^2} = \frac{2e_0^2 n_s n_0}{kT\epsilon\epsilon_0 n_{0w}} \frac{\sinh(\Psi(x))}{1 + \frac{2n_0}{n_{0w}} \cosh(\Psi(x))}, \quad (23)$$

where  $\varepsilon$  is the permittivity of electrolyte solution,  $\varepsilon_0$  the permittivity of the free space, and  $n_s$  is the number density of lattice sites:  $n_s = 1/a_s^3$ , where  $a_s$  is the width of the single lattice site. The  $x$ -axis is perpendicular to the membrane surface and points to the bulk solution. The bulk number density of water  $n_{0w}$  is connected to number density of lattice sites  $n_s$  and ion bulk number density  $n_0$  as  $n_{w0} = n_s - 2n_0$ .

The two boundary conditions are

$$\left. \frac{d\Psi(x)}{dx} \right|_{x \rightarrow \infty} = 0, \quad \left. \frac{d\Psi(x)}{dx} \right|_{x=0} = -\frac{\sigma \varepsilon_0}{kT\varepsilon\varepsilon_0}, \quad (24)$$

$\sigma$  is the surface charge density of the bilayer membrane surface. The first boundary condition states that the electric field is zero, far away from the charged surface, while the second boundary condition demands the electroneutrality of the whole system.

The corresponding ion distribution functions are [8,27]

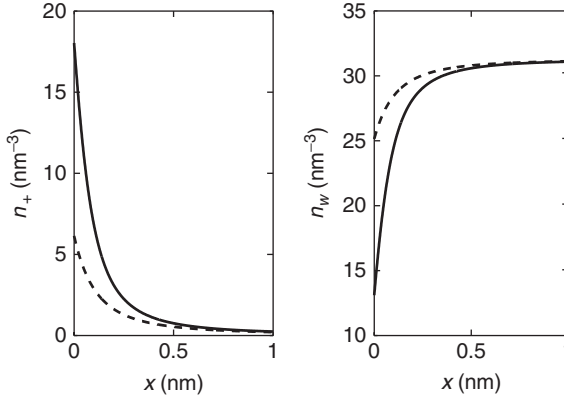
$$n_j(x) = \frac{n_s(n_0/n_{0w}) \exp(-j\Psi(x))}{1 + \frac{2n_0}{n_{0w}} \cosh(j\Psi(x))}, \quad j = +, -, \quad (25)$$

where  $j = +$  for cations and  $j = -$  for anions. The above described equations of the PB theory modified by the excluded volume effect assumes that the center of ions can approach to the  $x = 0$  plane. The number density of water (Langevin) dipoles  $n_w$  can be then calculated from the known  $n_+$  and  $n_-$  as

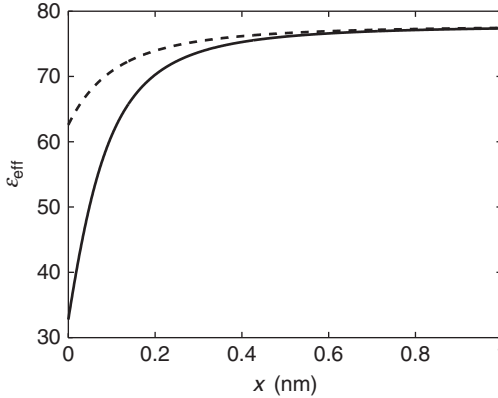
$$n_w(x) = n_s - n_+(x) - n_-(x). \quad (26)$$

Figure 3 shows that for higher values of the surface charge density ( $|\sigma|$ ), the counterion number density  $n_+$  increases. For very high  $|\sigma|$  the counterion number density  $n_+$  may saturate close to the charged surface to its close packing value, while the classical PB theory predicts unreasonable high values beyond the close-packing value (see also [8,27]). The PB theory modified by the excluded volume effect given by Eq. (25) thus predicts the saturation of the counterions near the charged surface for ions of finite size [8,27,28].

Due to accumulation of counterions near the charged membrane surface (Fig. 3, left panel), the number density of water molecules in this region may be reduced substantially (Fig. 3, right panel). Even not considered in a self-consistent way (i.e., within the above described PB theory modified by excluded volume the permittivity is a constant), the space dependency of the permittivity of the electrolyte solution in contact with a charged membrane surface may be estimated (Fig. 4) by adopting the assumption



**Figure 3** The number density of counter-ions ( $n_+$ ) as a function of the distance from the planar charged membrane surface ( $x$ ) for two values of surface charge density  $\sigma$ :  $-0.2 \text{ As/m}^2$  (dashed line) and  $-0.4 \text{ As/m}^2$  (full line)(left figure) and the corresponding number density of Langevin dipoles  $n_w = (n_s - n_+ - n_-)$  (right figure). The model parameters are: lattice constant  $a_s = 0.318 \text{ nm}$ ,  $\varepsilon = 78.5$ ,  $T = 310 \text{ K}$ , bulk salt concentration  $n_0/N_A = 0.1 \text{ mol/l}$ , where  $N_A$  is Avogadro number.



**Figure 4** The effective permittivity  $\varepsilon_{\text{eff}}(x) = 78.5 n_w(x)/n_{0w}$  of the electrolyte solution calculated for the number densities of counter-ions given in Fig. 3.

that the permittivity is proportional to the relative density of water molecules (Langevin dipoles):

$$\varepsilon_{\text{eff}}(x) = 78.5 \frac{n_w(x)}{n_{0w}}. \quad (27)$$

In the previous two sections, the orientation of water dipoles and the finite size of ions in electrolyte solution were treated separately by two models.

In the second section (Section 2), we considered the orientation of point-like water molecules, while in the third section (Section 3), the finite volume of ions and water molecules was taken into account. In the next section (Section 4), the orientational ordering of water molecules and excluded volume effect near the planar bilayer membrane surface are considered simultaneously by modification of PB equation.

## 4. EXCLUDED VOLUME EFFECT AND ORIENTATION OF WATER MOLECULES

### 4.1. Modified Poisson–Boltzmann Equation

As before (see Section 2), we consider a planar charged membrane bilayer surface in contact with a solution of ions and Langevin dipoles of finite size. The Langevin dipoles describe water molecules with nonzero dipole moments ( $\mathbf{p}$ ). The membrane bilayer surface is charged with surface charge density  $\sigma$ . The lattice with an adjustable lattice site is introduced in order to describe the system of Langevin dipoles and salt ions. All lattice sites are occupied by ions or Langevin dipoles. For the sake of simplicity, we assume that the volume of each ion and the volume of a single Langevin dipole are equal. The free energy of the system  $F$ , measured in units of thermal energy  $kT$ , can be written as [12]

$$\begin{aligned} \frac{F}{kT} = & \frac{1}{8\pi l_B} \int (\Psi')^2 dV \\ & + \int \left[ n_+(x) \ln \frac{n_+(x)}{n_0} + n_-(x) \ln \frac{n_-(x)}{n_0} + n_w(x) \ln \frac{n_w(x)}{n_{0w}} \right] dV \quad (28) \\ & + \int n_w(x) \langle \mathcal{P}(\omega) \ln \mathcal{P}(\omega) \rangle_\omega dV \\ & + \lambda \int [n_s - n_w(x) - n_+(x) - n_-(x)] dV, \end{aligned}$$

where the averaging over all angles  $\omega$  is defined as

$$\langle F(x) \rangle_\omega = \frac{1}{4\pi} \int F(x, \omega) d\Omega. \quad (29)$$

The first term in Eq. (28) corresponds to the energy of the electrostatic field. Here  $\Psi(x)$  is the reduced potential,  $dV = A dx$  is the volume element with thickness  $dx$ , where  $A$  is the membrane area. The second line in Eq. (28) accounts for the mixing free energy contribution of the positive and negative salt ions,  $n_+$  and  $n_-$  are the number densities of positively and negatively charged ions, respectively,  $n_w$  is the number density of Langevin

dipoles,  $n_0$  is the bulk number density of positively and negatively charged ions, while  $n_{0w}$  is the bulk number density of Langevin dipoles. We assume  $\phi(x \rightarrow \infty) = 0$ . The third line in Eq. (28) accounts for the orientational contribution of Langevin dipoles to the free energy.  $\mathcal{P}(x)$  is the probability that the Langevin dipole located at  $x$  is oriented for an angle  $\omega$  with respect to the normal to the charged membrane bilayer surface. The last line in Eq. (28) is constraint due to finite size of particles, imposing the condition that each site of the lattice is occupied by only one particle (coion, counterion, or Langevin water dipole),  $n_s$  is the number density of lattice sites:  $n_s = 1/a_s^3$  and where  $a_s$  is the width of the single lattice site. At any position  $x$ , we require the normalization condition

$$\langle \mathcal{P}(x, \omega) \rangle_\omega = 1 \quad (30)$$

to be fulfilled. The above expression for the free energy can be rewritten in the form:

$$\begin{aligned} \frac{F}{kT} &= \frac{1}{8\pi l_B} \int (\Psi')^2 dV \\ &+ \int \left[ n_+(x) \ln \frac{n_+(x)}{n_0} + n_-(x) \ln \frac{n_-(x)}{n_0} \right] dV \\ &+ \int \left\langle n(x, \omega) \ln \frac{n(x, \omega)}{n_{0w}} \right\rangle_\omega dV \\ &+ \lambda \int [n_s - \langle n(x, \omega) \rangle_\omega - n_+(x) - n_-(x)] dV, \end{aligned} \quad (31)$$

where the Langevin dipole distribution function is defined as

$$n(x, \omega) = n_w(x) \mathcal{P}(x, \omega). \quad (32)$$

By averaging over all angles  $\omega$  in Eq. (32), the number density of Langevin dipoles is obtained:

$$\langle n(x, \omega) \rangle_\omega = \langle n_w(x) \mathcal{P}(x, \omega) \rangle_\omega = n_w(x) \langle \mathcal{P}(x, \omega) \rangle_\omega = n_w(x), \quad (33)$$

where we took into account Eq. (30).

The charges of counterions, coions, and Langevin dipoles contribute to the average microscopic volume charge density:

$$\varrho(x) = e_0(n_+(x) - n_-(x)) - \frac{dP}{dx}. \quad (34)$$

The polarization  $P$  is given by

$$P(x) = n_w(x) \langle \mathbf{p}(x, \omega) \rangle_B, \quad (35)$$

where  $\langle \mathbf{p}(x, \omega) \rangle_B$  is the average value of the Langevin dipole moments  $\mathbf{p}$  at coordinate  $x$  (see Eq. (7)).  $P(x)$  is positive if the polarization vector  $\mathbf{P}$  points in the direction of  $x$ -axis and negative if  $\mathbf{P}$  points in direction from the bulk to the charged membrane surface. The rotational averaging is performed over all values of  $\omega$ . The Langevin function  $\mathcal{L}(p_0 |\Psi'| / e_0)$  describes the average magnitude of Langevin dipole moments at given  $x$ .

The free energy  $F = F(n_+, n_-, n(x, \omega))$  fully specifies the system. In thermal equilibrium,  $F$  adopts minimum with respect to the functions  $n_+(x)$ ,  $n_-(x)$ , and  $n(x, \omega)$ . The results of the variational procedure are

$$n_+(x) = n_0 e^{-\Psi + \lambda}, \quad (36)$$

$$n_-(x) = n_0 e^{\Psi + \lambda}, \quad (37)$$

$$n(x, \omega) = n_{0w} e^{(-p_0 |\Psi'| \cos \omega / e_0) + \lambda}. \quad (38)$$

Inserting Eqs. (36)–(38) into the constraint (the last line of Eq. (31))

$$n_s = n_+(x) + n_-(x) + \langle n(x, \omega) \rangle_\omega, \quad (39)$$

yields

$$n_s = n_0 e^{-\Psi + \lambda} + n_0 e^{\Psi + \lambda} + n_{0w} e^\lambda \left\langle e^{-p_0 |\Psi'| \cos \omega / e_0} \right\rangle_\omega, \quad (40)$$

from where we calculate the parameter  $\lambda$ :

$$e^\lambda = \frac{n_s}{\mathcal{H}}, \quad (41)$$

where the function  $\mathcal{H}$  is related to the finite particle size:

$$\mathcal{H} = 2n_0 \cosh \Psi + \frac{e_0 n_{0w}}{p_0 |\Psi'|} \sinh \frac{p_0 |\Psi'|}{e_0}. \quad (42)$$

In the above derivation of  $\lambda$ , we took into account (see Eq. (19))

$$\left\langle e^{-p_0 |\Psi'| \cos \omega / e_0} \right\rangle_\omega = \frac{e_0}{p_0 |\Psi'|} \sinh \frac{p_0 |\Psi'|}{e_0}. \quad (43)$$

Using Eqs. (33) and (38), we get the following expression for the number density of Langevin dipoles  $n_d(x)$ :

$$n_w(x) = \langle n(x, \omega) \rangle_\omega = n_{0w} e^\lambda \left\langle e^{-p_0 |\Psi'| \cos \omega / \epsilon_0} \right\rangle_\omega. \quad (44)$$

Taking into account Eqs. (41)–(43), it follows from Eq. (44)

$$n_w(x) = \frac{n_{0w} n_s}{\mathcal{H}} \frac{\epsilon_0}{p_0 |\Psi'|} \sinh \frac{p_0 |\Psi'|}{\epsilon_0}. \quad (45)$$

Combining Eqs. (35), (7), and (45) yields polarization:

$$P = -p_0 n_{0w} n_s \frac{\mathcal{F} \left( \frac{p_0 |\Psi'|}{\epsilon_0} \right)}{\mathcal{H}(\Psi, |\Psi'|)}, \quad (46)$$

where the function  $\mathcal{F}(u)$  is defined by Eq. (21). Based on Eq. (46), we can express the permittivity of the electrolyte solution ( $\epsilon$ ) in contact with the planar charged membrane bilayer surface as

$$\epsilon = 1 + \frac{1}{\epsilon_0} \frac{d|P|}{dE} = 1 + n_{0w} n_s \frac{p_0}{\epsilon_0} \frac{d(\mathcal{F}/\mathcal{H})}{dE}, \quad (47)$$

while the corresponding effective permittivity ( $\epsilon_{\text{eff}}$ ) is

$$\epsilon_{\text{eff}} = 1 + \frac{|P|}{\epsilon_0 E} = 1 + n_{0w} n_s \frac{p_0}{\epsilon_0} \frac{\mathcal{F}/\mathcal{H}}{E}, \quad (48)$$

where  $E = |\phi'|$  is the magnitude of the electric field strength.

Inserting the Fermi–Dirac-like distribution functions Eqs. (36), (37), and expression for polarization (Eq. (46)) into Eq. (34), we get the expression for the volume charge density in electrolyte solution

$$\varrho = -2e_0 n_0 n_s \frac{\sinh \Psi}{\mathcal{H}} + n_{0w} p_0 n_s \frac{d}{dx} \left[ \frac{\mathcal{F} \left( p_0 |\Psi'| / \epsilon_0 \right)}{\mathcal{H}} \right], \quad (49)$$

where we took into account also the equation for the parameter  $\lambda$  Eq. (41). Inserting the volume charge density (49) into Poisson equation

$$\Psi'' = -4\pi l_B \varrho / \epsilon_0, \quad (50)$$

we get [12]

$$\Psi'' = 4\pi l_B n_s \left( 2n_0 \frac{\sinh \Psi}{\mathcal{H}} - n_{0w} \frac{p_0}{e_0} \frac{d}{dx} \left[ \frac{\mathcal{F}(p_0 |\Psi'|/e_0)}{\mathcal{H}} \right] \right). \quad (51)$$

The differential equation (51) has two boundary conditions. The first boundary condition is obtained by integration of the differential equation (51):

$$\Psi'(x=0) = -4\pi \frac{l_B}{e_0} \left[ \sigma + n_s n_{0w} p_0 \frac{\mathcal{F}(p_0 |\Psi'|/e_0)}{\mathcal{H}} \Big|_{x=0} \right]. \quad (52)$$

The condition of electroneutrality of the whole system was taken into account. The second boundary condition is

$$\Psi'(x \rightarrow \infty) = 0. \quad (53)$$

## 4.2. Linearized Modified Poisson–Boltzmann Equation

In the approximation of small electrostatic energy and small energy of dipoles in electric field compared to thermal energy, that is, small  $\Psi$  and small  $p_0 |\Psi'|/e_0$ , Eq. (51) can be expanded in Taylor series up to third order to get [12]

$$\Psi'' = \frac{2\Psi + 2\left(-\frac{n_0}{n_s} + \frac{1}{6}\right)\Psi^3 + \frac{n_{0w}}{3n_s} \left(\frac{p_0}{e_0}\right)^2 \Psi \Psi'^2}{\frac{1}{4\pi l_B n_0} + \frac{n_{0w}}{3n_0} \left(\frac{p_0}{e_0}\right)^2 - \frac{n_{0w}}{3n_s} \left(\frac{p_0}{e_0}\right)^2 \Psi^2 + \frac{n_{0w}}{n_0} \left(-\frac{n_{0w}}{6n_s} + \frac{1}{10}\right) \left(\frac{p_0}{e_0}\right)^4 \Psi'^2}. \quad (54)$$

The corresponding boundary condition (52) expanded up to third order is

$$\Psi'(0) = \frac{-\sigma/e_0}{\left[ \frac{1}{4\pi l_B} + \frac{n_{0w}}{3} \left(\frac{p_0}{e_0}\right)^2 \left(1 - \frac{n_0}{n_s} [\Psi(0)]^2 + \mathcal{B}\right) \right]}, \quad (55)$$

where

$$\mathcal{B} = \left(\frac{p_0}{e_0}\right)^2 \left(-\frac{n_{0w}}{6n_s} + \frac{1}{10}\right) [\Psi'(0)]^2, \quad (56)$$



while the effective permittivity (Eq. (48)) can be expressed as

$$\varepsilon_{\text{eff}}(x) = \left( 1 + \frac{4\pi l_B}{3} n_{0w} \left( \frac{p_0}{\varepsilon_0} \right)^2 \left( 1 - \frac{n_0}{n_s} \Psi^2 + \left( -\frac{n_{0w}}{6n_s} + \frac{1}{10} \right) \left( \frac{p_0}{\varepsilon_0} \right)^2 \Psi'^2 \right) \right). \quad (57)$$

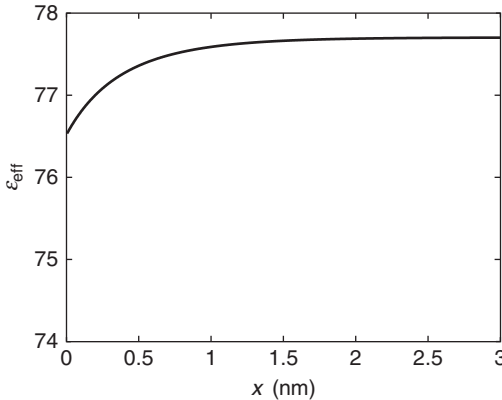
In the limit of very small  $\Psi$  and very small  $p_0|\Psi'|/\varepsilon_0$ , Eq. (57) transforms into the well-known expression

$$\varepsilon_{\text{eff}}(x) = 1 + \frac{n_{0w} p_0^2}{3\varepsilon_0 kT}. \quad (58)$$

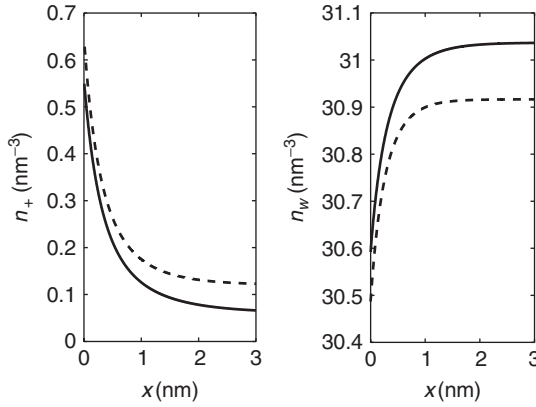
Hereafter, Eqs. (54)–(57) are used to calculate the spatial profile of permittivity of the medium.

Figure 5 shows the spatial variation of permittivity, calculated according to Eq. (57). The dipole moment of a single water (Langevin) dipole was chosen to be 5 Debyes (D) in order to reach the permittivity of pure water 78.5 far away from the charged membrane surface. The bulk water dipole concentration ( $n_{0w}/N_A$ ) was chosen 55 mol/l, where  $N_A$  is Avogadro number.

Figure 6 shows the number densities of counterions ( $n_+$ ) and water (Langevin) dipoles ( $n_w$ ) as functions of the distance from the charged membrane surface. The results are given for two different bulk concentrations of the involved ions. The number density of counterions decreases



**Figure 5** Calculated permittivity close to charged bilayer membrane surface. The dipole moment of water dipoles  $p_0 = 5D$ , the bulk concentration of water dipoles  $n_{0w}/N_A = 55$  mol/l, surface charge density  $\sigma = -0.05$  As/m<sup>2</sup>, the width of a single lattice site  $a_s = 0.318$  nm, the bulk concentration of ions is  $n_0/N_A = 0.1$  mol/l (adapted from [29]).



**Figure 6** Number densities of counterions ( $n_+$ ) and Langevin dipoles ( $n_w$ ) as functions of the distance from the charged bilayer membrane surface. The bulk concentration of ions: full line  $n_0/N_A = 0.1$  mol/l and dashed line  $n_0/N_A = 0.2$  mol/l. Model parameters: dipole moment of water  $p_0 = 5D$ , bulk concentration of Langevin dipoles  $n_{0w}/N_A = 55$  mol/l, membrane surface charge density  $\sigma = -0.05$  As/m<sup>2</sup>. The width of a single lattice site  $a_s = 0.318$  nm.

with increasing distance from the charged membrane surface. The number density of Langevin dipoles (i.e., water molecules) increases with increasing distance from the charged membrane surface and reaches a plateau value far away from the charged surface. The depletion of water molecules near the charged membrane surface also helps that water molecules can better organize their hydrogen bonding network without ions; therefore it is favorable that ions which disrupt the water–hydrogen–bonded water network are moved from the bulk towards the charged membrane surface [13]. Near the charged membrane surface, the number density of coions is negligible when compared with the number density of counterions. The thickness of EDL increases with decreasing bulk concentration of ions.

The average cosine of the angle  $\omega$  between the dipole vector of Langevin dipoles and the axis perpendicular to the metal surface is given by equation

$$\langle \cos \omega \rangle_B = \frac{\langle \cos \omega e^{-p_0 |\Psi'|} \cos \omega / \epsilon_0 \rangle}{\langle e^{-p_0 |\Psi'|} \cos \omega / \epsilon_0 \rangle_\omega} = -\mathcal{L}(p_0 |\Psi'| / \epsilon_0), \quad (59)$$

where  $\langle \dots \rangle_B$  means the averaging over all angles  $\omega$  weighted by Boltzmann factor (see Eq. (7)). The average cosine  $\langle \cos \omega \rangle_B$  as a function of the distance from the charged surface for different surface charge densities and bulk counterion number densities, is shown in Fig. 7. Figure 7 shows that the Langevin

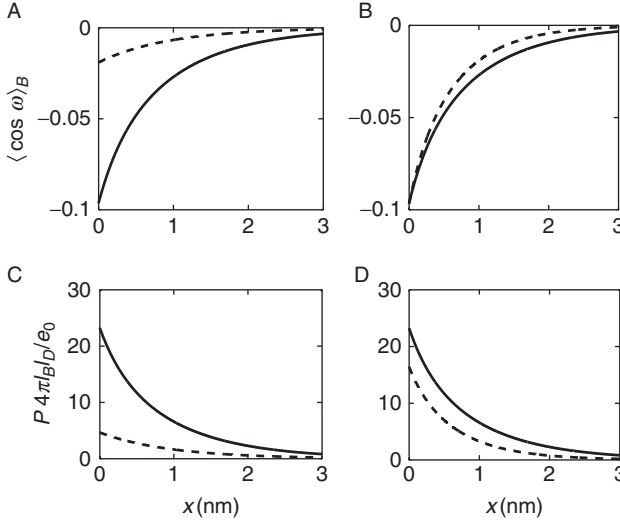


**Figure 7** Average cosine of angle of Langevin dipoles (A, B) and polarization (C, D) as functions of the distance from the charged membrane surface. (A) and (C)  $n_0/N_A = 0.1$  mol/l, surface charge densities  $\sigma = -0.05$  As/m<sup>2</sup> (full line) and  $\sigma = -0.01$  As/m<sup>2</sup> (dashed line). Figures B and D:  $\sigma = -0.05$  As/m<sup>2</sup>, bulk salt concentrations  $n_0/N_A = 0.1$  mol/l (full line),  $n_0/N_A = 0.2$  mol/l (dashed line). The width of a single lattice site  $a_s = 0.318$  nm (adapted from [29]).

dipole moment vectors at the charged membrane surface are predominantly oriented towards the surface. Far away from the charged membrane surface all orientations of dipoles are equally probable; therefore  $\langle \cos \omega \rangle_B = 0$  (see Fig. 7). The absolute value of  $\langle \cos \omega \rangle_B$  increases with increasing  $\sigma$  corresponding to stronger orientation of Langevin dipoles. Due to stronger screening, the absolute value of  $\langle \cos \omega \rangle_B$  is decreasing with increasing  $n_0$ .

## 5. PHENOMENOLOGICAL MODEL OF SPATIAL VARIATION OF PERMITTIVITY AND THE MEMBRANE SURFACE POTENTIAL

We have shown that close to the charged membrane surface the permittivity profile (Fig. 5) is mainly determined by the depletion of water dipoles due to accumulated counterions (Fig. 6) and by orientational ordering of water dipoles (Fig. 7). In this section, the space dependency of permittivity, previously determined only at small  $\Psi$  and small  $|\Psi'|$  (i.e., at small potential, see Fig. 5), is assumed to be more pronounced. In the phenomenological model presented in this section, we assume a strong

space variation of the permittivity, which corresponds to large magnitude of the surface charge density (see also Fig. 4). Based on the results given in Figs. 4 and 5, the space dependency of the effective permittivity is approximately described by a simple step function. Similarly, as in Section 4, the volume charge density in an electrolyte solution is written as

$$\rho(x) = \sum_i v_i e_0 n_i(x), \quad (60)$$

where for monovalent ions, the valence  $v_i$  is

$$v_+ = 1, \quad v_- = -1. \quad (61)$$

The ions are assumed to be distributed according to the Boltzmann distribution [5,6]:

$$n_i(x) = n_0 \exp(-v_i e_0 \phi(x)/kT). \quad (62)$$

According to the schematic on Fig. 8, the permittivity of the electrolyte solution is approximately described by a step function (see Fig. 9):

$$\varepsilon(x) = \begin{cases} \varepsilon_2, & x < a, \\ \varepsilon_1, & x \geq a. \end{cases} \quad (63)$$

By inserting Eqs. (60)–(63) into Poisson's equation, we obtain the PB differential equation (see also [5,6]) corresponding to two different regions:

$$\frac{d^2\phi}{dx^2} = \begin{cases} \frac{2e_0 n_0}{\varepsilon_2 \varepsilon_0} \sinh(e_0 \phi(x)/kT), & 0 \leq x < a, \\ \frac{2e_0 n_0}{\varepsilon_1 \varepsilon_0} \sinh(e_0 \phi(x)/kT), & a \leq x < \infty. \end{cases} \quad (64)$$

The boundary condition at  $x = 0$  is consistent with the condition of electroneutrality of the whole system:

$$\left. \frac{d\phi}{dx} \right|_0 = -\frac{\sigma_{\text{eff}}}{\varepsilon_2 \varepsilon_0}. \quad (65)$$

The validity of Gauss law at  $x = a$ , respectively, is fulfilled by the following equation:

$$\varepsilon_2 \left. \frac{d\phi}{dx} \right|_{a-} = \varepsilon_1 \left. \frac{d\phi}{dx} \right|_{a+}. \quad (66)$$

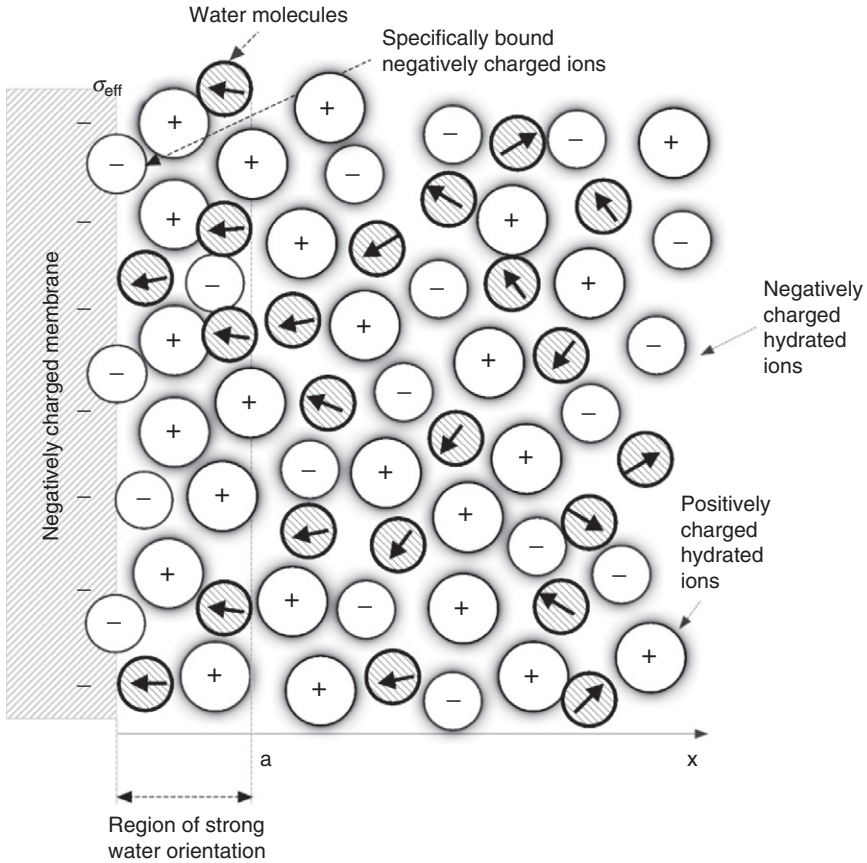


**Figure 8** Schematic figure of electrical double layer near the negatively charged planar membrane surface. Here  $a$  is the region of strong water orientation, where the permittivity substantially differs from the bulk value. The surface charge density  $\sigma_{\text{eff}}$  incorporates the negatively charged surface as well as the specifically bound negatively charged ions.

Due to the screening effect of the negatively charged membrane surface caused by the accumulated cations, we assume that far away from the charged metal surface the strength of electric field tends to zero:

$$\left. \frac{d\phi}{dx} \right|_{\infty} = 0. \quad (67)$$

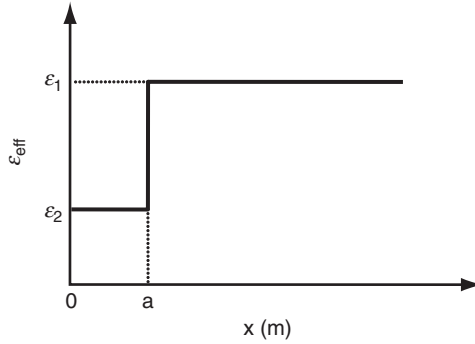


**Figure 9** Model of the space variation of permittivity in electrolyte solution near the charged membrane surface assuming a step function. Here  $a$  is the region of strong orientation of water molecules. The value of  $\varepsilon_1 \cong 78.5$  corresponds to the bulk value, while  $\varepsilon_2$  is in the range of 10 – 60.

Equations (64) are rewritten in dimensionless form:

$$\frac{d^2\Psi}{d\xi^2} = \begin{cases} 2K \sinh(\Psi), & 0 \leq \xi < 1, \\ 2L \sinh(\Psi), & 1 \leq \xi < \infty, \end{cases} \quad (68)$$

where the reduced potential  $\Psi(x) = e_0 \phi(x)/kT$  is defined as previously (Eq. (3)) and the reduced length is

$$\xi = \frac{x}{a}, \quad (69)$$

while the constants are defined as

$$K = \frac{e_0^2 n_0 a^2}{\varepsilon_2 \varepsilon_0 kT}, \quad L = \frac{e_0^2 n_0 a^2}{\varepsilon_1 \varepsilon_0 kT}. \quad (70)$$

Respectively, the boundary conditions for the dimensionless case are

$$\left. \frac{d\Psi}{d\xi} \right|_0 = -\frac{\sigma_{\text{eff}} a e_0}{\varepsilon_2 \varepsilon_0 kT}, \quad (71)$$

$$\varepsilon_2 \left. \frac{d\Psi}{d\xi} \right|_{-1} = \varepsilon_1 \left. \frac{d\Psi}{d\xi} \right|_{1+}, \quad (72)$$

$$\left. \frac{d\Psi}{d\xi} \right|_{\infty} = 0. \quad (73)$$

In addition to Eqs. (71)–(73), we consider also the continuity of the electric potential at  $x = a$ . Hereafter, we have a closer look at the derivation of the solutions of Eq. (68). Equation (68) is multiplied at both sides by  $2 \frac{d\Psi}{d\xi}$

$$\frac{d}{d\xi} \left( \frac{d\Psi}{d\xi} \right)^2 = 2 \frac{d\Psi}{d\xi} \frac{d^2\Psi}{d\xi^2}. \quad (74)$$

By taking into account the continuity of the electric potential at  $x = a$  and after integration we get

$$\int d \left( \frac{d\Psi}{d\xi} \right)^2 = \int 4K \sinh(\Psi) d\Psi, \quad 0 \leq \xi < 1, \quad (75)$$

$$\int d \left( \frac{d\Psi}{d\xi} \right)^2 = \int 4L \sinh(\Psi) d\Psi, \quad 1 \leq \xi < \infty. \quad (76)$$

These transformations lead to

$$\frac{d\Psi}{d\xi} = \begin{cases} \sqrt{C + 4K \cosh\Psi}, & 0 \leq \xi < 1, \\ -\sqrt{8L \sinh(\Psi/2)}, & 1 \leq \xi < \infty, \end{cases} \quad (77)$$

where

$$C = \left( \frac{\sigma_{\text{eff}} \epsilon_0 a}{\epsilon_2 \epsilon_0 k T} \right)^2 - 4K \cosh\Psi(0). \quad (78)$$

Applying the boundary condition (72) and taking into account Eqs. (77) and (78) yields

$$\epsilon_2 \left( \left( \frac{\sigma_{\text{eff}} \epsilon_0 a}{\epsilon_2 \epsilon_0 k T} \right)^2 - 4K [\cosh\Psi(0) - \cosh\Psi(1)] \right)^{1/2} = -\epsilon_1 \sqrt{8L} \sinh(\Psi(1)/2). \quad (79)$$

Now we proceed with the solution of Eq. (77) in the interval  $1 \leq \xi < \infty$ . We first rearrange the corresponding expression from Eq. (77) as

$$d\xi = \frac{-d\Psi}{\sqrt{8L} \sinh \frac{\Psi}{2}}. \quad (80)$$

Integrating Eq. (80)

$$\int_1^\xi d\xi = -\frac{1}{\sqrt{8L}} \int_{\Psi(1)}^{\Psi(\xi)} \frac{d\Psi}{\sinh \frac{\Psi}{2}} \quad (81)$$

gives the following solution:

$$\xi - 1 = \frac{1}{\sqrt{2L}} \ln \left( \frac{\tanh \frac{\Psi(1)}{4}}{\tanh \frac{\Psi}{4}} \right). \quad (82)$$

By transforming Eq. (82), we get the final result for  $\Psi$  in the form:

$$\Psi = 4 \tanh^{-1} \left( \tanh \frac{\Psi(1)}{4} \exp \left( \sqrt{2L}(1 - \xi) \right) \right), \quad 1 \leq \xi < \infty. \quad (83)$$

It follows from Eq. (83)

$$\Psi(0) = 4 \tanh^{-1} \left( \tanh \frac{\Psi(1)}{4} \exp \left( \sqrt{2L} \right) \right). \quad (84)$$

Eqs. (79) and (84) are two equations for two unknown quantities  $\Psi(0)$  and  $\Psi(1)$ . Eqs. (79) and (84) can be solved numerically to determine the surface electric potential  $\phi(0) = \Psi(0)kT/e_0$ . Figure 10 shows the electric membrane surface potential  $\phi(0)$  as a function of the relative permittivity in the highly ordered region of water molecules ( $\epsilon_2$ ) (see Fig. 9). It becomes clear that the absolute value of the electric potential increases with the decrease of the permittivity  $\epsilon_2$ .

## 6. CONCLUSIONS

Most of the models describing the EDL assume that the permittivity in the whole system is constant [5–7]. The classical PB theory does not consider the solvent structure. Therefore the PB theory has been upgraded by hydration models, where the interplay between solvent polarization and diffuse double layer takes place [10,12,18,22,30,31]. The study of the orientational ordering of dipoles at the charged surface has shown that dipoles predominantly orient perpendicularly to the charged surface [12]. Langevin dipoles were introduced into the PB theory to study the polarization of the solvent and the space dependency of the permittivity close to the charged membrane surface [12,18,29]. The spatial decay of the solvent polarization for increasing distance from the charged membrane surface was predicted [12].

The presence of ions changes the permittivity of the electrolyte solution [12,13,18]. Recently, the modified PB equation, taking into account the finite volumes of ions, was solved numerically in the limit of small electric



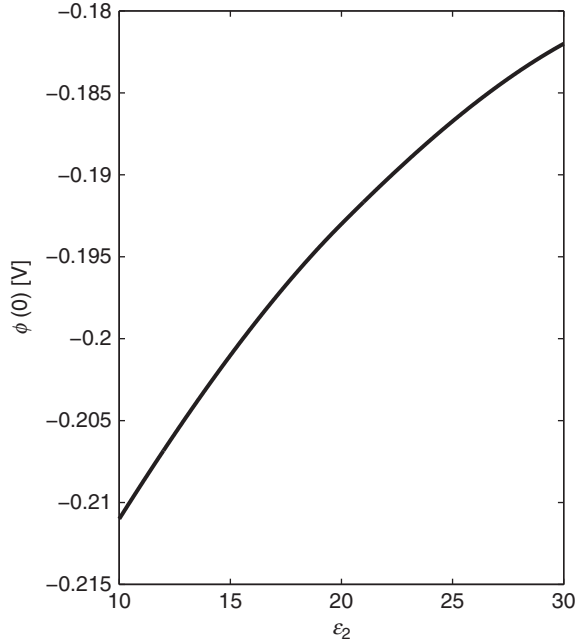


**Figure 10** Membrane surface potential  $\phi(0)$  as a function of the permittivity in the ordered region of water molecules ( $\epsilon_2$ ) (see Figs. 8 and 9) for surface charge density:  $\sigma_{\text{eff}} = -0.4 \text{ As/m}^2$ , thickness of the ordered water layer  $a = 0.2 \text{ nm}$ , bulk salt concentration  $n_0/N_A = 0.1 \text{ mol/1}$ , permittivity of the region  $x > a$ :  $\epsilon_1 = 78.5$ .

potential and small electric field, where the dipolar nature of water molecules was introduced by Langevin dipoles [12]. The dependence of the permittivity as a function of the electric potential was given analytically (Eq. (48)), while the spatial dependency of the effective permittivity was calculated numerically in the limit of small electric potential and small electric field (Fig. 5) [12].

In this chapter, the orientational ordering of water dipoles and the excluded volume effect were explicitly taken into account in the described modified PB model in order to estimate the space variation of the permittivity in the vicinity of a charged membrane surface in contact with an electrolyte solution [12,29]. In the limit of small electric potential and small electric field, it was shown that the dipole moment vectors of water molecules at the charged membrane surface are predominantly oriented towards the negatively charged surface, while all orientations of water dipoles far away from the charged membrane surface are equally probable (Fig. 7). It was shown that the permittivity profile close to the charged membrane surface may be significantly influenced by the depletion of water molecules due to accumulation of counterions. Due to strong accumulation

of counterions near the charged membrane surface at higher surface charge densities (Figs. 3 and 6), it can be anticipated that the permittivity near the charged membrane surface may be significantly decreased at high magnitude of the surface charge density of the membrane. Therefore, a simple phenomenological model assuming a step function for the space variation of the permittivity was introduced to study the influence of the space variation of the permittivity on the membrane surface potential at higher magnitudes of surface charge density. Both models (phenomenological and statistical mechanical) complement each other, since the phenomenological model is not so restricted to small magnitudes of the surface charge, making it a good supplement to the statistical mechanical approach. Although for larger surface charge density (as for example in Figs. 3, 4 and 10) the so-called electrostatic coupling parameter [22] is well above 1, we expect that the conclusions based on presented results are qualitatively correct and may help to better understand the combined role of water ordering and finite size of ions in the properties of the electric double layer.

## REFERENCES

- [1] H. Helmholtz, Studien über elektrische Grenzschichten, *Ann. Phys.* 243(7) (1879) 337–382.
- [2] M.G. Gouy, Sur la constitution de la charge électrique à la surface d'un électrolyte, *J. Phys. (France)* 9 (1910) 457–468.
- [3] D.L. Chapman, A contribution to the theory of electrocapillarity, *Philos. Mag.* 25 (1913) 475–481.
- [4] O. Stern, Zur Theorie der elektrolytischen Doppelschicht, *Z. Elektrochem.* 30 (1924) 508–516.
- [5] S. Safran, *Statistical Thermodynamics of Surfaces, Interfaces and Membranes*, Addison-Wesley Publishing Company, Colorado, 1994.
- [6] S. McLaughlin, The electrostatic properties of membranes, *Ann. Rev. Biophys. Chem.* 18(1989) (1989) 113–136.
- [7] J.N. Israelachvili, H. Wennerström, Role of hydration and water structure in biological and colloidal interactions, *Nature* 379 (1996) 219–225.
- [8] V. Kralj-Iglič, A. Iglič, A simple statistical mechanical approach to the free energy of the electric double layer including the excluded volume effect, *J. Phys. II (France)* 6 (1996) 477–491.
- [9] S. Lamperski, C.W. Outhwaite, Exclusion volume term in the inhomogeneous Poisson-Boltzmann theory for high surface charge, *Langmuir* 18 (2002) 3423–3424.
- [10] D.W.R. Gruen, S. Marčelja, Spatially varying polarization in water, *J. Chem. Soc. Faraday Trans. II* 79 (1983) 225–242.
- [11] H.J. Butt, K. Graf, M. Kappl, *Physics and Chemistry of Interfaces*, Wiley-VCH, Weinheim, 2003.
- [12] A. Iglič, E. Gongadze, K. Bohinc, Excluded volume effect and orientational ordering near charged membrane surface in solution of ions and Langevin dipoles, *Bioelectrochemistry* (2010), doi:10.1016/j.bioelechem.2010.05.003.
- [13] M. Manciu, E. Ruckenstein, The polarization model for hydration/double layer interactions: the role of the electrolyte ions, *Adv. Coll. Int. Sci.* 112 (2004) 109–128.

- [14] D.H. Mengistu, K. Bohinc, S. May, The Poisson-Boltzmann model in a solvent of interacting Langevin dipoles, *Europhys. Lett.* 88 (2009) 14003.
- [15] S. Maset, K. Bohinc, Orientations of dipoles restricted by two oppositely charged walls, *J. Phys. A* 40 (2007) 11815–11826.
- [16] S.L. Carnie, D.Y.C. Chan, J. Stankovich, Computation of forces between spherical colloidal particles-nonlinear Poisson-Boltzmann theory, *J. Coll. Interface Sci.* 165 (1994) 116–128.
- [17] E. Gongadze, V. van Rienen, V. Kralj-Iglič, A. Iglič, Impact of spacial variation of permittivity on the electrical properties of implants' titanium surface, *Comp. Meth. Biomech. Biomed. Eng. A* (submitted).
- [18] A. Abrashkin, D. Andelman, H. Orland, Dipolar Poisson-Boltzmann equation: ions and dipoles close to charge surface, *Phys. Rev. Lett.* 99 (2007) 077801.
- [19] V. Freise, Zur Theorie der Diffusendoppelschicht, *Z. Elektrochem.* 56 (1952) 822–827.
- [20] M. Eigen, E. Wicke, The thermodynamics of electrolytes at higher concentrations, *J. Phys. Chem.* 58 (1954) 702–714.
- [21] C.W. Outhwaite, A modified Poisson-Boltzmann equation for the ionic atmosphere around a cylindrical wall, *J. Chem. Soc., Faraday Trans. II* 82 (1986) 789–794.
- [22] M.Z. Bozont, M.S. Kilic, B. Storey, A. Ajdari, Towards an understanding of induce-charge electro kinetics at large applied voltages in concentrated solutions, *Adv. Coll. Int. Sci.* 152 (2009) 48–88.
- [23] T. Das, D. Bratko, L.B. Bhuiyan, C.W. Outhwaite, Modified Poisson-Boltzmann Theory Applied to Linear Polyelectrolyte Solutions, *J. Phys. Chem.* 99 (1995) 410–418.
- [24] P.M. Biesheuvel, M. van Soestbergen, Counterion volume effects in mixed electrical double layers, *Coll. Int. Sci.* 316 (2007) 490–499.
- [25] L.B. Bhuiyan, C.W. Outhwaite, Comparison of exclusion volume corrections to the Poisson-Boltzmann equation for inhomogeneous electrolytes, *J. Coll. Int. Sci.* 331 (2009) 543–547.
- [26] M. Manciu, E. Ruckenstein, Lattice site exclusion effect on the double layer interaction, *Langmuir* 18 (2002) 5178–5185.
- [27] I. Borukhov, D. Andelman, H. Orland, Steric effects in electrolytes: a modified Poisson Boltzmann equation, *Phys. Rev. Lett.* 79 (1997) 435–438.
- [28] K. Bohinc, V. Kralj-Iglič, A. Iglič, Thickness of electrical double layer. Effect of ion size, *Electrochim. Acta* 46 (2001) 3033–3040.
- [29] K. Bohinc, E. Gongadze, V. Kralj-Iglič, U. van Rienen, A. Iglič, Metal surface in contact with electrolyte solution - influence of spatial variation of dielectric constant, *Electr. Rev.* (in print).
- [30] E. Ruckenstein, M. Manciu, The coupling between the hydration and double layer interactions, *Langmuir* 18 (2002) 7584–7593.
- [31] M.L. Berkowitz, D.L. Bostick, S. Pandit, Aqueous solutions next to phospholipid membrane surfaces: Insights from Simulations, *Chem. Rev.* 106 (2006) 1527–1539.

# WHAT IS THE DIFFERENCE BETWEEN A SUPPORTED AND A FREE BILAYER? INSIGHTS FROM MOLECULAR MODELING ON DIFFERENT SCALES

Chenyue Xing<sup>1</sup> and Roland Faller<sup>2,\*</sup>

## Contents

1. Introduction	128
2. Modeling of Lipid Bilayers	132
2.1. Models on Different Length Scales	132
2.2. Free Bilayers	133
2.3. Supported Bilayers	134
3. Observables for Characterization of Bilayer Systems in Molecular Modeling	136
4. Characteristics of Supported and Unsupported Bilayers	140
4.1. Visualization	140
4.2. Density Asymmetry	142
4.3. Structure	143
4.4. Pressure Distribution	145
4.5. Water Layer Thickness and Entropic Repulsion	146
4.6. Dynamics	147
4.7. Mechanical Properties	149
5. Influence of Corrugation	150
6. Conclusions and Outlook	151
Acknowledgments	152
References	153

\* Corresponding author. Tel.: +530-752-5839; Fax: +530-752-1031  
E-mail address: [rfaller@ucdavis.edu](mailto:rfaller@ucdavis.edu)

<sup>1</sup> MAP Pharmaceuticals Inc., Mountain View, California, USA

<sup>2</sup> Department of Chemical Engineering & Materials Science, University of California-Davis, One Shields Avenue, Davis, California, USA

## Abstract

Supported lipid bilayers are an abundant research platform for understanding the behavior of real cell membranes as they allow for mechanical stability and enable characterization techniques not reachable otherwise. However, in computer simulations, these systems have been studied only rarely. Here, we discuss systematically the changes that a support inflicts on a phospholipid bilayer, using molecular modeling on different length scales. We characterize density and pressure profiles as well as the density imbalance induced by the support. It turns out that the changes in pressure profile are strong enough that protein function should be impacted leading to a previously neglected mechanism of transmembrane protein malfunction in supported bilayers. We also discuss the diffusion and reorientation behavior and characterize the influence of different corrugations of the support. The free energy of transfer of phospholipids between the proximal (close to the surface) and distal leaflet of a supported membrane shows that there is at equilibrium about a 3–4% higher density in the proximal leaflet.

## 1. INTRODUCTION

Cell membranes are crucial for the biological functions of cells as they provide the compartmentalization needed for life to work [1]. Thus, it is not surprising that many model systems have been devised to understand these complex entities in a simplified fashion [2]. One such model system is a supported lipid bilayer (SLB) where lipids form a bilayer membrane as in cell membranes but at the same time they are supported by a solid substrate. There are actually several different techniques to manufacture such systems [2]. In these models, proteins are often not included and the number of different lipids is limited for simplicity.

Vesicle fusion onto solid substrates [3] and Langmuir Blodgett deposition are typical techniques used in the lab to make SLBs [2, 4]. Despite significant simplifications, SLBs maintain crucial structural and dynamic properties of biological membranes and are valuable tools. SLBs have been shown to be stable on a diverse range of solid substrates [5–8]. Several techniques aim at cushioning bilayers on the solid support [9]. This, however, will not be discussed here.

SLBs are not only used as model systems for understanding of cellular and intracellular membranes but they also have high technological importance due to their applicability in biosensors [10–13] where the solid surface lends stability to the membrane which is then normally used as a two-dimensional (2D) solvent for proteins. Hence, the proper functioning of the protein has to be ensured. It is well known that proteins often are not functional in proximity to a surface [12, 13]. There may be direct and

indirect influences on the protein. Only the indirect ones are of interest here as they are mediated by the membrane. We need to understand the surface membrane interactions to alleviate any detrimental effects on proteins.

Although SLBs are widely used as model systems, there is experimental evidence that the structure and phase behavior of supported bilayers is different from their free counterparts [14]. One example is that alcohols and other anesthetics can induce interdigitation in biomembranes. This has been established for a myriad of model systems like giant unilamellar vesicles (GUVs) [15] which are the closest experimental model system to a truly free bilayer as well as multilamellar dispersions [16], and supported bilayers [17]. The formation of an interdigitated phase under alcohol is undisputed, but the alcohol concentration needed to induce this phase varies significantly between “free” and supported bilayer studies.

Between a hydrophilic solid substrate and the bilayer one always finds a water layer. So much is undisputed and experimentally well established [18]. The structure and thickness of this layer, however, are a matter of significant debate. This layer has been reported to be between 0.5 and 2 nm thick as shown by proton NMR, neutron reflectivity, and fluorescence interference-contrast microscopy results [18–23].

Actually, real cell membranes are not free lipid bilayers as they are tied to the cytoskeleton which lends a particular type of support. The direct membrane–cytoskeleton interactions cannot be revealed by SLBs but we can suspect that general physical mechanisms may be similar.

Generally, despite the many applications of SLBs it is far from understood how the membrane changes when it is supported by a hard substrate. Experimentally it is almost impossible to address local changes as extremely high resolution data would be required. Nonetheless, this understanding is critical if the full potential of SLBs as biomimetic platform has to be explored. In this review, we will address the fundamental differences and similarities between supported and unsupported lipid bilayers as they have been elucidated by recent biomolecular modeling.

Molecular simulations, especially Molecular Dynamics, have become a powerful and ubiquitous tool to reveal structures, dynamics, and mechanisms of biomolecules. They have been performed for a diverse spectrum of biomembranes composed of different lipids, mainly phospholipids and sterols [24–33]. Our understanding of unsupported lipid bilayers relies heavily on a myriad of MD simulations [34–38]. The main advantage of simulations over experiments is the direct access to particle positions and momenta. Therefore, the structure and dynamics are fully characterized as long as the underlying model is reliable. The molecular models for lipids have achieved a great level of maturity and the confidence range and limitations of most models are characterized. Also, not only averages or local averages can be accessed but the full distribution of any property can be measured with spatial and temporal resolution. So, molecular simulations

and SLBs are complimentary powerful tools to provide insights into complex biological systems.

It is striking that although SLBs have been extensively studied in experiments, they have been largely neglected in simulations and only very recently a few simulations have appeared [39–46]. With their unparalleled access to high resolution atomic information simulations are ideally suited to address the changes a support inflicts on a membrane. As these changes are expected on a wide variety of length scales, there is an urgent need for supported bilayer models on all scales. We present a summary of molecular simulations on a variety of length scales to study SLB systems and we discuss various properties of the lipids supported on different model surfaces.

The bilayer consisting of DPPC (dipalmitoylphosphatidylcholine) lipids is probably from a simulation standpoint the most studied and best understood. It therefore comes as no surprise that the first specific studies of supported bilayers have used this system as well [39, 42]. Heine et al. used an atomistic model based on an unsupported DPPC bilayer [47]. Xing and Faller studied a system derived from an unsupported DPPC bilayer using the Martini model (V 1.4) [48]. The system was in the liquid  $L_\alpha$  state where most simulations have been performed. This state is a fluid lipid bilayer. So we have a 2D fluid arrangement of lipids. Technically, the system as a whole is a smectic liquid crystal as the layering is normal to the membrane. The temperature was above the main phase transition temperature of DPPC. The area per molecule was fixed at the area determined by simulations of unsupported DPPC bilayers. Due to 3D periodic boundary conditions, the system is effectively an infinite stack of support, water, lipids, water and then repeated by the support. This is the typical arrangement (see Fig. 1). One often does not exclude any interactions coming from periodic images through the support as long as they are within the cutoff. Other possibilities would be to introduce vacuum layers or additional layers of support. It turns out, however, that within the approximations one has to make anyway in such coarse-grained models this does not play an important role [42].

Simulations of free phospholipid membranes are typically performed under vanishing surface tension by simply performing simulations under constant pressure with independently fluctuating directions. In a SLB this is in general not possible. We find strong effects on the density and pressure profile. It has been realized that the pressure distribution within a membrane is crucial for protein function. Some simulations indicate a change in pressure profile within the membrane. This is highly significant, as lateral pressure has been connected to the dysfunctionalization of proteins [49]. We suspect that this pressure change is one of the fundamental reasons for protein configurational changes in supported membranes.

A key issue in the study and further development of biomimetic structures for biochemical sensors is the effect of the underlying support on

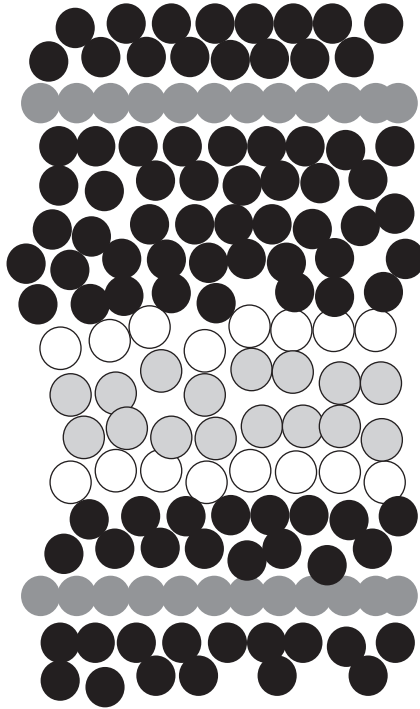


**Figure 1** Sketch explaining the interactions across periodic boundary conditions. The black circles represent water molecules, the white circles are lipid headgroups, the striped circles represent the tails, and the light gray circles represent the surface. The resolution is coarse-grained such that every circle represents several atoms.

membrane organization. In order to mimic cell membranes, certain structural and dynamic features have to be reliably reproduced in the artificially constructed lipid bilayers. It is critical for membranes to exhibit the correct thermodynamic phase, namely a fluid lipid bilayer, to respond to environmental stress such as temperature and pressure changes.

There are several important driving forces in the formation of supported membranes which have to be considered in any modeling attempt. The interactions of vesicles and resulting bilayers with surfaces is a subtle balance between van der Waals, electrostatic, hydration, and steric forces [50] as the interaction of vesicles and the surface plays the determining role in the successful fusion and spreading of lipid bilayers. Hydrophilic (or more correctly lipophilic) surfaces that have strong attractive interactions with lipid headgroups lead often to bilayer formation. The formation process has experimentally been studied by atomic force microscopy (AFM) [3], quartz crystal microbalance [51], and single vesicle fluorescence assays [52]. The details of this process and subsequently the governing interactions are,



however, not understood. One open question in the interaction between membranes and a support is the structure and dynamics of the water cushion underneath the membrane.

A model which is very appropriate to study SLBs is the Martini model of lipid bilayers [48, 53] where 3–5 nonhydrogen atoms are represented by one interaction site allowing simulations of systems of several thousand lipid molecules for several microseconds. To simulate SLBs the model had to be slightly adapted in order to avoid freezing of water at the surface [54].

## 2. MODELING OF LIPID BILAYERS

As biomembranes have a variety of characteristic length scales, we need to use different models in order to address these scales. We also expect the effects of the support on many scales. Therefore, let us first discuss a few common membrane models. This list is not meant to be exhaustive and the interested reader is referred to several recent reviews on multiscale modeling or coarse-graining of biomembranes [55, 56].

### 2.1. Models on Different Length Scales

For modeling biomembranes, mainly three levels of details have been used. The most detailed degree is atomistic modeling where real atoms are represented—at least all the heavy atoms. Combining atoms into larger interaction centers, we arrive next at a family of models where about five heavy atoms are combined [53, 57–59] and one can study collective phenomena of membranes. If these models are still too slow or complex, one resorts to water-free models [60–63]. These models still contain individual lipids; however, the number of interaction sites per lipid is often less than five. Water is replaced by interaction potentials which lead to a self-assembly of lipids into a fluid bilayer without explicit solvent. We will not discuss field based models here.

#### 2.1.1. Atomistic models

Most molecular simulations of lipid bilayers are performed in atomistic detail [24, 26, 32, 47, 64–68]. Atomistic models accurately describe not only the molecular structure, but also the intra- and intermolecular interactions such as chemical bonds, electrostatic, and van der Waals interactions. In general, simulations employ a timestep as short as one-tenth of the period of the fastest mode in the system. This fastest mode in an atomistic model is normally the stretching or bending of a covalent bond implying timesteps of about 1 fs. Such models are able to study membranes of a few tens of nanometers over about a hundred nanoseconds using currently available computing facilities. Direct comparison with experiments (e.g., NMR [69])

has shown the effectiveness and accuracy of such models. Some atomistic attempts to model SLBs have been reported [39, 45, 46].

### 2.1.2. Explicit water coarse-grained models

There is a family of molecular models which have a degree of detail of about 3–5 heavy atoms per interaction center. These are generally referred to as coarse-grained models [53, 57–59]. The most abundantly used model on this length scale is probably the Martini model developed over several years [48, 53, 70] which uses one interaction site to represent four heavy atoms on average. This model is relevant here as it has a variant which has been adapted for modeling SLBs [42].

### 2.1.3. Water-free models

If one is interested in the behavior of the bilayer alone, the solvent—typically water—is essentially nothing but dead weight on the simulation time. However, the solvent plays one crucial role: only the hydrophilic–hydrophobic interactions make the self-assembly of the bilayer possible. So, in any water-free model one needs to represent these effects implicitly in the lipid potentials.

As the hydrophilic–hydrophobic interactions are removed the bilayer structure has to be maintained by including additional forces to ensure that the bilayer structure has the lowest free energy. Some models also include planarity potentials [59] that segregate tail particles and polar head particles to different sides of an imaginary plane or by using modified cohesive forces among tail particles in order to keep the system planar [60]. Representations of three to seven particles per molecule are common [55, 59–63, 71]. Although two-particle amphiphiles which are obviously the minimum number of interactions if one sticks to radially symmetric potentials were some of the earliest self-assembling structures to be treated in solvent-free simulations of soft materials [72], three-particle lipid representations have become quite popular recently [60, 61]. Cooke and Deserno presented a three-particle coarse-grained model [60] which uses only two types of interactions for one lipid molecule: a simple repulsive interaction for polar–polar (head–head) and polar–nonpolar (head–tail) particles and a long range attraction between the tails to ensure that the bilayer self-assembles and stays fluid. This model has been used to model SLBs [40].

## 2.2. Free Bilayers

As we focus here on the differences of supported bilayers to free bilayers as elucidated by molecular modeling, we need to briefly summarize some typical results for free bilayers. We can stay very brief as there are many reviews in this field [24, 55, 56, 73]. Below we will introduce a number of observables which are commonly used to describe both—free and supported—bilayers.

Many simulations focus on the structure of the membrane and its dependence on lipid composition. Generally, the 2D fluidity and the transversal structure are well reproduced in comparison to experiment. Free membranes are in equilibrium symmetric if the fluid on the two sides is the same. Also, the interplay between structure, dynamics, and phase behavior has been deduced such that we expect that as soon as the membrane structure is changed dynamics and phase behavior change as well.

### 2.3. Supported Bilayers

Recently, simulations of supported lipid membranes were carried out by several groups using different models [39, 40, 42–46]. Very few are in atomistic details [39, 45, 46]. Simulations using a variant of the Martini model have been performed to larger extent [42–44]. Simulations of up to 512 lipids and for several microseconds have become standard. It has been shown that the equilibration of the water layer between substrate and bilayer takes several microseconds which mean that a coarse-grained model was essential for the study of supported bilayer systems. Roark and Feller recently circumvented that problem in an atomistic study by drilling a hole into the support [45].

If we want or need to model supported bilayers, we clearly need to think how to model the substrate. As already mentioned, a variety of well tested lipid models on a variety of scales are available [56]. As SLBs are a very young field of modeling, this is not the case for the substrate and particularly for the substrate–lipid interaction. There are a few additional decisions one has to make in order to model the substrate. But first it is obvious that the support model has to be on the same degree of detail as the lipid model. If we have a fully atomistic lipid model, it is recommended that also the support will be modeled in atomistic detail. This immediately mandates that we focus not only on the generic type of support but also on the specific chemistry.

On the atomistic level one might be tempted to just use an atomistic surface model off the shelf and combine it with the lipid and water models of choice. However, combination of independently developed models is often problematic and needs to be evaluated carefully. Therefore, a good approach is to use a model which ideally has been tested in its interaction with water and then adapt it to the particular needs.

Typically, a defect-free lattice is used as support in atomistic simulations. As mentioned above, there is a wide variety of solid supports that have been studied experimentally [74]; so we have to restrict ourselves to a few specific examples. The simplest supports are homoatomic support structures, specifically carbon and silicon have been modeled. These are admittedly experimentally not the most popular supports but the simplest ones being actually used. Mica or glass—popular support materials—are structurally and chemically more complex. The homoatomic models use a hexagonal lattice with an

interatomic distance of 0.14 nm for graphite and 0.23 nm for silicon [41]. The simulations were performed with 128 lipids. Lipophobic supports tend to destabilize the membranes, whereas we are able to study lipophilic supports without significant problems. We see that the water between the membrane and the support is at least partially ordered and that the membrane becomes asymmetric. Heine et al. found stable DPPC bilayers on mica where they found the water layer between the support and the membrane around 0.34 nm [39]. Hartshorn et al. recently presented simulations of several lipids on a quartz surface [46]. Roark and Feller recently performed an atomistic study by drilling a hole in the support [45]. However, in that study the size of the hole was a significant portion of the overall bilayer area. The thickness of the proximal water layer in a Martini level study [42] turned out to be roughly 1 nm in agreement with experiments [19, 23, 50].

On the CG level, the problem of the support is not as severe. This may be one of the reasons that in contrast to free membrane simulations most SLB simulations use a mesoscale model. The surface has to be hydrophilic otherwise we end up with a monolayer [75]. The binding strength is chosen such that the membrane adsorbs and the adsorption does not induce a phase transition. Hoopes et al. have shown that there is often a large range of parameters to choose from and the specific numbers are not crucial as long as qualitative or semiquantitative effects are of interest [40]. We take the above discussed Cooke–Deserno model as example. One has to define the interaction between the surface and the lipids. The surface is made of particles on a hexagonal lattice since this provides the best packing density for spheres. Generally, surface particles are not allowed to move at all. The head beads interact with surface particles using a standard Lennard-Jones 12–6 potential while the two tail particles of the lipid and the surface particles are interacting only repulsively. The effect of granularity of the surface has been studied. In order to realize the (almost) same surface energy density with different granularities one compensates increased packing density, which leads due to the particle overlap to a smoother surface, with correspondingly decreased interaction per particle. So if one halves the distance between particles, one divides the interaction energy by a factor of four to arrive at the same energy per unit area. For a detailed discussion of the implementation and the results, the reader is referred to Ref. [40]. Here we only note that the surface energy density per unit area is the crucial parameter and bilayers behave very similar if the granularity is changed.

On the Martini level it turned out that also the water model has to be chosen carefully as otherwise artifacts like freezing of water at the surface may be induced. As one introduces a hydrophilic support where the interactions are a scaled down version of the polar headgroup water interaction, one realizes that with the regular interaction strength of water, there is ice instead of fluid water at temperatures around 325 K [54]. In order to avoid this water freezing at the surface which is a known problem in the Martini force-field, one reduces the water interaction strength to 76% of the original strength

proposed by Marrink in 2004. In more recent implementations of the Martini model, this problem has been alleviated somewhat by modeling water as a binary mixture [53]; however, with a surface the adapted model tends to demix [42].

Molecular modeling traditionally uses periodic boundary conditions to minimize artifacts due to the limited system size. In free membranes, this essentially leads to the case of an infinite bilayer stack. Such systems are normally simulated either under constant pressure or under constant surface tension. One has to ensure in the constant pressure case that the area per molecule and the thickness do not become artificially coupled by the algorithm, that is, one has to use so-called anisotropic pressure coupling where the different directions are coupled independently to the pressure. If this target pressure tensor is truly anisotropic, we have a constant surface tension ensemble. In the case of a support we can, however, not use pressure coupling in the lateral plane if we make the surface out of individual particles as one would change the interaction density by changing the area. In the case of a homogeneous surface potential this is clearly not a problem. However, unpatterned nonspecific surfaces have not traditionally been used with molecule based simulations.

One system we are discussing here is a lipid bilayer of DPPC lipids using the adapted version of the Martini model at 323 K, above the main phase transition temperature of DPPC which is  $T_c = 314$  K [76]. It contains 128 lipids and 2593 CG waters or 512 lipids and 10,372 CG waters. A free bilayer using the above explained changed water interaction leads to about  $76 \text{ \AA}^2$  area per molecule which is clearly larger than desired. The amount of water on either side of the lipid membrane equilibrates by itself within a few microseconds, simulations started with a water cushion of about 1 nm thickness. Five hundred twelve lipids are supported by 1760 support atoms at 0.3 nm spacing in a simple square lattice; there is no expected difference to the hexagonal packing in the other models. The support particles have the same 0.47 nm radius as the other sites; adjacent particles overlap. The surface particles do not interact among themselves. Here one does not exclude water–water or water–lipid interactions through the support as long as they are within the cutoff. In  $x$  and  $y$  direction, the box size was commensurate with the lattice spacing. The direction normal to the bilayer is coupled to a pressure of 1 bar.

### **3. OBSERVABLES FOR CHARACTERIZATION OF BILAYER SYSTEMS IN MOLECULAR MODELING**

Computer simulations in principle can calculate any physical property based on the configurations generated by a Monte Carlo or Molecular Dynamics algorithm. Let us describe a few properties to characterize biomembranes in simulations in detail. These are used for both free and supported systems.

*Area per molecule:* The area per molecule (sometimes called area per headgroup) can for many systems be determined experimentally [77–79]. In supported bilayers, we cannot use the standard approach to measure the area per molecule of a free bilayer where one just fixes the number of particles per leaflet and simulates under constant pressure or constant surface tension. The area per molecule is then just the lateral size of the box divided by the numbers of particles per leaflet. For SLBs, the simulations have to be performed with fixed area per molecule and fixed normal pressure which is set to ambient pressure. So, one effectively measures pressure–area isotherms under constant area but varying numbers of particles or fixed number of particles and varying area.

*Density profile and membrane thickness:* A standard observable in the study of lipid bilayers is the density profile. The system is separated into slabs along a given axis (the bilayer normal is a good choice) and the density is measured in these slabs. We learn a lot about the structure of the system in this way. The highest density is normally in the headgroup region and the lowest in the middle. We can also calculate density profiles of specific atoms. For a free bilayer density profiles are symmetrical. In a supported system this is generally not the case. The density profile is directly connected to the electron density profiles—instead of assigning masses to atoms we just assign electron numbers. Electron densities are then related to X-ray scattering. If we assign local charges, we obtain a charge density profile and the electrostatic field and potential can be calculated by integration of this based on the Poisson equation.

The thickness of a membrane can be determined by the density profile. There are several measures which in the case of free membranes lead to only slightly different values. One can use the peak-to-peak distance, the full width at half maximum, or the distance between the average position of the choline or the phosphate group. As long as the membrane is symmetric, there are no qualitative differences in choosing any one of these measures. However, in supported membranes the symmetry is broken and the density profile changes qualitatively so there is often now a qualitative difference between different measures. The typical definitions of thickness can still be used but in addition the shape of the underlying density profile has to be characterized in detail. An important consequence of changing bilayer thickness is that integral membrane proteins, which one wants to embed for biosensors or similar applications, may no longer match this thickness and a so-called hydrophobic mismatch ensues having strong implications on protein function [80].

*Pressure and surface tension:* An important thermodynamic property is pressure, which in free bilayer simulations can be kept constant in the three Cartesian directions through the use of a barostat. In an anisotropic medium, pressure is not a scalar but a second rank tensor which is defined in terms of forces, velocities, and positions. With only pair forces, the overall pressure is defined as

$$P = \sum_{\text{pairs}} \vec{F} \times \vec{r} + \frac{1}{2} \vec{u} \times \vec{u}$$

where the multiplication is the tensor (outer) product of the corresponding vectors. A surface tension arises from the difference between the normal pressure and the lateral pressure. The normal pressure  $P_n$  is the diagonal matrix element  $P_{zz}$  and the lateral pressure  $P_l$  the average of  $P_{xx}$  and  $P_{yy}$  where  $z$  is chosen as the bilayer normal.

$$\gamma = \int [P_n(z) - P_l(z)] dz$$

A negative lateral pressure sometimes found in a supported bilayer system means a positive surface tension and furthermore implies a smaller equilibrium area per headgroup than the one chosen. The surface tension of a supported bilayer can be decomposed into the contributions of the wall/water and the two water/lipids interfaces.

For many applications, the overall pressure calculation, even as a tensor, is not accurate enough and hence a more localized pressure calculation via formulations such as the Irving–Kirkwood equation is necessary [81]. We do not discuss these methods in detail here, but note that one can obtain pressure as a function of position. If we measure pressure as a function of the position along with only the bilayer normal, we obtain a pressure profile which is very important in the understanding of transmembrane protein function.

*Interdigitation:* The interdigitation between leaflets is normally defined based on the overlap integral of the leaflet densities (cf. Fig. 2). After the density profile has been determined for the two leaflets separately, we integrate the overlap region, that is the product of the two density profiles. Interdigitation can be used to calibrate the different models against each other and against experiments.

*Tilt of headgroup or tails:* Another structural quantity is the tilt of both the headgroup as well as of the tails with respect to the bilayer normal. One

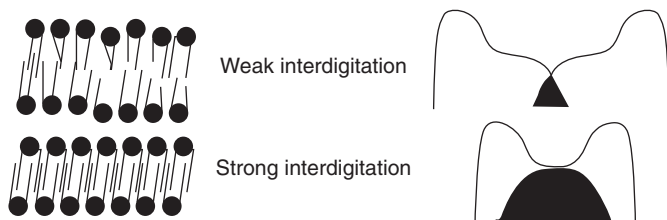


**Figure 2** Interdigitation and its quantitative measurement in terms of density profiles of overlapping leaflets.

defines a unit vector representing the orientation of the part of the molecule one is interested in. For the headgroup in a phosphatidylcholine one normally chooses the P–N vector, for a tail the canonical choice is the vector connecting the first and last carbon. The access to the tilt allows addressing the phase the membrane (or leaflet) is in and the headgroup tilt is important in understanding the membrane electric potential as it determines the vertical separation of charges. Additionally, we can measure the orientation of water molecules neighboring the lipids and determine therefore the structural influence of the membrane on its environment.

*Order parameter:* A very important structural characteristic is the chain order parameter which can be accessed in NMR experiments [82]. This allows higher resolution access to the local orientation than the tilt. Since the hydrocarbon chain structures even in fully atomistic simulations are normally based on united atom models, hydrogen atoms are not explicitly represented and the C–H bonds have to be reconstructed assuming tetrahedral geometry of the CH<sub>2</sub> groups. The order parameter is defined as

$$-S_{\text{CD}} = \frac{2}{3} S_{xx} + \frac{1}{3} S_{yy},$$

$$S_{\alpha\beta} = \langle 3 \cos \Theta_{\alpha} \cos \Theta_{\beta} - \delta_{\alpha\beta} \rangle, \quad \alpha, \beta = x, y, z$$

$$\cos \Theta_{\alpha} = \hat{e}_{\alpha} \hat{e}_z,$$

where  $S_{\text{CD}}$  is the angle between the experimentally measured carbon deuterium (CD) bond and the bilayer normal in experiments. In simulations, the CD bond is replaced by a regular carbon hydrogen bond. In coarse-grained simulations, one typically defines an order parameter in an equivalent manner where the vector is chosen to define the local orientation of the chain.

*Radial distribution functions:* A structural property which is typically accessed in molecular modeling is the radial distribution function. Its general 3D definition measures the number of particles at a given radial distance from the tagged particle and divides that by the known number for an ideal gas at the same density. As the radial symmetry is broken in bilayers, it is often more useful to apply its 2D equivalent. Radial distribution functions give us information about morphology and structure complementary to density profiles. Radial distribution functions  $g_{\text{AB}}(r)$  between particles of type A and B are defined as

$$g_{\text{AB}}(r) = \frac{\langle \rho_{\text{B}}(r) \rangle}{\langle \rho_{\text{B}} \rangle_{\text{local}}} = \frac{1}{\langle \rho_{\text{B}} \rangle_{\text{local}}} \frac{1}{N_{\text{A}}} \sum_{i,j}^{N_{\text{A}}, N_{\text{B}}} \frac{\delta(r_{ij} - r)}{4\pi r^2}$$

with  $\langle \rho_{\text{B}}(r) \rangle$  the particle density of type B at a distance  $r$  around particle A, and  $\langle \rho_{\text{B}} \rangle_{\text{local}}$  the particle density of type B averaged over all spheres around particles A with radius  $r$ . If we are interested in the 2D RDFs, we define the



distance as the in-plane distance and change the normalization accordingly. In the 2D case, leaflets can be studied separately.

*Mean-squared displacements and diffusion:* Up to now, we discussed static and thermodynamic properties of lipids. Since Molecular Dynamics also allows access to particle momenta, the dynamics can also be studied. The most often used dynamical property is the mean-squared displacement (MSD) which for long times also gives access to the diffusion coefficient. The MSD is defined as

$$\text{MSD}(t) = \langle [\vec{x}(t_0 + t) - \vec{x}(t_0)]^2 \rangle_{t_0}.$$

One averages over all possible intervals of length  $t$ , a so-called running time average. This leads to a decreasing statistical accuracy for increasing time interval.

From the MSD, one can calculate the lateral diffusion coefficient using the Einstein relation:

$$D_{\text{lat}} = \frac{1}{4} \lim_{t \rightarrow \infty} \frac{\text{MSD}(t)}{t}.$$

Practically, one performs not the limit to infinity but chooses a time long enough such that the MSD rises linearly with time. Due to the statistical problems at very long times, one should discard data for time lags larger than a third of the runtime.

*Reorientation:* Not only diffusional displacements but also rotation can be measured in a simulation. One example is the reorientation correlation function of the first Legendre polynomial

$$C_1(t) = \langle \vec{u}(t) \vec{u}(0) \rangle.$$

Higher Legendre polynomials can be used as well. The second Legendre polynomial is relevant for direct comparison to NMR. As discussed in the section about tilt, any possible unit vector can be chosen to represent local directions.

## 4. CHARACTERISTICS OF SUPPORTED AND UNSUPPORTED BILAYERS

### 4.1. Visualization

Humans are visual and our intuition works best if we can see what is going on. So normally, the first thing one should do in a simulation is visualize the system. Then one immediately sees if the system we are modeling is actually

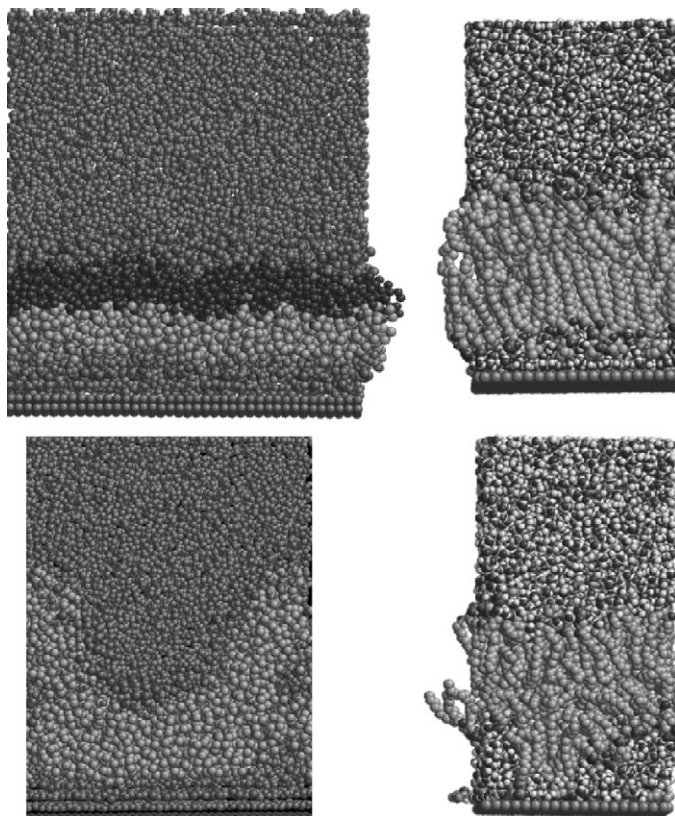


**Figure 3** Visualizations. Top left: Martini level simulation of DPPC on a hydrophilic surface with the two leaflets indicated in different colors (equilibrated), Top right: Atomistic simulation of DPPC on carbon (early stage of simulation), Bottom left: CG simulation of DPPE on a hydrophilic surface (unstable simulation), Bottom right: Atomistic sphingomyelin on silicon (unstable). Adapted in part with permission from Ref. [42]. Copyright (2008) American Chemical Society.

the one we are intending to model. In Fig. 3 several visualizations of supported bilayers using different models are depicted. First, these figures prove that in some cases one can obtain continuous stable membranes; so we actually see that we are modeling the system we are interested in, namely a SLB. In other cases, we show that such simulations can fail as well.

The asymmetry between different leaflets is clearly seen as well. It appears that the asymmetry becomes more pronounced with increasing coarseness of the model. One has to keep in mind that the effective surface thickness increases in these models as in all cases shown here the surface is one interaction site thick and the lattice spacing of the surface is on the order of the interaction unit. Also the direct interaction range of the surface rises as

the cutoff distance in the simulation is normally proportional to the size of the interaction site. This would suggest that one may need to adapt the interaction ranges for coarser models or one needs especially in the atomistic case several layers of surface atoms. In some simulations thicker support structure has been used [45]. The qualitative behavior is nonetheless similar in all cases. Visualization is useful but it does not provide us with quantitative data and therefore needs to be amended by the observables discussed above.

## 4.2. Density Asymmetry

As described above, density profiles are customary observables both in supported and unsupported bilayers. They are normally the first quantitative data which one analyses in a supported system. If we compare them to well-known density profiles in free systems, the first difference which strikes the eye is the lack of symmetry between the two sides in the SLB. Free bilayers have a well-defined symmetry plane which is the plane of lowest density in the center of the membrane and there are peaks of high density marking the headgroups at the water interface which contain the heavy phosphorus atoms in phospholipids. In supported bilayers, these general features are somewhat preserved. We still find a high density region at both water interfaces, especially in the distal (away from the surface) leaflet it is reminiscent of the typical shape of a free bilayer. Also the density drops toward the membrane center as the fatty acid tails are lighter than water. But there is significantly stronger localization of both, headgroups and tails and increased layering especially in the proximal leaflet. The closer a moiety is to the support the stronger it is localized. This stems from the fact that the support is orders of magnitude stiffer than the soft membrane and normally is modeled without any degrees of freedom. This localization effect is common to all models—the degree varies somewhat—and below we will discuss its effects on the entropy of the supported system. In some models an almost crystalline order in the proximal leaflet is obtained. This may indicate that the support can induce phase transitions or at least shift phase transition temperatures in agreement with experiments [14, 83]. All studies indicate that the proximal leaflet structure is more significantly altered than the distal.

Interestingly, the overall thickness of the bilayer does not change substantially if we define thickness as the peak-to-peak distance across the membrane [42]. However, especially in highly coarse-grained models one finds that the density peaks in the supported system are sharper indicating the already discussed localization effect [40]. The density peaks become significantly asymmetric. It turns out that the side facing the free water (away from the support) is less steep than the one facing the surface. Therefore, different measures of thickness will be differently affected and one has to be very careful if one compares results from different studies.

So the peak-to-peak thickness or the thickness defined as the integral over the density profile divided by the thickness in the middle is not severely affected and generally leads to a small compression whereas measures which rely on full width of half maximum are obtaining actually wider thicknesses. One can analyze the two leaflets separately and it has been shown that the proximal leaflet is thicker than the distal as the tails are more elongated due to the increase in order [40].

Most studies agree that compared to free bilayers the density profile of the proximal leaflet is significantly altered whereas the distal leaflet is only weakly affected. Generally, the coarser the model, the stronger the effects are found. Atomistic studies find normally some discrepancies due to the localization effect whereas in the highly coarse-grained water-free Cooke–Deserno model the two leaflets are probably in different thermodynamic phases. The main difference can be summarized that the symmetry of the membrane is broken and localization dominates the proximal leaflet. A recent atomistic study using several different lipids found a general thinning of the membrane on the support [46]. That study also found a significant change in the hydrogen bonding pattern in the two leaflets where the proximal leaflet has more hydrogen bonds than the distal. It has also been observed that interdigitation is slightly reduced which speaks for decoupling of the leaflets making it easier for the two leaflets to behave differently [40].

### 4.3. Structure

Lipid bilayer structure can be separated in lateral and normal structure. The normal structure is dominated by the hydrophilic–hydrophobic interactions as the headgroups shield the oily hydrophobic core from water and we started to discuss its effects in the density profile section above. Another important structural quantity which changes as a function of  $z$ -position is the order parameter. If one uses Xing’s variant of the Martini model at 323 K and with  $0.62 \text{ nm}^2$  per lipid in both leaflets, one obtains small but noticeable differences in the order of the leaflets as shown in Table 1.

**Table 1** Order parameters using the adapted Martini model resolved according to leaflets and averaged over both tails

Sites	Leaflet	$S_{CD}$
1–2–3	Proximal	0.296
1–2–3	Distal	0.292
2–3–4	Proximal	0.231
2–3–4	Distal	0.224

It turns out that interestingly the effect is slightly stronger deeper in the tail region. The increase from the part just behind the headgroups is almost negligible but we get about a 5% increase in close to the membrane center. Again the proximal leaflet is more highly ordered. Both are obviously far away from any gel transition where  $S_{CD}$  would be above 0.4 [84].

Simulations using very coarse-grained models have the advantage that lipid flip-flop, the change of a lipid from one leaflet to another, can be observed. This leads to the possibility to study directly in MD the difference of densities between leaflets. Hoopes et al. have studied such systems under different areas per molecule [40]. They selected the equilibrium area per molecule as the point where the surface tension vanishes. This is reasonable as many free simulations are done under vanishing surface tension. At that point, it turned out that the number of lipids in the proximal leaflet was about 3% higher than in the distal. This shows together with the weaker undulations that the proximal leaflet is probably closer to the gel transition. Recently, this asymmetry was confirmed using the adapted Martini model [44]. In an umbrella sampling study the free energy of lipid transfer from one leaflet to another was determined. The point when the two minima on either side of the membrane are at the same free energy is then the equilibrium distribution. This again turned out to be about 3–4% difference. The free energy distribution as a function of asymmetry is very shallow such that one expects a broad distribution of asymmetries around the minimum. At the same time, they determined that the flip-flop barrier is very similar to that in free bilayers.

We can, however, also expect a change in transversal structure as the density of the two leaflets is different. Therefore, the packing within the plane has to change to some extent. In the extreme case, we can even trigger a phase transition by this compression. Therefore, both lateral RDFs as well as density profiles are needed. Figure 4 shows an example of a RDF of a supported bilayer using the Xing variant of the Martini model at 323 K. Only the phosphate groups in the two leaflets are shown. We show a 3D RDF here and can identify a somewhat higher ordering in the bottom leaflet. Note that in this case the area per molecule of the two leaflets is the same so the ordering is not induced by a higher area density. Similar results have been found in atomistic studies [46].

The increased transversal order of the proximal leaflet also appears in a different structure of the headgroup tilt. While we find a broad single peaked distribution of the P–N vector in the distal leaflet, the two tiered stacking of headgroups in the proximal leaflet leads to a double peaked structure as discerned using the Xing variant of the Martini model (Fig. 5). Again, atomistic studies confirm differences in tilt between free and supported membranes although they are generally significantly less pronounced [45, 46].

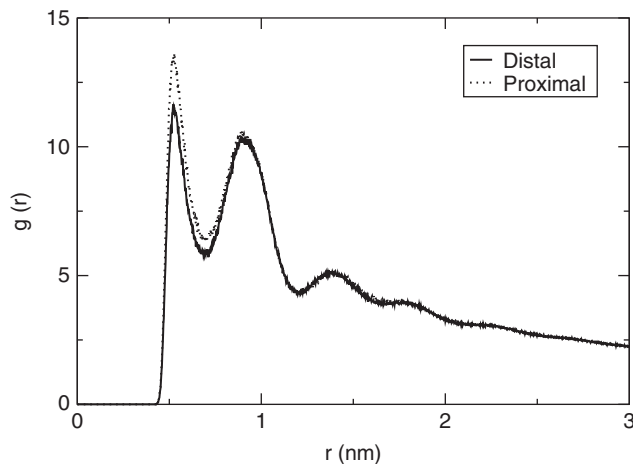


**Figure 4** Comparison of radial distribution functions of headgroups in leaflets under the same area per molecule.

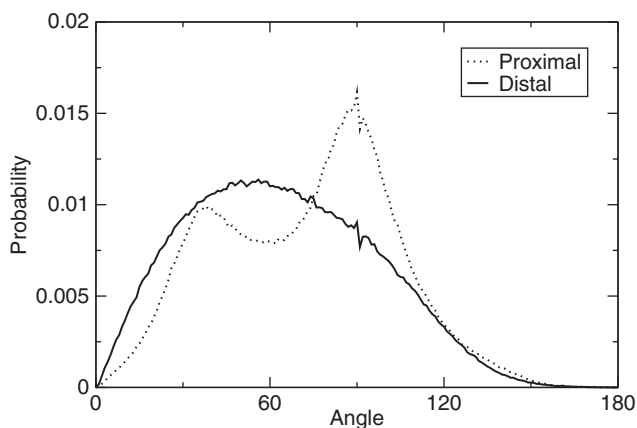


**Figure 5** Comparison of headgroup tilt in leaflets under the same area per molecule.

#### 4.4. Pressure Distribution

In recent years it has been realized that pressure profiles across the membrane are crucial for protein function [49, 85, 86]. Fundamentally, the idea is that transmembrane proteins are adapted to a certain pressure distribution which is far from homogeneous across the membrane. Changing this distribution by, for example, adding small molecules will change the protein environment and eventually interfere with cell functions. Effects as different as anesthesia and stuck wine fermentations have been linked to such

pressure profile changes [49, 87]. Simulations have been instrumental in understanding the pressure profile in membranes as they have a much better local resolution than experiments [26, 40, 43, 65]. Especially as protein function in supported bilayers is often significantly affected one might wonder if the change in pressure profile has an influence here.

As the structure in a supported bilayer is significantly affected by the surface it is reasonable to expect that the pressure profile changes as well. Several recent studies have addressed the change in pressure profiles due to the support [40, 43]. The main interest is the pressure profile normal to the membrane and one separates the lateral and the normal components. The more important one is the lateral pressure as this is the one proteins experience in the 2D solvent of lipids. The local lateral pressure in a membrane is surprisingly high. Changes over several hundreds of bar over a few nanometers are well established for free bilayers. All studies on pressure profiles in supported bilayers have established that the localization in the proximal leaflet is changing the pressure profile significantly. Again, the distal leaflet is reasonably close to a free bilayer. These studies have been done both with and without taking the above discussed change in area density into account and the results in both cases are similar.

One may wonder if the observed changes in the pressure profile are actually functionally significant. Xing et al. have compared their lateral pressure profiles to biologically relevant energies [43]. They integrated the difference between a free and a supported profile over the volume of a typical transmembrane channel. This obviously leads to an energy which turned out to be on the order of  $40 k_B T$ . This number is significant in two ways. First of all it may overshadow thermal energy and it is in the realm of the known activation energies of mechanosensitive channels which are around  $30\text{--}50 k_B T$  [88]. This means that the interaction of the membrane with the support can actually interfere with protein function even if the protein itself does not directly interact with the substrate.

#### 4.5. Water Layer Thickness and Entropic Repulsion

It is very well established by both experiment and simulation that there is a water layer between a hydrophilic substrate and the lipid headgroups in a bilayer. Only in the highly hydrophobic case where monolayers form sit the lipids directly on the substrate [75]. The nature and thickness of this water layer as well as the reason for its existence is some matter of debate. Experiments indicate a dependence on lipid type as systems with higher order and lower area per molecule like DPPE bilayers are sitting closer to the substrate than PC bilayers which have a higher area per molecule and lower order [23].

Simulations on intermediate to large length scales have established that we can equilibrate this water layer [42]. Atomistic simulations have used a

hole in a supporting substrate to allow this equilibration to happen more quickly [45]. It is very interesting that the equivalent of a water layer even appears in a model without explicit water [40]. Thus, the simple argument that the substrate is more attractive to water molecules than to headgroups does not hold. There is an entropic argument in favor of the existence of this water layer as the binding of a membrane to a substrate suppresses undulations. If there was no water layer at all we would find that the undulational entropy of the membrane is not only reduced but also completely erased. On the other hand, it has been established by simulations that a thin water layer is to some extent ordered such that the entropy of the solvent in this layer is reduced as well. So we expect that there is a water layer and we also suggest that it has to have some minimum thickness. It should depend on the mechanical properties of the membrane which is experimentally supported [18, 23].

For the case of the water-free Cooke–Deserno model the entropic repulsion of the membrane by the substrate has been studied based on the (von Neumann) entropy which associates the entropy with the lipid height distributions  $p_i(z)$ . The connection is given as:

$$S_i = S[p_i(z)] = -k_B \int dz p_i(z) \ln[p_i(z)\ell]$$

where  $\ell$  is an arbitrary length necessary for dimensional reasons. For a Gaussian probability density of width  $w$  the entropy is  $S_{\text{Gauss}}(w)/k_B = \text{const.} + \ln(w)$ . Increasing the width increases entropy and reduces the free energy by  $\Delta F = -T \Delta S = -\ln(2) k_B T$ . We are using the Helmholtz free energy as we are in the canonical NVT ensemble. Clearly, a localization which narrows the headgroup distribution increases the free energy. The exact calculation of this free energy is rather involved as the localizations of the different parts of the lipid are not independent. But a lower bound of this effective repulsion is the change in the proximal headgroup distribution. This was estimated to be  $\Delta F = 0.84 k_B T$ . So the free energy of adsorption is clearly diminished by localization and this effect prevents the direct adsorption on the surface. We expect that for stiffer membranes this repulsion is weaker as the headgroups are already more localized.

## 4.6. Dynamics

### 4.6.1. Diffusion

Dynamical aspects of lipid behavior in supported bilayers have been studied. Experimentally it has been shown that the lipid mobility is at least a factor of three smaller in supported compared to free standing bilayers [89]. Very recently the Loesche group has also determined the difference in dynamics



between different leaflets in a sparsely tethered bilayer and the difference in diffusivity is again about a factor of three [83].

In simulations, the difference of diffusional dynamics of lipids in different leaflets has been determined. The MSDs in the supported bilayer study by Xing et al. [42] obtained long-term diffusion coefficients which differ by about an order of magnitude ( $1.95 \times 10^{-8}$  and  $2.78 \times 10^{-7}$  cm<sup>2</sup>/s). It also appeared that the MSDs were qualitatively different and the proximal leaflet resembled at short to intermediate times (several nanoseconds) a cage like dynamics which is known from glassy systems [90] (Fig. 6). The diffusion coefficients themselves were in the experimentally relevant range. Interestingly this study was performed with the same area per molecule in both leaflets such that only the different structures could have contributed. One has to expect that with the higher area density which would be the more realistic case an even stronger dynamical asymmetry would ensue. The atomistic study by Roark and Feller qualitatively found the same results [45].

#### 4.6.2. Reorientation

We show in Fig. 7 an example of a headgroup reorientation resolved by leaflet again using the Xing variant of the Martini model. It is known that at the phase transition the headgroup orientation becomes very slow [91]. We see a very clear distinction of the reorientation function in both cases indicating that the bottom layer is slower and possibly closer to a phase transition. In both cases, the functions do not completely decay to zero which indicates that the headgroup is on average not randomly oriented and the complete decorrelation would need a flip-flop which is too slow to be observed.

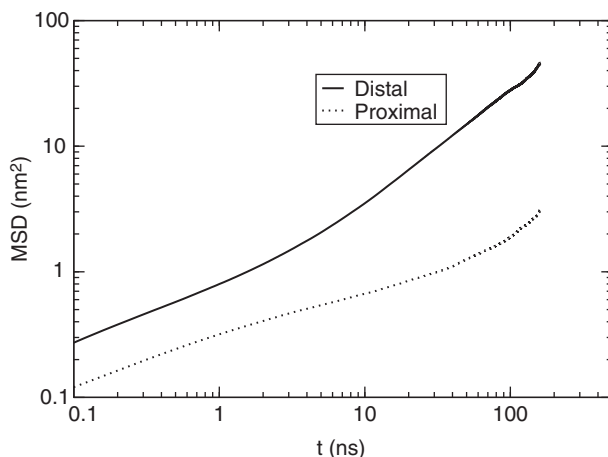


**Figure 6** Comparison of mean-squared displacements of headgroups (short to intermediate times) in leaflets under the same area per molecule. Note: we do not use the time rescaling as suggested by Marrink [48] here or in any other figure.

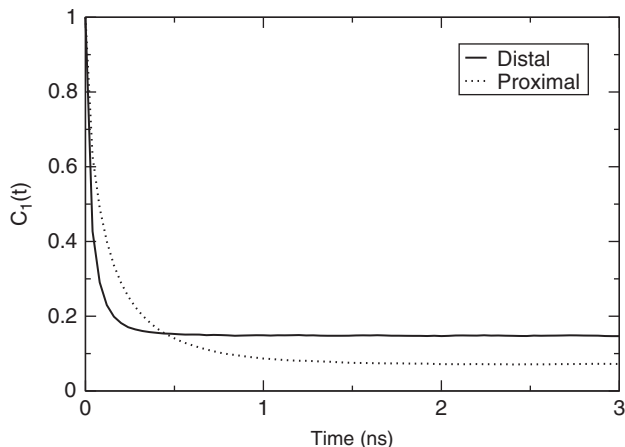


**Figure 7** Comparison of reorientation correlation functions of headgroups in leaflets under the same area per molecule.

#### 4.7. Mechanical Properties

The mechanical behavior of soft materials is in general not an easy task for a simulation to determine. From statistical mechanics there are fundamentally two different ways to determine mechanical properties. We can measure stress strain curves (or the opposite; see e.g., Ref. [40]) or we can measure the fluctuation spectrum. In the first case we induce a perturbation to the system and measure the strength of its response, or in some cases we induce a certain level of response and measure the strength of the needed perturbation [92]. These simulations are nice and give relatively good signal. However, as in general only for very small perturbations a linear cause–effect relationship exists we need to be sure that we are still in linear response. So several perturbation strengths need to be applied and the response in the limit of perturbation to zero needs to be elucidated.

According to fundamental statistical mechanics, fluctuations in any property are related to generalized susceptibilities. An example is fluctuations in the area per molecule which are related to the area compressibility modulus. In the case of membranes, we have two different types of fluctuations: the in-plane fluctuations which are connected to the area compressibility and out-of-plane bending leading to the bending modulus. If our simulations are large enough to allow the fluctuations and long enough to sample them in a statistically meaningful manner, we can obtain the values. Most of the time one cannot sample the complete fluctuation spectrum but assume that the system can for free membranes on large scales be modeled by a Helfrich Hamiltonian description [93]. In that case, one fits the

spectrum to the known spectrum for the Helfrich behavior where the mechanical properties are the fitting parameter.

However, it has been shown that by introducing a support the Helfrich Hamiltonian description breaks down and the typical bending elasticity cannot be determined from a supported bilayer simulation [40]. This is not surprising as the total system, namely support plus membrane clearly cannot be bent. And the membrane alone cannot bend more than the support allows it. So essentially, it becomes questionable if one should even talk about a bending elasticity here. Very recent studies on curved substrates may in the future lead a way out of this dilemma [7].

A different case is the area compressibility as fluctuations should be clearly possible in the plane. However, due to the already discussed technical issues the only way to measure area compressibility in a supported system is to measure the pressure or surface tension for different area densities. In the large-scale simulations by Hoopes et al., it turned out that although the effect of the support on the average area per molecule was only about 2% as discussed above, the change in the area compressibility modulus as obtained by pressure area curves under constant area was 65% [40]. They determined the tension as a function of area for a wide range of area densities for supported and free bilayers under constant volume conditions. As they showed at the same time that the undulation spectrum was completely changed from the free bilayer we suspect that in general fluctuation based properties are prone to larger artifacts by substrate interaction than simple averages

## 5. INFLUENCE OF CORRUGATION

Simulations have the advantage that we can generate and control any possible surface configuration and corrugation. Thus, roughness can be perfectly controlled and different roughnesses can be implemented. As simulations of SLBs in general are not very abundant simulations of different surface corrugations are even less available. But they are inevitable if one wants to understand how membranes conform to different corrugations. When the topological complexity increases, analytical shape equations become difficult to solve analytically, whereas molecular modeling is not in any way fundamentally more difficult with a different surface. Analytical treatments treat the membrane as an infinitely thin elastic film but in reality (and simulations), lipid membranes do not conform homogeneously to a substrate but typically the proximal and distal leaflet over a curved substrate are different.

As discussed above Hoopes et al. showed that with controlled surface energy density, variations in corrugations of one nanometer or less do not

significantly change the equilibrium structure of the membrane [40]. So small corrugations cannot really be considered a corrugation here as they are just a way to implement a smooth surface based on particles. Using the already discussed variant of the Martini model it has been determined that surface topology can have significant influence on the structural and dynamic properties of the lipid bilayer. Differently patterned surfaces were covered with bilayers of DPPC [42]. Supported bilayer systems on three different surfaces were studied. In the substrate plane all implementations were a perfect crystal on a simple cubic lattice. The first implementation was that just all particles were in the same plane. This is the choice which we have discussed in detail above. A second surface was constructed where 25% of the total surface area is made of particles which are 0.3 nm lower than the rest. Thus, the surface has several big dips. In a third surface the particles are randomly assigned into two  $z$ -planes 0.3 nm apart.

The degree of ordering as elucidated by the density profile decreases as the roughness of the surface increases. The above described layering in the proximal leaflet is significantly decreased in the two rougher implementations. The lateral pressure profiles of differently rough surfaces show qualitative agreement but significant quantitative differences [7]. The rougher a surface is the smoother a pressure profile is found. This shows that a perfectly flat surface imposes the strongest surface-induced artifacts onto a bilayer. This is also understandable from the entropy argument above as the rougher substrate imposes a smaller entropic repulsion to the fluctuating surface.

Also the diffusivity of lipids is also influenced by roughness as the less structured system induces a higher mobility. So, one finds that some degree of surface roughness is actually advantageous to alleviate substrate induced artifacts.

Very recently, some preliminary data of larger scale curved substrates have been shown using the Cooke–Deserno model [7]. It turns out that lipids are easily conforming to even very small local radii of curvature and that they can wrap around cylinders or spheres very easily. Clearly more work in this area is highly needed.

## 6. CONCLUSIONS AND OUTLOOK

The field of molecular modeling of lipid bilayers supported on substrates is clearly a very young one and the models are therefore still in their infancy. There are significant model dependencies but a general picture is emerging. All simulations indicate that on hydrophilic substrates the bilayer remains intact in agreement with experiments but there are nonnegligible influences of the support on all levels.

The structure, dynamics, and possibly phase behavior of supported bilayers have distinct characteristics which are different from their free counterparts. One has to be very careful if one wants to deduce results for free membranes or even biological systems.

We are learning that the substrate induces asymmetries in density and pressure profiles, in the diffusion behavior as well as to some extent in the order parameter. In all cases studied to date higher densities and pressures are found in the proximal leaflet of the supported bilayer. The ordering and the suppression of undulations induce an entropic penalty to bilayer binding which acts as an additional repulsive force reducing the free energy of adsorption. We also find that leaflets decouple to some extent as seen by reduced interdigitation. The overall thickness of the membrane becomes somewhat ambiguous as the density profiles are qualitatively different from free bilayers.

The average area per molecule decreases slightly at zero tension but the area compression modulus changes dramatically which again depends on the change in fluctuation spectrum.

Clearly more studies are needed on all levels to elucidate influence on the hydrogen bonding network, the exact structure and thickness of the water layer or on the large-scale response to corrugation.

The change in the pressure profile exceeds thermal energy by more than an order of magnitude and we expect that it is even harder than previously thought to integrate functional transmembrane proteins into supported systems.

Generally, we learned that the current picture of supported bilayer simulations is consistent on many scales and that the effects of the support are very strong on the proximal side and decay towards the water. So we expect that with multilayers the effect of a “supported free” membrane may eventually be achieved.

It also turns out that the coarser the model is the stronger an effect of the surface we find. One explanation for this may be that the effect drops with the interaction distance of the sites as well as the cutoff. In coarser models, we are using larger sites which have a larger interaction distance and additionally the cutoff is normally scaled proportionally to the interaction distance. Therefore, we may expect for very coarse-grained models somewhat an overestimation of the effects on the structure.

## **ACKNOWLEDGMENTS**

The authors thank their present and former collaborators who contributed significantly to the body of understanding presented here. This includes Matthew Hoopes, Samuli Ollila, Markus Deserno, Ilpo Vattulainen, Tonya Kuhl, and Margie Longo. Some of the work presented here was supported by the NSF NIRT Program and an NSF-IREE international

travel supplement (grant CBET 0506662). Computer time at NICS, the Texas Advanced Computing Center and the Pittsburgh Supercomputer Center (all under Teragrid allocation MCB070076N) and at the Pacific Northwest National Lab (Proposal 30792 in the Molecular Science Computing Facility) has been used.

## REFERENCES

- [1] H. Lodish, A. Berk, S.L. Zipursky, P. Matsudaira, D. Baltimore, J.E. Darnell, *Molecular Cell Biology*, fourth ed., W. H. Freeman, New York, 2000.
- [2] A. Ulman, *An Introduction to Ultrathin Organic Films: From Langmuir–Blodgett to Self-Assembly* Academic Press, San Diego, 1991.
- [3] Z.V. Leonenko, A. Carnini, D.T. Cramb, Supported planar bilayer formation by vesicle fusion: The interaction of phospholipid vesicles with surfaces and the effect of gramicidin on bilayer properties using atomic force microscopy, *Biochim. Biophys. Acta (Biomemb.)* 1509(1–2) (2000) 131–147.
- [4] G.L. Gaines, *Insoluble Monolayers at Liquid–Gas Interfaces*, Wiley, New York, 1996.
- [5] P. Lenz, C.M. Ajo-Franklin, S.G. Boxer, Patterned supported lipid bilayers and monolayers on poly(dimethylsiloxane), *Langmuir* 20(25) (2004) 11092–11099.
- [6] K.C. Weng, J.J.R. Stalgren, S.H. Risbud, C.W. Frank, Planar bilayer lipid membranes supported on mesoporous aerogels, xerogels, and Vycor(R) glass: An epifluorescence microscopy study, *J. Non-Cryst. Solids* 350 (2004) 46–53.
- [7] E.I. Goksu, M.I. Hoopes, B.A. Nellis, C. Xing, R. Faller, C.W. Frank, S.H. Risbud, J.H. Satcher Jr., M.L. Longo, Silica xerogel/aerogel-supported lipid bilayers: Consequences of surface corrugation, *Biochim. Biophys. Acta (Biomemb.)* 1798(4) (2010) 719–729.
- [8] R.P. Richter, A.R. Brisson, Following the formation of supported lipid bilayers on mica: A study combining AFM, QCM-D, and ellipsometry, *Biophys. J.* 88(5) (2005) 3422–3433.
- [9] M. Tanaka, E. Sackmann, Polymer-supported membranes as models of the cell surface, *Nature* 437(7059) (2005) 656–663.
- [10] B.A. Cornell, V.L.B. BraachMaksvytis, L.G. King, P.D.J. Osman, B. Raguse, L. Wiczorek, R.J. Pace, A biosensor that uses ion-channel switches, *Nature* 387 (6633) (1997) 580–583.
- [11] W. Knoll, F. Yu, T. Neumann, S. Schiller, R. Naumann, Supramolecular functional interfacial architectures for biosensor applications, *Phys. Chem. Chem. Phys.* 5(23) (2003) 5169–5175.
- [12] *Biosensors: A Practical Approach*, J.M. Cooper, T. Cass (Eds.), The Practical Approach Series, second ed., Oxford University Press, Oxford, 2004.
- [13] W.M. Huang, X.R. Yang, E.K. Wang, Mimetic membrane for biosensors, *Anal. Lett.* 38(1) (2005) 3–18.
- [14] A. Charrier, F. Thibaudau, Main phase transitions in supported lipid single-bilayer, *Biophys. J.* 89(2) (2005) 1094–1101.
- [15] H. Komatsu, P. Guy, E.S. Rowe, Effect of unilamellar vesicle size on ethanol-induced interdigitation in dipalmitoylphosphatidylcholine, *Chem. Phys. Lipids* 65(1) (1993) 11–21.
- [16] T. Adachi, H. Takahashi, K. Ohki, I. Hatta, Interdigitated structure of phospholipid-alcohol systems studied by X-ray diffraction, *Biophys. J.* 68(5) (1995) 1850–1855.
- [17] Z. Leonenko, E. Finot, D.T. Cramb, Afm study of interaction forces in supported planar dppc bilayers in the presence of general anesthetic halothane, *Biochim. Biophys. Acta (Biomemb.)* 1758(4) (2006) 488–492.

- [18] C.E. Miller, J. Majewski, T. Gog, T.L. Kuhl, Characterization of biological thin films at the solid-liquid interface by X-ray reflectivity, *Phys. Rev. Lett.* 94(23) (2005) 238104.
- [19] T.M. Bayerl, M. Bloom, Physical properties of single phospholipid bilayers adsorbed on micro glass beads, *Biophys. J.* 58(2) (1990) 357–362.
- [20] S.J. Johnson, T.M. Bayerl, D. McDermott, G.W. Adam, A.R. Rennie, R.K. Thomas, E. Sackmann, Structure of an adsorbed dimyristoylphosphatidylcholine bilayer measured with specular reflection of neutrons, *Biophys. J.* 59(2) (1991) 289–294.
- [21] B.W. Koenig, S. Krueger, W.J. Orts, C.F. Majkrzak, N.F. Berk, J.V. Silverton, K. Gawrisch, Neutron reflectivity and atomic force microscopy studies of a lipid bilayer in water adsorbed to the surface of a silicon single crystal, *Langmuir* 12(5) (1996) 1343–1350.
- [22] P. Fromherz, V. Kiessling, K. Kottig, G. Zeck, Membrane transistor with giant lipid vesicle touching a silicon chip, *Appl. Phys. A: Mater. Sci. Process* 69(5) (1999) 571–576.
- [23] C.E. Miller, J. Majewski, E.B. Watkins, D.J. Mulder, T. Gog, T.L. Kuhl, Probing the local order of single phospholipid membranes using grazing incidence X-ray diffraction, *Phys. Rev. Lett.* 100(5) (2008) 058103.
- [24] D.P. Tieleman, S.J. Marrink, H.J.C. Berendsen, A computer perspective of membranes: Molecular dynamics studies of lipid bilayer systems, *Biochim. Biophys. Acta (Rev. Biomemb.)* 1331(3) (1997) 235–270.
- [25] A.N. Dickey, W.-S. Yim, R. Faller, Using ergosterol to mitigate the deleterious effects of ethanol on bilayer structure, *J. Phys. Chem. B* 113(8) (2009) 2388–2397.
- [26] M.J. Skaug, M.L. Longo, R. Faller, Computational studies of texas red-1, 2-dihexadecanoyl-*sn*-glycero-3-phosphoethanolamine model building and applications, *J. Phys. Chem. B* 113(25) (2009) 8758–8766.
- [27] E. Falck, M. Patra, M. Karttunen, M.T. Hyvonen, I. Vattulainen, Lessons of slicing membranes: Interplay of packing, free area and lateral diffusion in phospholipid/cholesterol bilayers, *Biophys. J.* 87(2) (2004) 1076–1091.
- [28] A. Gurtovenko, M. Patra, M. Karttunen, I. Vattulainen, Cationic DMPC/DMTAP lipid bilayers: Molecular dynamics study, *Biophys. J.* 86(6) (2004) 3461–3472.
- [29] U. Essmann, M.L. Berkowitz, Dynamical properties of phospholipid bilayers from computer simulation, *Biophys. J.* 76(4) (1999) 2081–2089.
- [30] A.M. Smondryev, M.L. Berkowitz, Molecular dynamics simulation of DPPC bilayer in DMSO, *Biophys. J.* 76(5) (1999) 2472–2478.
- [31] R.J. Mashl, H.L. Scott, S. Subramaniam, E. Jakobsson, Molecular simulation of dioleoylphosphatidylcholine lipid bilayers at differing levels of hydration, *Biophys. J.* 81(6) (2001) 3005–3015.
- [32] A. Dickey, R. Faller, Examining the contributions of lipid shape and headgroup charge on bilayer behavior, *Biophys. J.* 95(6) (2008) 2636–2646.
- [33] A.M. Smondryev, M.L. Berkowitz, Molecular dynamics simulation of the structure of dimyristoylphosphatidylcholine bilayers with cholesterol, ergosterol and lanosterol, *Biophys. J.* 80(4) (2001) 1649–1658.
- [34] E. Lindahl, O. Edholm, Molecular dynamics simulation of NMR relaxation rates and slow dynamics in lipid bilayers, *J. Chem. Phys.* 115(10) (2001) 4938–4950.
- [35] S.J. Marrink, A.E. Mark, Effect of undulations on surface tension in simulated bilayers, *J. Phys. Chem. B* 105(26) (2001) 6122–6127.
- [36] E.A. Golovina, A.V. Golovin, F.A. Hoekstra, R. Faller, Water replacement hypothesis in atomic detail—Factors determining the structure of dehydrated bilayer stacks, *Biophys. J.* 97(2) (2009) 490–499.
- [37] T. Rog, M. Pasenkiewicz-Gierula, Cholesterol effects on the phosphatidylcholine bilayer nonpolar region: A molecular dynamics study, *Biophys. J.* 81(4) (2001) 2190–2202.

- [38] R.W. Pastor, R.M. Venable, S.E. Feller, Lipid bilayers NMR relaxation, and computer simulations, *Acc. Chem. Res.* 35(6) (2002) 438–446.
- [39] D.R. Heine, A.R. Rammohan, J. Balakrishnan, Atomistic simulations of the interaction between lipid bilayers and substrates, *Mol. Simul.* 33(4–5) (2007) 391–397.
- [40] M.I. Hoopes, M. Deserno, M.L. Longo, R. Faller, Coarse-grained modeling of interactions of lipid bilayers with supports, *J. Chem. Phys.* 129(17) (2008) 175102.
- [41] M.I. Hoopes, C. Xing, R. Faller, Multiscale modeling of supported lipid bilayers, in: *Biomembrane Frontiers Handbook of Modern Biophysics vol. 2* Springer–Humana Press, 2009, pp. 101–120, Chapter 4.
- [42] C. Xing, R. Faller, Interactions of lipid bilayers with supports: A coarse-grained molecular simulation study, *J. Phys. Chem. B* 112(23) (2008) 7086–7094.
- [43] C. Xing, O.H.S. Ollila, I. Vattulainen, R. Faller, Asymmetric nature of lateral pressure profiles in supported lipid membranes and its implications for membrane protein functions, *Soft Matter* 5(17) (2009) 3158–3161.
- [44] C. Xing, R. Faller, Density imbalances and free energy of lipid transfer in supported lipid bilayers, *J. Chem. Phys.* 131(17) (2009) 175104.
- [45] M. Roark, S.E. Feller, Structure and dynamics of a fluid phase bilayer on a solid support as observed by a molecular dynamics computer simulation, *Langmuir* 24(21) (2008) 12469–12473.
- [46] C.M. Hartshorn, C.M. Jewett, J.A. Brozik, Molecular effects of a nanocrystalline quartz support upon planar lipid bilayers, *Langmuir* 26(4) (2010) 2609–2617.
- [47] S.E. Feller, R.M. Venable, R.W. Pastor, Computer simulation of a dppc phospholipid bilayer: Structural changes as a function of molecular surface area, *Langmuir* 13(24) (1997) 6555–6561.
- [48] S.J. Marrink, A.H. de Vries, A. Mark, Coarse grained model for semi-quantitative lipid simulation, *J. Phys. Chem. B* 108(2) (2004) 750–760.
- [49] R.S. Cantor, The lateral pressure profile in membranes: A physical mechanism of general anesthesia, *Biochemistry* 36(9) (1997) 2339–2344.
- [50] J.N. Israelachvili, *Intermolecular and Surface Forces: With Applications to Colloidal and Biological Systems*, second ed., Academic Press, Amsterdam, 1992.
- [51] C.A. Keller, B. Kasemo, Surface specific kinetics of lipid vesicles adsorption measured with a quartz crystal microbalance, *Biophys. J.* 75(3) (1998) 1397–1402.
- [52] J.M. Johnson, T. Ha, S. Chu, S.G. Boxer, Early steps of supported bilayer formation probed by single vesicle fluorescence assays, *Biophys. J.* 83(6) (2002) 3371–3379.
- [53] S. Marrink, H. Risselada, S. Yefimov, D. Tieleman, A. de Vries, The Martini force field: Coarse grained model for biomolecular simulations, *J. Phys. Chem. B* 111(27) (2007) 7812–7824.
- [54] S.V. Bennun, A.N. Dickey, C. Xing, R. Faller, Simulations of biomembrane and water: Important technical aspects, *Fluid Phase Equilib.* 261(1–2) (2007) 18–25.
- [55] G. Brannigan, L. Lin, F.L.H. Brown, Implicit solvent simulation models for biomembranes, *Eur. Biophys. J.* 35(2) (2006) 104–124.
- [56] S.V. Bennun, M.I. Hoopes, C. Xing, R. Faller, Coarse grained modeling of lipids, *Chem. Phys. Lipids* 159(2) (2009) 59–66.
- [57] J.C. Shelley, M.Y. Shelley, R.C. Reeder, S. Bandyopadhyay, M.L. Klein, A coarse grain model for phospholipid simulations, *J. Phys. Chem. B* 105(19) (2001) 4464–4470.
- [58] M.J. Stevens, Coarse-grained simulations of lipid bilayers, *J. Chem. Phys.* 121(23) (2004) 11942–11948.
- [59] O. Lenz, F. Schmid, A simple computer model for liquid bilayers, *J. Mol. Liq.* 117(1–3) (2005) 147–152.
- [60] I.R. Cooke, K. Kremer, M. Deserno, Tunable generic model for fluid bilayer membranes, *Phys. Rev. E* 72(1) (2005) 011506, (1–4).



- [61] O. Farago, "Water-free" computer model for fluid bilayer membranes, *J. Chem. Phys.* 119(1) (2003) 596–605.
- [62] G. Brannigan, F.L.H. Brown, Solvent-free simulations of fluid membrane bilayers, *J. Chem. Phys.* 120(2) (2004) 1059–1071.
- [63] Takasu Noguchi, Self-assembly of amphiphiles into vesicles: A Brownian dynamics simulation, *Phys. Rev. E* 64 (2001) 041913.
- [64] A.H. de Vries, A.E. Mark, S.J. Marrink, The binary mixing behavior of phospholipids in a bilayer: A molecular dynamics study, *J. Phys. Chem. B* 108(7) (2004) 2454–2463.
- [65] P.S. Niemelä, S. Ollila, M.T. Hyvönen, M. Karttunen, I. Vattulainen, Assessing the nature of lipid raft membranes, *PLoS Comput. Biol.* 3(2) (2007) e34.
- [66] S.A. Pandit, D. Bostick, M.L. Berkowitz, Complexation of phosphatidylcholine lipids with cholesterol, *Biophys. J.* 86(3) (2004) 1345–1356.
- [67] L. Saiz, M.L. Klein, Electrostatic interactions in a neutral model phospholipid bilayer by molecular dynamics, *J. Chem. Phys.* 116(7) (2002) 3052–3057.
- [68] A.K. Sum, R. Faller, J.J. de Pablo, Molecular simulation study of phospholipid bilayers and insights of the interactions with disaccharides, *Biophys. J.* 85(5) (2003) 2830–2844.
- [69] S.E. Feller, C.A. Brown, D.T. Nizza, K. Gawrisch, Nuclear Overhauser enhancement spectroscopy cross-relaxation rates and ethanol distribution across membranes, *Biophys. J.* 82(3) (2002) 1396–1404.
- [70] L. Monticelli, S. Kandasamy, X. Periole, R. Larson, D. Tieleman, S. Marrink, The Martini coarse grained force field: Extension to proteins, *J. Chem. Theory Comput.* 4 (5) (2008) 819–834.
- [71] R. Goetz, R. Lipowsky, Computer simulations of bilayer membranes: Self-assembly and interfacial tension, *J. Chem. Phys.* 108(17) (1998) 7397–7409.
- [72] J. Drouffe, A. Maggs, S. Leibler, Computer simulations of self-assembled membranes, *Science* 254(5036) (1991) 1353–1356.
- [73] L. Saiz, M.L. Klein, Computer simulation studies of model biological membranes, *Acc. Chem. Res.* 35(6) (2002) 482–489.
- [74] E. Sackmann, Supported membranes: Scientific and practical applications, *Science* 271 (5245) (1996) 43–48.
- [75] C. Xing, R. Faller, Coarse-grained simulations of supported and unsupported lipid monolayers, *Soft Matter* 5(22) (2009) 4526–4530.
- [76] B. Silver, *Physical Chemistry of Membranes: An Introduction to the Structure and Dynamics of Biological Membranes*, Kluwer, Dordrecht, NL, 1985.
- [77] J.F. Nagle, Area/lipid of bilayers from NMR, *Biophys. J.* 64(5) (1993) 1476–1481.
- [78] J.F. Nagle, R.T. Zhang, S. Tristram-Nagle, W.J. Sun, H.I. Petrache, R.M. Suter, X-ray structure determination of fully hydrated L( $\alpha$ ) phase dipalmitoylphosphatidylcholine bilayers, *Biophys. J.* 70(3) (1996) 1419–1431.
- [79] J.F. Nagle, S. Tristram-Nagle, Structure of lipid bilayers, *Biochim. Biophys. Acta (Rev. Biomemb.)* 1469(3) (2000) 159–195.
- [80] J.A. Killian, Hydrophobic mismatch between proteins and lipids in membranes, *Biochim. Biophys. Acta (Rev. Biomemb.)* 1376(3) (1998) 401–415.
- [81] J.H. Irving, J.G. Kirkwood, The statistical mechanical theory of transport processes. IV. The equations of hydrodynamics, *J. Chem. Phys.* 18(6) (1950) 817–829.
- [82] A. Seelig, J. Seelig, Effect of a single cis double-bond on structure of a phospholipid bilayer, *Biochemistry* 16(1) (1977) 45–50.
- [83] S. Shenoy, R. Moldovan, J. Fitzpatrick, D.J. Vanderah, M. Deserno, M. Lösche, In-plane homogeneity and lipid dynamics in tethered bilayer lipid membranes (tBLMs), *Soft Matter* 6(6) (2010) 1263–1274.
- [84] B.Y. Wong, R. Faller, Phase behavior and dynamic heterogeneities in lipids: A coarse-grained simulation study of DPPC–DPPE mixtures, *Biochim. Biophys. Acta (Biomemb.)* 1768(3) (2007) 620–627.

- [85] R.S. Cantor, Receptor desensitization by neurotransmitters in membranes: Are neurotransmitters the endogenous anesthetics? *Biochemistry* 42(41) (2003) 11891–11897.
- [86] A. Blicher, K. Wodzinska, M. Fidorra, M. Winterhalter, T. Heimburg, The temperature dependence of lipid membrane permeability, its quantized nature, and the influence of anesthetics, *Biophys. J.* 96(11) (2009) 4581–4591.
- [87] L.F. Bisson, Stuck and sluggish fermentations, *Am. J. Enol. Vitic.* 50(1) (1999) 107–119.
- [88] S.I. Sukhraev, W.J. Sigurdson, C. Kung, F. Sachs, Energetic and spatial parameters for gating of the bacterial large conductance mechanosensitive channel, *MscL*, *J. Gen. Physiol.* 113(4) (1999) 525–593.
- [89] M. Przybylo, J. Sykora, J. Humpolickova, A. Benda, A. Zan, M. Hof, Lipid diffusion in giant unilamellar vesicles is more than 2 times faster than in supported phospholipid bilayers under identical conditions, *Langmuir* 22(22) (2006) 9096–9099.
- [90] C. Xing, How Solid Substrates Affect a Lipid Bilayer: A Molecular Dynamics Study, 2009, Ph.D. thesis, University of California Davis.
- [91] R. Faller, S.-J. Marrink, Simulation of domain formation in mixed DLPC–DSPC lipid bilayers, *Langmuir* 20(18) (2004) 7686–7693.
- [92] F. Müller-Plathe, P. Bordat, Reverse non-equilibrium molecular dynamics, *Novel Methods in Soft Matter Simulations* vol. 640 Springer, Heidelberg, 2004, p. 2256.
- [93] W. Helfrich, Elastic properties of lipid bilayers: theory and possible experiments, *Z. Naturforsch. C* 28(11) (1973) 693–703.

# X-RAY AND NEUTRON SCATTERING STUDIES OF LIPID–STEROL MODEL MEMBRANES

Bibhu Ranjan Sarangi,<sup>1</sup> Sanat Karmakar,<sup>2</sup> and  
V.A. Raghunathan<sup>1,\*</sup>

## Contents

1. Introduction	160
2. Scattering Studies on Model Membranes	161
3. Influence of Sterols on the Structure and Phase Behavior of Lipid Bilayers	167
3.1. Phase Behavior of Pure Lipid Bilayers	167
3.2. Influence of Cholesterol on the Structure and Properties of Lipid Bilayers	168
3.3. Orientation of Cholesterol in the Lipid Bilayer	171
3.4. Phase Behavior of Lipid–Cholesterol Membranes	173
3.5. Scattering Studies on other Sterols in Lipid Bilayers	176
4. Fluid–Fluid Phase Separation in Raft Mixtures	178
4.1. Partitioning of Cholesterol between the $l_o$ and $l_d$ Phases	182
4.2. Relevance to Biomembranes	182
References	183

## Abstract

Sterols are major components of many biomembranes and are known to play an important role in several biological processes. In order to understand the complex lipid–sterol interactions and their influence on membrane structure and properties, model membranes containing cholesterol and other sterols have been widely studied using a variety of experimental techniques. This chapter gives a brief review of X-ray and neutron scattering studies of these systems, highlighting the detailed structural information they provide.

\* Corresponding author: Tel.: +91-80-2361-0124; Fax: +91-80-2361-0492  
E-mail address: [varaghu@rri.res.in](mailto:varaghu@rri.res.in)

<sup>1</sup> Raman Research Institute, Bangalore 560 080, India

<sup>2</sup> Department of Physics, Jadavpur University, Kolkata 700 032, India

## 1. INTRODUCTION

Sterols are essential components of many biomembranes. Plasma membranes of higher eukaryotes contain substantial amounts of cholesterol, whereas ergosterol is present in membranes of lower eukaryotes, such as yeast and fungi [1]. Sitosterol and stigmasterol are structurally related to cholesterol and are found mainly in plasma membranes of higher plants (Fig. 1) [2]. Cholesterol is known to influence various membrane properties, such as fluidity and lateral membrane organization, and to play a central role in various biological processes involving the plasma membrane [3–5]. Cholesterol is also believed to be responsible for organizing membrane lipids into submicrometer-sized domains, commonly referred to as rafts [6]. Although direct evidence for their existence is still a matter of some debate, lipid rafts have been invoked in several cellular functions, such as intracellular trafficking of lipids and lipid-anchored proteins, and signal transduction [6–10].

The complex nature of biological membranes, especially the presence of innumerable molecular species, makes them unsuitable for many quantitative experiments. Therefore, model membranes containing one or a few lipid species have been widely studied in order to gain insights into the behavior of biomembranes. Not surprisingly, cholesterol was perhaps the

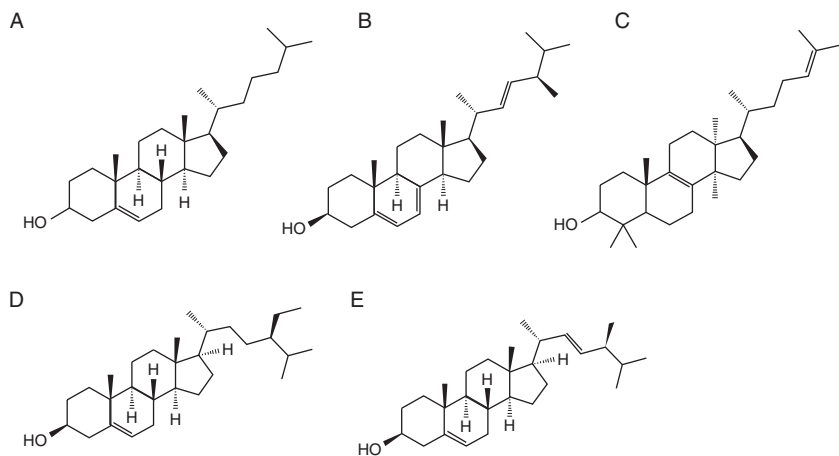


**Figure 1** Structures of some representative sterols: (A) cholesterol, (B) ergosterol, (C) lanosterol, (D) sitosterol, and (E) stigmasterol. Cholesterol is a major component of animal plasma membranes, whereas ergosterol is found in the cell membranes of fungi. Lanosterol is an important precursor in the biosynthesis of cholesterol. Sitosterol and stigmasterol are found in plants.

first biologically relevant molecule whose influence on model membranes was investigated in detail, and over the past few decades there have been a very large number of studies on the influence of cholesterol and other sterols on model membranes using a variety of techniques [8,11,12]. Although spectroscopic techniques have been employed in the majority of these investigations, X-ray and neutron scattering experiments have provided invaluable information about many aspects of the organization of sterols in membranes. In recent years, there has been renewed interest in lipid–sterol systems in light of the raft hypothesis [6]. In this review, we give a brief account of X-ray and neutron scattering studies on lipid–sterol mixtures with emphasis on recent work. In Section 2, the general methodology of these techniques is discussed. Studies on the influence of sterols on the structure and phase behavior of lipid membranes are discussed in Section 3. In Section 4, we discuss the phase behavior of “raft mixtures”, which are ternary mixtures containing cholesterol and two species of lipids with very different chain melting transition temperatures. They exhibit fluid–fluid immiscibility, and hence have been used as models for raft forming plasma membranes.

## 2. SCATTERING STUDIES ON MODEL MEMBRANES

X-ray scattering has been widely used to study the structure and phase behavior of lipid–sterol bilayers. The easy availability of laboratory X-ray sources makes it possible to carry out detailed experiments on the phase behavior of these systems, whereas the high intensity of synchrotron sources facilitates investigations on the kinetics of phase transformations.

The methods used for the structural analysis of lipid–sterol mixtures are essentially the same as those used to probe pure lipid bilayers, and have been reviewed in Ref. [13]. Almost all X-ray diffraction experiments on lipid–water systems are carried out either on liposomal preparations or on samples aligned on substrates. Both these systems consist of periodic stacks of bilayers; in the former case, they form multilamellar vesicles and in the latter they are aligned parallel to the substrate. All bilayer forming lipids exhibit a fluid lamellar ( $L_\alpha$ ) phase at higher temperatures with liquid-like in-plane order. It is this phase of lipids that is biologically most relevant. At low temperatures, they form a lamellar gel phase, where the hydrocarbon chains of the lipid molecules form a two-dimensional (2-D) lattice in the plane of the bilayer. There are two types of gel phases; in the  $L_\beta$  phase, the long axes of the chains are aligned along the bilayer normal, whereas in the  $L_{\beta'}$  phase, the chains are tilted at an angle of about  $30^\circ$ . Some lipids also show an intermediate phase between these two called the ripple or  $P_{\beta'}$  phase. In this phase, the bilayers have a periodic height modulation and stack into a 2-D lattice (Fig. 2).

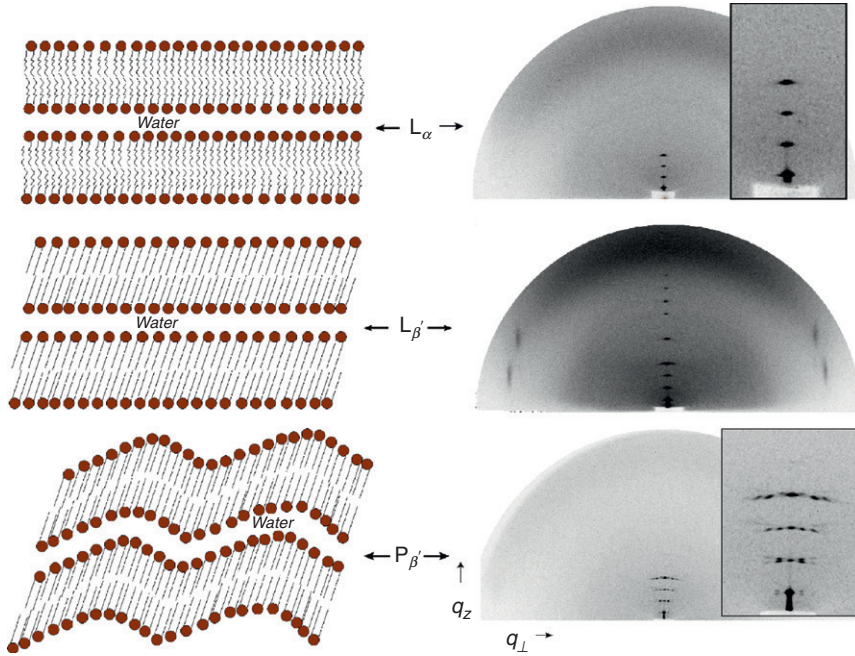


**Figure 2** Schematic of the structures of the fluid ( $L_\alpha$ ), gel ( $L_{\beta'}$ ), and ripple ( $P_{\beta'}$ ) phases of lipid–water systems and their diffraction patterns. The lamellar  $L_\alpha$  and  $L_{\beta'}$  phases give rise to a set of reflections in the small angle region along  $q_z$ ,  $z$  being the direction of the bilayer normal. The sharp wide angle reflections in the  $L_{\beta'}$  phase arise from the 2-D crystalline arrangement of the chains of the lipid molecules, whose long axes are tilted at an angle from  $z$ . The height modulated bilayers in the  $P_{\beta'}$  phase give rise to a 2-D oblique unit cell.

The lattice parameter(s) of the different structures formed by the bilayers can be directly determined from the position of the peaks in the small angle region of their diffraction patterns. The wide angle region of these patterns contains information about the conformation of the hydrocarbon chains. The disordered chains in the fluid phase give rise to a broad peak in the wide angle region, reflecting the liquid-like in-plane positional order within the bilayer. The corresponding peaks in the gel phase are much sharper due to the in-plane crystalline order. In the  $L_\beta$  gel phase, the untilted chains give rise to a pair of reflections in the wide angle region at  $q_z = 0$  and  $q_\perp = 4\pi/(\sqrt{3}a)$ ,  $a$  being the lattice parameter of the 2-D hexagonal lattice formed by the chains, and  $\hat{z}$  the direction of the bilayer normal. In the  $L_{\beta'}$  gel phase, the tilted chains give rise to two or three pairs of reflections in the wide angle region, from whose positions along  $q_z$  both the magnitude and the direction of the chain tilt with respect to the orientation of the 2-D hexagonal lattice can be determined. Aligned samples are advantageous in

this regard since the  $q_z$  values of these reflections can be directly obtained from their diffraction patterns [14], whereas only the values of  $q = \sqrt{q_z^2 + q_{\perp}^2}$ , can be obtained using unoriented samples.

The phase diagram of a lipid–water system can be determined from its diffraction patterns, since a change of phase is accompanied by changes in the stacking periodicity of the bilayers and/or in the in-plane order within each bilayer (Fig. 3). Regions of multiphase coexistence can also be easily determined if the sample separates into bulk phases with different values of the lattice parameters. On the other hand, if the sample phase separates to form uncorrelated domains in the bilayer, it is difficult to deduce the occurrence of phase separation due to the presence of a single lamellar periodicity. However, if the in-plane order in the domains is different from that in the rest of the membrane, phase separation can often be inferred from the coexisting wide angle chain reflections.

More detailed structural information about the bilayer is contained in the transbilayer electron density profile  $\rho(z)$ , which can be calculated from the diffraction data. The Lorentz corrected scattered intensity from a stack of bilayers is given by [13],

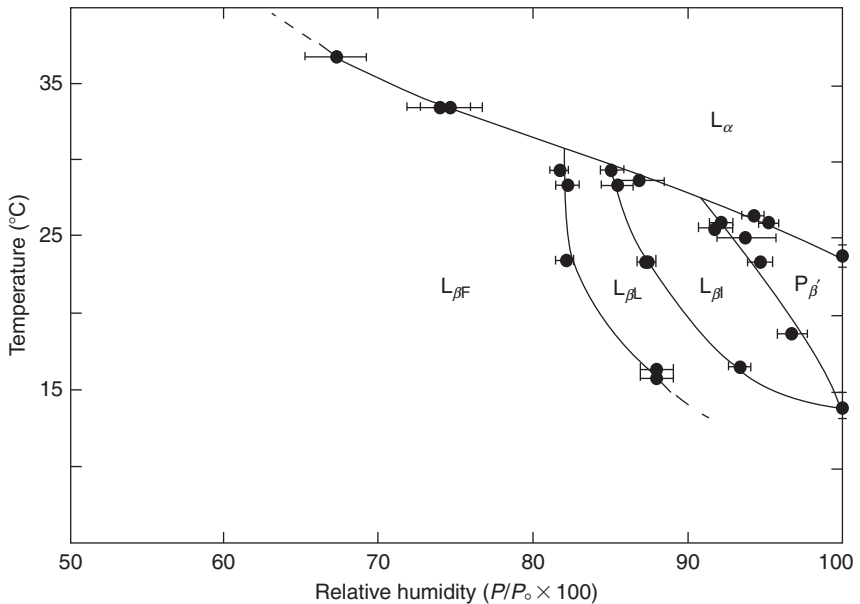


**Figure 3** Temperature–relative humidity phase diagram of DMPC–water system deduced from X-ray diffraction data. The three  $L_{\beta'}$  phases correspond to different orientations of the chain tilt with respect to that of the chain lattice, namely, toward nearest neighbor (NN), toward next nearest neighbor (NNN), and toward an in-between direction (from Ref. [27]).

$$I(q) = S(q)|f(q)|^2, \quad (1)$$

where  $S(q)$  is the structure factor, and  $f(q)$  the form factor.  $f(q)$  is the Fourier transform of  $\rho(z)$ . In the simplest description, the membrane stack can be looked upon as a 1-D lattice of lamellar periodicity  $d$ , and then  $S(q)$  is a set of delta functions at  $q = hq_0$ , with  $q_0 = 2\pi/d$  and  $h = 1, 2, 3$ , etc. The intensities of the set of lamellar reflections can then be written as

$$I(hq_0) = |f(hq_0)|^2. \quad (2)$$

$\rho(z)$  can be calculated by Fourier inversion of  $f(q)$ , if the phases of these reflections can be somehow determined. This problem is simplified by the fact that the phases of the reflections are constrained to be either 0 or  $\pi$ , since the flat bilayer is symmetric about its mid-plane. Hence,

$$\rho(z) = \sum_h f(hq_0) \cos(hq_0 z). \quad (3)$$

Two methods have been used to phase the reflections from the lamellar phases of bilayers. In the first method, diffraction data are collected at different levels of swelling of the lamellar phase, by changing the amount of water in the sample. The zeros of  $f(q)$ , and hence the phases of the reflections, can be deduced from these diffraction data, if the lamellar periodicity  $d$  can be varied over a sufficient range, without altering the membrane structure in any way (Fig. 4).

In the second method, a model for  $\rho(z)$  is constructed based on some *a priori* knowledge of the structure of the phase. The unknown structural features are taken into account through a few adjustable parameters, whose values are determined from the best fit of the observed diffraction data with those calculated from the model. For example,  $\rho(z)$  can be written as the sum of three Gaussian functions corresponding to the two electron-rich headgroups and the electron-deficient terminal methyl group (Fig. 5),

$$\rho(z) = \rho_H \left\{ e^{-(z+z_h)^2/2\sigma_h} + e^{-(z-z_h)^2/2\sigma_h} \right\} - \rho_M e^{-z^2/2\sigma_m}, \quad (4)$$

where  $\rho_H$  and  $\sigma_h$  are the height and width of headgroup Gaussian function, and  $\rho_M$  and  $\sigma_m$  the corresponding parameters for the terminal methyl groups. The values of these parameters as well as that of  $z_h$ , which is related to the thickness of the bilayer, are obtained from the best fit of the observed values of the intensities with those calculated from the model. The phases of the reflections obtained from the model are then combined with their observed magnitudes and Fourier transformed to get the bilayer electron



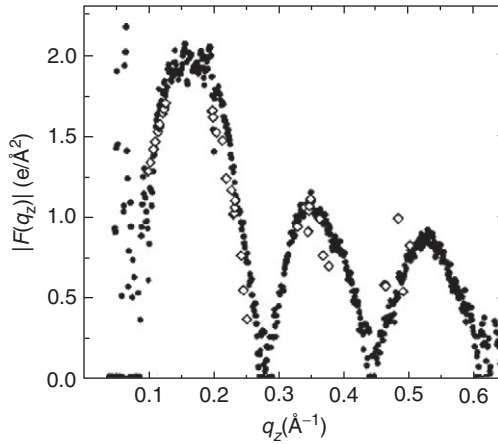


**Figure 4** The magnitude of the bilayer form factor  $f(q)$  obtained from swelling experiments. The zeroes of  $f(q)$ , and hence the relative phases of the reflections, can be determined from such a plot (from Ref. [24]).

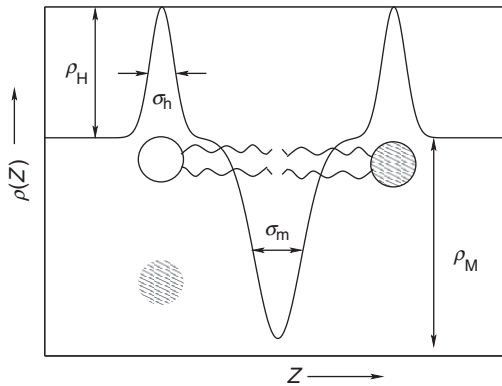


**Figure 5** A widely used model for the transbilayer electron density  $\rho(z)$ . The head-group regions are taken as Gaussians of magnitude  $\rho_H$  and width  $\sigma_h$ , and the central methyl region as a Gaussian of magnitude  $-\rho_M$  and width  $\sigma_m$ . The electron densities of the water and methylene regions are taken to be equal. The values of these model parameters are obtained from the best fit of the calculated diffraction data with the observed ones.

density profile  $\rho(z)$ . Several important structural parameters, such as the membrane thickness and number of water molecules per lipid, can be estimated once  $\rho(z)$  is known [13,15].

Thermal fluctuations destroy true long-range positional order in a 1-D system, such as a stack of bilayers; instead, one has quasi-long range order characterized by power-law decay of correlations [16,17]. As a result,  $S(q)$  of

a lamellar phase does not consist of a set of delta functions at the reciprocal lattice points, but of cusp-like singularities, whose heights decrease rapidly with increasing  $q$ , reaching the limiting value of 1 rather rapidly (Fig. 6). Approximate analytical expressions for  $S(q)$  have been obtained, which can be used to fit the observed  $I(q)$  over its entire range of  $q$  [18–22]. Although proper analysis of the data requires the use of this  $S(q)$ , it turns out that some important features of the electron density profile, such as the separation between the two peaks corresponding to the headgroups ( $d_{\text{HH}}$ ), which is a measure of the bilayer thickness, are not sensitive to these corrections [23].

As mentioned above, thermal undulations of the bilayers lead to cusp-like singularities at the reciprocal lattice points, with  $I(q) \sim (q - hq_0)^{-1+\eta}$  for unoriented liposomal samples, where  $\eta = h^2 q_0^2 k_B T / (8\pi\sqrt{KB})$ ,  $K$  and  $B$  being the bulk moduli for bending and compression of the lamellar phase, and  $T$  the temperature [16,17].  $K = K_c d$ , where  $K_c$  is the bending rigidity of the bilayer and  $d$  the lamellar periodicity. In addition, an in-plane correlation length  $\xi$ , which is proportional to the ratio of  $K$  and  $B$  can be measured from the  $q_{\perp}$  dependence of the scattered intensity from aligned samples at large values of  $q_z$  [24]; it can also be obtained from the scattered intensity at very small angles from an unoriented sample if  $K_c$  is sufficiently small [20]. Hence,  $K_c$  can be estimated once  $\eta$  and  $\xi$  are known.

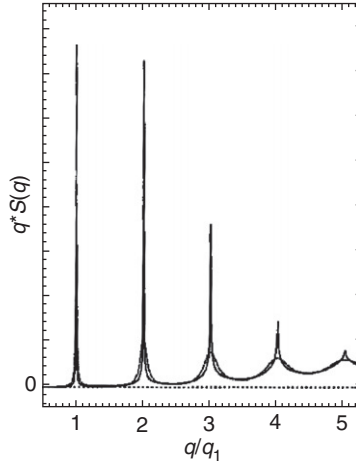


**Figure 6** Models for the structure factor  $S(q)$  of a lamellar phase. Dashed lines correspond to the paracrystalline theory, where the layers are assumed to be flat, but the lamellar stacking is assumed to be random with a nonzero mean. The solid line corresponds to the Caillé theory, where thermal undulations of the layers are taken into account. Note that both these models account for the drastic reduction in the intensities of the higher order peaks, but the line shapes predicted by them are different. High resolution experiments are in agreement with the cusp-like singularities predicted by the Caillé theory (from Ref. [21]).

Neutron beams, being much weaker, have some disadvantage over X-rays. Nevertheless, small angle neutron scattering (SANS) and quasielastic neutron scattering (QENS) have been very useful in studying certain aspects of membrane structure and dynamics [25]. The main advantage of neutron scattering lies in the fact that individual components can be selectively deuterated, thereby enhancing the local contrast, without affecting the structure of the system in any manner. Scattering length density profiles of the labeled and unlabeled samples, calculated on similar lines as for X-rays, can then be used to locate the position of labeled groups within the bilayer. SANS can also be used to study a dilute dispersion of uncorrelated bilayers in the form of vesicles, by enhancing the contrast between the bilayer and solvent, achieved either by deuterating the chains of the lipid or by replacing H<sub>2</sub>O by D<sub>2</sub>O. In these systems  $S(q) \approx 1$ , and the scattered intensity directly gives the size–polydispersity–averaged form factor of the vesicles. The structural details of the bilayer in this case are usually obtained by modeling the scattering length density profile of the vesicle and fitting the calculated  $I(q)$  with the observed one by tuning some of the model parameters.

The low energy of thermal neutrons makes it possible to study the dynamics of these systems using QENS, where the scattered intensity is measured as a function of the scattering vector  $q$  as well as the shift in the energy of the neutrons.

### 3. INFLUENCE OF STEROLS ON THE STRUCTURE AND PHASE BEHAVIOR OF LIPID BILAYERS

#### 3.1. Phase Behavior of Pure Lipid Bilayers

Most of the experiments on the influence of sterols on model membranes have been carried out using phospholipids, such as phosphatidylcholines (PCs), and sphingolipids, such as sphingomyelin (SM), since these are the two most abundant lipid species in many biological membranes. PCs with saturated chains, such as dipalmitoylphosphatidylcholine (DPPC) and dimyristoylphosphatidylcholine (DMPC), exhibit the  $L_\alpha$ ,  $P_{\beta'}$ , and  $L_{\beta'}$  phases as a function of decreasing temperature at high hydration (Fig. 3) [26,27]. Three distinct  $L_{\beta'}$  phases are observed, which differ in the direction of the chain tilt with respect to the orientation of the 2-D chain lattice [27]. The modulated bilayers in the ripple ( $P_{\beta'}$ ) phase usually stack in a 2-D oblique lattice [28]. The  $P_{\beta'} \rightarrow L_\alpha$  transition is referred to as the main or chain melting transition, whereas the  $L_{\beta'} \rightarrow P_{\beta'}$  transition is called the pretransition. Phosphatidylethanolamines (PE) with saturated chains do not have a chain tilt in the gel ( $L_\beta$ ) phase and do not exhibit the intermediate ripple phase. PCs with unsaturated chains, such as dioleoylphosphatidylcholine (DOPC), exhibit only the fluid phase around the ambient temperature. This

is also the case with egg-PC and brain-SM, which are mixtures containing lipids having the same headgroup, but with chains differing in their lengths and degree of unsaturation.

### 3.2. Influence of Cholesterol on the Structure and Properties of Lipid Bilayers

Addition of cholesterol to a lipid bilayer brings about various structural changes, thereby influencing its physical properties and phase behavior. Early experiments found that 20–33 mol% of cholesterol suppresses the gel phase of lipids with saturated chains and stabilizes the fluid phase over a wide range of temperature and water content [29,30]. From the decrease in the angular spread of the wide angle reflections in the diffraction patterns of oriented stacks of PC–cholesterol bilayers, it was established that cholesterol increases the orientational ordering of the lipid chains in the fluid phase [29,31]. These early observations have been quantified in recent experiments, where an average orientational order parameter ( $S$ ) of the chains has been determined from the wide angle data (Fig. 7) [32].  $S$  is found to increase with increasing cholesterol concentration. Further, the increase in  $S$  depends on the degree of unsaturation of the chains; it being maximum for lipids with saturated chains. The headgroup-to-headgroup separation ( $d_{\text{HH}}$ ) obtained from the electron density profiles is found to be insensitive to the level of hydration, unlike in the case of pure lipids where it changes significantly; cholesterol has hence been called a membrane thickness buffer [31,33,34]. The bilayer thickness of lipids with saturated and monounsaturated chains is found to increase with increasing cholesterol concentration and reach a maximum value slightly before the solubility limit is reached [32,34]. The influence of cholesterol on bilayers of monounsaturated PCs has also been studied using SANS on unilamellar vesicles (ULVs). The membrane thickness, lateral area per lipid, and the headgroup hydration are found to monotonically increase with increasing cholesterol concentration up to 45 mol% [35]. Since the increase in the bilayer thickness occurs at constant volume of the lipid, the lateral area of a lipid molecule in the bilayer decreases with increasing cholesterol concentration. Hence, cholesterol is often said to condense the bilayer. The cholesterol-induced enhancement of membrane thickness has been measured for many lipids and some representative data are presented in Table 1.

Influence of cholesterol on the membrane rigidity of some PCs has been probed using X-ray and neutron diffraction. From the amount of swelling of the  $L_{\alpha}$  phase on approaching the chain melting transition from higher temperatures, which has been interpreted as arising from a lowering of the membrane rigidity on approaching this transition, it is found that the rigidity of DMPC bilayers first decreases with increasing cholesterol concentration and then starts to increase at around 3–4 mol% of cholesterol [36].

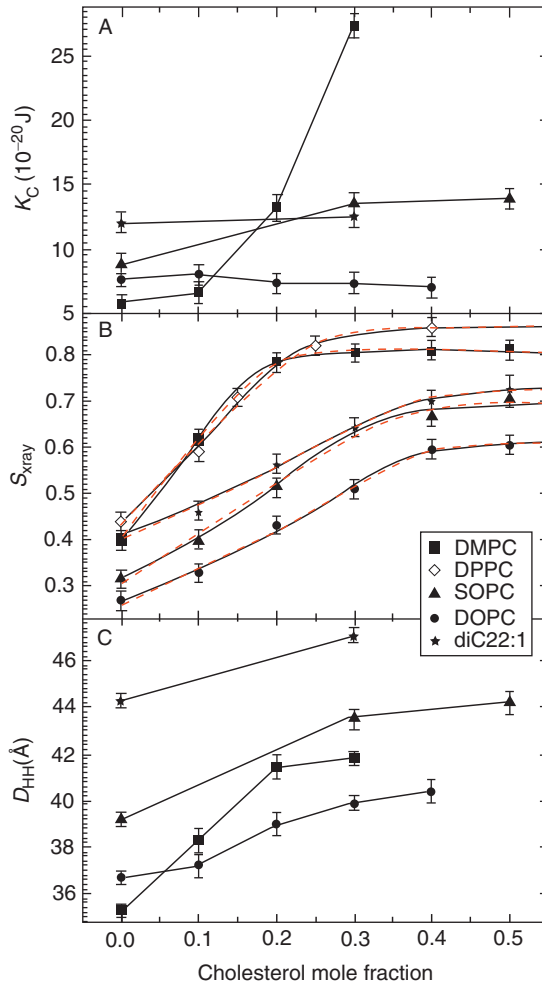


**Figure 7** Variation of the membrane rigidity  $K_C$  (A), chain order parameter  $S$  (B), and bilayer thickness  $D_{\text{HH}}$  (C) with cholesterol concentration obtained from X-ray diffraction studies on aligned multilayers of lipids with two saturated chains (DPPC and DMPC), one monounsaturated chain (SOPC), and two monounsaturated chains (DOPC and diC22:1) (from Ref. [32]).

The influence of higher concentrations of cholesterol on the membrane rigidity of some PCs with saturated and monounsaturated chains has also been measured using X-ray diffraction from bilayer stacks aligned on a substrate (Fig. 7) [32].  $K_C$  of DMPC bilayers, with two saturated chains, is found to increase substantially with cholesterol concentration, whereas  $K_C$  of DOPC, with two monounsaturated chains, is unaffected by cholesterol; SOPC with one saturated and one monounsaturated chain shows an

**Table 1** Changes in the bilayer thickness of some lipids due to different sterols, extracted from scattering data in the literature.  $X_s$  in the sterol concentration

Lipid	Sterol	T (°C)	$X_s$ (mol%)	$\Delta d$ (nm)	Ref.
DMPC	Cholesterol	35	5	0.20	[61]
			10	0.25	
			20	0.49	
			40	0.55	
	Sitosterol	35	5	0.19	
			10	0.24	
			20	0.40	
			40	0.46	
	Stigmasterol	35	5	0.14	
			10	0.31	
			20	0.33	
			40	0.35	
DOPC	Cholesterol	-	17	0.15	[35]
			29	0.28	
			38	0.48	
			45	0.61	
DMPC	Cholesterol	30	10	0.30	[32]
			20	0.62	
DOPC	Cholesterol	30	10	0.05	[32]
			20	0.23	
			30	0.32	
			40	0.37	
SOPC	Cholesterol	30	10	0.15	[32]
			20	0.30	
			30	0.44	
			40	0.47	
			50	0.50	
DMPC	Cholesterol	30	10	0.29	[34]
			20	0.52	
			30	0.67	
			40	0.74	
DOPC	Cholesterol	30	10	0.15	[34]
			20	0.30	
			30	0.41	
			40	0.34	
SOPC	Cholesterol	30	10	0.20	[34]
			20	0.37	
			30	0.50	
			40	0.56	

intermediate behavior. It is often said that cholesterol fluidizes the gel phase and rigidifies the fluid phase. While the first part of this statement is always true, above results suggest that the second part is not true in all cases. Although the addition of cholesterol always seems to increase the ordering of the chains in the fluid phase, it may not result in a higher bilayer rigidity in the case of lipids with unsaturated chains.

X-ray diffraction has also been used to determine the maximum solubility of cholesterol in PC and PE bilayers, by monitoring the reflections from the phase-separated cholesterol crystallites. The solubility limits are found to be 66 mol% for PCs and 51 mol% for PEs and were found to be rather insensitive to variations in the acyl chains [37]. Other studies also indicate that cholesterol solubility in the bilayer is very sensitive to the nature of the headgroup, decreasing in the order PC > PG ~ PE > PS. In the case of PCs, polyunsaturation of the chains is found to strongly promote the phase separation of cholesterol [38].

In addition to changes in the bilayer structure and properties discussed above, cholesterol is known to induce nonlamellar phases in some lipids, which might be important in processes such as membrane fusion. An inverted hexagonal phase has been observed at high temperatures in mixtures of cholesterol with lipids with monounsaturated chains [39]. Cholesterol has also been shown to induce a bicontinuous cubic phase in some unsaturated PCs and also in a PC with saturated, branched chains, near the  $L_{\alpha}$ -hexagonal ( $H_{II}$ ) transition of the mixtures [40].

### 3.3. Orientation of Cholesterol in the Lipid Bilayer

Comparing the transbilayer electron density profiles of lipid–cholesterol membranes determined from diffraction data with those obtained from molecular models, the cholesterol molecule was shown to be largely immersed in the hydrocarbon core of the egg-PC bilayer, with its hydroxyl group near the water interface [41]. This orientation of cholesterol was confirmed by neutron scattering studies on deuterium labeled cholesterol in egg-PC bilayers [42]. More recent experiments, prompted by suggestions in the literature that cholesterol is expelled from the bilayer at a temperature corresponding to the fluid-to-gel transition of the pure lipid, have firmly established these earlier findings and show that cholesterol remains embedded in the bilayer even at lower temperatures (Fig. 8) [43].

Although cholesterol is oriented normal to the bilayer with its hydroxyl group at the bilayer water interface in most membranes, recent experiments on polyunsaturated lipids show that this is not always the case. Neutron scattering studies on selectively deuterated cholesterol–diarachidonyl phosphatidylcholine (DAPC) samples reveal that the hydroxyl group of cholesterol resides at the center of the bilayer (Fig. 9) [44,45]. This change in the orientation of cholesterol is attributed to the high degree of disorder of the

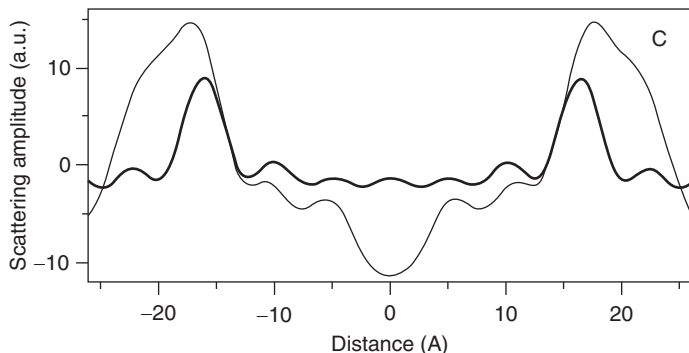


**Figure 8** Transbilayer scattering length density profile of  $[2,2,3,4,6\text{-}^2\text{H}_6]$ cholesterol in DMPC bilayers (bold line) and that of the entire bilayer with 30 mol% labeled cholesterol (thin line) (from Ref. [43]).

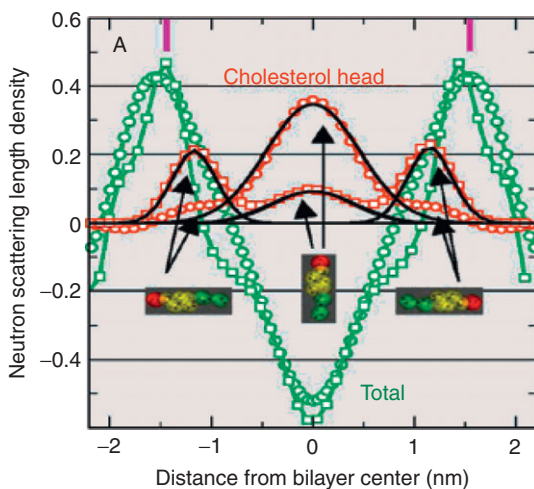


**Figure 9** Total transbilayer scattering length density profiles (green) of diarachidonyl phosphatidylcholine (DAPC) containing 10 mol%  $[2,2,3,4,6\text{-}^2\text{H}_6]$ cholesterol and the difference profile between bilayers with labeled and unlabeled cholesterol headgroups (red, multiplied by 5) obtained from experiments (circles) and simulations (squares). The arrows indicate the density maxima arising from the two different orientations of cholesterol in the bilayer (from Ref. [45]). (For interpretation of the references to color in this figure legend, the reader is referred to the Web version of this chapter.)

polyunsaturated chains, which makes any close contact with the planar, rigid steroid moiety very unfavorable. A similar reorientation of cholesterol has also been suggested in DMPC bilayers above 50 °C [46], but does not seem to have been confirmed by subsequent experiments.



QENS studies on DPPC–cholesterol mixtures reveal highly anisotropic diffusion of cholesterol within the bilayer. The rather high amplitude out-of-plane diffusion parallel to the bilayer normal observed at higher temperatures strongly suggests that cholesterol can move between the apposite leaflets of the bilayer, whereas it remains predominantly confined within its host monolayer at lower temperatures. The in-plane motion of cholesterol is dominated by discrete large-angle rotational jumps, rather than a quasi-continuous rotational diffusion by small angle jumps [47]. Similar studies have also been carried out with lanosterol and ergosterol [48]. These sterols are found to exhibit a much smaller out-of-plane motion compared to cholesterol, confining them to the host monolayer. Thus, slight alterations in the structure of the sterol can affect their dynamics in the bilayer, which in turn may be relevant to the membrane micromechanical properties.

### 3.4. Phase Behavior of Lipid–Cholesterol Membranes

A temperature–composition phase diagram of lipid–cholesterol bilayers in excess water conditions has been constructed using X-ray diffraction by tracking the lamellar periodicity of DPPC–cholesterol mixtures as a function of temperature and cholesterol content (Fig. 10) [49]. The coexistence of two lamellar phases was observed below 30 °C for a range of cholesterol concentrations from about 3 to 10 mol%. The phase with the longer spacing was found to persist at higher cholesterol concentrations and, therefore, was identified as the cholesterol-rich phase. No phase separation was observed in any other part of the phase diagram.

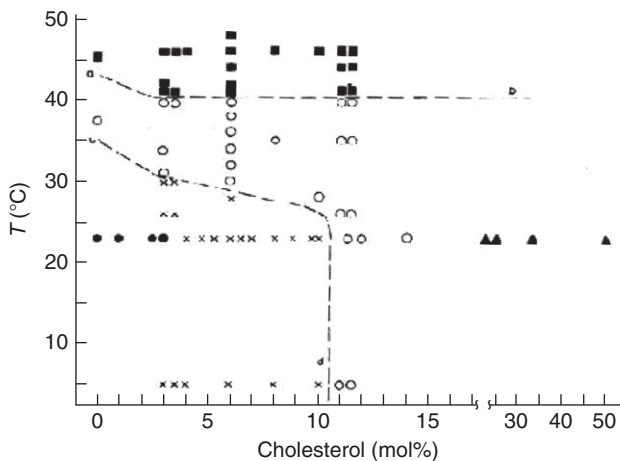


**Figure 10** Phase diagram of DMPC–cholesterol bilayers deduced from X-ray diffraction data. Two-phase regions are indicated by ‘x’ (from ref. [49]).

Lateral phase separation in DMPC–cholesterol membranes has also been probed using SANS [50]. In the  $L_\alpha$  phase, complete miscibility was clearly established up to a cholesterol concentration of 0.14 mol% and strong evidence was presented that this extends up to a concentration of about 0.45 mol%, beyond which cholesterol crystallites phase separate out from the mixture. Below the chain melting transition temperature, a two-phase region was observed between 8 and 24 mol% of cholesterol, where a cholesterol-poor tilted gel phase coexists with a cholesterol-rich phase. A detailed phase diagram of DMPC–cholesterol mixtures was later constructed from SANS data (Fig. 11) [51]. The chain melting transition of the lipid is found to be rather insensitive to the cholesterol concentration up to about 20 mol%, beyond which it drops precipitously. The intermediate ripple phase of DMPC is found to be stabilized by the introduction of cholesterol. Further, temperature and composition dependences of the ripple wavelength suggest additional phase boundaries at 15 °C and at 8 mol% of cholesterol, respectively.

Phase behavior of saturated PC–cholesterol mixtures has been investigated in detail more recently using X-ray diffraction from aligned bilayers (Fig. 12) [52–55]. No phase separation was observed above the chain melting transition in any of the systems, in agreement with earlier diffraction

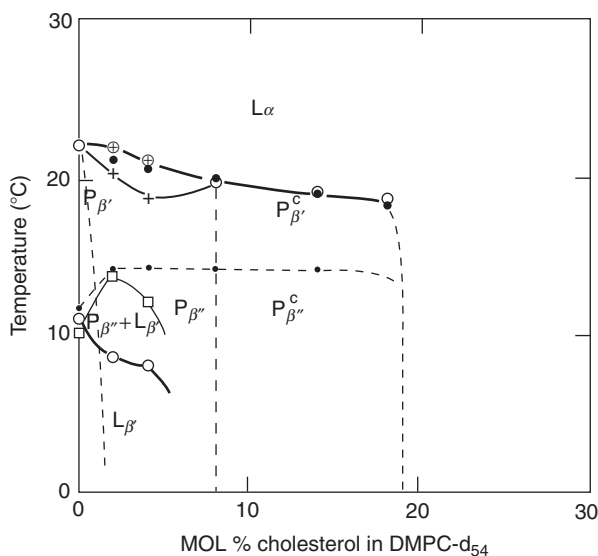


**Figure 11** Phase diagram of DMPC–cholesterol bilayers deduced from neutron diffraction data.  $P_{\beta'}$  is the normal ripple phase seen in DMPC, whereas  $P_{\beta''}$  refers to a different ripple phase seen at lower temperatures. The superscript ‘c’ indicates stabilization of these structures by cholesterol (from Ref. [51]).

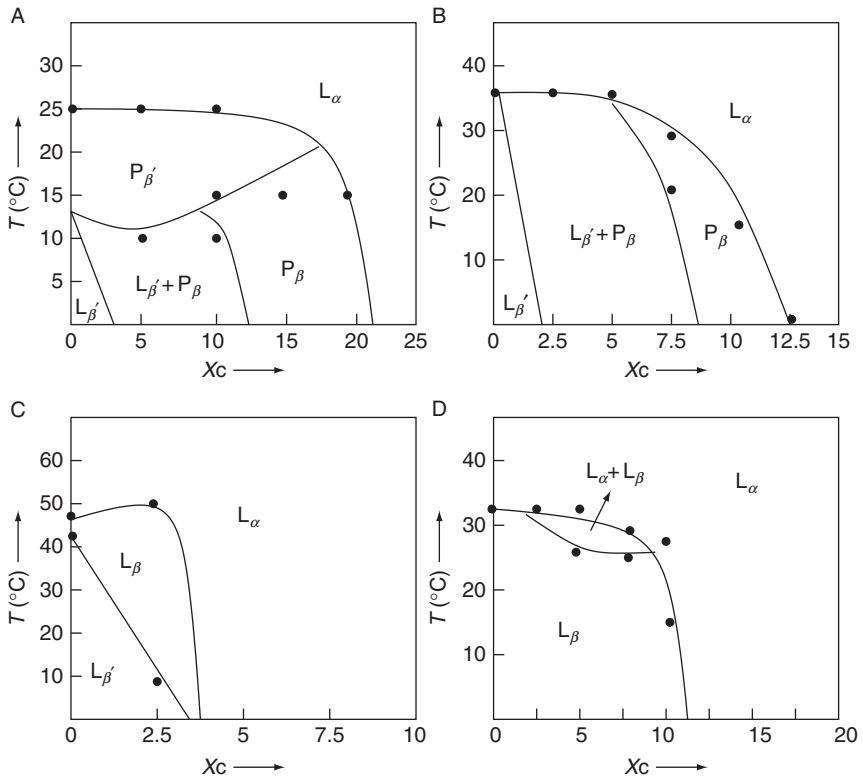


**Figure 12** Phase diagrams of DMPC–cholesterol bilayers at 98% (A), 75% (B) and 30% (C) relative humidity. Phase diagram of dilaurylphosphatidylethanolamine (DLPE)–cholesterol bilayers at 98% relative humidity (D). Note the absence of the  $P_{\beta}$  phase in (C) and (D), where the untilted  $L_{\beta}$  phase is present below the chain melting transition.

experiments. A major surprise from these experiments was the observation of a modulated phase ( $P_{\beta}$ ) at intermediate cholesterol concentrations at 98% relative humidity (Fig. 12A). This phase was shown to be different from the normal ripple phase ( $P_{\beta}'$ ) exhibited by lipids such as DMPC in between the gel and fluid phases. For example, unlike the  $P_{\beta}'$  phase the cholesterol-induced  $P_{\beta}$  phase was found to be stable at lower humidities (Fig. 12B). However, this phase was found to be absent at extremely low humidities where DPPC shows an untilted gel ( $L_{\beta}$ ) phase, instead of the tilted gel ( $L_{\beta}'$ ) phase seen at higher humidities (Fig. 12C). At these humidities, the phase behavior of DMPC–cholesterol mixtures resembles that of DLPE–cholesterol mixtures (Fig. 12D). This suggests that chain tilt is necessary to form the  $P_{\beta}$  phase. On the basis of these observations, a model has been proposed for this phase, which takes into account the coupling of cholesterol concentration to the chain tilt (Figs. 13 and 14). In excess water conditions, the

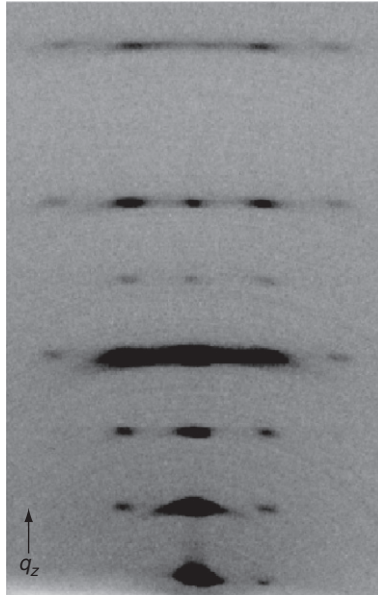


**Figure 13** Diffraction pattern of the  $P_\beta$  phase in an oriented multilayer stack of DPPC-cholesterol bilayers at 75% relative humidity. Note that the unit cell is rectangular, unlike the oblique unit cell seen in the ripple ( $P_\beta'$ ) phase of PCs.

$P_\beta$  phase is not observed, but the corresponding region of the phase diagram is occupied by a fluid phase with a higher lamellar periodicity compared to that at higher temperatures [55].

Unlike the scattering experiments described above, many spectroscopic studies on similar systems report a two-phase coexistence region above the chain melting transition for cholesterol concentrations in the range  $\sim 5\text{--}20$  mol% (Fig. 15) [56–58]. One possible reason for the discrepancy might be that the nonuniform concentration of cholesterol found in the  $P_\beta$  phase might persist as concentration fluctuations at higher temperatures. Then at the time scale of the spectroscopic experiments, two chain conformations would be observed, whereas no phase separation would be seen with diffraction and optical fluorescence microscopy techniques, which probe the system at much longer time scales. More work is needed to resolve this issue.

### 3.5. Scattering Studies on other Sterols in Lipid Bilayers

Although cholesterol has been the most widely studied sterol, there have also been a few scattering studies on the influence of other sterols on lipid membranes. Using SANS on ULVs, it has been shown that ergosterol and lanosterol, which are structurally closely related to cholesterol, produce

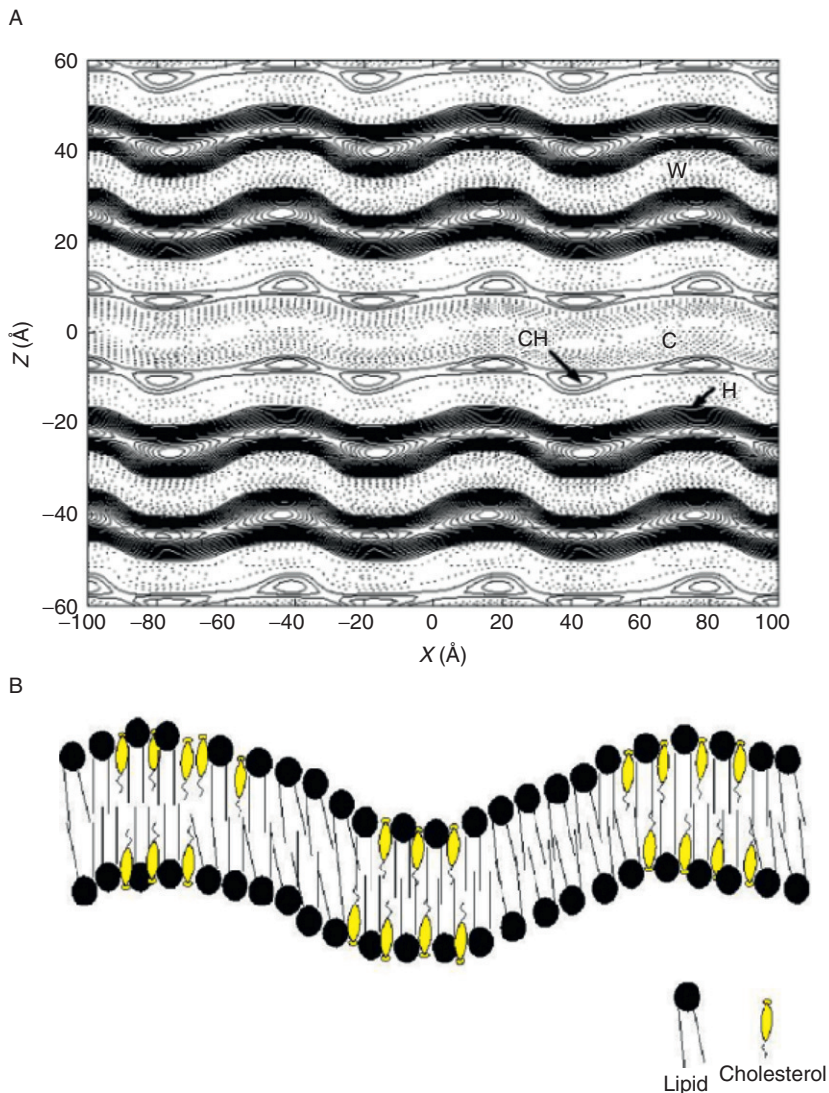


**Figure 14** Electron density map of the  $P_{\beta}$  phase calculated from the diffraction data (A). Regions denoted as W, H, and C correspond to water, headgroups, and chains, respectively. Ch denotes the band arising due to the presence of cholesterol in the bilayer. (B) A model for the  $P_{\beta}$  phase proposed on the basis of the diffraction data. Note that cholesterol molecules occupy regions with untilted chains which alternate with regions containing chains tilted with respect to the local normal.

similar changes in the bilayer thickness, although large differences in their influence on the membrane thermal expansion coefficient are observed [59].

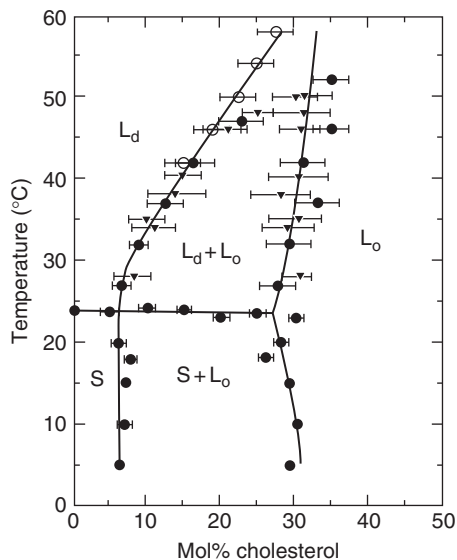


**Figure 15** Phase diagram of DPPC–cholesterol mixtures determined using electron spin resonance spectroscopy techniques. Note the two-phase region at temperatures above the chain melting transition (from Ref. [58]).

Recent experiments on DPPC–ergosterol mixtures report the observation of two coexisting phases above the chain melting transition temperature of DPPC [60]. These two phases, which differ only by about 0.1 nm in their lamellar spacings, coexist up to a critical temperature. This difference in the behaviors of cholesterol and ergosterol is very surprising and needs to be investigated further.

The influence of the plant sterols, stigmasterol, and sitosterol on membrane properties has been studied using SAXS. For all the lipids studied, these sterols were found to be not as efficient as cholesterol in increasing the bilayer thickness and rigidity, which is attributed to the additional ethyl group in their alkyl chains [61]. SANS studies reveal that sitosterol is more efficient than stigmasterol in ordering the acyl chains of soybean PC lipids [62].

#### 4. FLUID–FLUID PHASE SEPARATION IN RAFT MIXTURES

Fluid–fluid ( $l_o$ – $l_d$ ) phase separation in model membranes consisting of a ternary mixture of cholesterol and two lipids with very different chain melting transition temperatures has often been compared to the raft and

nonraft domains in biological membranes. This has led to a large number of investigations on the behavior of these so-called raft mixtures [12].

The main role of cholesterol in these mixtures seems to be the conversion of the fluid–gel phase separation seen in the binary lipid mixtures [63] to a fluid–fluid coexistence. The region of fluid–fluid coexistence in the phase diagrams of these mixtures has been delineated using fluorescence microscopy experiments on giant unilamellar vesicles (GUVs) [64] and by fluorescence anisotropy measurements on liposomal preparations [65]. Although both these techniques show the occurrence of  $l_o$ – $l_d$  coexistence in these mixtures, the phase diagrams obtained are qualitatively different (Figs. 16 and 17). This difference is related to differences seen in the behavior of binary lipid–cholesterol mixtures using different techniques, discussed in the previous section.

Somewhat surprisingly, the  $l_o$ – $l_d$  coexistence was not observed in earlier X-ray diffraction studies on equimolar SM–DOPC–cholesterol mixtures at ambient temperature, which led the authors to suggest that phase separation might be taking place within each bilayer as seen in fluorescence microscopy studied of GUVs, without the domains in different bilayers coming together to form a bulk phase [66]. However, phase separation has been observed in raft mixtures more recently [55,67,68]. Using oriented bilayers of DPPC–DOPC–cholesterol mixtures, a demixing transition has been demonstrated on lowering the temperature (Fig. 18). The relative transbilayer electron density profiles of the two phases have been calculated from

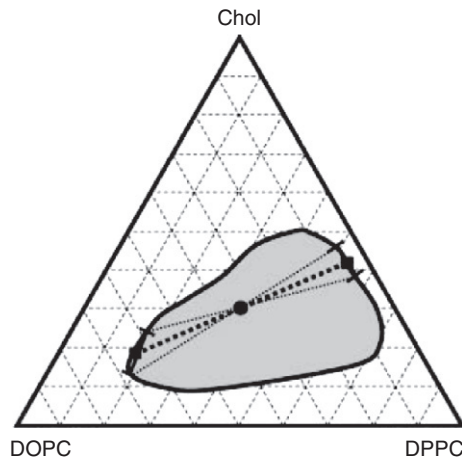


**Figure 16** Phase diagram of DPPC–DOPC–cholesterol raft mixtures at 30 °C determined using fluorescence microscopy techniques. The shaded region corresponds to the coexistence of two fluid phases. Note that the tie lines are almost parallel to the lipid–lipid axis, which indicates that the cholesterol concentrations in the coexisting  $l_o$ – $l_d$  phases are not very different (from Ref. [64]).

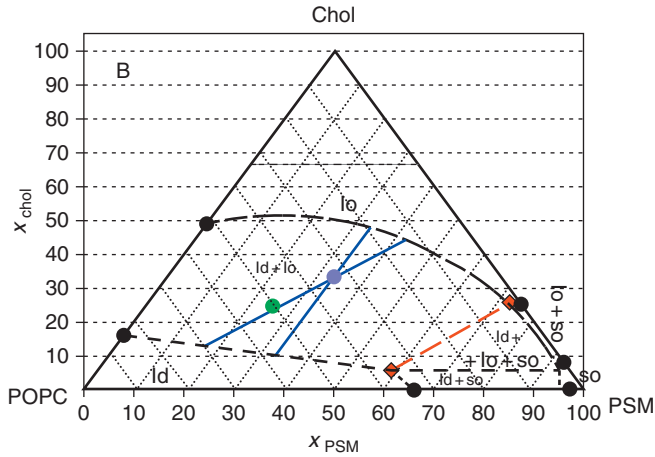


**Figure 17** Phase diagram of POPC–PSM–cholesterol raft mixtures at 37 °C determined using fluorescence anisotropy, lifetime, and quenching. Note the two-phase region and the tie lines which are almost parallel to the POPC–cholesterol axis, indicating that cholesterol concentrations in the coexisting  $l_o$ – $l_d$  phases are very different (from Ref. [65]).

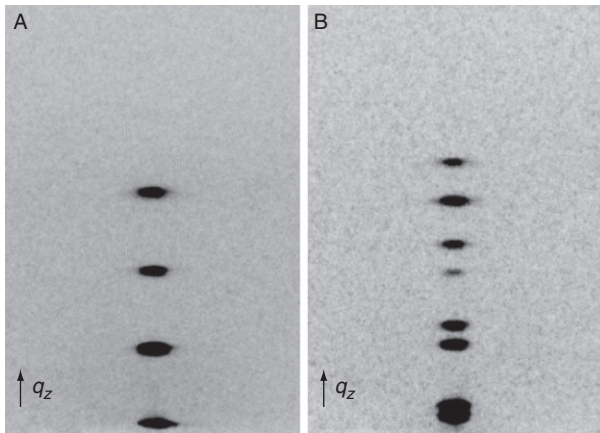


**Figure 18** Diffraction patterns of an oriented multilayer stack made from an equimolar mixture of DPPC and DOPC with 25 mol% cholesterol showing a single fluid phase at 40 °C (A) and  $l_o$ – $l_d$  phase separation at 10 °C (B).

the diffraction data (Fig. 19). By comparing these profiles with those of binary lipid–cholesterol mixtures, one can conclude that the  $l_o$  phase is DPPC-rich and contains a significant amount of cholesterol. Similarly, the  $l_d$  phase is found to be DOPC-rich; however, its cholesterol content cannot



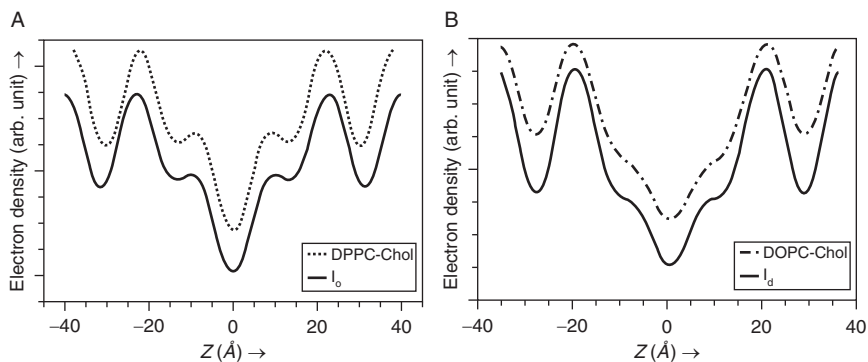


**Figure 19** Transbilayer electron density profiles of the  $l_o$  (A) and  $l_d$  (B) phases of DPPC–DOPC–cholesterol mixtures. Note that the electron density profiles of these phases are very similar to those of DPPC–cholesterol and DOPC–cholesterol binary mixtures (both containing about 20 mol% cholesterol), indicating that the former phase is DPPC-rich and the latter DOPC-rich. The peaks at around 1 nm from the bilayer centre in the two curves in (A) arise from the presence of cholesterol. Hence, we can conclude that the  $l_o$  phase contains significant amounts of cholesterol. Such a feature is absent in the electron density profile of DOPC–cholesterol mixtures. Hence, no conclusion can be drawn about the cholesterol content of the  $l_d$  phase without further detailed analysis.

be ascertained because the electron density profile of DOPC bilayers do not alter significantly on the addition of cholesterol [55].

Wide angle X-ray scattering (WAXS) has been used recently to study phase separation in oriented multilayers of DPPC–DOPC–cholesterol mixtures [69]. WAXS is a more powerful tool to look at phase separation than SAXS, since it is capable of detecting the presence of small domains in the bilayer, whereas SAXS can only detect the coexistence of two bulk phases with dissimilar lamellar spacings. It is found that two molecular orientational distribution functions are necessary to account for the data at lower temperatures, whereas only one is sufficient at higher temperatures. The phase with the higher value of the order parameter was identified as the  $l_o$  phase and the other as the  $l_d$  phase.

SANS has been used recently to detect phase separation in ULVs of an equimolar DPPC–DOPC–cholesterol mixture, and also to distinguish between ULVs containing a single large domain and those with several small domains [70]. By using chain deuterated DPPC and matching the scattering length density of the solvent with that of the uniform bilayer at higher temperatures, it was possible to increase the sensitivity of this technique. It was found that ULVs with an average radius of about 30 nm typically contained 30 domains of about 10 nm radius at low temperatures. The miscibility transition was found to occur at a similar temperature as that observed in fluorescence microscopy studies of GUVs of the same

composition, in spite of the three orders of magnitude difference in the sizes of the GUVs and the ULVs, thereby demonstrating that domain formation is not influenced by vesicle size or curvature. However, it is not clear why the domains on each ULV do not coalesce to form a single large domain as found often in the case of GUVs. In this context, it should be pointed out that the morphology of phase separation on GUVs has been shown to depend on the membrane tension [71]. Coarsening of the domains takes place in tense domains, but in floppy ones, the domains tend to bulge out and their coalescence is hindered by the repulsive interaction due to membrane curvature. It is, therefore, possible that the ULVs used in the SANS studies were floppy and hence led to the formation of a large number of small domains.

Time resolved synchrotron small angle X-ray scattering (TR SAXS) has been used to study the kinetics of phase separation in DPPC–DOPC–cholesterol mixtures [68]. It is found to be reversible and rather rapid, with the phases appearing and disappearing within the 25 ms resolution of the technique.

#### 4.1. Partitioning of Cholesterol between the $l_o$ and $l_d$ Phases

The partitioning of cholesterol between the coexisting  $l_o$  and  $l_d$  phases is a topic of some debate in the literature, as there are considerable differences between the results of different studies using different techniques. This is exemplified by the different orientations of the tie lines in the phase diagrams shown in Figs. 16 and 17. In Fig. 16, the tie lines are almost parallel to the DPPC–DOPC axis, indicating comparable concentrations of cholesterol in the  $l_o$  and  $l_d$  phases. On the other hand, in Fig. 17, the tie lines are almost parallel to the POPC–cholesterol axis, and hence the cholesterol contents in the two phases are very different.

The partitioning of cholesterol between the gel,  $l_d$  and  $l_o$  phases of DPPC–DOPC–cholesterol mixtures has been studied utilizing the fact that the composition of these three coexisting phases does not change over their coexistence range at fixed temperature [67]. Cholesterol contents of these phases are found to be 10, 9, and 29 mol% respectively. The value obtained for the gel phase is somewhat surprising as all DPPC–cholesterol binary phase diagrams reported in the literature show that the gel phase becomes unstable at much lower concentrations of cholesterol [49,51,54,56]. More detailed experiments are necessary to clarify this situation.

#### 4.2. Relevance to Biomembranes

Although  $l_o$ – $l_d$  phase separation in raft mixtures has been widely believed to mimic the heterogeneities in cell membranes, it should be emphasized that the former systems are in thermodynamic equilibrium, whereas the latter

are not. It is possible that the origin of inhomogeneities in cell membranes is qualitatively different from that of domains in raft mixtures, especially considering the fact that they are typically three orders of magnitude smaller in size [10]. However, domains have been seen recently in patches of plasma membranes detached from certain cells on blebbing [72]. At 37 °C, these vesicles are uniform, but on cooling below 25 °C, micron-sized domains, reminiscent of domains in raft mixtures, appear indicating the occurrence of a demixing transition. One difference between the plasma membrane of the cell and the detached blebs is that the actin cytoskeleton present in the former is absent in the latter. Therefore, it has been suggested that the demixing transition in the blebs might be a consequence of the absence of cytoskeletal constraints, which are known to affect the lateral diffusion of molecules in the membrane. Further experiments are clearly needed to ascertain if the observed phase separation is entirely a consequence of the absence of the cytoskeleton, or if other factors are also involved.

## REFERENCES

- [1] B. Alberts, A. Johnson, J. Lewis, M. Raff, K. Roberts, P. Walter, *Molecular biology of the cell*, Fourth ed., Garland science, New York, 2002.
- [2] R.A. Demel, B.D. Kruyff, The function of sterols in membranes, *Biochim. Biophys. Acta* 457 (1976) 109–132.
- [3] F.W. Pfrieger, Role of cholesterol in synapse formation and function, *Biochim. Biophys. Acta* 1610 (2003) 271–280.
- [4] A. Filippov, G. Oradd, G. Lindblom, The effect of cholesterol on the lateral diffusion of phospholipids in oriented bilayers, *Biophys. J.* 84 (2003) 3079–3086.
- [5] J.R. Silvius, Role of cholesterol in lipid raft formation: lessons from lipid model systems, *Biochim. Biophys. Acta* 1610 (2003) 174–183.
- [6] K. Simons, E. Ikonen, Functional rafts in cell membranes, *Nature* 389 (1997) 569–572.
- [7] D.A. Brown, E. London, Structure and function of sphingolipid- and cholesterol-rich membrane rafts, *J. Bio. Chem.* 275 (2000) 17221–17224.
- [8] M. Edidin, The state of lipid rafts: From model membranes to cells, *Annu. Rev. Biophys. Biomol. Struct.* 32 (2003) 257–283.
- [9] K. Simons, W.L.C. Vaz, Model systems, lipid rafts, and cell membranes, *Annu. Rev. Biophys. Biomol. Struct.* 33 (2004) 269–295.
- [10] S. Mayor, M. Rao, Rafts: Scale-dependent, active lipid organization at the cell surface, *Traffic* 5 (2004) 231–240.
- [11] T.P.W. McMullen, R.N.A.H. Lewis, R.N. McElhaney, Cholesterol - phospholipid interactions, the liquid-ordered phase and lipid rafts in model and biological membranes, *Curr. Opin. Colloid Int. Sci.* 8 (2004) 459–468.
- [12] F.M. Goni, A. Alonso, L.A. Bagatoli, R.E. Brown, D. Marsh, M. Prieto, J.L. Thewalt, Phase diagrams of lipid mixtures relevant to the study of membrane rafts, *Biochim. Biophys. Acta* 1781 (2008) 665–684.
- [13] J.F. Nagle, S. Tristram-Nagle, Structure of lipid bilayers, *Biochim. Biophys. Acta* 1469 (2000) 159–195.
- [14] J. Katsaras, V.A. Raghunathan, Aligned lipid-water systems, in: T. Gutberlet, J. Katsaras (Eds.), *Lipid Bilayers Springer, Structure and Interactions*, 2001, p. 25.

- [15] J.F. Nagle, M.C. Wiener, Relations for lipid bilayers, *Biophys. J.* 55 (1989) 309–313.
- [16] A. Caillé, Physique cristalline: remarques sur la diffusion des rayons X dans les smectiques A, *C. R. Acad. Sci. Paris, Series. B* 274 (1972) 891–893.
- [17] C.R. Safinya, D. Roux, G.S. Smith, S.K. Sinha, P. Dimon, N.A. Clark, A.M. Bellocq, Steric interactions in a model multimembrane system: A synchrotron x-ray study, *Phys. Rev. Lett.* 57 (1986) 2718–2721.
- [18] F. Nallet, R. Laversanne, D. Roux, Modelling x-ray or neutron scattering spectra of lyotropic lamellar phases: interplay between form and structure factors, *J. Phys. II* 3 (1993) 487–502.
- [19] R. Zhang, R.M. Suter, J.F. Nagle, Theory of the structure factor of lipid bilayers, *Phys. Rev. E* 50 (1994) 5047–5060.
- [20] N. Lei, C.R. Safinya, R. Bruinsma, Discrete harmonic model for stacked membranes: Theory and experiment, *J. Phys. II* 5 (1995) 1155–1163.
- [21] R. Zhang, S. Tristram-Nagle, W. Sun, R.L. Headrick, T.C. Irving, R.M. Suter, J.F. Nagle, Small-angle x-ray scattering from lipid bilayers is well described by modified Caillé theory but not by paracrystalline theory, *Biophys. J.* 70 (1996) 349–357.
- [22] G. Pabst, M. Rappolt, H. Amenitsch, P. Lagner, Structural information from multilamellar liposomes at full hydration: Full q-range fitting with high quality x-ray data, *Phys. Rev. E* 62 (2000) 4000–4009.
- [23] J.F. Nagle, R. Zhang, S. Tristram-Nagle, W. Sun, H.I. Petrache, R.M. Suter, X-ray structure determination of fully hydrated phase dipalmitoylphosphatidylcholine bilayers, *Biophys. J.* 70 (1996) 1419–1431.
- [24] Y. Lyatskaya, Y. Liu, S.T. Nagle, J. Katsaras, J.F. Nagle, Method for obtaining structure and interactions from oriented lipid bilayers, *Phys. Rev. E* 63 (2000) 011907.
- [25] J. Fitter, T. Gutberlet, J. Katsaras, *Neutron Scattering in Biology*, First ed., Springer, New York, 2006.
- [26] M.J. Janiak, D.M. Small, G.G. Shipley, Nature of the thermal pretransition of synthetic phospholipids: dimyristoyl and dipalmitoyl-lecithin, *Biochemistry* 15 (1976) 4575–4580.
- [27] G.S. Smith, E.B. Sirota, C.R. Safinya, R.J. Plano, N.A. Clark, X-ray structural studies of freely suspended ordered hydrated DMPC multimembrane films, *J. Chem. Phys.* 92 (1990) 4519–4529.
- [28] D.C. Wack, W.W. Webb, Measurement by x-ray diffraction methods of the layer compressional elastic constant B in the lyotropic smectic-A ( $L\alpha$ ) phase of the lecithin-water system, *Phys. Rev. A* 40 (1989) 1627–1636.
- [29] T.J. McIntosh, The effect of cholesterol on the structure of phosphatidylcholine bilayers, *Biochim. Biophys. Acta* 513 (1978) 43–58.
- [30] S.W. Hui, N.-B. He, Molecular organization in cholesterol-lecithin bilayers by x-ray and electron diffraction measurements, *Biochemistry* 22 (1983) 1159–1164.
- [31] Y.K. Levine, M.H.F. Wilkins, Structure of oriented lipid bilayers, *Nature New Biol.* 230 (1971) 69–76.
- [32] J. Pan, T.T. Mills, S.T. Nagle, J.F. Nagle, Cholesterol perturbs lipid bilayers nonuniversally, *Phys. Rev. Lett.* 100 (2008) 198103.
- [33] N.P. Franks, W.R. Lieb, The structure of lipid bilayers and the effects of general anaesthetics: An x-ray and neutron diffraction study, *J. Mol. Biol.* 133 (1979) 469–500.
- [34] W.-C. Hung, M.-T. Lee, F.-Y. Chen, H.W. Huang, The condensing effect of cholesterol in lipid bilayers, *Biophys. J.* 92 (2007) 3960–3967.
- [35] N. Kučerka, J. Pencner, M.P. Nieh, J. Katsaras, Influence of cholesterol on the bilayer properties of monounsaturated phosphatidylcholine unilamellar vesicles, *Eur. Phys. J. E* 23 (2007) 247–254.
- [36] J. Lemmich, T. Honger, K. Mortensen, J.H. Ipsen, R. Bauer, O.G. Mouritsen, Solutes in small amounts provide for lipid-bilayer softness: cholesterol, short-chain lipids, and bola lipids, *Eur. Biophys. J.* 25 (1996) 61–65.

- [37] J. Huang, J.T. Buboltz, G.W. Feigenson, Maximum solubility of cholesterol in phosphatidylcholine and phosphatidylethanolamine bilayers, *Biochim. Biophys. Acta* 1417 (1999) 89–100.
- [38] D. Bach, E. Wachtel, Phospholipid/cholesterol model membranes: formation of cholesterol crystallites, *Biochim. Biophys. Acta* 1610 (2003) 187–197.
- [39] R.M. Epand, R.F. Epand, D.W. Hughes, B.G. Sayer, N. Borochof, D. Bach, E. Wachtel, Phosphatidylcholine structure determines cholesterol solubility and lipid polymorphism, *Chem. Phys. Lipids* 135 (2005) 39–53.
- [40] B.G. Tenchov, R.C. MacDonald, D.P. Siegel, Cubic phases in phosphatidylcholine-cholesterol mixtures: cholesterol as membrane “fusogen” *Biophys. J.* 91 (2006) 2508–2516.
- [41] N.P. Franks, Structural analysis of hydrated egg lecithin and cholesterol bilayers I. X-ray diffraction, *J. Mol. Biol.* 100 (1976) 345–358.
- [42] D.L. Worcester, N.P. Franks, Structural analysis of hydrated egg lecithin and cholesterol bilayers II. Neutron diffraction, *J. Mol. Biol.* 100 (1976) 359–378.
- [43] A. Léonard, C. Escribe, M. Laguerre, E. Pebay-Peyroula, W. Néri, T. Pott, J. Katsaras, E.J. Dufourc, Location of cholesterol in DMPC membranes. A comparative study by neutron diffraction and molecular mechanics simulation, *Langmuir* 17 (2001) 2019–2030.
- [44] T.A. Harroun, J. Katsaras, S.R. Wassall, Cholesterol hydroxyl group is found to reside in the centre of a polyunsaturated lipid membrane, *Biochemistry* 45 (2006) 1227–1233.
- [45] S.J. Marrink, A.H. de Vries, T.A. Harroun, J. Katsaras, S.R. Wassall, Cholesterol shows preference for the interior of polyunsaturated lipid membranes, *J. Am. Chem. Soc.* 130 (2008) 10–11.
- [46] F. Richter, G. Rapp, L. Finegold, Miscibility gap in fluid dimyristoylphosphatidylcholine as “seen” by x rays, *Phys. Rev. E* 63 (2001) 051914.
- [47] C. Gliss, O. Randel, H. Casalta, E. Sackmann, R. Zorn, T. Bayerl, Anisotropic motion of cholesterol in oriented DPPC bilayers studied by quasielastic neutron scattering: The liquid-ordered phase, *Biophys. J.* 77 (1999) 331–340.
- [48] E. Endress, H. Heller, H. Casalta, M.F. Brown, T.M. Bayerl, Anisotropic motion and molecular dynamics of cholesterol, lanosterol, and ergosterol in lecithin bilayers studied by quasi-elastic neutron scattering, *Biochemistry* 41 (2002) 13078–13086.
- [49] R.P. Rand, V.A. Parsegian, J.A.C. Henry, L.J. Lis, M. McAlister, The effect of cholesterol on measured interaction and compressibility of dipalmitoylphosphatidylcholine bilayers, *Can. J. Biochem.* 58 (1980) 959–968.
- [50] W. Knoll, G. Schmidt, K. Ibel, E. Sackmann, Small-angle neutron scattering study of lateral phase separation in dimyristoylphosphatidylcholine-cholesterol mixed membranes, *Biochemistry* 24 (1985) 5240–5246.
- [51] K. Mortensen, W. Pfeiffer, E. Sackmann, W. Knoll, Structural properties of a phosphatidylcholine-cholesterol system as studied by small-angle neutron scattering: ripple structure and phase diagram, *Biochim. Biophys. Acta* 945 (1988) 221–245.
- [52] S. Karmakar, V.A. Raghunathan, Cholesterol-induced modulated phase in phospholipid membranes, *Phys. Rev. Lett.* 91 (2003) 098102.
- [53] S. Karmakar, V.A. Raghunathan, S. Mayor, Phase behaviour of dipalmitoyl phosphatidylcholine (DPPC) - cholesterol membranes, *J. Phys: Condens. Matter* 17 (2005) S1177–S1182.
- [54] S. Karmakar, V.A. Raghunathan, Structure of phospholipid-cholesterol membranes: An x-ray diffraction study, *Phys. Rev. E* 71 (2005) 061924.
- [55] S. Karmakar, B.R. Sarangi, V.A. Raghunathan, Phase behaviour of lipid-cholesterol membranes, *Solid State Commun.* 139 (2006) 630–634.

- [56] M.R. Vist, J.H. Davis, Phase equilibria of cholesterol/dipalmitoylphosphatidylcholine mixtures: nuclear magnetic resonance and differential scanning calorimetry, *Biochemistry* 29 (1990) 451–464.
- [57] M.B. Sankaram, T.E. Thompson, Cholesterol-induced fluid-phase immiscibility in membranes, *Proc. Natl. Acad. Sci. USA* 88 (1991) 8686–8690.
- [58] P.F.F. Almeida, W.L.C. Vaz, T.E. Thompson, Lateral diffusion in the liquid phases of dimyristoylphosphatidylcholine/cholesterol lipid bilayers: A free volume analysis, *Biochemistry* 31 (1992) 6739–6747.
- [59] J. Pencer, M.-P. Nieh, T.A. Harroun, S. Krueger, C. Adams, J. Katsaras, Bilayer thickness and thermal response of dimyristoylphosphatidylcholine unilamellar vesicles containing cholesterol, ergosterol and lanosterol: A small-angle neutron scattering study, *Biochim. Biophys. Acta* 1720 (2005) 84–91.
- [60] R. Krivanek, C. Jeworrek, C. Czeslik, R. Winter, Composition fluctuations in phospholipid-sterol vesicles - a small-angle neutron scattering study, *Z. Phys. Chem.* 222 (2008) 1679–1692.
- [61] A. Hodzic, M. Rappolt, H. Amenitsch, P. Laggner, G. Pabst, Differential modulation of membrane structure and fluctuations by plant sterols and cholesterol, *Biophys. J.* 94 (2008) 3935–3944.
- [62] M.P. Marsan, E. Bellet-Amalric, I. Muller, G. Zaccai, A. Milon, Plant sterols: a neutron diffraction study of sitosterol and stigmasterol in soybean phosphatidylcholine membranes, *Biophys. Chem.* 75 (1998) 45–55.
- [63] W. Knoll, G. Schmidt, E. Sackmann, Critical demixing in fluid bilayers of phospholipid mixtures. A neutron diffraction study, *J. Chem. Phys.* 79 (1983) 3439–3442.
- [64] S.L. Veatch, I.V. Polozov, K. Gawrisch, S.L. Keller, Liquid domains in vesicles investigated by NMR and fluorescence microscopy, *Biophys. J.* 86 (2003) 2910–2922.
- [65] R.F.M. de Almeida, A. Fedorov, M. Prieto, Sphingomyelin/phosphatidylcholine/cholesterol phase diagram: Boundaries and composition of lipid rafts, *Biophys. J.* 85 (2003) 2406–2416.
- [66] M. Gandhavadi, D. Allende, A. Vidal, S.A. Simon, T.J. McIntosh, Structure, composition, and peptide binding properties of detergent soluble bilayers and detergent resistant rafts, *Biophys. J.* 82 (2002) 1469–1482.
- [67] L. Chen, Z. Yu, P.J. Quinn, The partition of cholesterol between ordered and fluid bilayers of phosphatidylcholine: A synchrotron x-ray diffraction study, *Biochim. Biophys. Acta* 1768 (2007) 2873–2881.
- [68] C. Jeworrek, M. Pühse, R. Winter, X-ray kinematography of phase transformations of three-component lipid mixtures: A time-resolved synchrotron x-ray scattering study using the pressure-jump relaxation technique, *Langmuir* 24 (2008) 11851–11859.
- [69] T.T. Mills, S.T. Nagle, F.A. Heberle, N.F. Morales, J. Zhao, J. Wu, G.S. Toombes, J.F. Nagle, G.W. Feigenson, Liquid-liquid domains in bilayers detected by wide angle x-ray scattering, *Biophys. J.* 95 (2008) 682–690.
- [70] J. Pencer, T. Mills, V. Anghel, S. Krueger, R.M. Eppard, J. Katsaras, Detection of submicron-sized raft-like domains in membranes by small-angle neutron scattering, *Eur. Phys. J. E* 18 (2005) 447.
- [71] M. Yanagisawa, M. Imai, T. Masui, S. Komura, T. Ohta, Growth dynamics of domains in ternary fluid vesicles, *Biophys. J.* 92 (2007) 115–125.
- [72] T. Baumgart, A.T. Hammond, P. Sengupta, S.T. Hess, D.A. Holowka, B.A. Baird, W.W. Webb, Large-scale fluid/fluid phase separation of proteins and lipids in giant plasma membrane vesicles, *Proc. Natl. Acad. Sci. USA* 104 (2007) 3165–3170.

# SUBJECT INDEX

- Alvarez–Latorre system, 38–39  
Atomistic surface model, 134
- Benz system, 37–38  
Bilayer lipid membrane (BLM)  
  microfluidic technology  
    blowing vesicle method (*see* Blowing vesicle method)  
    contact method (*see* Contact method)  
    microarray technology, 97–98  
    silicon microfabrication (*see* Silicon microfabrication techniques)
- Blowing vesicle method  
  capillary jet nozzle, 93–94  
  gentle hydration method, 93  
  liposomes, 93  
  microfluidic device  
    GFP gene expression, 96  
    poly(dimethylsiloxane) (PDMS), 94–95  
    vesicle formation, fluorescence image, 95–96  
  monodisperse water-in-oil-in-water emulsions, 93  
  reverse emulsion method, 93  
  schematic view, 94
- Budding model, 2–3
- Capacitance (C), planar lipid bilayer  
  discharge method, 49–50  
  period conversion method, 51–52  
  voltage conversion method, 52–53
- Carius system, 46–47  
Chanturya system, 39  
Cholesterol, lipid bilayers  
  DPPC-cholesterol mixtures  
    lateral phase separation, 174  
    neutron diffraction data, 174  
    phase diagram, 173  
    X-ray diffraction, 174–176  
  neutron scattering, 172–173  
  nonlamellar phases, 171  
  spectroscopic studies, 176  
  transbilayer scattering length density profile, 171, 172  
  X-ray diffraction, 171  
    bilayer thickness, 170  
    membrane rigidity, 168–169  
    saturated and monounsaturated chains, 169, 171  
    unsaturated chains, 171
- Contact method  
  contacted membrane, 89–90  
  lipid bilayer array  
    antibiotic ion channel recording, 91–93  
    microfluidic device, 91–92  
    multiple lipid membranes, 91–92  
  microfluidic channel, 90  
  multiple membrane, 89–90  
  schematic views, 89  
  single channel current recording, 90–91
- Cooke–Deserno model, 135
- Electrical double layer (EDL)  
  Langevin dipoles (*see* Langevin dipoles, electrical double layer)  
  permittivity and membrane surface potential  
    boundary condition, 122  
    dimensionless form, 121  
    electric potential continuity, 122  
  Gauss law, 119  
  negatively charged planar membrane surface, 120  
  space variation model, 121  
  surface electric potential, 123  
  volume charge density, 119  
  water molecule orientation  
    average microscopic volume charge density, 104  
    Bjerrum length, 105  
    Boltzmann distribution function, 106–108  
    counterion and coion distribution, 103  
    effective permittivity, 105–107  
    electrostatic forces, 103  
    function F, 107  
    Poisson equation, 105  
    polarization P, 104
- Excluded volume effect  
  boundary conditions, 109  
  effective permittivity, 109–110  
  ion distribution functions, 109  
  lattice statistics model, 108  
  number density, 109–110  
  water molecule orientation  
    linearized modified Poisson–Boltzmann equation, 115–118  
    modified Poisson–Boltzmann equation, 111–115
- Fluid–fluid phase separation  
  biomembranes, 182–183  
  cholesterol partitioning, 182  
  DPPC-DOPC-cholesterol mixtures  
    demixing transition, 179, 180  
  SANS studies, 181–82  
  time resolved synchrotron small angle X-ray scattering, 182  
  wide angle X-ray scattering (WAXS), 181

- Fluid-fluid phase separation (*cont.*)  
 fluid-fluid coexistence, 179  
 POPC-PSM-cholesterol raft mixtures, 180  
 Folding method, 72, 73  
 Free Gibbs energy, 6–7
- Gallucci–Micelli system, 42–43  
 Gouy–Chapman model, 102
- Hanai–Haydon–Taylor system, 33–34  
 Hanyu–Yamada–Matsumoto system, 43–44  
 Helfrich Hamiltonian description, 149–150
- Infrared absorption spectroscopy (IRAS), 73–78  
 Ion channel proteins, 72
- Kalinowski–Figaszewski system, 48–49  
 Kramar–Miklavcic–Macek Lebar system, 44–46
- Langevin dipoles, electrical double layer  
 average cosine of angle, 117–118  
 average microscopic volume charge density, 112  
 dipole moment, 113, 116  
 distribution function, 112  
 effective permittivity, 105–107  
 number density, 112, 114, 116–117
- Linearized modified Poisson–Boltzmann equation  
 average cosine, 117–118  
 boundary condition, 115  
 effective permittivity, 116  
 number densities, 116–117
- Lipid bilayer model  
 different length scales  
 atomistic models, 132–133  
 coarse-grained models, 133  
 water-free models, 133  
 free bilayers, 133–134  
 supported bilayers  
 anisotropic pressure coupling, 136  
 atomistic surface model, 134  
 Cooke–Deserno model, 135  
 homoatomic models, 134–135  
 lipophilic supports, 135  
 lipophobic supports, 135  
 Martini force-field, 135–136  
 simulations, 134  
 substrate-lipid interaction, 134
- Lipid droplet biogenesis  
 molecular interpretation, 11–12  
 phospholipid demixing, 23  
 budding mechanism, 21  
 fully matured LD, 22  
 size distributions, 22  
 TAG depots, 22  
 very low-density lipoproteins, 23  
 spherical protuberance, 24–25
- theoretical model  
 free Gibbs energy, 6–7  
 Helfrich Hamiltonian, 4  
 local lipid composition, 5  
 parameter estimation, 7–11  
 potential energy, single lipid, 4–5  
 shape approximation, 5–6
- Lipid-sterol bilayers. *See also* Cholesterol, lipid bilayers  
 sterols  
 cholesterol, 168–171  
 lipid-cholesterol membranes, 173–176  
 phase behavior, 167–168  
 scattering studies, 176–178  
 structure, 160
- X-ray scattering  
 cusp like singularities, 166  
 diffraction patterns, 162–163  
 lipid-water system, 163  
 quasielastic neutron scattering (QENS), 167  
 small angle neutron scattering (SANS), 167  
 structure factor  $S(q)$ , 166  
 thermal fluctuations, 165–166  
 transbilayer electron density profile  $r(z)$ , 164–165  
 two-dimensional (2-D) lattice, 161–163
- Mean-squared displacements (MSD), 140
- Microarray technology  
 $\mu$ -fluidic trap, 97, 98  
 hydrodynamic approach, 97  
 microbeads, 98  
 releasing mechanism, 97, 98
- Microfabricated silicon chips. *See* Silicon microfabrication techniques
- Microfluidic technology  
 blowing vesicle method (*see* Blowing vesicle method)  
 contact method (*see* Contact method)  
 microarray technology, 97–98
- Modified Poisson–Boltzmann equation  
 average microscopic volume charge density, 112  
 boundary conditions, 115  
 effective permittivity, 114  
 function  $H$ , 113  
 Langevin dipole distribution function, 112  
 number density, 112  
 polarization, 113  
 probability, 112  
 volume charge density, 114–115
- Montal–Mueller system, 36–37
- Multiple-internal reflection-infrared absorption spectroscopy (MIR-IRAS), 73–78
- Naumowicz–Petelska–Figaszewski system, 44
- Neutral lipids (NL), 2



- Painting method, 72–73
- Phospholipid demixing. *See also* Lipid droplet biogenesis
- budding model, 2–3
  - bud-off diameter, 17–18
  - curved membrane regions, 19–20
  - endoplasmic leaflet, 23–24
  - energy barrier disappearance, 17
  - energy change, 15, 16
  - ER's PL reservoir, 18
  - lipid droplet
    - biogenesis, 23
    - budding mechanism, 21
    - fully matured LD, 22
    - size distributions, 22
    - TAG depots, 22
    - very low-density lipoproteins, 23
  - membrane curvature, 20–21
  - molecular area ratio, 14–15
  - nascent LD, 16–17
  - neck formation, 24
  - neutral lipids (NL), 2
  - protein recruitment, ER, 21
  - spherical cap approximation, 24
  - total free Gibbs energy, 17, 19
  - yeast, 3–4
- Planar lipid bilayer
- breakdown voltage ( $U_{br}$ ), 54–57
  - capacitance (C)
    - discharge method, 49–50
    - period conversion method, 51–52
    - voltage conversion method, 52–53
  - current clamp method
    - Carius system, 46–47
    - Kalinowski-Figaszewski system, 48–49
    - Robello-Gliozzi system, 47
  - elasticity ( $E$ ), 59–60
  - electrical properties, 31, 32
  - fluctuations ( $\psi$ ), 57–58
  - folding method, 31
  - measuring concepts, 31, 32
  - painted technique, 30, 31
  - resistance (R), 53–54
  - surface tension ( $\sigma$ ), 59–60
  - thickness ( $d$ ), 58–59
  - voltage clamp method
    - Alvarez-Latorre system, 38–39
    - Benz system, 37–38
    - Chanturya system, 39
    - Gallucci-Micelli system, 42–43
    - Hanai-Haydon-Taylor system, 33–34
    - Hanyu-Yamada-Matsumoto system, 43–44
    - Kramar-Miklavcic-Macek Lebar system, 44–46
    - Montal-Mueller system, 36–37
    - Naumowicz-Petelska-Figaszewski system, 44
    - Rosen-Sutton system, 34–35
    - Sharma-Stebe-Tung system, 41–42
    - White system, 35
    - Wilhelm-Winterhalter-Zimmermann-Benz system, 39–40
    - Wobschall system, 35–36
    - Yamaguchi-Nakanishi system, 41
- Poisson-Boltzmann (PB) theory. *See* Electrical double layer (EDL)
- Poly(dimethylsiloxane) (PDMS) microfluidic T-junction device, 94–95
- Quasielastic neutron scattering (QENS), 167
- Reproducible BLM formation, MIR-IRAS
  - microfabricated apertures, 75
  - microfabricated silicon chips, 73–74
  - painting method, 75–78
- Robello-Gliozzi system, 47
- Rosen-Sutton system, 34–35
- Sharma-Stebe-Tung system, 41–42
- Silicon microfabrication techniques
  - reproducible BLM formation, MIR-IRAS, 73–74
  - stable free-standing BLMs
    - background current noise, 83
    - design, 79, 80
    - gramicidin channel, 83–84
    - membrane lifetime, 81–82
    - precoating, 81
    - single-channel current recoding, 82–83
    - Si<sub>3</sub>N<sub>4</sub> septum, 81
    - solution exchanges, 78–79
    - transient currents, 84
    - vs.* patch-clamped membranes, 78
- Spherical cap approximation, 24
- Spherical protuberance, 24–25
- Stable free-standing BLMs
  - microfabricated apertures, 79, 81
  - microfabricated silicon chips
    - background current noise, 83
    - design, 79, 80
    - gramicidin channel, 83–84
    - membrane lifetime, 81–82
    - precoating, 81
    - single-channel current recoding, 82–83
    - Si<sub>3</sub>N<sub>4</sub> septum, 81
    - solution exchanges, 78–79
    - transient currents, 84
    - vs.* patch-clamped membranes, 78
- Stern model, 102
- Sterols
  - lipid bilayers
    - cholesterol, 168–171
    - lipid-cholesterol membranes, 173–176
    - phase behavior, 167–168
    - scattering studies, 176–178
    - structure, 160

- Supported and unsupported bilayers  
 characterization  
 area per molecule, 137  
 density profile, 137  
 head group/tail tilt, 138–139  
 mean-squared displacements and diffusion, 140  
 membrane thickness, 137  
 order parameter, 139  
 pressure and surface tension, 137–138  
 radial distribution functions, 139–140  
 reorientation, 140  
 density asymmetry, 142–143  
 dynamics  
 diffusion, 147–148  
 reorientation, 148–149  
 entropic repulsion, 147  
 lipid bilayer structure, 143–145  
 mechanical properties  
 compressibility, 150  
 fluctuations, 149–150  
 Helfrich Hamiltonian description, 149–150  
 perturbation, 149  
 pressure distribution, 145–146  
 visualization, 140–142  
 water layer thickness, 146–147
- Supported lipid bilayer (SLB)  
 biochemical sensors, 130–131  
 dipalmitoylphosphatidylcholine (DPPC)  
 lipids, 130  
 direct and indirect influences, 128–129  
 giant unilamellar vesicles (GUVs), 129  
 Martini model, 132  
 molecular simulations, 129–130  
 vesicle interactions, 131–132
- Time resolved synchrotron small angle X-ray scattering (TRSAXS), 182
- Tip-dip method, 72, 73
- Transbilayer electron density profile  $r(z)$ , 164–165
- Water molecule orientation  
 average microscopic volume charge density, 104  
 Bjerrum length, 105
- Boltzmann distribution function, 106–108  
 counterion and coion distribution, 103  
 effective permittivity, 105–107  
 electrostatic forces, 103  
 function  $F$ , 107  
 linearized modified Poisson–Boltzmann equation  
 average cosine, 117–118  
 boundary condition, 115  
 effective permittivity, 116  
 number densities, 116–117  
 modified Poisson–Boltzmann equation  
 average microscopic volume charge density, 112  
 boundary conditions, 115  
 effective permittivity, 114  
 function  $H$ , 113  
 Langevin dipole distribution function, 112  
 number density, 112  
 polarization, 113  
 probability, 112  
 volume charge density, 114–115  
 Poisson equation, 105  
 polarization  $P$ , 104
- White system, 35
- Wide angle X-ray scattering (WAXS), 181
- Wilhelm–Winterhalter–Zimmermann–Benz system, 39–40
- Wobschall system, 35–36
- X-ray scattering, lipid-sterol bilayers. *See also*  
 Cholesterol, lipid bilayers  
 cusp like singularities, 166  
 diffraction patterns, 162–163  
 lipid-water system, 163  
 quasielastic neutron scattering (QENS), 167  
 small angle neutron scattering (SANS), 167  
 structure factor  $S(q)$ , 166  
 thermal fluctuations, 165–166  
 transbilayer electron density profile  $r(z)$ , 164–165  
 two-dimensional (2-D) lattice, 161–163
- Yamaguchi–Nakanishi system, 41